ABSTRACT

Title of Dissertation: AUTHIGENESIS, BIOMINERALIZATION, AND CARBON-SULFUR CYCLING IN THE EDIACARAN OCEAN

Huan Cui
Doctor of Philosophy, 2015

Dissertation directed by: Dr. Alan J. Kaufman
Department of Geology

Fossil record of the Ediacaran Period (635-541 Ma) reveals unprecedented rise of early animal life (metazoan) in Earth history. Coupled with this evolutionary milestone, the Earth's atmosphere and hydrosphere experienced dramatic redox fluctuations. In order to better constrain the redox architecture of the Ediacaran ocean margin, an integrated chemostratigraphic correlation of the Doushantuo Formation in basin scale was conducted (see Chapter 2). The revised redox model suggests that euxinic conditions on the platforms were mainly restricted in lagoonal settings, which helps us to better understand Ediacaran fossil distributions and fluctuated $\delta^{13}C$ records in the Ediacaran strata in South China.

One of the most distinct features of the Ediacaran chemostratigraphy is the $\delta^{13}C$ negative excursion (i.e. Shuram Excursion, or SE) reported globally, which is the largest known C cycle anomaly in Earth history. In order to understand the biogeochemical processes that gave rise to the SE expressed in the upper Doushantuo Formation, systematic petrographic and geochemical investigations were conducted

for the outer shelf sections in the Yangtze block (see Chapter 3). Methane-derived authigenic calcite cements and nodules with extreme ^{13}C-depletion were discovered and interpreted as the first empirical evidence of authigenic mineralization associated with the SE. In light of these novel observations, it is proposed that the globally distributed SE may be formed by widespread syndeposition of authigenic carbonates in a sulfate-methane transitional zone positioned at the sediment-water interface in response to a global seawater sulfate increase.

Finally, to provide environmental context for the terminal Ediacaran biomineralization of animals, we conducted a high-resolution elemental and isotopic study of the richly fossiliferous Gaojiashan Member (see Chapter 4). Coincident with the first appearance of *Cloudina* are significant C-S-Ca-Sr cycle anomalies. It is proposed that the onset of calcarious biomineralization of animals may have coincided with an increase in terrestrial weathering fluxes of sulfate, alkalinity, and nutrients to the depositional basin. Enhanced concentration of Ca ion in seawater may have promoted the calcarious biomineralization of the early animals. Integrated chemo-, bio- and litho-stratigraphy of the Doushantuo and Dengying formations presented in this dissertation emphasized intimate co-evolution of Earth-life system during the Ediacaran Period.

AUTHIGENESIS, BIOMINERALIZATION, AND CARBON-SULFUR CYCLING IN THE EDIACARAN OCEAN

by

Huan Cui

Dissertation submitted to the Faculty of the Graduate School of the
University of Maryland, College Park, in partial fulfillment
of the requirements for the degree of
Doctor of Philosophy
2015

Advisory Committee:
Professor Alan J. Kaufman, Chair
Professor Shuhai Xiao
Professor Roberta L. Rudnick
Professor James Farquhar

© Copyright by
Huan Cui
2015

Preface

Studies presented in this dissertation cannot be completed without the support of the following collaborators and grant institutions. Here I would like to sincerely acknowledge them.

Chapter 2: Cui, H., Kaufman, A.J., Xiao, S., Zhu, M., Zhou, C., Liu, X-M., 2015. Redox architecture of an Ediacaran ocean margin: Integrated chemostratigraphic ($\delta^{13}C$–$\delta^{34}S$–$^{87}Sr/^{86}Sr$–Ce/Ce*) correlation of the Doushantuo Formation, South China. *Chemical Geology*, 405: 48-62.

I acknowledge Richard Walker, Igor Puchtel, Jingao Liu and Katherine Bermingham for the guidance of Sr isotope measurements in the UMD Isotope Geochemistry Laboratory. I also thank Yongbo Peng, Mike Evans, Rebecca Plummer, and Brittney Gaeta for their assistance in the UMD Paleoclimate CoLaboratory. This research was supported by funding from NASA Exobiology (NNX12AR91G), National Basic Research Program of China (2013CB835000), NSF Sedimentary Geology and Paleontology program (EAR0844270), an Explorers Club Exploration Fund Grant, an International Association of Sedimentologist (IAS) Graduate Student Research Grant, and an Society of Economic Geologists (SEG) Student Research Grant.

Chapter 3: Cui, H., Kaufman, A.J., Xiao, S., Zhou C., A Global Authigenic Response to Ediacaran Surface Oxidation. *About to be submitted soon.*

I thank Rebecca Plummer and Mike Evans for their assistance in the UMD Paleoclimate CoLaboratory, Peter Zavalij for the assistance on XRD analysis in the UMD X-ray Crystallographic Center, Phil Piccoli for the assistance on BSE imaging in the UMD Electron Probe Microanalyzer Laboratory, Timothy Rose for the assistance on cathodoluminescence imaging in the Smithsonian Institution, Richard Walker and Igor Puchtel for the guide on Sr isotope analysis in the UMD Isotope Geochemistry Laboratory, and Chengguo Guan for his help in sample collections.

This research was funded by NASA Exobiology (NNX12AR91G to AJK and NNX15AL27G to SX), NSF Sedimentary Geology and Paleontology (EAR0844270 and EAR1528553 to AJK; EAR1528553 to SX), Chinese Academy of Sciences (KZZD-EW-02 to CZ), and multiple graduate student research grants to HC, including the Mineralogical Society of America (MSA) Grant for Student Research in Mineralogy and Petrology, the Society of Economic Geologists (SEG) Student Research Grant, the Explorers Club Exploration Fund Grant, International Association of Sedimentologists Graduate Student Research Grant, and financial support from International Geoscience Program (IGCP) 587: Identity, Facies and Time - The Ediacaran Puzzle (PI: Patricia Vickers-Rich).

Chapter 4: Cui, H., Kaufman, A.J., Xiao, S., Peek, S., Cao, H., Min, X., Cai, Y., Siegel, Z., Liu, X-M., Peng, Y., Schiffbauer, J.D., Martin, A.J., Environmental

context for the terminal Ediacaran biomineralization of animals. In review for *Geobiology*.

I thank Mike Evans and Brittney Gaeta for their assistance in the UMD Paleoclimate CoLaboratory. This research is supported by funding from the NASA Exobiology Program (NNX12AR91G) to AJK, the NSF Sedimentary Geology and Paleontology program (EAR0844270 and EAR1528553) to AJK, the AAPG Grants-In-Aid Program to HC, and the Explorers Club Washington Group Exploration and Field Research Grant to HC.

Acknowledgements

In the past several months, I have been thinking on how to write this acknowledgement for many times with mixed feelings. For each time, it ends with a different version. My past four years in UMD was an adventure with joy, enrichment, gratitude, perhaps also including some frustration and depression. Here I would like to sincerely thank my advisor Dr. Alan Jay Kaufman, who led me into this research field, and trained me hand by hand from scratch. Jay's passion on this research field, and on presenting the beauty of science to the students, has always inspired, and will continue to inspire me in my future career. Lots of memories pop up into my mind. I still remember how Jay showed me the Ediacara-type fossil for the first time in an afternoon in Novosibirsk, with sunset casting light on the specimen surface. I still remember one day in Jay's office, he held a glacial drop stone sample collected from Namibia in front me, introducing an amazing world of the Snowball Earth to me. Memory also leads me into another day along the shore in Newfoundland, Jay kneed down for a long time on a surface of an outcrop, scrutinizing the soft-bodied animal impressions for a long time, as if that was the whole world at that moment. I also would not forget Jay's beautifully-outlined teaching slides for his Biogeochemistry course, which always made me feel so enjoyable when sitting in his class. Jay's creativity in teaching science, and the devotion to his students makes me feel so lucky in the past four years working with him. I sincerely thank Jay for his tremendous efforts, great passion and patience in guiding me into this exciting research field.

It’s a great fortune in my life to have Drs. Shuhai Xiao, Roberta Rudnick, and James Farquhar in my Ph.D. committee. They are all my role models in my future career. Collaborating with Shuhai in several projects was a great experience, during which I have been deeply influenced by Shuhai in so many ways. Shuhai’s thoughtful ideas, detailed field notes, considerable efforts on the student’s research and manuscripts, nice attitude in front of everyone, comprehensive knowledge on both palaeontology and geochemistry have inspired me deeply in the process working with him.

Every time when I think of Roberta, her big smile emerges in my mind. Roberta’s considerate attitude to everyone around her, realistic, serious and decisive style when at work, have influenced me significantly. I deeply appreciate Roberta’s considerable efforts on directing my Ph.D. program as my committee member. I feel lucky to have the chance to teach the High Temperature Geochemistry course with Roberta as a teaching assistant. Roberta’s class is always full of fun with lots of pleasant interaction among the students. I benefit so much as the TA for Roberta. I also feel a little sad when realizing that I could hardly see Zella and Sunny (the two four-legged sweeties) any more after graduation.

It is always fruitful when having coffee talks or email communications with Dr. James Farquhar. James’ emphasis on basic derivation from scratch of the equations or formula in both class and resserch inspired me a lot. Thanks James for

sharing your own experience in research with me! Your advice and suggestions make our talks very helpful. I deeply appreciate your support!

Thanks to William (Bill) McDonough for his inspiring and encouraging advises. Bill's perspectives on leadership, working attitude, and research styles have deeply impacted me. Bill, thank you so much! I really appreciate!

I also want to thank my research collaborators and labmates, including Chuanming Zhou (NIGPAS), Maoyan Zhu (NIGPAS), Yaoping Cai (NWU), Yongbo Peng (UMD, now in LSU), Xiaoming Liu (UMD, now in UNC), Rebecca Plummer (UMD), Sara Peek (UMD, now in USGS), Palma Jean Jarboe (UMD, now in USGS), Aaron Martin (UMD, now in IPICYT), Iadviga N. Zhelezinskaia (UMD) and Hansheng Cao (UMD, now in JLU). I am particularly grateful to the two great Paleoclimate lab managers Yongbo Peng (UMD, now in LSU), Rebecca Plummer (UMD) and Prof. Michael Evans (lab director, UMD). Without all your helps, I would not have finished my projects.

I feel so lucky that I have been working with so many considerate officemates. They are Lisa Schleicher (UMD, now in U.S.NRC), Sara Peek (UMD, now in USGS), Palma Jean Jarboe (UMD, now in USGS), Allison Greaney (now having fun exploring the geochemistry of the continental crust) and Scott Wipperfurth (now playing happily with geoneutrinos). Thank you so much for your kindness and tolerance!

As an international student from China, I also want to particularly thank Ming Tang, Hailong Bai, Kang Chen, Yongbo Peng, Hansheng Cao, Guijie Zhang, Yunpei Gao, Dongping Hu, Dandan Li, Xiaolin Zhang, Xiaoming Liu, Jingao Liu, Yu Huang, Nanping Wu, Chao Gao, Jiangyi Hou, Xu Yao, Su Li, Shaobing Zhang, Longlong Gou, Lihui Chen and Nicole (Siyu) Shan in the Geology Department. Days with you make my past four years full of joy.

Last but not least, I thank my families in China! Without their unconditional love, I would not have gone this far!

Table of Contents

List of Tables

List of Figures

Chapter 1: Introduction

1.1 Introduction on the Ediacaran Period (635-541 Ma)

One of the most important breakthrough in science during the 19th century is the rise of Darwin's theory of evolution, which fundamentally revolutionized our understanding on the Earth's life system (**Fig. 1.1**). Based on this theory, life evolved from its ancestor and selected by its adaptation capability to the environment. However, in the book *The Origin of Species*, Charles Darwin realized a challenge to his theory of evolution (Darwin, 1859). The sudden appearance of small shelly fossils in the lower Cambrian rock record as a prelude of the animal life biodiversification event (i.e. Cambrian Explosion) lacks its corresponding ancestors in the older rocks. To address this issue, Darwin proposed that there existed a significant hiatus in the geological record that erased the fossil evidence of Cambrian animal ancestors (Darwin would have known them as from the Silurian Period). As a critical interval spanning from the Marinoan glaciation (ca. 635 Ma; Condon et al., 2005) to the dawn of modern animal life (ca. 542 Ma; Amthor et al., 2003; Chen et al., 2015), the Ediacaran Period stands out as one of the most important transitions in Earth history (Knoll et al., 2006; Narbonne et al., 2012). Indeed, intensive studies through this geologic period reveal the presence of abundant fossils predating the Cambrian Explosion (**Fig. 1.1**), but that these are preserved in unusual circumstances and have no clear connection to modern phyla. Thus, a close look at the geobiology and biogeochemistry during the Ediacaran Period may help us to better understand some

of Charles Darwin's unsolved questions, and more profoundly, guide our society to strike a better balance between science and religion in the future (**Fig. 1.1**).

Figure 1.1: The statue of Charles Darwin in the British Museum (A), and a series of cover photos on the origin and evolution of life in the universe (from B to S). Cover photos are all from the internet. (B) Science's celebration of Charles Darwin's 200th birthday and the 150th anniversary of the publication of On the Origin of Species on 9 January 2009. (C) Snowball Earth glaciation (Hoffman et al., 1998a). (D) Three-dimensional preservation of animal embryos discovered in the Doushantuo Formation, South China (Xiao et al., 1998). (E) Rare helical spheroidal fossils from the Doushantuo Lagerstätte (Xiao et al., 2007). (F) The acritarch *Meghystrichosphaeridum chadianesis* from the Doushantuo formation (Peterson and Butterfield, 2005). (G) Reconstructed Ediacara biota (Xiao and Laflamme, 2009). (H) Soft-bodied organism *Pteridinium simplex* in sandstone beds of the terminal Proterozoic (~550 Ma) Nama Group in Namibia (Knoll and Carroll, 1999). (I) An example of the oldest known complex life forms on Earth (Narbonne, 2004). (J) The sharply outcropping cap carbonate at the base of the Nafun Group above the Marinoan glacial in Oman (Shields-Zhou and Och, 2011). (K) Reconstructed

Ediacara biota and the soft-bodied impressions presered on the rock record (Fedonkin et al., 2007). (L) Ediacaran algal fossils in Doushantuo Formation (Xiao and Kaufman, 2006). (M) Reconstructed early Cambrian animal (Erwin and Valentine, 2012). (N) The Great Unconformity in the Grand Canyon separating the Cambrian sandstone from the underlying Paleoproterozoic sedimentary rocks (Peters and Gaines, 2012). (O) The Cambrian Explosion (i.e. Evolution's Big Bang) reported by Time magazine in December 4th, 1995 edition. (P-R) The Curiosity rover exploration on Mars reported by Science magazine. (S) Debate on "God vs. Science" reported by Time magazine in Nov. 13, 2006.

The focus of my dissertation is the Ediacaran Period. Ratified by the IUGS (International Union of Geological Sciences) in 2004, the Ediacaran Period (ca. 635–542 Ma) is the first stratigraphically defined geological period proposed since 1891 (Knoll et al., 2004; Knoll et al., 2006) (**Fig. 1.2**). The GSSP (Global Boundary Stratotype Section and Point) for the Ediacaran Period lies at the base of the Nuccaleena Formation cap carbonate, directly above glacial diamictites in the Flinders Ranges of South Australia. Coeval strata have been found in different continents all over the world, including Namibia, Newfoundland, Australia, Mongolia, Oman, South China and Siberia (Narbonne et al., 2012).

Although Precambrian fossil records are relatively rare and scattered compared with those of the Phanerozoic, discoveries from Ediacaran successions in different localities worldwide by paleontologist for the past several decades reveal a many amazing albeit enigmatic fossils (**Figs. 1.1, 1.2**). Most of the macroscopic Ediacaran biota are preserved as soft-body impressions (Narbonne, 2005) in fine-grained sandstone or siltstone, but occasionally they are also preserved as carbonaceous compressions in black shale (Xiao et al., 2002; Yuan et al., 2011) and carbonate (Xiao et al., 2005; Grazhdankin et al., 2008; Chen et al., 2013). Although

few macroscopic Ediacaran animals have been discovered in the intensively studied Doushantuo and Dengying formations of South China (Ding and Chen, 1981; Xiao et al., 2005; Chen et al., 2014a), this Lagerstätte preserves abundant microfossils, including algae (Yuan et al., 2005), animal embryos (Xiao et al., 1998), acritarchs (Liu et al., 2014; Xiao et al., 2014b), and sponge fossils (Yin et al., 2015a). Researchers have also reported the typical late Ediacaran biomineralized animal *Cloudina* in the Dengying Formation (Bengtson and Zhao, 1992; Hua et al., 2005).

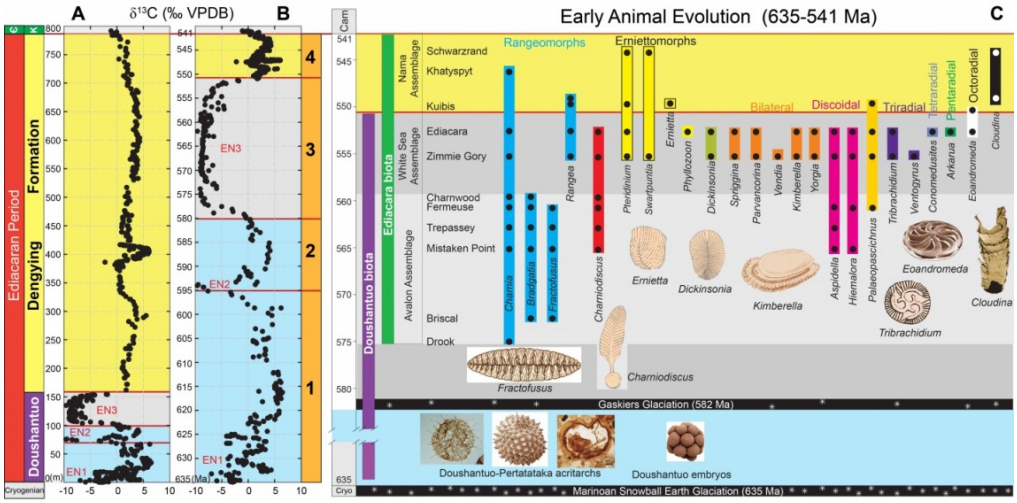

Figure 1.2: A simplified chemo- and bio-stratigraphy of the Ediacaran Period. (A) Carbon isotope record for the Ediacaran Period plotted against height in a generalized stratigraphic column for strata in South China. Data for the Doushantuo Formation were determined from samples collected in the Three Gorges Area (McFadden et al., 2008). Data for the Dengying Formation were taken from samples from the Gaojiashan section (see Chapter 4). (B) Carbon isotope record for the Ediacaran Period plotted against time (see alsoAn et al., 2015 for a critical re-evaluation). The comparison between A and B suggests enhanced sedimentation rate during the deposition of the Dengying Formation. Based on the C isotope trend, the Ediacaran Period could roughly be divided into four intervals (shown on the right side of column B). (C) Early animal life evolution during the Ediacaran Period, modified after Xiao and Laflamme (2009). Note that the time-scale in C is different from that in B. Based on the fossil record, most of the macroscopic Ediacaran fossils are found after the Gaskiers glaciation (ca. 582 Ma) (Bowring et al., 2003), whereas fossils revealed before this glaciation are dominated by microfossils. EN=Ediacaran carbon isotope Negative excursion.

The exceptionally preserved Ediacaran fossils discovered from scattered localities, on one hand, greatly fill the knowledge gaps in Precambrian animal evolution, and on the other hand, lead people to think more deeply about the causal link between biotic innovations and paleoenvironmental conditions at the dawn of animal life. Insofar as megascopic life requires oxygen to maintain basic eukaryotic metabolism (Nursall, 1959; Cloud, 1976), a rise of oxygen in both atmosphere and hydrosphere (aka. the Neoproterozoic Oxygenation Event or NOE) has been proposed to occur during the Ediacaran Period (Derry et al., 1992; Kaufman et al., 1993; Kaufman et al., 2007; Shields-Zhou and Och, 2011; Och and Shields-Zhou, 2012; Lyons et al., 2014).

Based on the C isotope trend revealed in South China, the Ediacaran Period could be roughly divided into four sub-units using EN2 and EN3 as boundaries (**Fig. 1.2**). Combined with the fossil record, more detailed divisions for the Ediacaran Period have been proposed in Narbonne et al. (2012) using microfossil assemblages as an additional tool for stratigraphic subdivision. However, how to project (i.e. correlate) local C isotope excursions (e.g., EN2) and microfossil assemblages in South China (e.g., Liu et al., 2014), and glaciation event (i.e., Gaskier glaciation) in Newfoundland and the Varanger penninsula onto the global stage for broader integration of the Ediacaran strata wordwide still remains unresolved. Nevertheless, the Shuram Excursion and the first appearance of biomineralized animals (i.e., *Cloudina*) have been widely reported in the Ediacaran strata worldwide, which stand out as the best marker horizon for Ediacaran subdivision regardless of whether it is a

primary or diagenetic phenomenon, or a combination of both. Thus, a better understanding of the biogeochemical origin of the Shuram Excursion (see Chapter 2 and 3) and the environmental context for the terminal Ediacaran biomineralization of animals (see Chapter 4) will hopefully guide us better understanding the Ediacaran Earth system and temporal subdivsion.

To date, a series of studies by biogeochemists support this hypothesized Neoproterozoic Oxygenation Event (Derry et al., 1992; Kaufman et al., 1993; Shields-Zhou and Och, 2011; Och and Shields-Zhou, 2012 and references therein). Based on iron speciation analyses and sulfur isotope measurements of Ediacaran deep-water sediments on the Avalon Peninsula of Newfoundland, Canfield et al. (2007) proposed that the deep ocean was *ferruginous* before and during the Gaskiers glaciation ca. 580 million years ago, but thereafter became progressively *oxidized*. Subsequent studies of the paired carbon (carbonate carbon and organic carbon) and paired sulfur (pyrite sulfur and sulfate sulfur) isotope analyses of the Ediacaran Huqf Suergroup in Oman (Fike et al., 2006) and the Ediacaran Doushantuo Formation in South China (McFadden et al., 2008) reveal the possibility of several *pulsed oxygenation events* after the Marinoan Snowball Earth glaciation. The Shuram carbon isotope excursion (the most negative carbon isotope anomaly recorded in Earth history) in both of these sections might be the tipping point between predominantly reduced and generally (but not pervasively) oxidized Ediacaran oceans. Recently, based on the enrichment of redox-sensitive trace element of the early Ediacaran organic-rich black shales (~632 Ma) in the basal Doushantuo Formation, it is revealed

that the ocean was likely oxygenated in the immediate aftermath of the Marinoan glaciation (Sahoo et al., 2012).

However, other studies indicate that the trajectory of surface oxygenation, thought to be uni-directional, irreversible and widespread, might be more complex. Carbon and sulfur isotopes of different sections across the Doushantuo basin indicate that the early Ediacaran ocean in South China may have been strongly stratified with a profound dissolved inorganic carbon (DIC) pool (Jiang et al., 2007), and an oceanic sulfate gradient from shelf to deep basin (Li et al., 2010). In this geochemical model the deep ocean remained ferruginous at that time. Geochemical reconstructions on Ediacaran strata in NW Canada and southern Namibia reveal dominantly anoxic conditions in the Ediacaran ocean, conflicting with the hypothesized oxygenation in late Ediacaran Period (Johnston et al., 2013; Wood et al., 2015). Moreover, studies of Late Cambrian strata reveals that there might exist a widespread euxinic (containing free H_2S) ocean (Gill et al., 2011). Thus the redox condition of the ocean appears to have fluctuated or was heterogeneous from basin to basin across the late Neoproterozoic–Cambrian transitional period. Further studies on the Ediacaran carbonate-dominant successions may help us better understand the redox evolution of the ocean at that time.

1.2 Redox architecture of the Ediacaran ocean

Ediacaran successions in most locations are normally siliciclastic-dominant or variably altered by diagenesis and metamorphism. As such they are less useful for

biogeochemical studies. In contrast, the Ediacaran successions in South China are carbonate-dominated and fossiliferous (Jiang et al., 2011), and are thus promising research targets for the time-series elemental and isotopic studies. *In this dissertation, I systematically reconstructed chemostratigraphic profiles of the Doushantuo Formation at Yangjiaping (see Chapter 2) and Zhongling (see Chapter 3), as well as the Dengying Formation in the Gaojiashan section (see Chapter 4) in South China.*

The Ediacaran successions in South China, which widely blanket the Yangtze block, are mainly composed of two units, the Doushantuo (ca. 635–551 Ma) and Dengying formations (ca. 551–542 Ma) (Condon et al., 2005; Zhou and Xiao, 2007; Zhu et al., 2007; Jiang et al., 2011). The Doushantuo Formation is typically floored by a lithologically and geochemically distinct cap carbonate immediately above the Marinoan Nantuo diamictite. The formation is capped by thick black shale below the massive Dengying dolostone. Abundant three-dimensional algae, animal embryos, and acritarchs have been discovered in phosphorite or chert nodules of the Doushantuo Formation (Xiao et al., 1998; Liu et al., 2014; Xiao et al., 2014a; Xiao et al., 2014b). Generally the deposition of the Doushantuo Formation in South China is divided into two stages: (A) the Marinoan cap carbonate and its overlying shale layers were deposited in an open shelf environment, and (B) the upper part of the Doushantuo Formation was formed in a rimmed shelf environment (Jiang et al., 2011). Thus, the late Ediacaran paleogeography in South China suggests an increase in the water depth from the platform in the northwest to deep basin in the southeast. Two belts, including an inner shelf lagoonal facies and an outer shelf shoal facies,

between the NW platform and the SE slope and deep basin environment appear in recent reconstructions (Jiang et al., 2011).

The current reconstructed redox architecture of the Ediacaran ocean margin during deposition of the Doushantuo Formation is controversial. On the one hand, Li et al. (2010) proposed a sandwich configuration, comprised of a thin oxic layer on the surface ocean, a euxinic wedge on the open shelf and a ferruginous deep basin. On the other, Jiang et al. (2011) proposed that the euxinia along the Doushantuo margin was restricted to lagoonal facies based on their paleogeographic and sedimentological reconstructions. *In Chapter 2, I conducted a basin-scale $\delta^{13}C$-$\delta^{34}S$-$^{87}Sr/^{86}Sr$ chemostratigraphic correlation of the Doushantuo Formation in inner shelf (NXF section), intra shelf (Jiulongwan sections) and outer shelf (Yangjiaping and Zhongling sections), in order to test these two competing hypotheses.*

1.3 Biogeochemistry of the Ediacaran Shuram excursion

A distinct feature of the time-series C isotope record measured from the Doushantuo Formation in Three Gorges area is its large and consistent C isotope negative excursion (EN3 or DOUNCE) in the upper section (Jiang et al., 2007; McFadden et al., 2008; Lu et al., 2013; Zhu et al., 2013b). This dramatic excursion is well correlated with the Shuram Excursion (SE) first reported in the Shuram Formation of Oman (Burns and Matter, 1993; Fike et al., 2006), which is regarded as the most negative carbon isotope anomaly in Earth history (Le Guerroué and Cozzi, 2010; Grotzinger et al., 2011). For the past decade, intensive studies of the SE have

been conducted and carbon isotope excursions of similar magnitude have been found globally in Death Valley and Mexico (Kaufman et al., 2007; Loyd et al., 2013), South Australia (Calver, 2000; Husson et al., 2015), Siberia (Pokrovskii et al., 2006a; Melezhik et al., 2009), and Western Canada (Macdonald et al., 2013).

Several hypotheses have been proposed for the interpretation of the origin of this enigmatic carbon cycle anomaly:

- DOC Hypothesis: Mainly based on decoupling between paired C isotopes, it is proposed that during the Ediacaran Period, there existed an overwhelming dissolved organic carbon (DOC) reservoir in the deep ocean (Rothman et al., 2003). Microbial oxidation of this deep ocean DOC reservoir created ^{12}C alkalinity that was subsequently recorded in carbonate sediment (Fike et al., 2006).
- Stratified Ocean Hypothesis: Based on platform to basin chemostratigraphic correlations of the Doushantuo Formation in South China, it is proposed that there existed a DIC gradient in seawater. In this model the Ediacaran ocean is stratified with a thin oxic surface layer on top and an anoxic deep ocean below a chemocline (Jiang et al., 2007; Ader et al., 2009). The SE may thus have been a result of a rise in chemocline or an upwelling event (Zhou et al., 2012).
- Fossil Organic Carbon Hypothesis: Based on parallel decrease in paired sulfur $\delta^{34}S_{py}$ and $\delta^{34}S_{CAS}$ isotopes during the SE, it is suggested that enhanced oxidative chemical weathering occurred during a sea level regression. In this scenario an intensive amount of oxidized fossil organic carbon and pyrite sulfur are delivered into the ocean by riverine inputs, which caused a decrease in both carbon and

sulfur isotopes (Kaufman et al., 2007). This scenario is also consistent with a continuous rise in $^{87}Sr/^{86}Sr$ from 0.7080 during pre-SE to 0.7090 at the end of the SE globally (Burns et al., 1994; Melezhik et al., 2009; Sawaki et al., 2010; Cui et al., 2015).

- Diagenesis Hypothesis: Mainly based on the notable positive correlation between $\delta^{13}C_{carb}$ and $\delta^{18}O_{carb}$ during the SE, it is proposed that the biogeochemical event was a result of burial diagenesis (Derry, 2010). In this model, meteoric waters containing remineralized organic carbon from land plants penetrated carbonate strata during migration thereby resulting in altered carbonate that is both depleted in $\delta^{13}C_{carb}$ and $\delta^{18}O_{carb}$ (Knauth and Kennedy, 2009).
- Methane oxidation hypothesis: Bjerrum and Canfield (2011) explained the SE as the result of massive release of methane hydrates from an anoxic DOC-rich ocean. It was also proposed that the negative $\delta^{18}O_{carb}$ excursion during SE may be due to a rise in temperature caused by an increase in greenhouse gases. However, the hypothesis is model driven and lacks direct geological evidence.
- Authigenic Carbonate Hypothesis: A recent model proposed that variations in the abundance of organic carbon, oxidants [Fe(III), sulfate and oxygen] and DIC led to the production of authigenic carbonates in marine sediments, especially during times of low oxygen (Higgins et al., 2009). Based on this model and observations of modern authigenic carbonates along the continental margin, it was proposed that the SE might be formed by mixing of DIC-depleted authigenic carbonates during a sea level transgression (Schrag et al., 2013).
- The Acraman impact hypothesis: Recently, it has been suggested that the Acraman

impact recorded by a crater in South Australia may be time-equivalent to the SE (Young, 2013; Young, 2015). A series of paleoenvironmental feedbacks caused by this impact event may have triggered the SE, but a detailed biogeochemical mechanism is lacking.

Although these different hypotheses paint remarkably different scenarios for the SE, future studies should incorporate the following geological and geochemical observations:

- Widespread appearance of SE in different continents globally.
- A sudden drop of carbonate carbon isotope $\delta^{13}C_{carb}$ from +5‰ followed by consistent values of around -10‰ during SE with little sample-to-sample variations.
- Decoupling of paired carbon $\delta^{13}C_{carb}$ and $\delta^{13}C_{org}$ isotopes during SE.
- Coupling of an increase in $^{87}Sr/^{86}Sr$ and a decrease in paired sulfur $\delta^{34}S_{py}$ and $\delta^{34}S_{CAS}$ isotopes.
- A tight positive correlation of $\delta^{13}C_{carb}$ and $\delta^{18}O_{carb}$ in the carbonate records of SE.
- Rock records during SE show both high energy environment (represented by oolites with hummocky cross bedding) and deep water environment (represented by fine grain sized sediments like shale).
- Sea level transgression during the declining part of the SE in Oman, South Australia and Death Valley and a sea level highstand in SE of South China (Grotzinger et al., 2011).

In Chapter 3, I conducted detailed petrographic and geochemical investigations of authigenic carbonates in the Doushantuo Formation from the Zhongling sections. I discovered methane-derived authigenic calcite associated with the SE, thus suggesting that the biogeochemical anomaly was created by proportional mixing of primary and syndepositional authigenic carbonates.

1.4 Environmental context of animal biomineralization

The late Ediacaran Dengying Formation in South China hosts some of the earliest skeletal animals fossils, including *Cloudina* and *Sinotubulites* (Bengtson and Zhao, 1992; Hua et al., 2003; Hua et al., 2005; Hua et al., 2007; Cai et al., 2015), various Ediacara-type fossils (Xiao et al., 2005; Chen et al., 2014a), and numerous animal trace fossils (Chen et al., 2013; Meyer et al., 2014). Radiometric dates from the Yangtze Gorges area constrain the Dengying Formation to have been deposited between 551 and 541 Ma, representing the last 10 million years of the Ediacaran Period (Amthor et al., 2003; Condon et al., 2005; Chen et al., 2015). In chapter 4, I focus on the Gaojiashan Member of the Dengying Formation at the Gaojiashan section, where the Gaojiashan biota are preserved (Cai et al., 2010; Cai et al., 2012).

Largely based on the boring holes found in biomineralized fossils, it was hypothesized that the driving force for animal biomineralization is the ecological pressure imposed by predation (Bengtson and Zhao, 1992; Hua et al., 2003; Porter, 2011). Once armed with skeletons, animals have been engaged in positive ecological

feedbacks with their predators, and such ecological feedbacks greatly accelerated the evolutionary rates and culminated in the Cambrian Explosion (Xiao, 2014). Another hypothesis explaining the onset of biomineralization is based on environmental change associated with variations in the chemistry of ambient seawater. It was suggested that seawater alkalinity played a key role in the formation of the calcareous microbialites (Kempe and Kazmierczak, 1994). Similarly, animals living in an alkaline ocean likely evolved the function of biocalcification as a mechanism for detoxification due to too much calcium in the ocean (Simkiss, 1977). Indeed, massive seafloor-precipitated aragonite fans in coeval strata of the Nama Group suggest high alkalinity in the contemporaneous ocean (Grotzinger et al., 2005).

In chapter 4, based on integrated C, S isotope and trace element chemostratigraphy of the Gaojiashan Member, it is revealed that the onset of animal biomineralization in the Gaojiashan biota is closely associated with dynamic biogeochemical C and S perturbations likely driven by enhanced weathered flux into the ocean. A comparison with other Ediacaran sections in Oman and Namibia suggests possible temporal coupling between animal evolution and changing oceanic biogeochemistry on a global scale.

Chapter 2: Redox architecture of an Ediacaran ocean margin: Integrated chemostratigraphic ($\delta^{13}C$–$\delta^{34}S$–$^{87}Sr/^{86}Sr$–Ce/Ce*) correlation of the Doushantuo Formation, South China

2.1 Abstract

Early diagenetic silicification and phosphatization of the Ediacaran Doushantuo Formation (ca. 635 to 551 Ma) in South China offer extraordinary taphonomic windows into the early evolution of multicellular eukaryotes, including various algal groups and potentially animals. In order to understand how the ecological and taphonomic distribution of these Ediacaran eukaryotes was controlled by oceanic redox conditions, it is critical to reconstruct the redox architecture of the sedimentary basin. Recently two alternative redox models have been proposed to account for the geochemical and sedimentary features of the Doushantuo Formation. One argues that the unit was deposited on a continental margin where a metastable sulfidic wedge was dynamically maintained by a sulfate concentration gradient between shelf and basinal environments. The other contends that the sulfidic water mass was largely restricted to the intra-shelf basin behind a rimmed margin. These two models make different predictions about the stratigraphic completeness and correlation of the Doushantuo Formation. To test these predictions, we generated high-resolution time-series trends of multiple isotopic and elemental tracers, including $\delta^{34}S$, $^{87}Sr/^{86}Sr$ and Ce/Ce*, to facilitate an integrated chemostratigraphic

correlation between inner shelf (Xiaofenghe), intra shelf (Jiulongwan), and outer shelf (Yangjiaping and Zhongling) sections. Our correlations suggest that both the inner and outer shelf sections are stratigraphically incomplete relative to the intra shelf section. The euxinic wedge model should be reconsidered insofar as it is based on a miscorrelation between sections. Viewed from our revised chemostratigraphic framework, euxinic conditions on the platform appear to have been largely restricted to the intra shelf basin. Carbonates in the upper Doushantuo Formation at Jiulongwan and their stratigraphic equivalents are characterized by a profound negative carbon isotope anomaly (i.e., the Shuram Excursion) coincident with a drop in pyrite sulfur isotope values and a significant rise in $^{87}Sr/^{86}Sr$ from 0.7080 to 0.7090. The integrated stratigraphic data from South China suggest that the onset of the Shuram Excursion is associated with enhanced oxidative continental weathering that delivered radiogenic strontium, as well as sulfate, to the Ediacaran basin.

2.2 Introduction

The unrestricted Modern ocean is pervasively oxygenated from the surface to the abyssal deep (with oxygen content ranging from 3.5 to 7 ml/L depending on the salinity and temperature of various ocean masses) with the exception of oxygen minimum zones where the remineralization of particulate organic matter by aerobic bacteria draws the breathing gas to its lowest concentration (ca. 0.2 ml/L) (Deutsch et al., 2011). Nitrate can also become limiting in these zones as denitrifying bacteria use the oxidant for respiration. Animals living in oxygen minimum zones must either have a reduced metabolic rate or be very efficient at extracting O_2 from seawater.

Some of these animals have evolved to have large gill surface areas, resulting in short diffusion distances from the water to the blood. Given that even the simplest animals require a few percent of present atmospheric levels (Mills et al., 2014) and more complex organisms need much more to engage in more active life styles, it is important to understand the redox state of the water column and how oxygen contents in shallow marine ecosystems might be modified by future global warming (Mora et al., 2013)

Determining the redox architecture of ancient ocean margins is particularly important in the Ediacaran Period (635 to 541 Ma) when the first large complex life forms (including animals) evolved (Xiao and Laflamme, 2009), assuming the Ediacara biota required O_2 for their metabolic activities and acquired the gas through diffusion (Laflamme et al., 2009). Most, if not all, fossils of the Ediacara biota appear in the sedimentary record following a profound negative carbon cycle anomaly known as the Shuram Excursion (Grotzinger et al., 2011; Macdonald et al., 2013) named after strata in Oman where the event was first described (Burns and Matter, 1993). During this event the carbon isotopic compositions of bedded carbonates, including some oolitic and stromatolitic facies (*cf.* Melezhik et al., 2009; Lu et al., 2013), fell to a nadir of less than –10‰ and stabilized for millions of years before returning to pre-event conditions. This profound negative carbon cycle anomaly has been interpreted in various ways, including 1) modification of global seawater compositions through oxidation of dissolved organic compounds in the oceans (Rothman et al., 2003), fossil organic carbon exposed on land (Kaufman et al., 2007),

or methane in clathrates (Bjerrum and Canfield, 2011), 2) mixing of normal seawater precipitates with authigenic carbonates of anomalous isotopic composition formed through anaerobic metabolic activities (Schrag et al., 2013), or 3) alteration of carbonate sediments through interaction with diagenetic fluids of terrestrial origin (Knauth and Kennedy, 2009; Derry, 2010).

The Shuram Excursion is well developed in Ediacaran successions throughout South China (Jiang et al., 2007; Zhu et al., 2007; McFadden et al., 2008; Jiang et al., 2011; Wang et al., 2012b; Lu et al., 2013; Tahata et al., 2013; Zhu et al., 2013b), including the well-studied intra-shelf section near Jiulongwan (**Fig. 2.1A, B**) where the onset of the carbon isotope event occurs in dolostone and limestone facies immediately above a thick cherty horizon (McFadden et al., 2008). Notably, in both the proximal inner shelf section at Xiaofenghe, as well as the distal outer shelf sections at Zhongling and Yangjiaping, the Shuram carbon isotope anomaly is missing altogether, or is very poorly expressed (Zhu et al., 2007; Li et al., 2010; Kunimitsu et al., 2011; Xiao et al., 2012; Liu et al., 2013; Zhu et al., 2013b). Based on iron-speciation analyses and a clear sulfur isotope contrast between sections in the uppermost Doushantuo Formation at Jiulongwan and Zhongling (believed at the time to represent deep water deposition on the continental slope), Li et al. (2010) proposed that a metastable euxinic wedge was maintained dynamically across the ramp by a gradient of sulfate concentration between shallow and deep settings (**Fig. 2.1C**). Such redox modeling is based on the assumption that sections of the Doushantuo Formation in inner shelf Jiulongwan and outer shelf Zhongling section are continuous

and well correlated (see Fig. S7 of Li et al., 2010). Sedimentary facies analyses, however, suggest that the sections at Zhongling and nearby Yangjiaping accumulated in shallow waters along an elevated margin rim, suggesting that euxinic conditions on the platform may have been restricted to an intra shelf setting (Zhu et al., 2007; Jiang et al., 2011; Zhu et al., 2013b). Similar conditions may have also characterized deep-water slope settings distal from the rimmed shelf based on the preponderance of framboidal relative to euhedral pyrite preserved in the sediments and abundances of redox-sensitive trace elements (**Fig. 2.1D**; Sahoo et al., 2012; Wang et al., 2012a). These observations suggest that euxinia may have been patchy across Doushantuo margin environments, and that the wedge model needs to be reconsidered in light of improved stratigraphic correlation and integrated geochemical data.

To search for the Shuram Excursion in the outer shelf environments preserved at Zhonging and Yangjiaping (~90 km to the southwest of Jiulongwan) where phosphorite is abundant in the upper reaches of the Doushantuo Formation, and to test the hypothesis that the shoal complex in this setting is stratigraphically incomplete, we applied time-series $\delta^{13}C$, $\delta^{34}S$, and $^{87}Sr/^{86}Sr$ isotope data from four sections (with Ce/Ce* from two of these) that span across the platform margin (**Fig. 2.1E**). The integrated results provide a systematic framework of chemostratigraphic correlations that allow us to test the two competing redox reconstructions for the Ediacaran basin. In addition, the time-series trends provide environmental context for the Laggerstätten of unicellular and multicellular eukaryotes preserved in the Doushantuo

Formation, and also allow us to evaluate the role of continental weathering at a time of rising atmospheric oxygen as a critical driver of the Shuram Excursion.

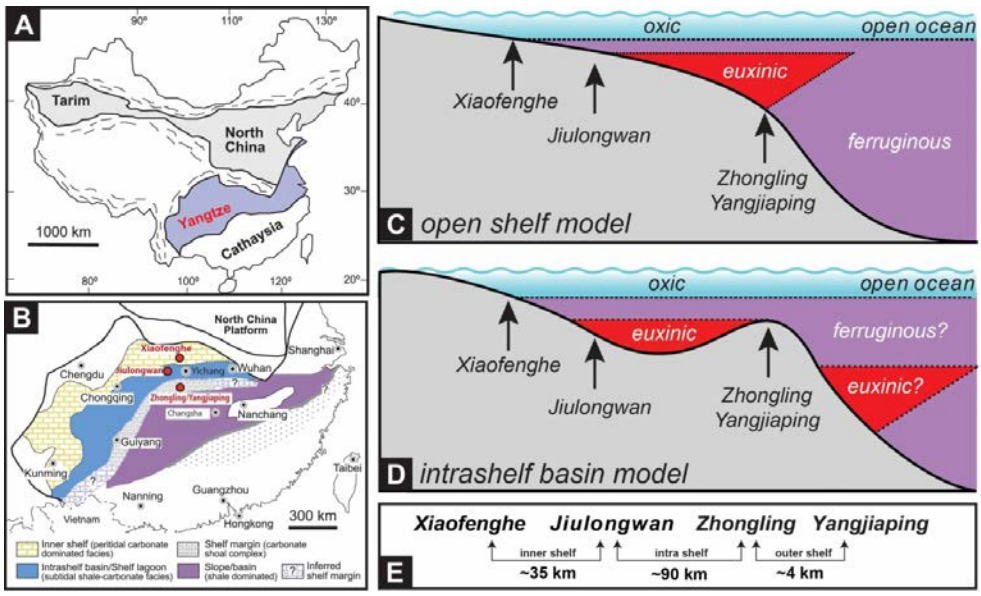

Figure 2.1: (A) Geological map of China, with the Yangtze Craton highlighted in color. (B) Reconstructed Ediacaran depositional environments on the Yangtze Craton (Jiang et al., 2011). Red dots mark the location of the four sections discussed in this paper. (C) Open shelf model with a metastable sulfidic wedge maintained dynamically by overall low oceanic sulfate concentrations and a gradient of sulfate concentration between shallow and deep environments (Li et al., 2010). (D) Intra-shelf basin model with euxinic water mass largely restricted in lagoonal and deep basin settings (Jiang et al., 2011; Sahoo et al., 2012; Wang et al., 2012a). (E) Distance between each correlated sections.

2.3 Geologic setting

Ediacaran successions in South China that blanket the Yangtze block include the richly fossiliferous Doushantuo and Dengying formations. Abundant three-dimensionally preserved eukaryotes, including multicellular algae, sponge, putative animal embryos, and acritarchs, have been discovered from phosphorites and chert nodules of the Doushantuo Formation (Xiao et al., 1998; Liu et al., 2014; Xiao et al., 2014b; Muscente et al., 2015; Yin et al., 2015b), while Dengying strata contain

macroscopic Ediacara fossils and trace fossils (Chen et al., 2013; Chen et al., 2014a; Meyer et al., 2014). The basal Doushantuo Formation is underlain by the Nantuo diamictite and begins with a ca. 635 Ma cap carbonate (Condon et al., 2005). In the Yangtze Gorges area, this formation is informally divided into four distinct members (McFadden et al., 2008) and is typically capped by black shale below massive dolostone of the Dengying Formation (Jiang et al., 2011). The boundary between the two formations is constrained in age to be <551 Ma (Condon et al., 2005), suggesting that the Doushantuo carbonate platform accumulated over a period of 84 million years or more. Hence, the Doushantuo Formation is remarkably thin for the geological time it occupies. The mixed shale and carbonate in the inner shelf Jiulongwan section, which is well exposed along a road cut during the construction of the Yangtze Gorges Dam, has a thickness of only ~160 meters. In contrast, the carbonate-rich outer shelf section at Zhongling and Yangjiaping have thicknesses of 260 and 180 meters, respectively (Zhu et al., 2007; Jiang et al., 2011; Muscente et al., 2015). Continental slope and basinal environments of the Doushantuo Formation further to the southeast are significantly thinner and are dominated by fine-grained siliciclastics with only thin carbonate turbidite interbeds (Jiang et al., 2007; Zhu et al., 2007).

The Doushantuo Formation formed in two stages, with an open ramp shelf environment building up to a rimmed shelf protecting an intra-shelf lagoon (Jiang et al., 2011). Paleogeographic reconstructions of strata on the Yangtze Platform indicate an increase in the water depth from proximal intertidal environments in the northwest

to distal deep basinal settings in the southeast. Three platform facies belts are apparent, including proximal inner shelf peritidal carbonates, an intra-shelf lagoon containing mixed carbonate and shale, and an outer shelf shoal complex (**Fig. 2.1B**). The Doushantuo section at Zhongling previously studied by Li et al. (2010) is representative of the shoal complex facies, as is the Yangjiaping section some four kilometers distant that was sampled in this study. At Zhongling and Yangjiaping, the Doushantuo Formation is mainly composed of interbeded shale and carbonate, with an increasing preponderance of intraclastic and oolitic facies up-section, indicating shallower and higher-energy depositional environments. The Doushantuo in the shoal complex is terminated by several phosphorite horizons that occur just below the overlying Dengying Formation (**Fig. 2.2**; Jiang et al., 2007; Jiang et al., 2011; Kunimitsu et al., 2011), which is characterized by massive dolostone deposited in peritidal environments.

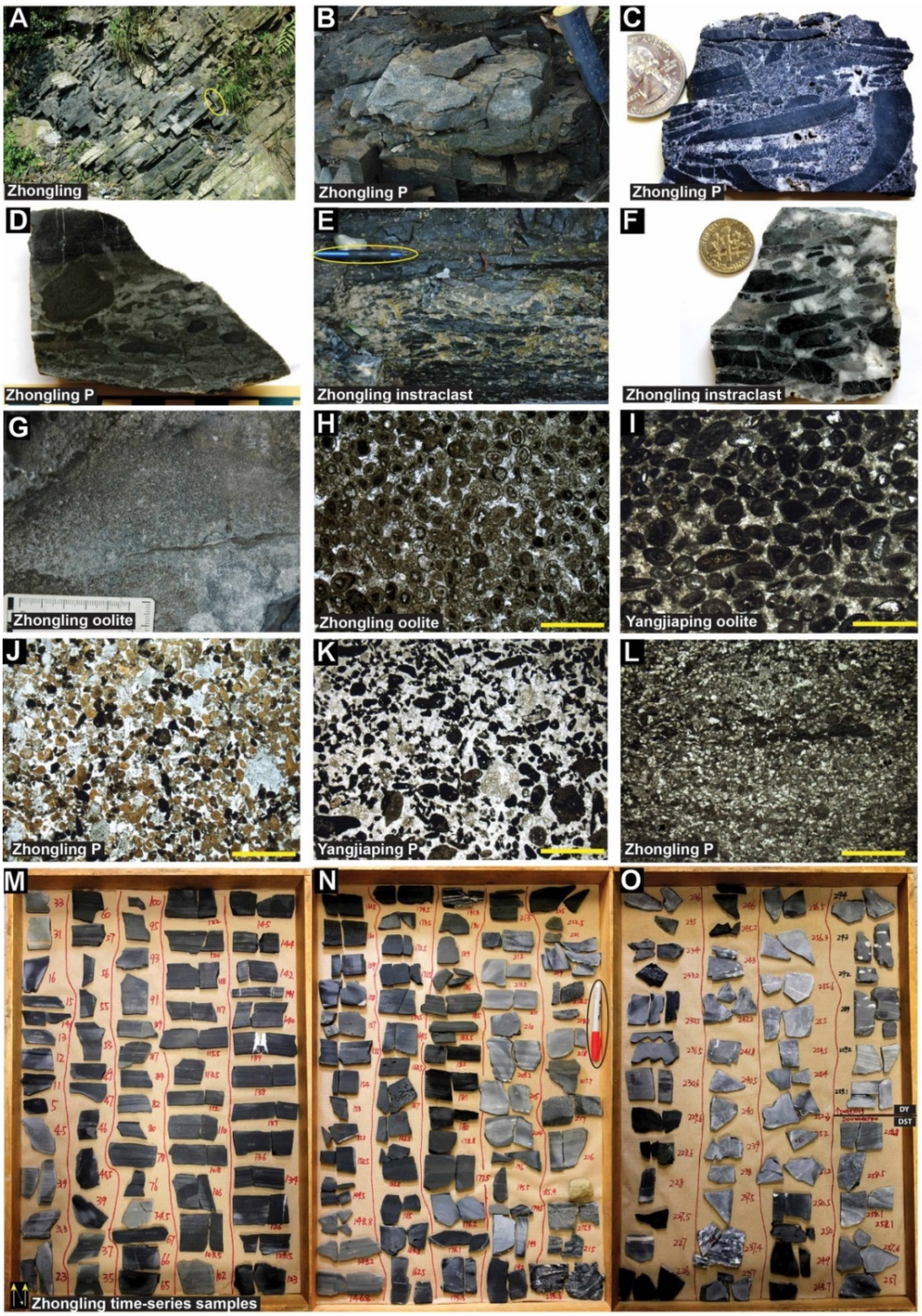

Figure 2.2: Sedimentological observations of the Doushantuo Formatoin at outer shelf Zhongling and Yangjiaping sections. (A) Thin bedded, dark gray limestone of the Doushantuo Formation at Zhongling, about 120 meters above the Nantuo diamictite. The geological hammer is circled as a scale. (B) Intraclastic phosphorite interbedded with black shale about 42 m below the Doushantuo/Dengying (DST/DY)

boundary at Zhongling. (C) Phosphorite (12ZL-45.4) about 45.4 m below the DST/DY boundary at Zhongling. (D) Intraclastic phospharite (14ZL-1.3) about 1.3 m below the DST/DY boundary at Zhongling. (E) Intraclastic dolostone about 22 m below the DST-DY boundary at Zhongling. The pencil is circled as a scale. (F) Intraclastic dolostone (12ZL-21.6) about 21.6 m below the DST/DY boundary at Zhongling. (G) Oolitic dolostone about 18.5 m below the DST-DY boundary at Zhongling. (H) Petrographic thin section of oolitic dolostone (12ZL-21) with calcite cements under plane polarized light. Sample was collected about 21 m below the DST/DY boundary at Zhongling. (I) Petrographic thin section of oolitic limestone (Yd-21) under plane polarized light. Sample was collected about 26 m below the DST/DY boundary at Yangjiaping. (J) Petrographic thin section of intraclastic phosphorite (12ZL-42) under plane polarized light. Sample was collected about 42 m below the DST/DY boundary at Zhongling. (K) Petrographic thin section of phosphorite (Yd-26) under plane polarized light. Sample was collected from the uppermost Doushantuo Formation at Yangjiaping. (L) Petrographic thin section of phosphorite (12ZL-0.9) under plane polarized light. Sample was collected from the uppermost Doushantuo Formation at Zhongling. (M, N, O) Time-series samples from the Doushantuo and Dengying formations at Zhongling. Numbers mark stratigrahic heights above the Nantuo diamictite. The marker pen is circled as a scale. The lower ~200 m of the Doushantuo Formation mainly consists of dark-colored carbonates or shale, and above ~200 m height, more and more light-colored dolostone with intraclasts and ooids dominated the upper section, indicating shallower, higher-energy environment. Scales in petrographic images (H–L) are 2 mm. Coins in (C) and (F) are 24 mm and 17 mm in diameter respectively.

2.4 Methods

2.4.1 Field sampling

In this study, the uppermost 100 meters of the Doushantuo Formation at the Yangjiaping section and the entire Doushantuo Formation at the Zhongling section near the town of Hupingshan were sampled at a high resolution for petrographic observation and time-series elemental and isotope analysis. At the Yangjiaping section, the lower part of the section is poorly exposed beneath thick vegetation and was not sampled. The upper part of the Doushantuo is characterized by organic-rich oolitic limestone (**Fig. 2.2I**), with a thin interval containing shale and interbedded

phosphorite breccia (**Fig. 2.2K**), which is immediately overlain by cherty dolostone of the Dengying Formation (Zhu et al., 2007). The Zhongling section (**Fig. 2.2M, N, O**) is lithostratigraphically similar, with oolitic (**Fig. 2.2 G, H**) and intraclastic carbonates (**Fig. 2.2D, E, F**) near the top of the Doushantuo Formation, which are overlain by a prominent phosphorite horizon (**Fig. 2.2D**). All samples collected from these two sections were analyzed and archived in the Geochemical Laboratories at the Department of Geology, University of Maryland.

2.4.2 Elemental analyses

Approximately 5–7 mg of micro-drilled sample powders were weighed and dissolved in 2 ml distilled 0.4 M HNO_3. The resulting solutions were centrifuged and 1 ml of the supernatants were pipetted and diluted with distilled 3 ml 0.4 M HNO_3 for elemental analysis. Major, trace, and REE concentrations were determined with a Thermo Scientific® iCAP-Q ICP-MS (Inductively Coupled Plasma – Mass Spectrometry) at the Carnegie Institution for Science. Calibration curves were created using multi-elemental standards made from pure element solutions (Alfa Aesar®). Both standard and sample solutions were doped with 4 ppb In to correct for instrumental drift. Precision of the analyses determined by repeated analyses of a house standard carbonate were better than 5% (2σ) for major elements with high concentrations and better than 10% (2σ) for the REEs.

2.4.3 Carbonate carbon and oxygen isotope analyses

Carbonate carbon and oxygen isotopes were measured by continuous flow isotope ratio mass spectrometry in the University of Maryland Paleoclimate CoLaboratory using a refined method for the analysis and correction of carbon ($\delta^{13}C$) and oxygen ($\delta^{18}O$) isotopic compositions of 100 μg carbonate samples (Spötl, 2011). Up to 180 samples loaded into 3.7 mL Labco Exetainer vials and sealed with Labco septa were flushed with 99.999% helium and manually acidified at 60℃. The carbon dioxide analyte gas was isolated via gas chromatography, and water was removed using a Nafion trap prior to admission into an Elementar Isoprime stable isotope mass spectrometer fitted with a continuous flow interface. Data were corrected via automated Matlab scripting on the Vienna PeeDee Belemnite and LSVEC Lithium Carbonate (VPDB-LSVEC) scale (Coplen et al., 2006) using periodic in-run measurement of international reference carbonate materials and/or in-house standard carbonates, from which empirical corrections for signal amplitude, sequential drift, and one or two-point mean corrections were applied. Precision for both isotopes is routinely better than 0.1‰. Including acidification, flush fill, reaction and analysis, true throughput exclusive of correcting standards is 2–3 samples/hour, or up to 144 samples over a 40-hour analytical session.

2.4.4 Organic matter carbon and pyrite sulfur isotope analyses

The organic carbon and pyrite sulfur isotope compositions were measured by combustion to CO_2 or SO_2 with a Eurovector elemental analyzer in-line with a second Elementar Isoprime isotope ratio mass spectrometer. Approximately 10 g of sample trimmed with a rock saw to remove weathered surfaces and secondary veins was

crushed to 200 mesh and finer, and then repeatedly acidified with 3 M HCl and washed with ultra-pure Milli-Q water until the solution reached neutral pH. Decalcified residues were dried overnight and quantified to determine carbonate percentages, and then accurately weighed and folded into small tin cups.

For pyrite sulfur measurements, V_2O_5 was mixed with the decalcified residues (assuming pyrite S >> organic S) to enhance combustion to SO_2. The tin cups were sequentially dropped with a pulsed O_2 purge of 12 ml into a catalytic combustion furnace operating at 1030℃. The frosted quartz reaction tube was packed with high purity reduced copper wire for quantitative oxidation and O_2 resorption. Water was removed from the combustion products with a 10-cm $Mg(ClO_4)_2$ column, and the SO_2 was separated from other gases with a 0.8-m PTFE GC column packed with Porapak 50–80 mesh heated to 115°C. The effluent from the elemental analysis (EA) was introduced in a flow of He (80–120 mL/min) to the IRMS through a SGE splitter valve that controls the variable open split. Timed pulses of SO_2 reference gas (Air Products 99.9% purity, ~3 nA) were introduced at the beginning of the run using an injector connected to the IRMS with a fixed open ratio split. The isotope ratios of reference and sample peaks were determined by monitoring ion beam intensities relative to background values. The cycle time for these analyses was 210 seconds with reference gas injection as a 30-second pulse beginning at 20 seconds. Sample SO_2 pulses begin at 110 seconds and return to baseline values between 150 and 180 seconds, depending on sample size and column conditions. Sulfur isotope ratios were determined by comparing integrated peak areas of m/z 66 and 64 for the reference

and sample SO_2 pulses, relative to the baseline that is approximately 1×10^{-11}A. The background height was established from the left limit of the sample SO_2 peak. Isotopic results are expressed in the delta notation as per mil (‰) deviations from the Vienna Canyon Diablo Troilite (V-CDT) standard. Two NBS 127 barite standards and two IAEA NZ1 silver sulfide standards were measured between each set of 10 samples and uncertainties for each analytical session based on these standard analyses were determined to be better than 0.3‰.

Measurements for organic carbon abundance and isotope composition with the elemental analyzer and isotope ratio mass spectrometer were similar to those of sulfur, except that the reaction column was packed with chromium oxide and silvered cobaltous/cobaltic oxide and heated to 1040°C and the analyte also flows through a second column at 1040°C packed with high purity reduced copper wire for quantitative reduction of NO_2 and N_2O and O_2 resorption. The CO_2 was separated from other gases with a 3-m stainless steel GC column packed with Porapak-Q heated to 60°C. Timed pulses of CO_2 reference gas (Airgas 99.999% purity, ~6 nA) were introduced at the beginning of the run using an injector connected to the IRMS with a fixed open ratio split. The isotope ratios of reference and sample peaks were determined by monitoring ion beam intensities relative to background values. The cycle time for these analyses was 430 s with reference gas injection as two a 30-s pulse beginning at 15 and 60 s. Sample CO_2 peaks begin at 200 s and return to baseline around 240 s. Carbon isotope ratios were determined by comparing integrated peak areas of m/z 45 and 44 for the reference and sample CO_2 pulses,

relative to the baseline that is approximately 2×10^{-11}A. The background height was established from the left limit of the sample CO_2 peak. Isotopic results are expressed in the delta notation as per mil (‰) deviations from the Vienna Pee Dee Belemnite (V-PDB) standard. Two urea standards were measured between each set of 10 samples and uncertainties for each analytical session based on these standard analyses were determined to be better than 0.1‰.

2.4.5 Strontium isotope analyses

For analysis of strontium isotopic ($^{87}Sr/^{86}Sr$) composition, only limestone or calcite samples were selected for extraction and measurement. Micro-drilled powders (ca. 5–10 mg) were leached three times in 0.2 M ammonium acetate (pH ~8.2) to remove exchangeable Sr from non-carbonate minerals, and then rinsed three times with Milli-Q water. The leached powder was centrifuged, decanted, and acidified with doubly distilled 0.5 M acetic acid overnight to remove strontium from the carbonate crystal structure. The supernatant was centrifuged to remove insoluble residues and then decanted, dried, and subsequently dissolved in 200 μl of 3M HNO_3. Strontium separation by cation exchange was carried out using a small polyethylene column containing ~1 cm of Eichrom®Sr specific resin. The column was rinsed with 400 μl of 3 M HNO_3 before the dissolved sample was loaded onto the column. After loading, the sample was sequentially eluted with 200 μl of 3 M HNO_3, 600 μl of 7 M HNO_3, and 100 μl of 3 M HNO_3 to remove the Ca, Rb and REE fractions; the Sr fraction adsorbs strongly to the resin in an acidic environment. The Sr fraction was removed by elution with ~800 μl of 0.05 M HNO_3 and the resultant eluate collected

and dried. Approximately 200–300 ng of the dried sample was transferred onto a degassed and pre-baked (~4.2 A under high vacuum) high purity Re filament with 0.7 μl of Ta_2O_5 activator. The prepared filaments were measured using the VG Sector 54 thermal ionization mass spectrometer in the TIMS facility of the University of Maryland Geochemistry Laboratories. Filaments were transferred to a sample carousel, heated under vacuum ($\sim 10^{-7}$ to 10^{-8} atm) to a temperature between 1450 and 1650°C, and analyzed when a stable signal (>1.0 V) was detected on the mass 88 ion beam. Approximately 100 $^{87}Sr/^{86}Sr$ ratios were collected for each sample. Final data have been corrected for fractionation using the standard value $^{86}Sr/^{88}Sr = 0.1194$. The fraction of ^{87}Sr resulting from in situ decay from ^{87}Rb was removed by measurement of rubidium abundance at mass 85. Repeated analysis of the NBS SRM987 standard yields an average value of $^{87}Sr/^{86}Sr = 0.710245 \pm 0.000011$ (2σ) during the analytical window.

2.5 Results

In this study, we systematically measured carbonate (wt.%, major and trace element concentrations, $\delta^{13}C_{carb}$, $\delta^{18}O$, and $^{87}Sr/^{86}Sr$), organic matter (wt.% and $\delta^{13}C_{org}$), and pyrite (wt.% and $\delta^{34}S_{pyrite}$) compositions in samples from the upper part of Doushantuo Formation at the Yangjiaping section (**Fig. 2.3; Table A.1**). Carbonate abundance of most bulk sample powders were >80% with the exception of a few samples near the bottom and top of the succession. Based on element ratios all samples have very low Mn/Sr ratio (ranging from 0.01 to 0.18), Fe/Sr (ranging from 0.18 to 17.17), and Rb/Sr (ranging from 0.0002 to 0.0154). Rare earth element concentrations were low as expected for carbonates, and were normalized to PAAS

(Post Archean Australian Shale) in order to calculate the magnitude of Ce anomalies $Ce/Ce^* = Ce_{PAAS}/([Pr]^2_{PAAS}/[Nd]_{PAAS})$ as presented by Ling et al. (2013). The Ce/Ce* ratios of the Yangjiaping samples ranged from 0.3 to 0.9 with significant oscillations through the succession, including a noted increase in values from samples in the uppermost 30 meters. Carbon isotope compositions of micro-drilled powders are relatively invariant with $\delta^{13}C$ values of +5‰ in most of the Yangjiaping section except in the three samples from the uppermost 10 meters; these reveal a decreasing trend from ca. +5‰ to a nadir value of –6.8‰. Similarly, the $\delta^{18}O$ values of the limestone samples are relatively invariant. Organic carbon isotope data ($\delta^{13}C_{org}$) range between –20 and –30‰ with a slight deceasing trend at the top of the section. Based on the measured carbonate carbon and organic carbon isotope values in individual samples, we calculated the magnitude of carbon isotope fractionation ($\Delta\delta^{13}C$). The $\Delta\delta^{13}C$ values average around 30‰ through most of the measured section, with the exception of a slightly decreasing trend to ~22‰ in the upper 30 meters. Pyrite sulfur isotope data show highly positive values (average ca. +20‰) throughout the section. Strontium isotope ($^{87}Sr/^{86}Sr$) data reveal steady values of ~0.7080 throughout most of the succession, except in the upper 20 meters where $^{87}Sr/^{86}Sr$ ratios rise up to a maximum of 0.7085 as recorded in phosphatic limestones.

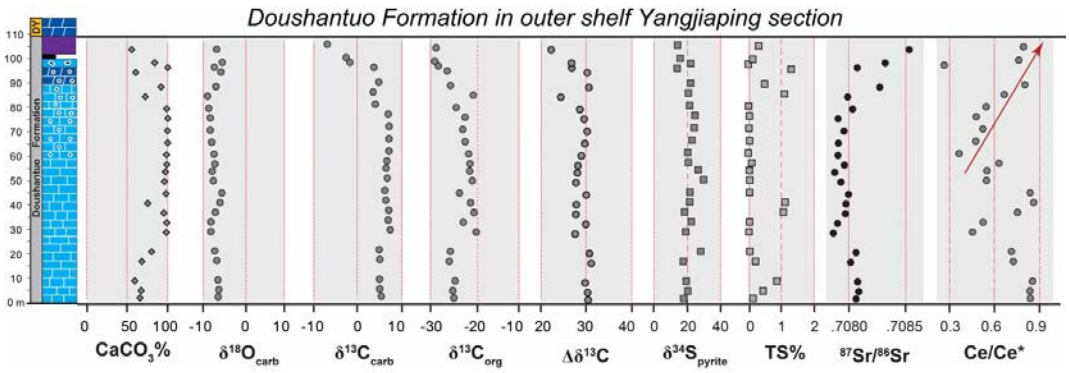

Figure 2.3: Integrated time-series elemental and isotopic data from the middle-upper Doushantuo Formation at the outer shelf Yangjiaping section.

The Zhongling samples were also analyzed for organic carbon, pyrite sulfur and strontium isotope compositions, in order to test regional variations and to facilitate chemostratigraphic correlation with the Yangjiaping section. The data are presented in **Table A.2**. Organic carbon isotope data in Zhongling show consistent values of ca. –25‰ in most of the section, except some more negative values (ca. –30‰) in the basal cap carbonate. Pyrite sulfur isotope data range between +20‰ to +40‰, with a slight decrease to ca. +20‰ near the top. Strontium isotope data shows consistent value of ca. 0.7080 in most of the section, with a sudden rise to 0.7083 in the upper 20 meters.

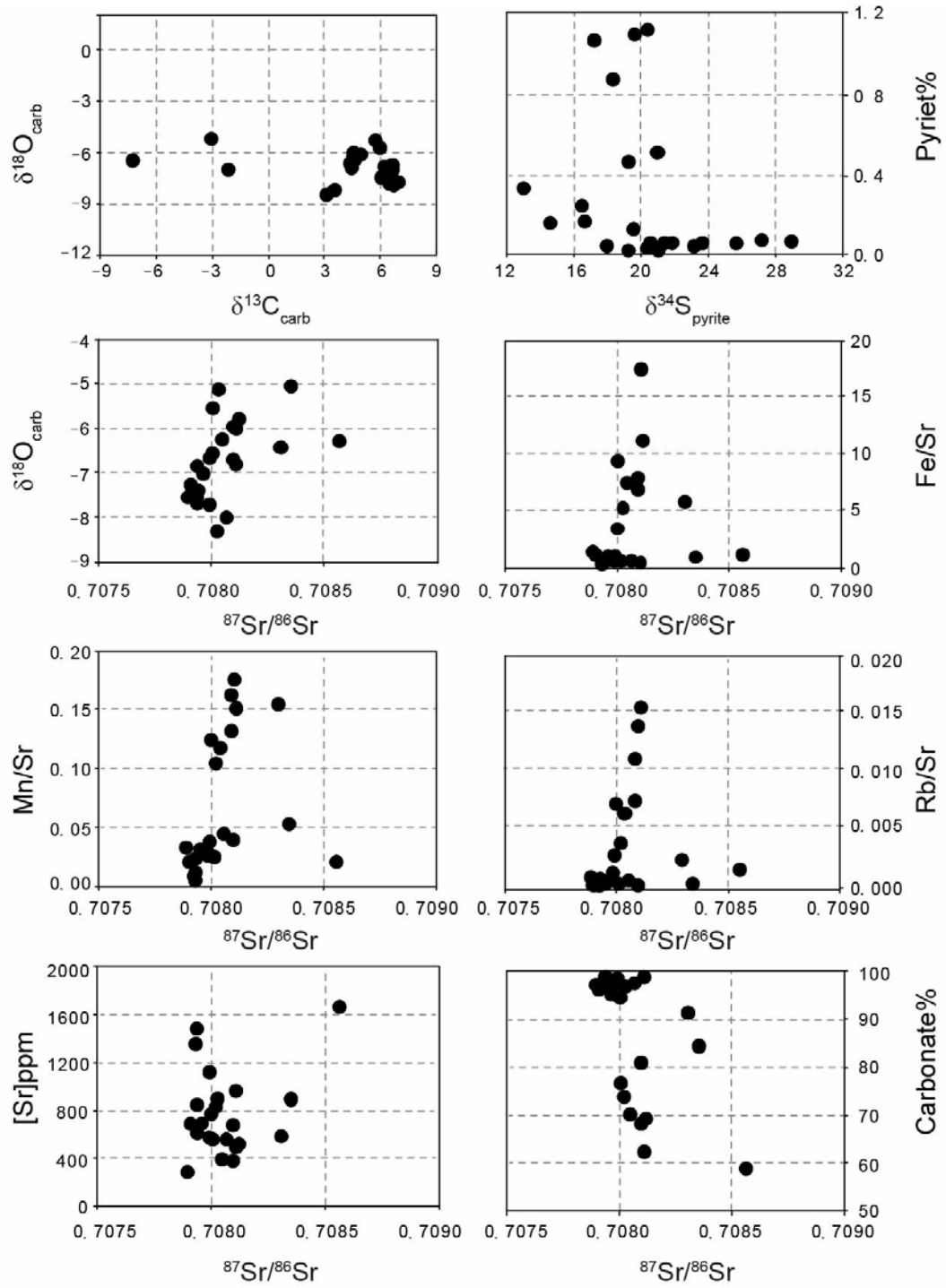

Figure 2.4: Cross plots of isotope and elemental data of the middle-upper Doushantuo Formation at Yangjiaping.

2.6 Discussion

2.6.1 Diagenesis

To evaluate the degree of preservation of the Yangjiaping and Zhongling samples, we investigated the petrography, elemental and isotope geochemistry of the samples, which were collected in a sedimentological and stratigraphic context. These measurements and observations allow for field and laboratory tests of the fidelity of the time-series isotope records. First, the outcrop samples used in this study were primarily composed of fine-grained limestone, although in the upper 20 meters of the section at Yangjiaping dolostone and phosphatic limestone were also sampled. Various phases were micro-sampled from polished billets to avoid weathered surfaces, secondary veins, and areas with visible silt and clay. Geochemical tests of diagenesis included the comparison of carbonate carbon and oxygen isotope abundances relative to the meteoric alteration trend defined by Knauth and Kennedy (2009). Our micro-samples fell away from this trend, and furthermore were rich in Sr (ranging from 286 to >1600 ppm in all specimens) and had very low Mn/Sr, Fe/Sr, and Rb/Sr ratios (**Fig. 2.4**) as expected for well-preserved phases. It is nonetheless clear that the development of the phosphorite horizon(s) (likely to be early diagenetic in origin) in the uppermost Doushantuo Formation at Yangjiaping and Zhongling are associated with the isotope shifts, and thus complicates our interpretation of secular variations in seawater chemistry across the basin. The samples from the upper interval are petrographically fine-grained and organic-rich, in comparison with bedded limestone lower in the succession these are geochemically well preserved.

2.6.2 Chemostratigraphic correlations of the platform sections

If the lithological and isotope shifts at the top of the Yangjiaping section are widespread and reflect changes in the redox and isotope architecture of the Doushantuo basin, they should also be present at the nearby Zhongling section (**Figs. 2.5–2.9**; Zhu et al., 2007; Li et al., 2010) and at the more proximal sections at Jiulongwan (McFadden et al., 2008) and Xiaofenghe (Xiao et al., 2012; Liu et al., 2013; Zhu et al., 2013b). The Zhongling section is located 4 km from the Yangjiaping section and both are lithostratigraphically similar. At Zhongling, the Doushantuo Formation begins with 5 m of cap carbonate atop the Nantuo glacial diamictite, followed by interbedded shale and carbonate, ~20 m of black shale, and finally ~140 m of limestone. The uppermost 50 meters of the Doushantuo Formation at Zhongling is dominantly composed of micritic, intraclastic, and oolitic dolostone and organic-rich shale with three prominent levels of phosphorite (**Fig. 2.2**). The shale and phosphorite horizons are believed by some researchers to be correlative with the uppermost Doushantuo throughout the basin. Pyrite sulfur and carbon isotope trends at the Zhongling section (Li et al., 2010; new data in this study) are remarkably similar to those in the Yangjiaping section (**Fig. 2.6**).

The most accessible and well-studied section of the Doushantuo Formation is near Jiulongwan, where the succession consists of mixed carbonate and shale facies deposited in an intra-shelf environment (**Figs. 2.5–2.9**). There the lower half of the succession above the Nantuo diamictite includes the ca. 635 Ma cap dolostone

(Member I) and a thick interval of argillaceous dolostone and mudstone (Member II). The upper half of the unit consists of medium-bedded dolostone overlain by interbedded dolostone and limestone (Member III), which is in turn overlain by black shale with large carbonate concretions (Member IV). No thick phosphorite is present in the upper Doushantuo Formation at this locality although there is minor phosphate enrichment in dolostone facies (McFadden et al., 2008). Sedimentary textures include ribbon rock, microbialaminite, grainstone, and intraclastic packstone, suggesting deposition in shallow subtidal marine environments. The Jiulongwan section preserves three negative carbon isotope excursions, including EN1 (down to –5‰) in the cap carbonate, EN2 (ca. –5‰) at the top of Member II and associated with rapid shallowing of facies (Jiang et al., 2007), and EN3 (ca. –10‰), which is remarkably stable and continues for nearly 50 meters through the upper half of Member III and large carbonate concretions in Member IV (Fig. 5; Zhou and Xiao, 2007; McFadden et al., 2008). Based on the shape of this $\delta^{13}C$ excursion, we follow McFadden et al. (2008) and use the subdivisions of EN3a, EN3b and EN3c to represent the decreasing, stable, and recovery intervals of the EN3 $\delta^{13}C$ excursion, respectively. This geochemical event is widely regarded as correlative with the globally expressed carbon cycle anomaly known as the Shuram Excursion (Fike et al., 2006; Zhu et al., 2007; Grotzinger et al., 2011; Lu et al., 2013; Zhu et al., 2013b). Time-series pyrite $\delta^{34}S$ values associated with EN3 at Jiulongwan record a negative trend from 0‰ to as low as –10‰ (**Fig. 2.6**), with a similar magnitude decreasing trend in the $\delta^{34}S$ composition of carbonate associated sulfate (McFadden et al., 2008).

The stark contrast in the time-series $\delta^{34}S$ compositions between the uppermost beds at Jiulongwan and Zhongling was used to support the sulfate gradient model (**Fig. 2.1C**; Li et al., 2010) for the Doushantuo ocean margin, with the assumption that the Doushantuo Formation in Zhongling section is continuous and can be fully correlated with the Jiulongwan section (see Fig. S7 of Li et al., 2010). However, the Shuram Excursion at Zhongling is poorly expressed, and in our section at Yangjiaping carbonate $\delta^{13}C$ values decline to a low value of –7‰ at the top of the section (**Fig. 2.5**), which is likely equivalent to EN3a. It appears possible that both EN3b and EN3c are missing in both of the shoal complex localities, either due to stratigraphic truncation of the upper Doushantuo Formation, or to the diachronous nature of the Doushantuo/Dengying boundary. If the latter is true, the Shuram Excursion should be expressed in the lower Dengying Formation at these localities.

To further evaluate correlations between the inner and outer shelf sections of the Doushantuo Formation, we compared $^{87}Sr/^{86}Sr$ trends constructed from well preserved high-Sr limestone samples (**Fig. 2.7**). At the intra-shelf Jiulongwan section, $^{87}Sr/^{86}Sr$ values are consistently low (ca. 0.7080) through most of the section, with a notable rise up to 0.7090 during the Shuram Excursion (Sawaki et al., 2010). Sawaki et al.'s (2010) data are replotted in **Fig. 2.7**, with the omission of their whole rock ICP-MS Sr isotope data from impure carbonates with high Mn/Sr (rejection criteria: carbonate wt.% < 60 and Mn/Sr > 1). Although Sawaki et al.'s data were derived from analyses of both dolostones and limestones and our TIMS analyses were exclusively from micro-sampled limestone samples, the stratigraphic patterns of

$^{87}Sr/^{86}Sr$ are similar at Jiulongwan, Zhongling, and Yangjiaping (**Fig. 2.7**), with the exception of values > 0.7085 in EN3b and EN3c at Jiulongwan that are missing in the shoal complex localities. Considering that a stratigraphic rise in $^{87}Sr/^{86}Sr$ from 0.7080 to 0.7090 also occurs across the Shuram Excursion at its type locality in Oman (Burns et al., 1994; Le Guerroué et al., 2006), it is likely that the $^{87}Sr/^{86}Sr$ profile (and the stratigraphy) at Jiulongwan is more complete than those at Zhongling and Yangjiaping.

Two possible interpretations can account for the incomplete Shuram-equivalent EN3 intervals in the outer shelf sections. (1) EN3b and EN3c may have been stratigraphically truncated during a sea level fall, so that these chemostratigraphic features were removed through erosion from the shoal complex facies; this interpretation is consistent with independent sedimentological evidence at these localities, which are dominated by phosphatic intraclasts and oolitic carbonates deposited in shallow high-energy environments (**Fig. 2.2**). (2) Alternatively, the lithostratigraphic boundary between the Doushantuo and Dengying formations may be diachronous, so that EN3b and EN3c in the rim sections were instead preserved in dolostone of the lower Dengying Formation. Support for this view comes from strongly negative $\delta^{13}C_{carb}$ data from the lower Dengying Formation at the Yangjiaping section (**Figs. 2.5–2.7**; Zhu et al., 2007; Ader et al., 2009; Ader et al., 2014). This possibility needs to be further tested by other high-resolution chemostratigraphic data (e.g., $^{87}Sr/^{86}Sr$ if limestone facies are preserved) which are currently unavailable.

In earlier publications (Xiao et al., 2012; Zhu et al., 2013b), we came to a similar conclusion about the truncation of strata for the Doushantuo Formation at the Xiaofenghe section, which was deposited in shallower inner shelf facies. The northern Xiaofenghe section (NXF) consists of a basal cap dolostone overlain by a succession of shale, phosphatic packstone or grainstone, and cherty dolostone passing upward into argillaceous limestone (**Fig. 2.5**). According the Zhu et al. (2013), the NXF can be traced to the southern Xiaofenghe section (SXF) where the succession, composed of shale and dolostone, continues upward. Regardless, neither the NXF nor SXF successions reveal carbon, sulfur, or strontium isotopic evidence of the Shuram Excursion (**Fig. 2.5**).

In this study, we additionally employed time-series Ce anomaly (Ce/Ce*) as a tool for stratigraphic correlation and to evaluate redox changes through the stratigraphic package (**Fig. 2.8**). Although REE concentrations in marine carbonates are notoriously low, and may easily be contaminated by the presence of high-REE clay minerals, we used a significantly diluted leach acid (0.4 M HNO_3) to avoid any admixture of non-carbonate phases. The time-series Ce/Ce* trend reported by Zhou et al. (2012) from the Jiulongwan section reveals a continuous increase from 0.4 to 0.8 through EN3a, followed by a plateau of 0.8 values in EN3b (**Fig. 2.8**). We find a similar trend in the top 50 meters of the Doushantuo Formation at Yangjiaping, with a steady increase in Ce/Ce* from 0.4 to 0.8 in our interpreted EN3a; the stabilized 0.8 plateau through EN3b at Jiulongwan is missing at Yangjiaping due to the inferred stratigraphic incompleteness of the section.

In summary, the integrated chemostratigraphic correlation of the Doushantuo Formation using $\delta^{13}C$–$\delta^{34}S$–$^{87}Sr/^{86}Sr$–Ce/Ce* suggests that the shallow inner shelf section (Xiaofenghe) and the outer shelf sections (Yangjiaping and Zhongling) are incomplete, with the preserved strata equivalent to the lower 1/2 and 3/4, respectively, of the well-studied Jiulongwan section that accumulated in intra-shelf lagoonal facies (**Figs. 2.5–2.8**).

2.6.3 Redox and isotopic architecture of the Doushantuo ocean margin

In light of the integrated chemostratigraphic correlations that suggest either stratigraphic truncation of the uppermost Doushantuo Formation in the inner and outer shelf sections, or diachroneity of the Doushantuo/Dengying boundary in the rimmed margin environments, the euxinic wedge model should be reconsidered given that it is based on a stratigraphic miscorrelation. The Shuram Excursion with associated ^{34}S depletion in pyrite and CAS (McFadden et al., 2008) and elevated Fe_{py}/Fe_{HR} (Li et al., 2010) is well preserved in the intra shelf basin succession at Jiulongwan. These indicators suggest that the enxinic water mass on the platform was largely restricted to the intra shelf lagoon, and may not be indicative of a euxinic wedge across the basin margin. While it remains possible that there was a strong surface-to-deep sulfate gradient across the Doushantuo platform, the data currently available do not require a euxinic wedge above a ramp geometry shelf.

Our time-series REE analyses provide additional constraints on changing redox conditions in the Doushantuo basin. Cerium exists in two redox states in marine environments: Ce(III) and Ce(IV). Trivalent Ce can be oxidized into tetravalent Ce in oxic environments, and then be scavenged by Mn-oxides and hydroxides and removed from the ocean. Thus, in oxygenated seawaters, tetravalent Ce is preferentially removed from the system, leaving the seawaters with a Ce negative anomaly in REE patterns. In contrast, Ce is more soluble in reduced environments, resulting in relatively high Ce/Ce* values. Therefore, Ce anomalies (Ce/Ce*) can be used to trace oxygenation changes in seawater (Ling et al., 2013). Our data show that, while the Ce/Ce* ratios oscillate in the middle-upper Doushantuo Formation at Zhongling there is a significant shift in Ce/Ce* from 0.4 to 0.8 starting at about 60 meters below the top of the formation (**Fig. 2.8**). Notwithstanding a single anomalous outlier, the overall Ce/Ce* trend preserved in the upper Doushantuo Formation at Yangjiaping is coupled with the declining trend in $\delta^{13}C_{carb}$ related to EN3a. This is consistent with similar patterns observed at Jiulongwan (**Fig. 2.8**) that support the view that negative $\delta^{13}C$ anomalies are related to widespread anoxia in a stratified depositional basin with enhanced production of ^{13}C-depleted authigenic carbonates (Higgins et al., 2009; Schrag et al., 2013).

Stratification of the Doushantuo seaway, including a pronounced surface-to-deep $\delta^{13}C$ gradient has previously been suggested from the carbonate record (Jiang et al., 2007; Ader et al., 2009). The stratified redox model suggests that the surface ocean preserves the primary signal of carbonate carbon isotope variations; on the

other hand, deep ocean sediments may have included a mixture of carbonate transported by pelagic rain or turbidites from shallow environments, as well as ^{13}C-depleted authigenic carbonates (*cf.* Schrag et al., 2013) that formed in association with microbially-mediated iron or sulfate reduction in anoxic environment.

Based on our detailed analysis of platform sections, we additionally note that there may have been a gradient of seawater organic carbon isotope compositions across the basin, with ^{13}C enrichment of up to 5‰ in the outer shelf section at Yangjiaping and Zhongling relative to the inner shelf sections at Xiaofenghe and Jiulongwan (**Fig. 2.9**). This organic carbon gradient may persist into the late Ediacaran Period and is recorded in multiple sections of the Dengying Formation (Wang et al., 2014). It is possible that these differences reflect a depth-dependent DOC pool with variable biological sources of organic matter, or alternatively that there was a buildup of ^{13}C-poor respired CO_2 in the intra-shelf lagoon that was subsequently incorporated by photoautotrophs and buried as organic carbon.

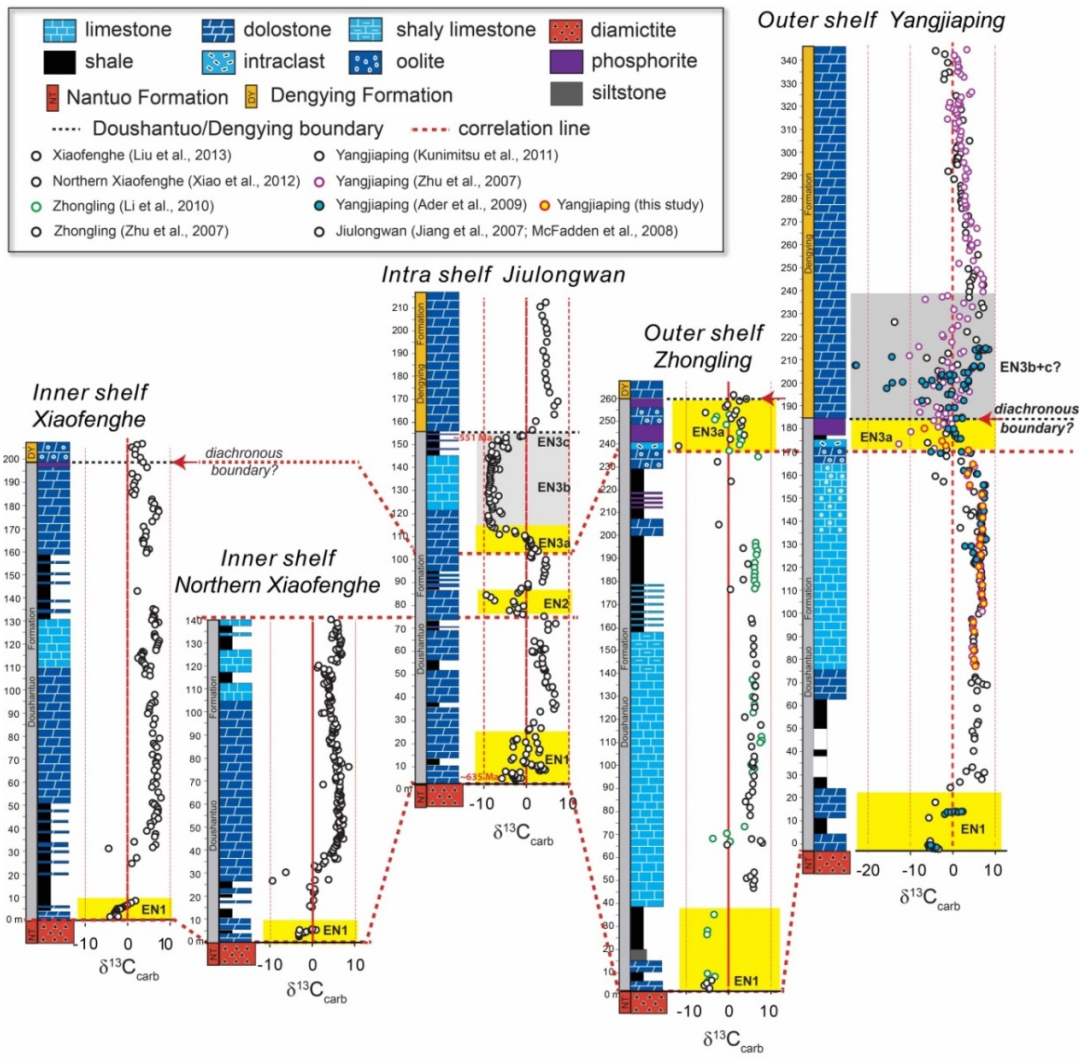

Figure 2.5: Carbonate carbon isotope ($\delta^{13}C_{carb}$) chemostratigraphic correlation of the Edaicaran Doushantuo Formation across the platform. Based on carbon, sulfur (Fig. 2.6), strontium isotope (Fig. 2.7), and Ce/Ce* (Fig. 2.8) trends, the shallow inner shelf sections at Xiaofenghe and outer shelf Zhongling and Yangjiaping sections are stratigraphically incomplete (see red dashed correlation lines). The Shuram Excursion (EN3) at Jiulongwan is completely missed in Northern Xiaofenghe and only partially recorded in the Doushantuo Formation at Zhongling and Yangjiaping. The red arrows point to possible diachronous boundary between Doushantuo and Dengying Formation.

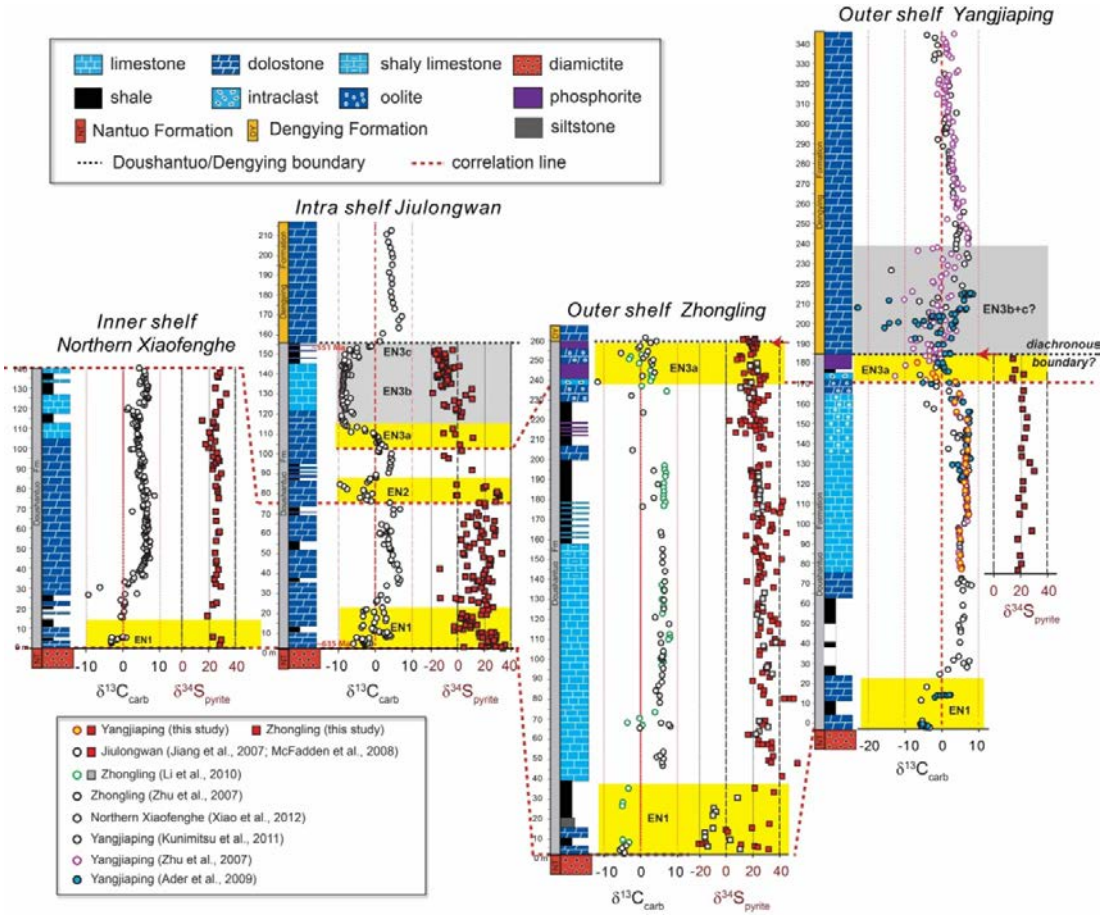

Figure 2.6: Pyrite sulfur isotope ($\delta^{34}S_{pyrite}$) chemostratigraphic correlation of the Ediacaran Doushantuo Formation across the platform. $\delta^{34}S_{pyrite}$ of the Shuram Excursion (EN3) at Jiulongwan is characterized by a decreasing trend from slightly positive values to strongly negative values, which is not recorded in either the inner or outer shelf sections. The red arrows point to possible diachronous boundary between Doushantuo and Dengying Formation.

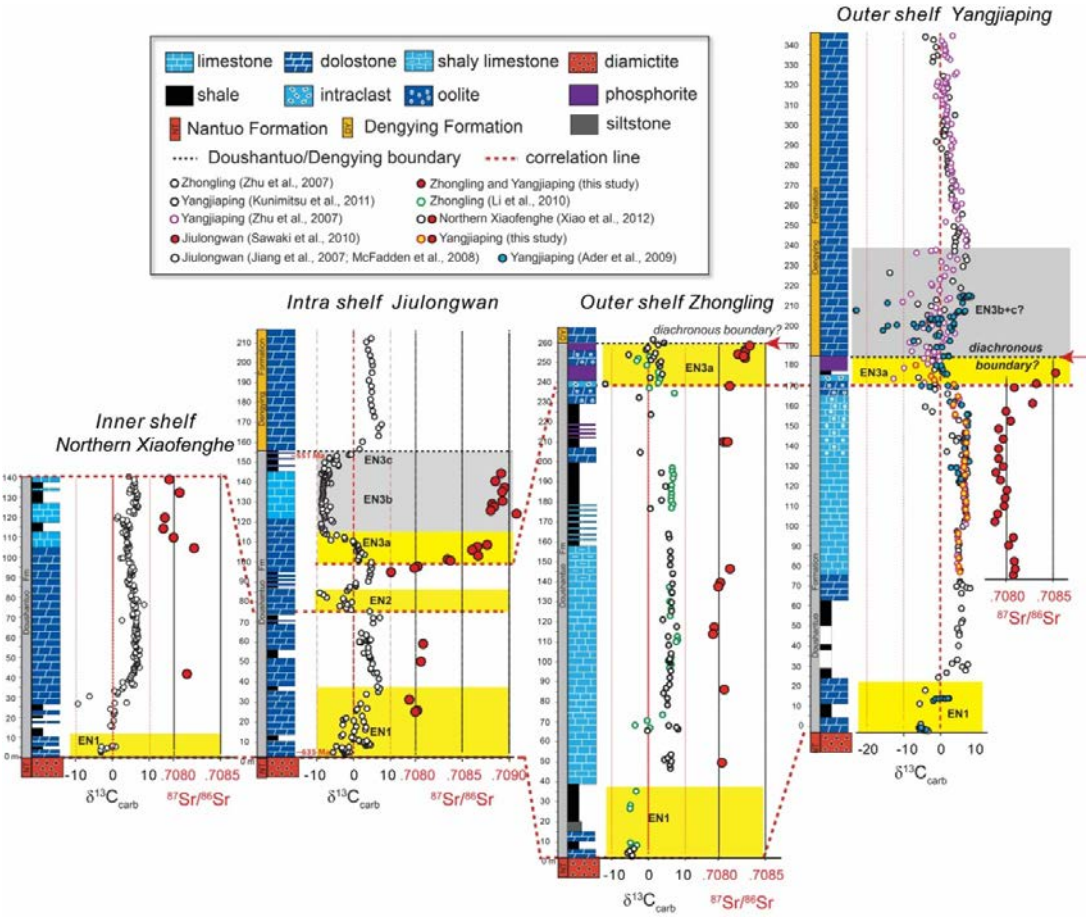

Figure 2.7: Strontium isotope ($^{87}Sr/^{86}Sr$) chemostratigraphic correlation of the Ediacaran Doushantuo Formation across the platform. $^{87}Sr/^{86}Sr$ trend in upper Doushantuo Formation at Jiulongwan shows a monotonic increase from 0.7080 to 0.7090, which is consistent with the $^{87}Sr/^{86}Sr$ trend of Shuram Excursion interval from Oman, Siberia and South Australia (see Fig. 2.10). High-resolution $^{87}Sr/^{86}Sr$ data of upper Doushantuo Formation in outer shelf Zhongling and Yangjiaping sections suggest that the upper Shuram Excursion or EN3b+c (characterized by $^{87}Sr/^{86}Sr$ values of 0.7085–0.7090) is missing from the Doushantuo Formation at outer shelf sections. The red arrows point to possible diachronous boundary between Doushantuo and Dengying Formation.

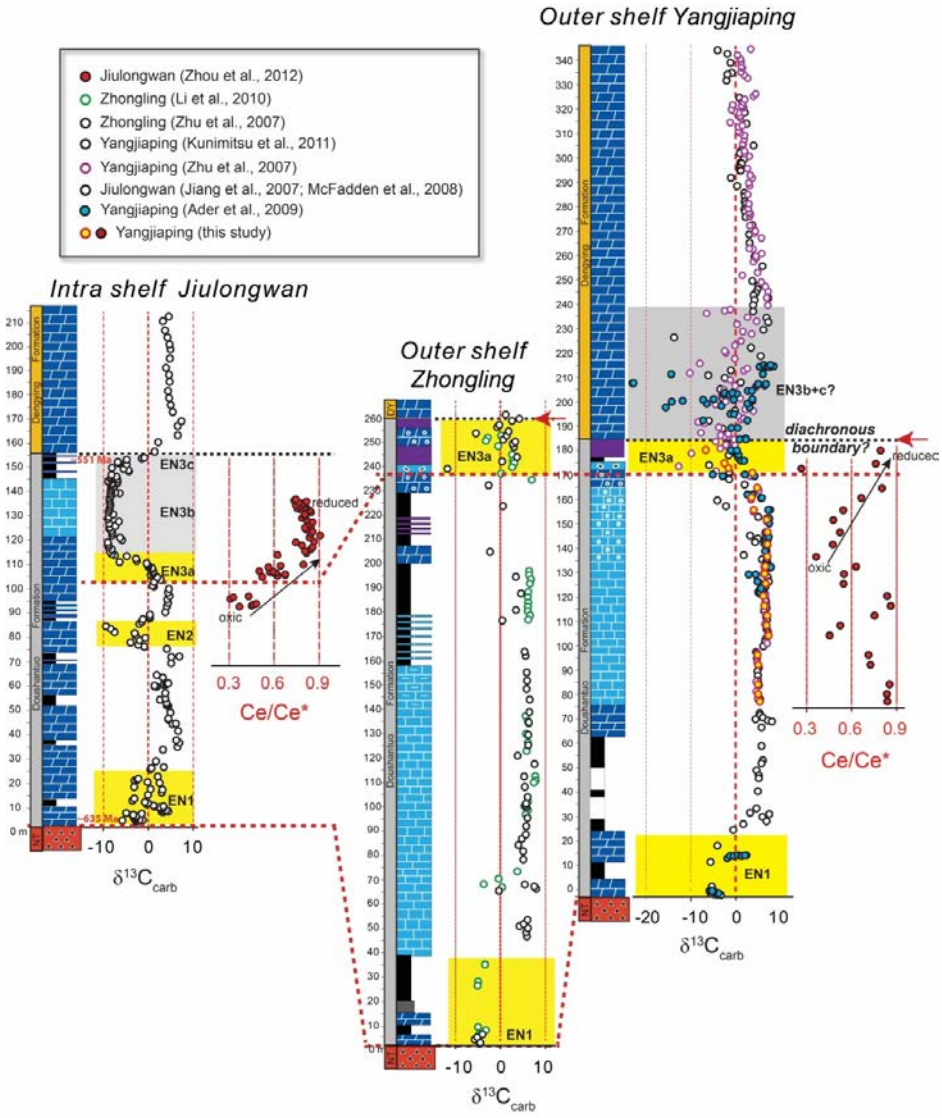

Figure 2.8: Ce anomaly (Ce/Ce*) chemostratigraphic correlation of the Ediacaran Doushantuo Formation between the intra-shelf Jiulongwan section and outer shelf Yangjiaping section. Data in both sections are calculated using the formula Ce/Ce* = $Ce_{PAAS}/([Pr]^2_{PAAS}/[Nd]_{PAAS}$ (Ling et al., 2013). At Jiulongwan, Ce/Ce* data progressively increase from 0.3 to 0.8 across EN3a (Zhou et al., 2012), and remain at a plateau of 0.8 during EN3b. The upper Doushantuo Formation at Yangjiaping also preserves a similar increasing trend of Ce/Ce* from around 0.4 to around 0.8 (60–105 m stratigraphic height), but the 0.8 plateau recorded in Jiulongwan is missing at Yangjiaping.

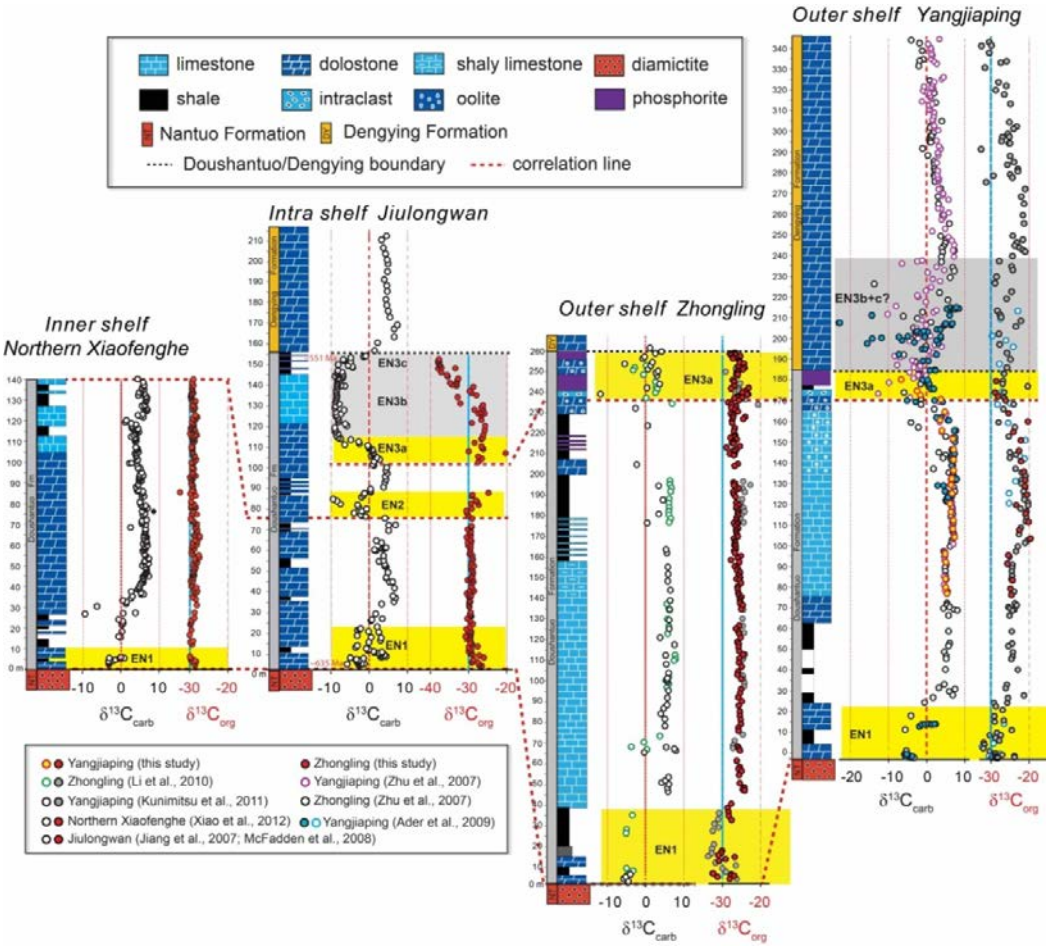

Figure 2.9: Paired carbonate carbon ($\delta^{13}C_{carb}$) and organic carbon ($\delta^{13}C_{org}$) isotopic trends of the Edaicaran Doushantuo Formation across the platform. $\delta^{13}C_{org}$ in the outer shelf (Zhongling and Yangjiaping, ca. –25‰) is ~5‰ greater than the inner shelf (Northern Xiaofenghe, ca. –30‰) and intra-shelf (Jiulongwan, ca. –30‰) sections, indicating an organic carbon isotope gradient across the platform.

2.6.4 Implications for the Shuram Excursion

Members III and IV of the Ediacaran Doushantuo Formation at Jiulongwan provide the clearest window into the Shuram Excursion in South China. However, the duration of this event, which is preserved through about 50 m of strata, is poorly constrained. The event was clearly over by 551 ± 0.7 Ma (Condon et al., 2005) based on a U–Pb zircon age for a volcanic ash at the stratigraphic contact between the

Doushantuo and Dengying formations, but there is no radiometric constraint for the onset of the excursion in the middle of Doushantuo Member III (also see An et al., 2015 for a critical re-evaluation). An imprecise Re–Os age of 595 ± 22 Ma (Zhu et al., 2013a) was recently determined from an organic-rich shale horizon at the base of Member IV, but this age provides only a minimum constraint of ca. 35 Myr for the duration of the event. With the caveat that stratigraphic thickness does not necessarily equate to time, Le Guerroué et al. (2006) applied a thermal subsidence model to the >400 m of strata encompassing the Shuram Excursion in Oman to suggest the event lasted at least 50 Myr. Here, we consider that the rise in $^{87}Sr/^{86}Sr$ during the Shuram event may provide an alternative estimate on the duration of the profound carbon cycle anomaly.

At Yangjiaping and Zhongling, our high-[Sr] limestone samples from the upper Doushantuo reveal a rise in $^{87}Sr/^{86}Sr$ compositions from a plateau of values near 0.7080 lower in the succession to 0.7085. Measurements of $^{87}Sr/^{86}Sr$ compositions in the upper Doushantuo at Jiulongwan, which captures the entirety of the Shuram Excursion, suggest that values may rise as high as 0.7090 (Sawaki et al., 2010) during the event. Confidence that the upper Doushantuo $^{87}Sr/^{86}Sr$ shift at Yangjiaping and Zhongling is primary and related to changes in seawater composition comes from our petrographic and geochemical observations, as well as regional and global comparisons (**Fig. 2.10**), in particular with the oolitic and stromatolitic limestones with remarkably high Sr abundances from the Patom Uplift of southern Siberia (Melezhik et al., 2009). There $^{87}Sr/^{86}Sr$ values through the lower

half of the Shuram Excursion rise monotonically from 0.7080 to 0.7085. A similar trend is recorded in Oman, where $^{87}Sr/^{86}Sr$ compositions rise steadily from 0.7080 to 0.7090 through the carbon cycle anomaly (Burns et al., 1994; Le Guerroué et al., 2006). As an analogue, a similar rise in $^{87}Sr/^{86}Sr$ (0.0005) is noted in the Cenozoic from the Oligocene to the middle Miocene associated with the rise of the Himalayas and the Tibetan plateau (McArthur et al., 2012). Assuming the Cenozoic event monitors the *maximal* possible rate of Sr isotope change, the duration of the Shuram Excursion would minimally be 15 Myr if values rose only to 0.7085, but would extend to 30 Myr if they climbed to 0.7090.

The driving force behind the Cenozoic and Ediacaran rise in $^{87}Sr/^{86}Sr$ recorded in seawater proxies is considered by many to be the result of enhanced delivery of radiogenic ^{87}Sr from the weathering of continental crust (DePaolo and Ingram, 1985; Derry et al., 1992; Richter et al., 1992; Kaufman et al., 1993; Paytan et al., 1993). Alternatively, the Sr isotope shift might also reflect a decrease in mantle Sr inputs or an increase in the $^{87}Sr/^{86}Sr$ of exposed rocks undergoing weathering (Shields, 2007). Based on: 1) the range of Sr isotope compositions of riverine sources today (Palmer and Edmond, 1992), 2) measurements of the isotopic composition of detrital Sr in shales (Goldstein, 1988), and 3) the unlikely scenario that seafloor spreading rates decreased during an interval of rapid continental reorganization, it is unlikely that either hydrothermal inputs of Sr decreased or that the radiogenic composition of exposed continental rocks increased (Shields, 2007) in the middle

Ediacaran Period. Accepting this argument, the most likely explanation for the Shuram rise in $^{87}Sr/^{86}Sr$ remains an overall increase in continental weathering rates.

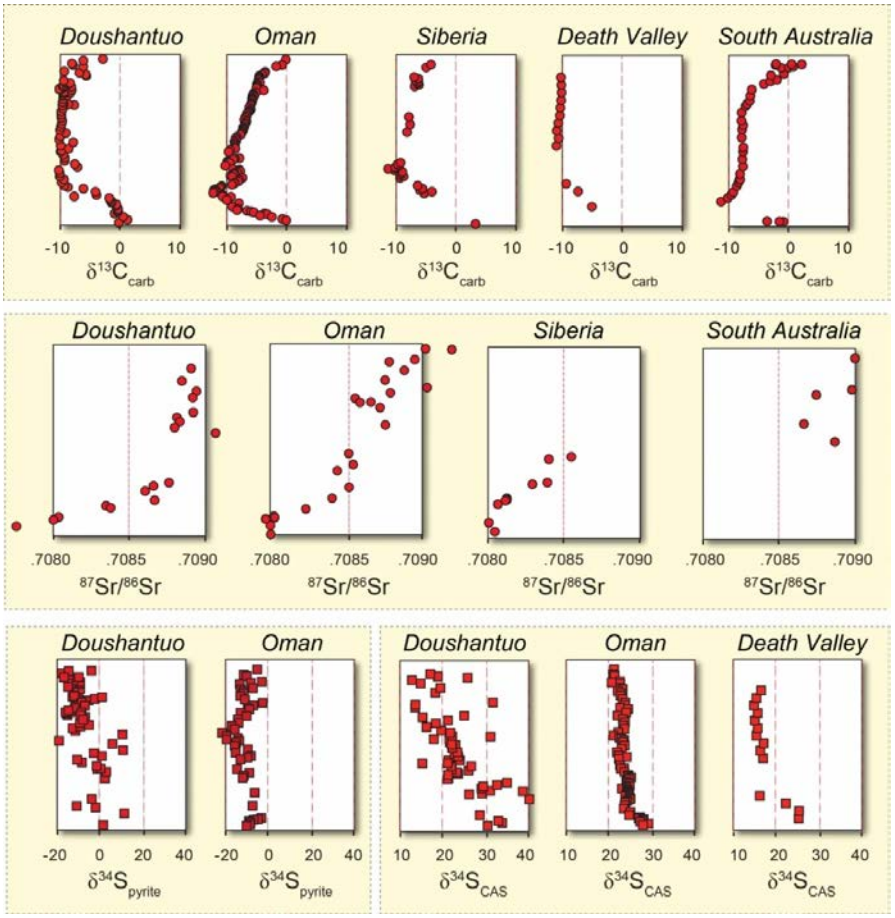

Figure 2.10: Compiled carbon, sulfur, and strontium isotope trends in association with the Shuram Excursion recorded in the upper Doushantuo Formation in South China (Jiang et al., 2007; McFadden et al., 2008; Sawaki et al., 2010) and presumably equivalent strata in Oman (Burns et al., 1994; Fike et al., 2006; Le Guerroué et al., 2006), Siberia (Pokrovskii et al., 2006a; Pokrovskii et al., 2006b; Melezhik et al., 2009; Pokrovsky and Bujakaite, 2015) , Death Valley (Kaufman et al., 2007), and South Australia (Wonoka Formation; Calver, 2000). The stratigraphic thickness of the Shuram Excursion is different at different sections, and thus the chemostratigraphic profiles are not shown to scale.

Support for the weathering hypothesis comes from coupled measurements of carbonate carbon and sulfur (both pyrite and CAS) isotope compositions in samples from Ediacaran successions in Oman (Fike et al., 2006), the western USA(Kaufman

et al., 2007) and South China (McFadden et al., 2008), each of which reveals pronounced $\delta^{34}S$ negative isotope shifts (**Fig. 2.10**) suggesting enhanced delivery of sulfate into the ocean. The effects of weathering would have been enhanced if the Shuram Excursion was coincided with a stepwise rise in the redox state of the Ediacaran ocean and atmosphere (aka Neoproterozoic Oxidation Event or NOE) (Fike et al., 2006; Canfield et al., 2007; Shields-Zhou and Och, 2011; Och and Shields-Zhou, 2012).

2.7 Conclusions

Our integrated basin-wide chemostratigraphic correlations of the Ediacaran Doushantuo Formation based on time-series carbon, sulfur, strontium isotope and Ce anomaly measurements suggest that the Doushantuo Formation in shallow marine environments at both proximal and distal rimmed settings are stratigraphically incomplete to variable degrees compared with the well-studied intra shelf Jiulongwan section. Such incompleteness can be explained by possible stratigraphic truncation in shallow environments. Alternatively, our time-series results may indicate that the lithostratigraphic boundary between the Doushantuo and Dengying formations may be diachronous across the platform. This view must be considered in geochemical models of the redox architecture of this (and other) Ediacaran basin(s), as well as our understanding of the distribution of early multicellular eukaryotes preserved in these ancient sedimentary archives.

Chapter 3: A global authigenic response to Ediacaran surface oxidation

3.1 Abstract

The middle Ediacaran (~580–550 Ma) is characterized by the most negative carbon isotope excursion in Earth history, the Shuram Excursion. Various hypotheses—including large-scale remineralization of dissolved organic, enhanced oxidation of fossil organic carbon, massive release of methane, meteoric alteration, or burial diagenesis—have been proposed as a source of ^{13}C-depleted carbon, but all have been challenged. Recently, it has been suggested that global scale precipitation of authigenic carbonate, driven by anaerobic microbial metabolism in unconsolidated sediments, may have caused the Shuram Excursion, but empirical evidence is lacking. Here we present a comprehensive analysis of the Shuram Excursion preserved in the upper Doushantuo Formation of South China. Our study reveals petrographic evidence of methane-derived authigenic calcites that are remarkably depleted in ^{13}C, suggesting the buildup of alkalinity in pore fluids by the anaerobic oxidation of methane. Authigenesis of these minerals was driven by a pulse of sulfate and nutrients to the ocean, likely triggered by enhanced continental weathering associated with a marked rise in atmospheric oxygen levels. Our novel observation of methane-derived authigenic calcite indicates that the Shuram Excursion reflects proportional mixing of primary and authigenic components during an unique environmental and evolutionary transition in Earth history.

3.2 Introduction

Authigenic minerals in marine sediments form through anaerobic microbial processes, including iron- and sulfate-reduction, which modify pore water chemistry and result in the dissolution and replacement, or cementation, of pre-existing sedimentary particles. Carbonate minerals (e.g. calcite or $CaCO_3$) that form in sediments due to microbial-induced increases in alkalinity are typically depleted in carbon-13 relative to seawater, depending on the organic sources that fuel their metabolic activities. The production of authigenic carbonate through organic remineralization, which is currently associated with gas hydrate cold seeps as well as anoxic upwelling zones (Campbell, 2006), may thus play a major role in the profound fluctuations of the carbon cycle that characterize Precambrian time (Schrag et al., 2013). Observational evidence for authigenic calcite, however, is lacking, in part due to the general fine grain size of most Ediacaran carbonate sedimentary rocks. Thus our novel discovery of calcite nodules, replacement fabrics, and cements, all significantly depleted in ^{13}C and preserved in phosphate-rich sedimentary rocks (**Fig. 3.1**), opens a unique window onto the syn-sedimentary growth of authigenic minerals. The purest calcite phases preserve $\delta^{13}C$ compositions as low as –37‰, suggesting that anaerobic oxidation of methane contributed to pore water carbonate alkalinity. Results of our study suggest that proportional mixing of authigenic calcite and primary sedimentary components may explain the globally-distributed middle Ediacaran Shuram Excursion, the largest negative carbon cycle anomaly in Earth history (Kaufman et al., 2007; Melezhik et al., 2009; Grotzinger et al., 2011). During this enigmatic event, initially observed in Ediacaran strata of Oman, the carbonate

carbon isotope composition plunge to a nadir of ca. –9‰ or less and then rise steadily over tens to hundreds of meters of stratigraphy before recovering to baseline values. The duration of this biogeochemical event is uncertain, but is likely to represent 15 million years or more (Cui et al., 2015). The Shuram Excursion is well-preserved in intra-shelf carbonate deposits of the uppermost Doushantuo Formation (Jiang et al., 2007; McFadden et al., 2008), but in both nearshore and basinal settings the excursion is variably expressed due to stratigraphic truncation or diachroneity (Cui et al., 2015), or based on our new observations, the variable admixture of fine-grained primary and authigenic carbonate sediments.

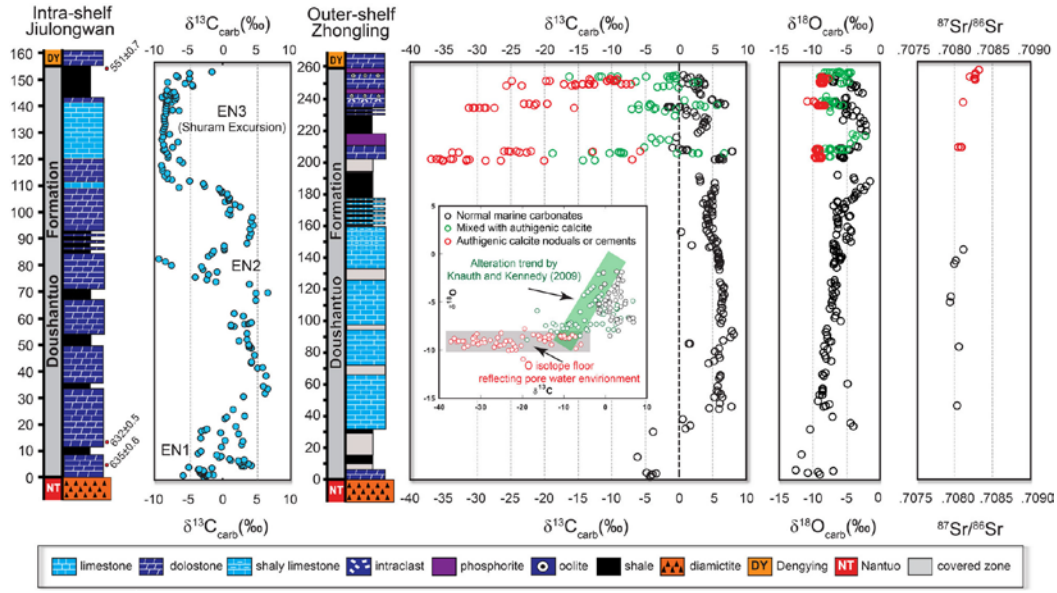

Figure 3.1: Time-series lithostratigraphy, chemostratigraphy, and age constraints for the Doushantuo Formation of intra shelf section at Jiulongwan and outer shelf section at Zhongling. The inset shows a cross-plot of carbon and oxygen isotope compositions of upper Zhongling carbonates. The "floor" (gray bar) of oxygen isotope compositions at ca. -10‰ reflects stable pore water conditions where the authigenic calcite nodules and cements formed. Green zone denotes the diagenetic stabilization or "lithification" trend defined by Knauth and Kennedy (2009). C and O isotope values are all reported relative to VPDB standard.

3.3 Geologic background

The richly fossiliferous Doushantuo Formation is a condensed carbonate-dominated succession of Ediacaran ages that blankets the Yangtze platform in South China. In the EN3 interval at Jiulongwan (**Fig. 3.1**), carbon isotope compositions fall precipitously to a stable negative plateau of ca. –9‰ that persists over 50 meters of section before returning rapidly to pre-event values. Coincident with the Shuram negative $\delta^{13}C$ anomaly in South China, and globally, are coupled excursions in oxygen, sulfur and strontium isotopes (Cui et al., 2015). It was the absence of a well-defined Shuram Excursion in the shallow marine shoal environment at Zhongling (Li et al., 2010) that drew our initial attention. The upper 50 meters of the formation at this locality is characterized by intraclastic, oolitic, or fine-grained dolomitic facies associated with three discrete levels of massive phosphorite (**Fig. 3.1**). The phosphorites are typical of uppermost Doushantuo strata across the basin, which is constrained in age to be >551 Ma (Condon et al., 2005; An et al., 2015). During systematic sampling of this interval, we observed centimeter-scale calcite nodules along bedding surfaces (**Fig 3.2**), and within the top eight meters we found distinctive sedimentary fabrics that are consistent with elevated sulfate concentrations and high rates of evaporation (i.e. chicken wire evaporites, **Fig. 3.2D**). These sedimentary textures are typical of sabkhas, which form in supratidal and arid marine environments like those along the coast of the Persian Gulf today.

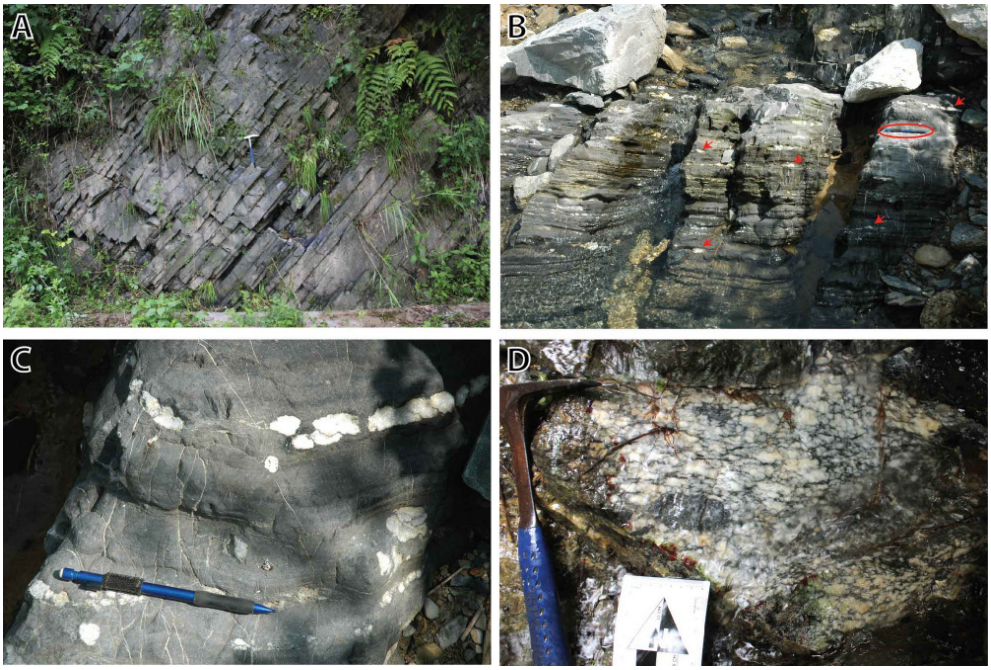

Figure 3.2: Outcrop photos of the Ediacaran Doushantuo Formation in Zhongling section, South China. (A) Bedded carbonates of the middle Doushantuo Formation (rock hammer for scale); (B) Stream exposure ~50 meters below the Doushantuo-Dengying boundary revealing interbedded calcitic and dolomitic layers with abundant (see arrows) white calcite nodules (pencil for scale); (C) Displacive calcite nodules along bedding planes in dolomicrite matrix; (D) Massive chicken-wire texture in dolostone ca. 3-4 meters below the Doushantuo-Dengying boundary.

3.4 Petrographic observations

In support of our extraordinary claim that the ^{13}C-depleted calcite nodules, replacement fabrics, and cements from the upper Doushantuo Formation at Zhongling and Yangjiaping are authigenic precipitates that formed from the oxidation of methane through microbial sulfate reduction, we conducted a detailed petrographic investigation of representative samples (**Figs. 3.3, 3.4**). These observations give a clear picture of the relative timing of mineral phases and the geochemical changes that accompanied their growth. As indicated in the main text, the methane-derived calcites are found in dolomite facies closely associated with the three phosphatic

horizons at Zhongling; these authigenic minerals were also discovered in a number of phosphate-rich float samples from the top of the Doushantuo Formation at nearby Yangjiaping.

The paragenetic history of the fossiliferous Doushantuo phosphorites is complicated by multiple events preceding the formation of the authigenic phases that are the focus of this study, including the buildup and sequestration of phosphate in the primary depositional environment. In the samples studied here the well-preserved phosphatic phases include intraclasts, granules, and oolites. The intraclasts are composed of rounded to sub-rounded plates (ranging up to several centimeters in length) that are either homogeneously fine-grained or composed of particle aggregates (i.e. grapestones including rounded isotropic or coated grains that are cemented with dolomicrite) (**Figs. 3.3A, B**). Accumulations of rounded to sub-rounded granules are typically sand-sized, amorphous, and isotropic (**Figs. 3.3C, D**), many of which reveal evidence for desiccation and contraction. Well-preserved sand-sized phosphatic oolites generally have homogeneous fine-grained phosphatic cores coated with multiple cortical layers of dolomicrite (**Figs. 3.3E, F**). All of the phosphatic allochems were formed in well agitated seawater and appear to have been partially to completely dolomitized along with fine-grained micrite in near-shore environments. The rounded intraclasts, grapestones, and granules suggest that primary sedimentary layers were eroded and clastic particles transported (including dolomitized oolites and dolomicrite) by normal wave activity or storm events to the ultimate site of deposition.

To variable degrees the primary phosphatic and dolomitic sediments were then dissolved and replaced, or cemented by authigenic silica or rhombohedral calcite. Ghost relics of these particles within the matrix and the nodules indicate that large voids and secondary porosity were created by dissolution of the primary sediments (**Fig. 3.3G**). This was most- likely due to an initial increase of acidity through microbial activity. Lower pore water pH promoted the authigenic formation of quartz, which occurs as fibrous shadows surrounding many of the intraclasts, granules, and ooids (**Fig. 3.3H**). Desiccation and contraction of these phosphatic allochems may have aided in the unusual growth of the fibrous silica cements. In contrast, the preservation of laminated intraclast and ooid cortices, but replacement of their cores by silica supports the view that the cores were primarily composed of fine-grained phosphatic particles (**Fig. 3.3I**). The replacement of dolomite allochems and dolomicrite by silica increases towards the large calcite nodules (**Fig. 3.3J**), which are also lined with silica (**Figs. 3.3K, L**). The grain size of the quartz increases towards the center of the sedimentary voids, and in some examples (**Figs. 3.3M, N**) hexagonal quartz crystals with pyramidal terminations were formed.

Within the nodules, coarse rhombohedral calcite then filled in the remaining void space (**Figs. 3.3O, P, Q**), and clearly replaces the pre-existing quartz crystals (**Fig. 3.3M**). This mineralogical transformation must have followed an increase in pore water alkalinity and pH, again modulated by microbial activity within the sedimentary environment. The coarse nodular calcite, however, is not in optical

continuity and appears as coalesced patches. This observation suggests that there are several generations of calcite preserved within the nodules, which could explain the wide range of carbon isotope compositions expressed through micro-drilling of these phases (Fig. 3.2 in main text). Coarse calcites are also noted to infill remaining voids within intraclasts and ooids, and variably replace the allochems and matrix cements (**Fig. 3.3R**). In fact, the lighter colored intraclasts (e.g. **Fig. 3.3A**) with progressively more negative $\delta^{13}C$ compositions are more pervasively replaced by the authigenic calcite cements.

While the dissolution of sediments and enrichment of silica could be explained by the influence of hydrothermal fluids into these phosphatic horizons (implying a stratigraphic control on the alteration process), one additional petrographic observation supports our view that the methane-sourced calcite nodules are a sedimentary phenomenon. In particular, the linings of the nodules as well as the infilled allochems contain abundant round pyrite grains (**Figs. 3.3F, S, T, U, V, W, X**), ranging from 1-10 μm in diameter, which under the highest power of magnification appear to be framboidal. Pyrite framboids are spheroidal clusters of cubic or octahedral pyrite microcrystals (Ohfuji and Rickard, 2005) that in aggregate are typically between 10 and 20 mm in diameter (Wilkin and Barnes, 1996; Wang et al., 2012a). Insofar as pyrite framboids are directly associated with microbial sulfate reduction (Wacey et al., 2015), the discovery of these crystallites in association with silica and calcite cements suggests a direct linkage between this microbial process (as opposed to iron reduction) and authigenesis.

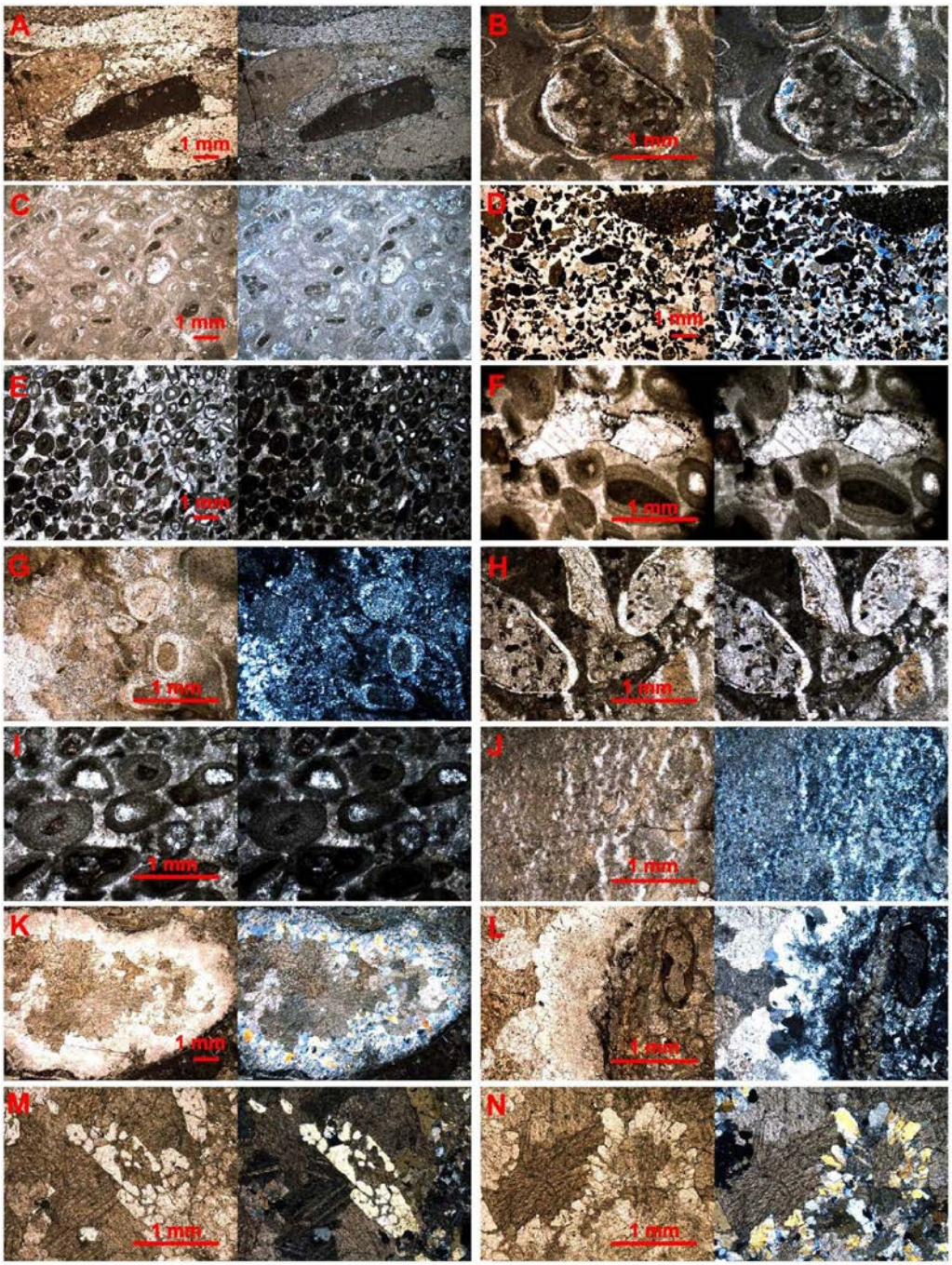
A
1 mm
B
1 mm
C
1 mm
D
1 mm
E
1 mm
F
1 mm
G
1 mm
H
1 mm
I
1 mm
J
1 mm
K
1 mm
L
1 mm
M
1 mm
N
1 mm

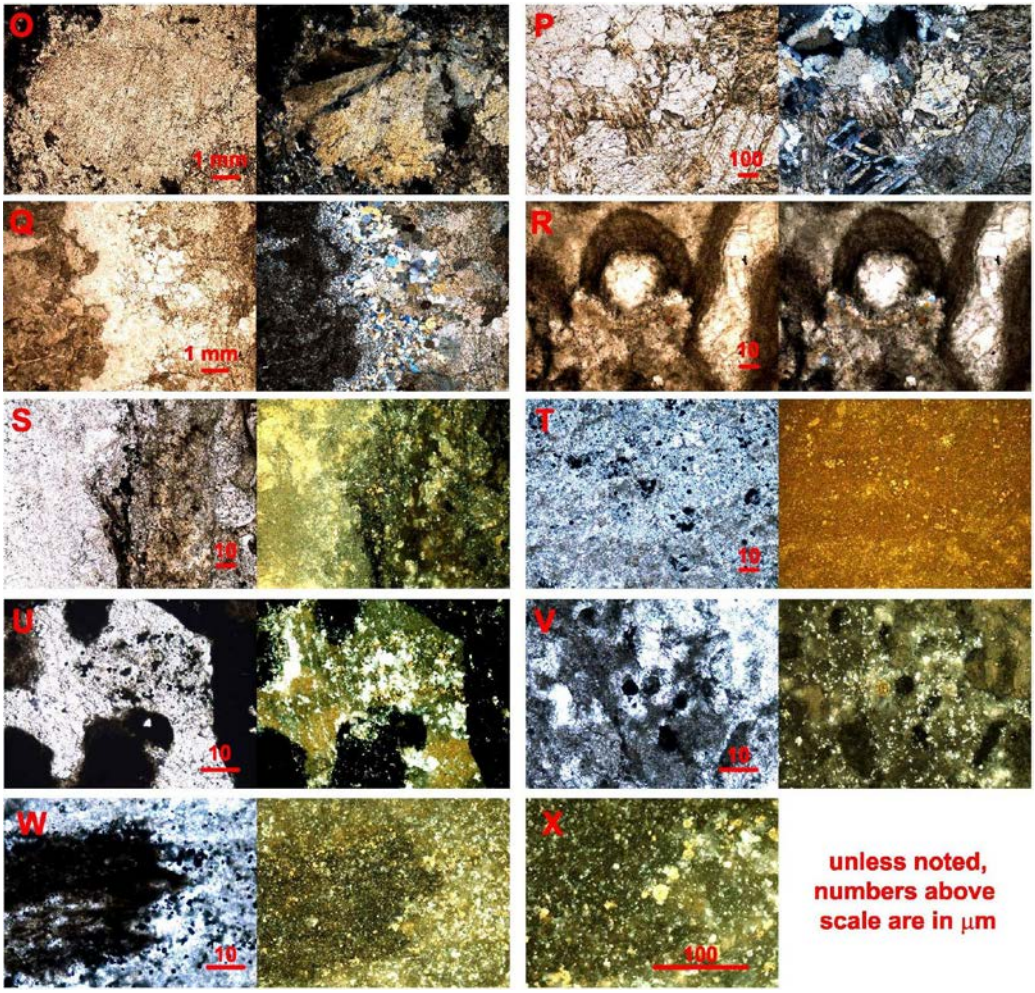

Figure 3.3: Paired plane light and crossed polar photomicrographs of phosphorite, silica, and carbonate textures in the upper Doushantuo Formation at Zhongling and Yangjiaping in South China. (A) 14-ZL-1.3 variably replaced phosphatic intraclasts; (B) YJP-R5-b grapestone intraclast with fibrous silica rim; (C) YJP-R1 rounded phosphate granules coated with dolomicrite; (D) Yd-26 phosphatic granules floating in a coarse calcite matrix; (E) Yd-21 phosphatic oolites and other coated grains cemented with coarse calcite; (F) Yd-21 partially dissolved and replaced phosphatic oolites and inter-granular rhombohedral calcite cement lined with round pyrite rim; (G) YJP-R5-OL ghosts of pre-existing coated grains replaced by silica; (H) YJP-R1 fibrous phosphatic intraclasts with fibrous silica rims; (I) Yd-21 phosphatic oolites with cores replaced by silica floating in a coarse calcite cement; (J) YJP-R5-C progressive silica replacement of phosphorite allochems and dolomicrite approaching nodule; (K) YJP-R1 quartz lined coarse calcite nodule; (L) YJP-R1 etched phosphatic matrix with allochems and increase in quzrtz grain size towards the center of the coarse calcite nodule; (M) 14-ZL-4.5 euhedral quartz crystal replaced by coarse calcite in nodule; (N) 14-ZL-4.5 quartz replaced by patchy rhombohedral calcite in nodule; (O) 14-ZL-4.5 silica replaced by coarse calcite in nodule; (P) YJP-R5-OL silica replaced by coarse calcite in nodule; (Q) YJP-R5-C transition from matrix

sediment to quartz to coarse calcite nodule; (R) Yd-21 partially replaced coated grain with coarse calcite core; (S) YJP-R1 pyrite at interface between matrix and silica cement in nodule; (T) 14-ZL-1.3 pyrite in silica cement; (U) Yd-26 pyrite in silica and calcite cement; (V) YJP-R4 pyrite rim in silica cement; (W) YJP-R5 pyrite in silica cement; (X) YJP-R5-b pyrite in silica cement.

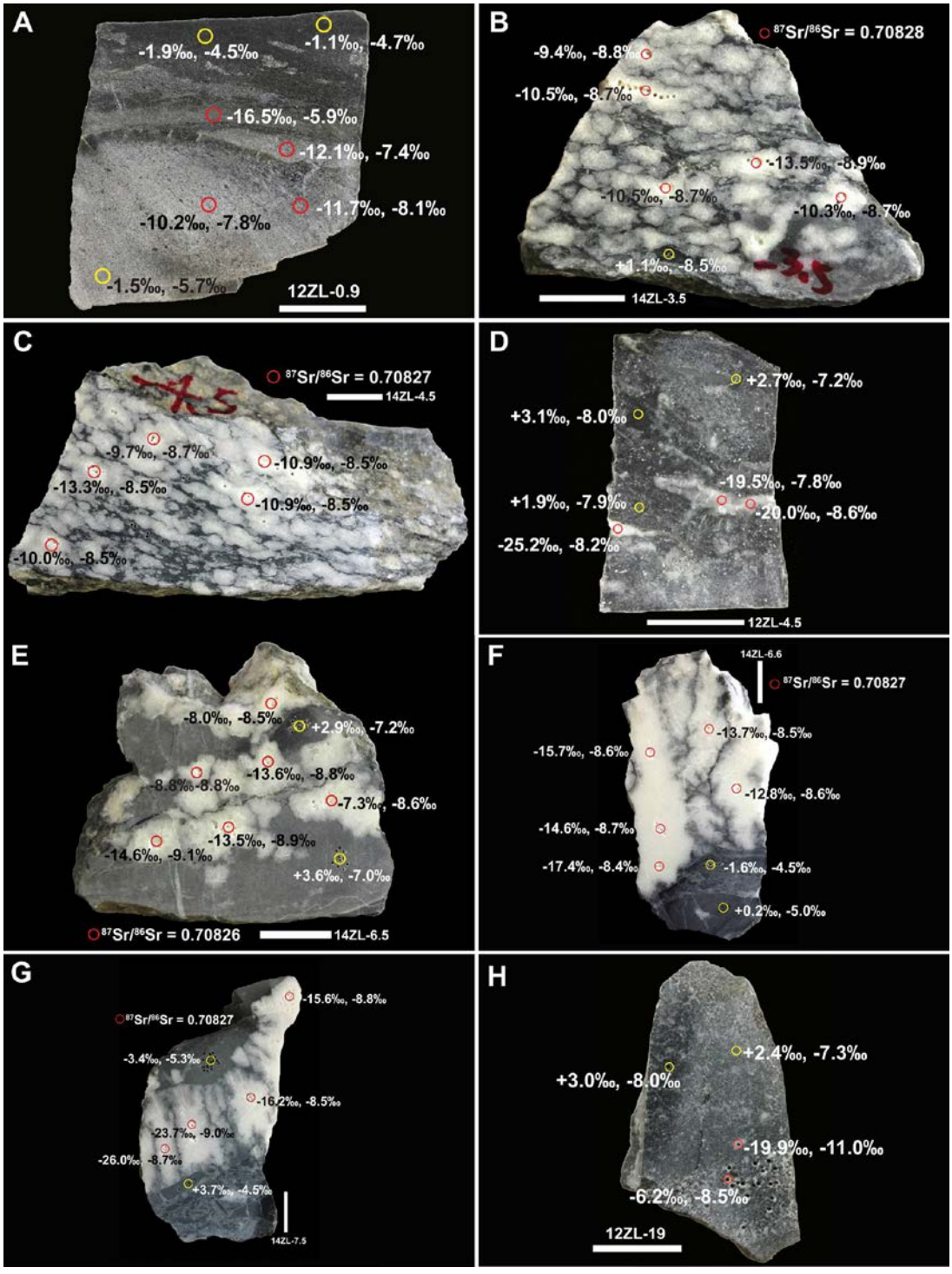

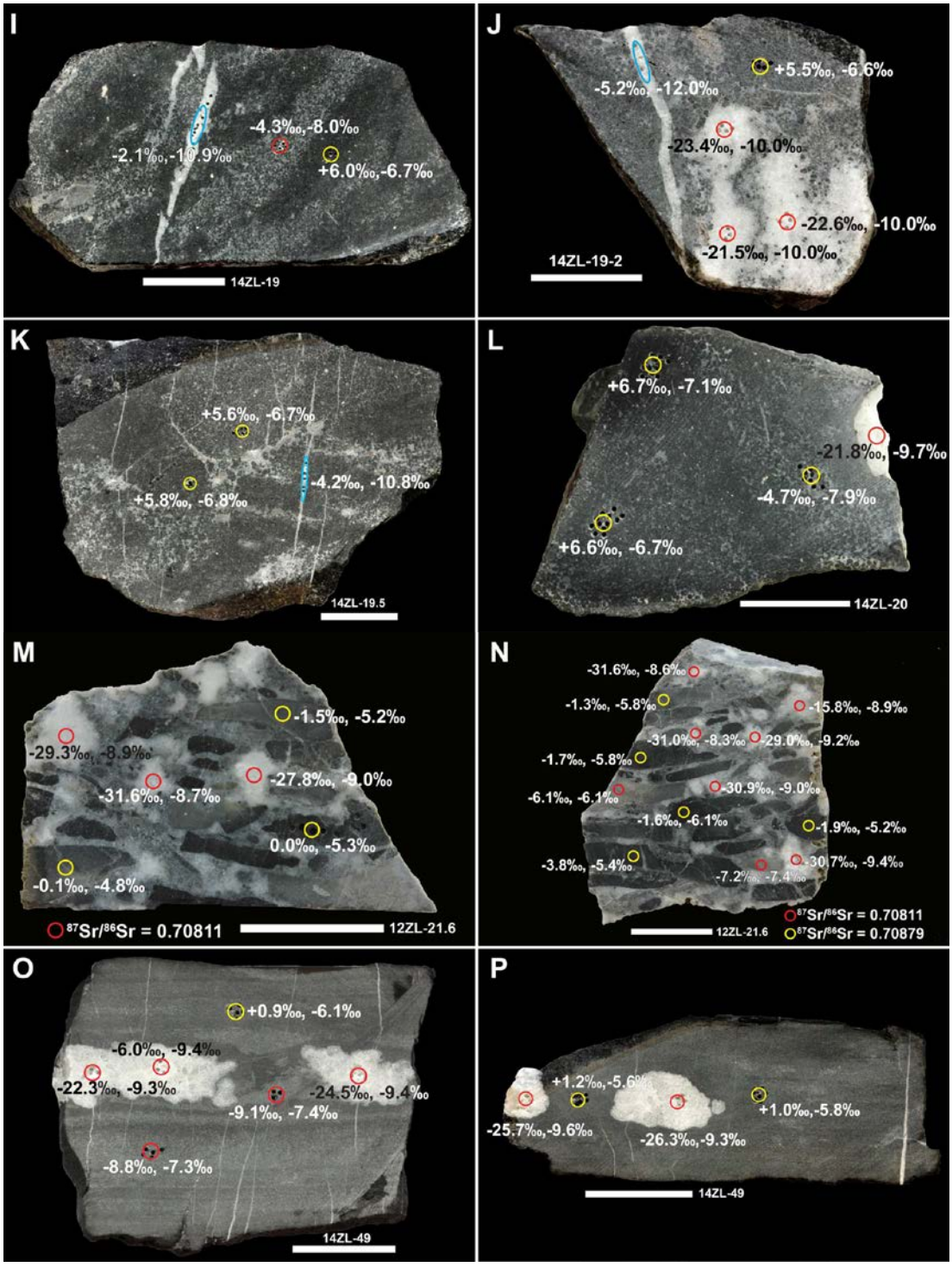
I
-4.3‰,-8.0‰
-2.1‰,-10.9‰
+6.0‰,-6.7‰
14ZL-19
J
+5.5‰, -6.6‰
-5.2‰, -12.0‰
-23.4‰, -10.0‰
-22.6‰, -10.0‰
-21.5‰, -10.0‰
14ZL-19-2
K
+5.6‰, -6.7‰
+5.8‰, -6.8‰
-4.2‰, -10.8‰
14ZL-19.5
L
+6.7‰, -7.1‰
-21.8‰, -9.7‰
-4.7‰, -7.9‰
+6.6‰, -6.7‰
14ZL-20
M
-1.5‰, -5.2‰
-29.3‰, -8.9‰
-27.8‰, -9.0‰
-31.6‰, -8.7‰
0.0‰, -5.3‰
-0.1‰, -4.8‰
87Sr/86Sr = 0.70811
12ZL-21.6
N
-31.6‰, -8.6‰
-1.3‰, -5.8‰
-15.8‰, -8.9‰
-31.0‰, -8.3‰
-29.0‰, -9.2‰
-1.7‰, -5.8‰
-6.1‰, -6.1‰
-30.9‰, -9.0‰
-1.6‰, -6.1‰
-1.9‰, -5.2‰
-3.8‰, -5.4‰
-30.7‰, -9.4‰
-7.2‰, -7.4‰
87Sr/86Sr = 0.70811
87Sr/86Sr = 0.70879
12ZL-21.6
O
+0.9‰, -6.1‰
-6.0‰, -9.4‰
-22.3‰, -9.3‰
-24.5‰, -9.4‰
-9.1‰, -7.4‰
-8.8‰, -7.3‰
14ZL-49
P
+1.2‰,-5.6‰
+1.0‰,-5.8‰
-25.7‰,-9.6‰
-26.3‰,-9.3‰
14ZL-49

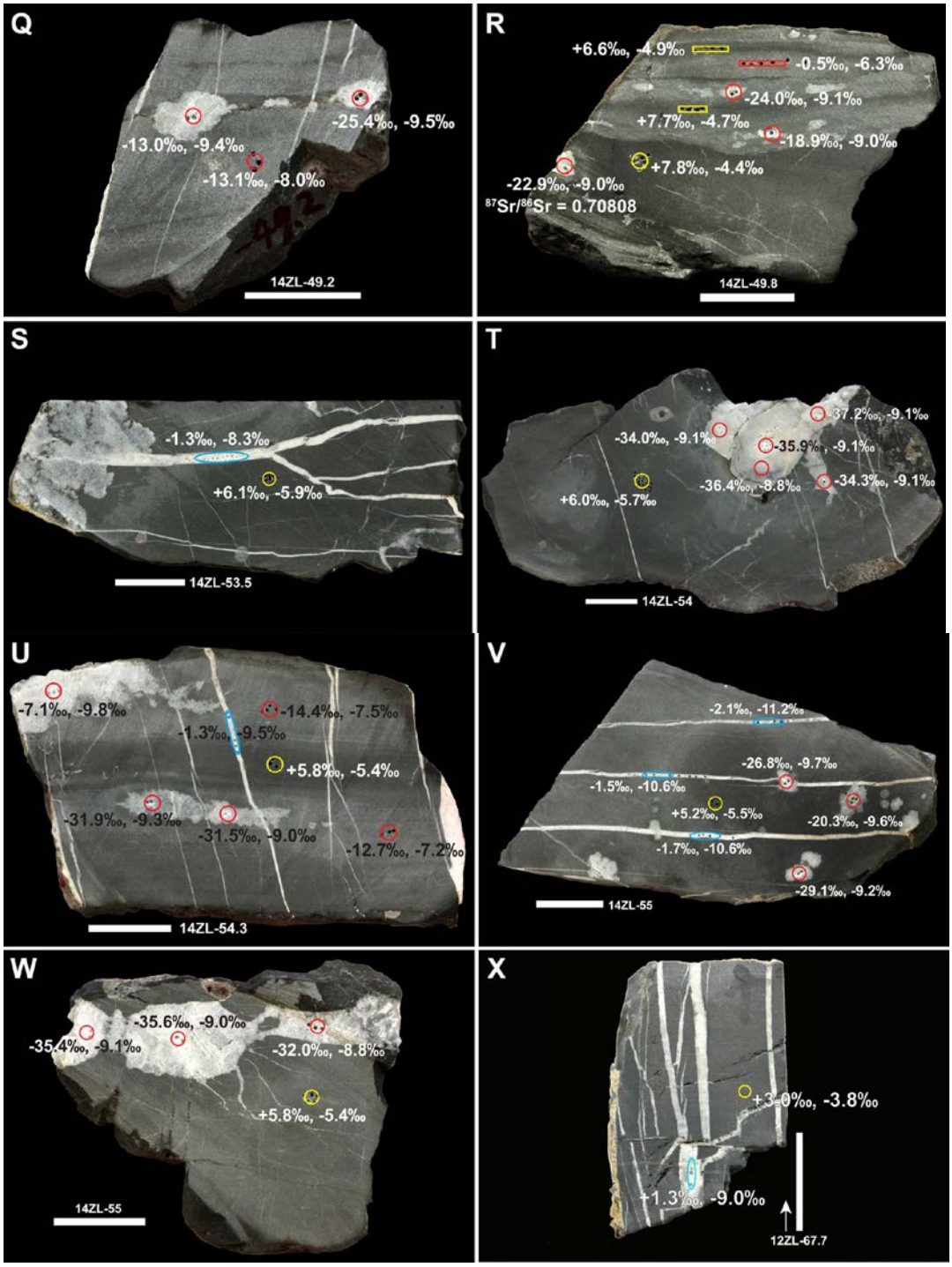
Q
-25.4‰, -9.5‰
-13.0‰, -9.4‰
-13.1‰, -8.0‰
14ZL-49.2
R
+6.6‰, -4.9‰
-0.5‰, -6.3‰
-24.0‰, -9.1‰
+7.7‰, -4.7‰
-18.9‰, -9.0‰
+7.8‰, -4.4‰
-22.9‰, -9.0‰
87Sr/86Sr = 0.70808
14ZL-49.8
S
-1.3‰, -8.3‰
+6.1‰, -5.9‰
14ZL-53.5
T
37.2‰, -9.1‰
-34.0‰, -9.1‰
-35.9‰, -9.1‰
-36.4‰, -8.8‰
-34.3‰, -9.1‰
+6.0‰, -5.7‰
14ZL-54
U
-7.1‰, -9.8‰
-14.4‰, -7.5‰
-1.3‰, -9.5‰
+5.8‰, -5.4‰
-31.9‰, -9.3‰
-31.5‰, -9.0‰
-12.7‰, -7.2‰
14ZL-54.3
V
-2.1‰, -11.2‰
-26.8‰, -9.7‰
-1.5‰, -10.6‰
+5.2‰, -5.5‰
-20.3‰, -9.6‰
-1.7‰, -10.6‰
-29.1‰, -9.2‰
14ZL-55
W
-35.6‰, -9.0‰
-35.4‰, -9.1‰
-32.0‰, -8.8‰
+5.8‰, -5.4‰
14ZL-55
X
+3.0‰, -3.8‰
+1.3‰, -9.0‰
12ZL-67.7

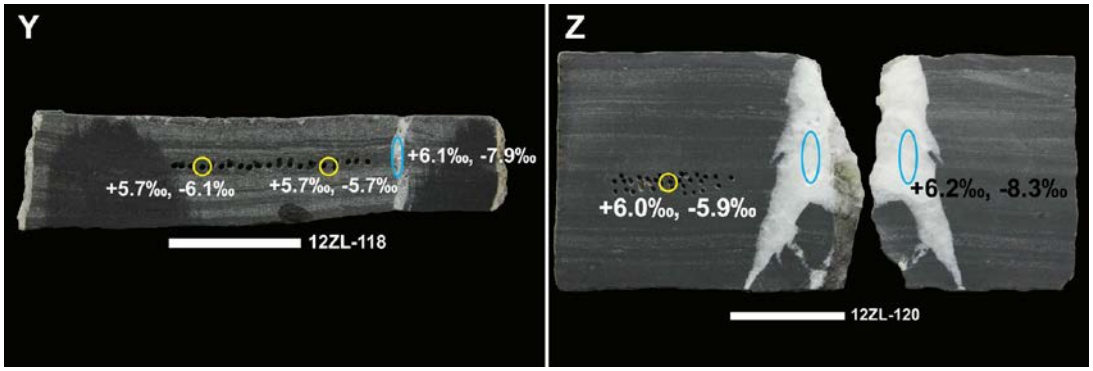

Figure 3.4: Rock slabs collected from Doushantuo Formation in Zhongling section marked with measured isotopic composition. All the scale bars in this figure are 2 cm long. Each pair of numbers for a measured spot shows carbonate carbon isotope ($\delta^{13}C$), and then oxygen isotope ($\delta^{18}O$) composition, respectively. Red, yellow and blue circles denote authigenic calcite zones, normal marine carbonate zones, and late intruded veins, respectively. The number in the sample name denotes the distance below the Doushantuo-Dengying boundary in the Zhongling section. (A) Phosphorite with authigenic calcite cements. The calcite phase in phosphorite has very negative $\delta^{13}C$ values. Sample 12ZL-0.9. (B, C) Massive chicken-wire texture replaced by authigenic calcite nodules. The calcite nodules are surrounded by authigenic sillica. Sample 14ZL-3.5 and 14ZL-4.5. (D) Phosphatic dolostone with authigenic calcite cements. Sample 12ZL-4.5. (E) Authigenic calcite nodules in dolostone. Each nodule shows different $\delta^{13}C$ values, indicating different proportion of mixing between methane signal and seawater signal. Sample 14ZL-6.5. (F, G) Big authigenic calcite nodules in phosphatic dolostone. Samples 14ZL-6.6 and 14ZL-7.5. (H-L) Oolite with authigenic calcite cements. $\delta^{13}C$ of the late intruded veins all have less negative values than the authigenic calcite cements. (M, N) Dolomitic intraclasts cemented by white-colored authgenic calcite. Sample 12ZL-21.6. (O-R) Authigenic calcite nodules in fine-grain sized dolostone. Note that the authigenic-calcite-dominated layers have more negative $\delta^{13}C$ and $\delta^{18}O$ values than dolomite-dominated layers. Samples 14ZL-49, 14ZL-49.2 and 14ZL-49.8. (S) Dolostone with late calcite veins. Sample 14ZL-53.5. (T) Authigenic calcite nodule in fine grain sized dolostone. Sample 14ZL-54. (U) Dolostone with calcite veins. Note that the authigenic-calcite-dominated layers have much more negative $\delta^{13}C$ values than those of the calcite veins or dolomite-dominated layers. Sample 14ZL-54.3. (V, W) Dolostone with authigenic calcite nodules and late intruded calcite veins. Note that the authigenic calcite nodules have much more negative $\delta^{13}C$ values than those of the calcite veins. Sample 14ZL-55. (X-Z) Dolostone with calcite veins. The arrow denotes the stratigraphic up direction. Samples 12ZL-67.7, 12ZL-118, and 14ZL-120.

3.5 Authigenic origin for the calcite nodules and cements

The $\delta^{13}C$ composition of the authigenic calcites reveal extraordinarily negative values, ranging from ca. -5 to as low as –37‰, whereas isolated primary depositional components ranged from ca. -2 to +7‰ (**Fig. 3.1**). The magnitude of ^{13}C depletion in the authigenic calcite cements suggest that carbonate alkalinity increased in pore fluids through the anaerobic oxidation of methane (AOM) and other organic substrates within a sulfate-methane transition zone (SMTZ). The SMTZ denotes a redox interface within an anoxic sediment column where pore water sulfate and methane concentration profiles intersect at non-detectable levels. The depth of the SMTZ depends on the upward methane flux from below and downward diffusion of sulfate from overlying seawater (Borowski et al., 1996). In Modern examples (Jørgensen and Kasten, 2006) where soluble ferrous iron and barium are available, ^{13}C depleted calcite, pyrite, and barite can be formed. The presence of pyrite framboids directly associated with the upper Doushantuo nodules, cements, and replacement fabrics suggest that sulfate reduction was the dominant microbial process that mediated AOM and authigenesis of calcite. Further supporting an authigenic origin for the calcite nodules and cements, their strontium isotope compositions, which range from 0.7080 to 0.7083 (**Figs. 3.1, 3.2**), are remarkably consistent with contemporaneous Ediacaran seawater as recorded in bedded limestone facies lower in the formation (Melezhik et al., 2009; Sawaki et al., 2010).

Geochemical models of microbial sulfate reduction (Meister, 2013) indicate that the onset of this metabolic strategy initially lowers pH, which would favor the

dissolution of pre-existing carbonate and fluorapatite, the formation of sedimentary voids, and the precipitation of silica (**Fig. 3.5**). Due to the absence of siliceous organisms in Ediacaran oceans the concentration of dissolved silica in marine waters is believed to have been elevated (Maliva et al., 1989; Xiao et al., 2010), especially in shallow marine evaporitic environments. Available ferrous iron in pore fluids or released from the dissolved minerals was sequestered as pyrite in the biogenic framboids. As sulfate reduction progresses, however, the pH is stabilized and calcite saturation increases with the buildup of alkalinity, especially if methane were the primary organic substrate (Moore et al., 2004). Carbonate saturation would also increase with microbially-mediated iron-reduction (Higgins et al., 2009; Schrag et al., 2013) or pyrite formation, but the presence of the framboids suggests that anaerobic sulfate reduction was the critical process associated with authigenesis. The concomitant rise in pH would favor the dissolution of silica in the nodules and the wholesale precipitation of coarse rhombic calcite remarkably depleted in ^{13}C.

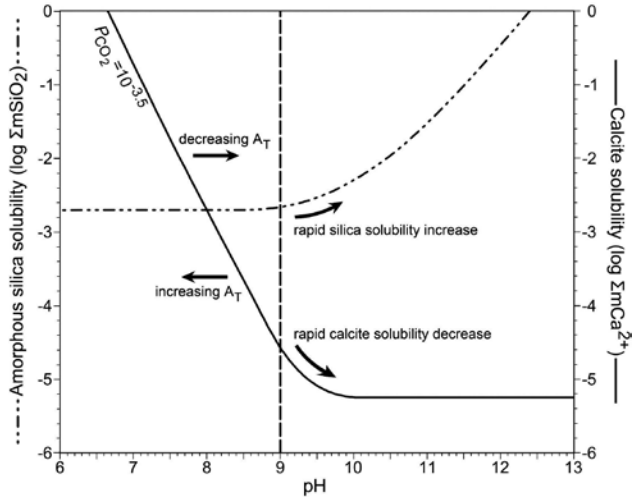

Figure 3.5: Solubility of amorphous silica and calcite at variable pH and alkalinity (A_T) with critical transitions at around pH = 9. Figure from Langmuir et al. (1997); Xiao et al. (2010).

3.6 Correlation between C and O isotopes

Additional SEM and XRD investigations further demonstrate that micron-sized authigenic calcite co-occurs with dolomicrite in both massive and laminated specimens (**Fig. 3.6**), and partially replaces pre-existing dolomitic and phosphatic intraclasts. Based on detailed isotopic analyses of these phases, we find tightly coupled depletions of ^{13}C and ^{18}O, the magnitude of which is dependent on the relative abundance of authigenic calcite (**Fig. 3.6**). Measurements of multiple discrete layers in a pervasively fine-grained specimen – typical of most Ediacaran carbonates including those deposited during the Shuram Excursion – reveal a well-correlated mixing line with one end member defined by dolomicrite, representing normal seawater alkalinity ($\delta^{13}C \sim +2‰$ and $\delta^{18}O \sim –6‰$), and the other recorded by authigenic calcite, representing alkalinity in pore waters ($\delta^{13}C \sim –37‰$ and $\delta^{18}O \sim –10‰$) influenced by the AOM. Notably $\delta^{18}O$ compositions of the purest calcite phases isolated from a wide range of nodules from several discrete levels define a stable "floor" of values near –10‰ (**Fig. 3.1**) that we suggest reflect pore water conditions. Analyses of upper Doushantuo authigenic calcite nodules and cements in other sections in the outer shelf region reveal a similar pattern of carbon and oxygen isotope compositions, including the same floor of $\delta^{18}O$ values (**Fig. 3.7**).

Both theoretical and experimental studies have shown that 3–4‰ enrichment in ^{18}O abundances of dolomite relative to calcite is expected for these carbonate minerals forming contemporaneously from the same solution (i.e., seawater in open oxygen isotope exchange with pore water) at expected temperatures (Horita, 2014).

An even greater magnitude of fractionation between primary and authigenic phases may additionally result from AOM through the buildup of alkalinity in pore fluids. While anaerobic sulfate reduction results in the production of alkalinity, protons may either be consumed (increasing pH) or produced (decreasing pH) depending on the source of electrons. In the case of AOM, protons are initially produced in excess thereby lowering pH (Meister, 2013), and hence serving to dissolve dolomicrite and dolomitic allochems and to precipitate silica cements. The subsequent buildup of alkalinity, however, drives pH higher, causing silica to dissolve and enhancing calcite saturation in pore fluids (**Fig. 3.5**). It has been elegantly demonstrated (Watkins et al., 2014) that the $\delta^{18}O$ difference between water and inorganically-formed calcite decreases systematically with increases in pH and alkalinity. The negative floor of $\delta^{18}O$ compositions in the purest authigenic calcite phases and the >4‰ difference in $\delta^{18}O$ between primary depositional components and authigenic calcite likely reflects this isotope effect. In sum, the paragenetic history of the sediments and isotopic compositions of the authigenic calcite phases support the view that these are early authigenic features, and not associated with hydrothermal events long after the rocks were lithified (Bristow et al., 2011).

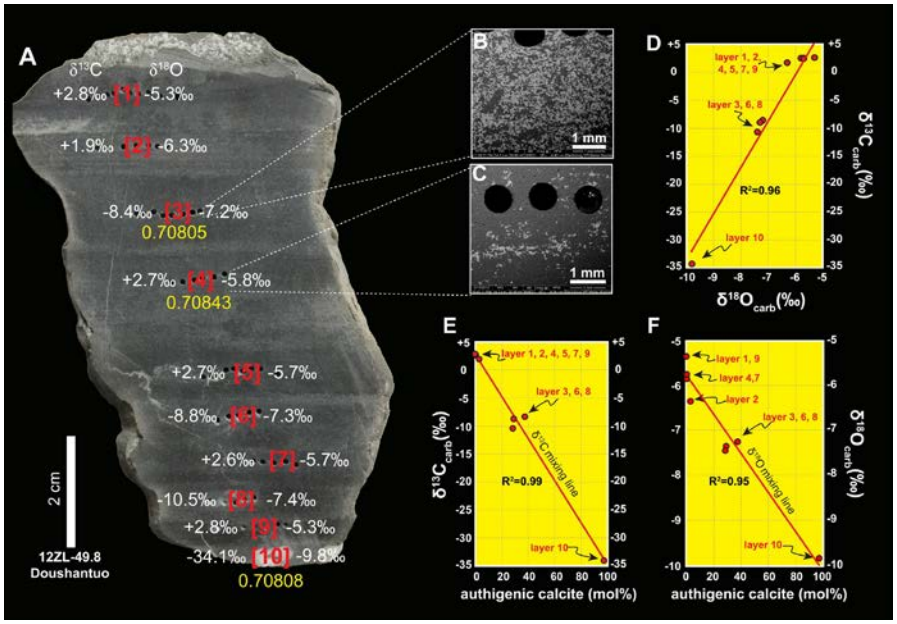

Figure 3.6: Photograph of a fine-grained dolomite sample from 49.8 meters below the Doushantuo/Dengying boundary at Zhongling (A), which is typical of most Ediacaran carbonates, with carbon and oxygen isotope compositions of 10 different micro-samples, including a small authigenic calcite nodule. (B, C) BSE (back scattered electron) images of authigenic calcite (light color) and dolomicrite (dark color) dominated zones, respectively. (D-F) The degree of ^{13}C and ^{18}O depletion [see $\delta^{13}C$ (left) and $\delta^{18}O$ (right) values for each drilling layer on the photograph] is shown in the cross-plots to be directly correlated to the percentage of authigenic calcite in each micro-sample as determined by quantitative XRD analysis.

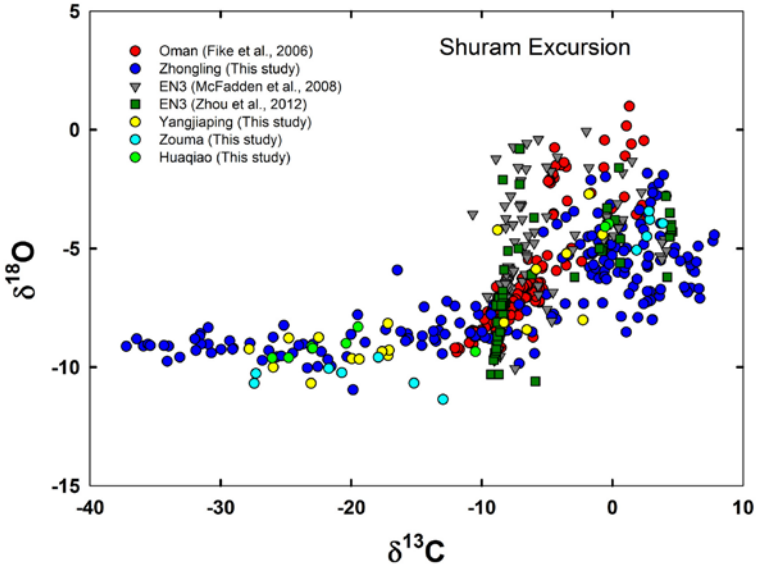

Figure 3.7: Analyses of Doushantuo normal marine and authigenic carbonates in Zhongling, Yangjiaping, Zouma, Huaqiao sections, South China. Data in Oman are from Fike et al. (2006). Data of EN3 interval are from McFadden et al. (2008); Zhou et al. (2012). All data are reported as ‰ relative the VPDB.

3.7 Biogeochemical model for the Shuram Excursion

Projected to the world stage, these coupled microbial and inorganic processes provide an explanation for the formation of ^{13}C-depleted authigenic calcite, as well as the covariance of carbon and oxygen isotopes observed during the middle Ediacaran Shuram Excursion – the most profound negative carbon cycle anomaly recorded in Earth history. Where the biogeochemical anomaly is best expressed in South China (Jiang et al., 2007), Oman (Bergmann, 2013), Siberia (Melezhik et al., 2009), and the western USA and Mexico (Kaufman et al., 2007; Loyd et al., 2013), the carbonates are primarily composed of limestone, suggesting a strong authigenic calcite component. The strong coupling of carbon and oxygen isotope compositions in Shuram carbonates has previously been interpreted as a function of globally-distributed diagenetic reactions associated with the flushing of meteoric waters depleted in both ^{13}C and ^{18}O through shallow marine sediments (Knauth and Kennedy, 2009) – implying widespread terrestrial photosynthesis during the middle Ediacaran Period – or thermal effects associated with deep burial long after the sediments had lithified (Derry, 2010). These speculations on the effects of alteration, however, are inconsistent with the excellent preservation of sedimentary textures. In addition, where the Shuram Excursion is best expressed by high-resolution sampling of mixed fine-grained limestone and dolomite facies at Jiulongwan (McFadden et al., 2008), the coupled carbon, sulfur, and strontium isotope trends along with the progressive enrichment of strontium and barium (**Figs. 3.8, 3.9**) support an oceanographic origin for the biogeochemical anomaly. In our alternative view, the

enigmatic excursion and the coupled chemical responses recorded in seawater proxies from equivalent successions around the globe stems from the proportional mixture of primary and authigenic components.

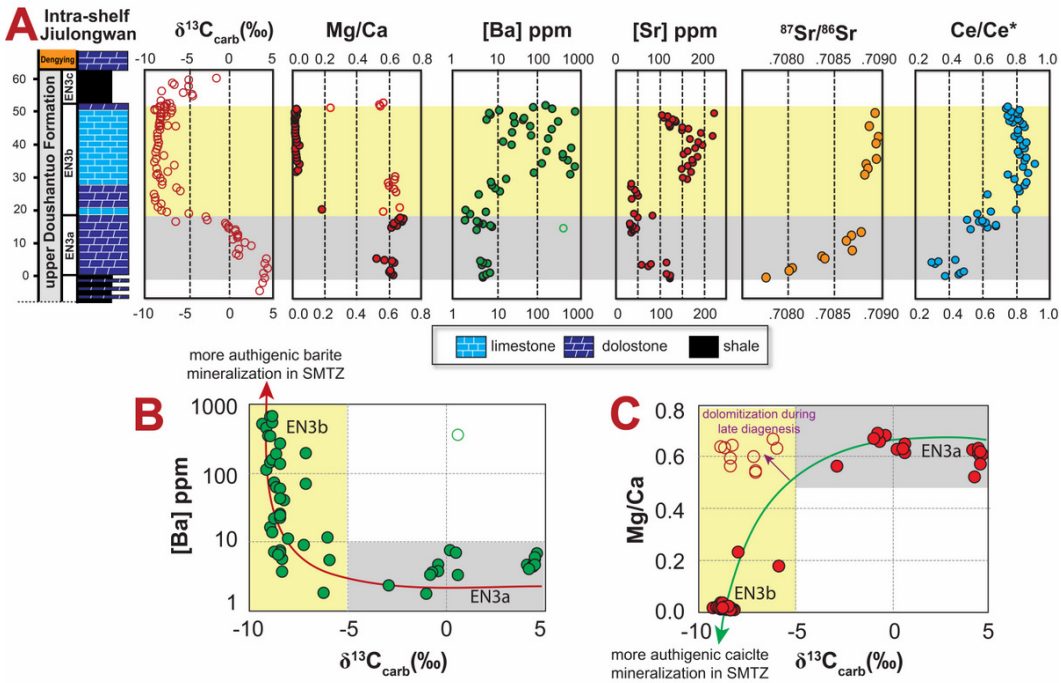

Figure 3.8: Litho- and chemo-stratigraphy of the upper Doushantuo Formation in the Jiulongwan section. (A) Time-series geochemical data for the Shuram-equivalent EN3 interval of the upper Doushantuo Formation, including carbonate carbon isotopes ($\delta^{13}C_{carb}$) (McFadden et al., 2008), barium elemental concentration ([Ba] ppm), strontium elemental concentration ([Sr] ppm) (Zhou et al., 2012) , strontium isotopes ($^{87}Sr/^{86}Sr$) (Sawaki et al., 2010), Mg/Ca ratio and Ce anomaly (Ce/Ce*) (Zhou et al., 2012). (B) Cross plot of the $\delta^{13}C_{carb}$ and [Ba] data for EN3a and EN3b interval. (C) Cross plot of the $\delta^{13}C_{carb}$ and Mg/Ca data for the EN3a and EN3b interval. Some samples altered by late dolomitization are shown as open circles. Detailed petrographic evidence of late dolomitization is shown in **Fig. 3.9.**

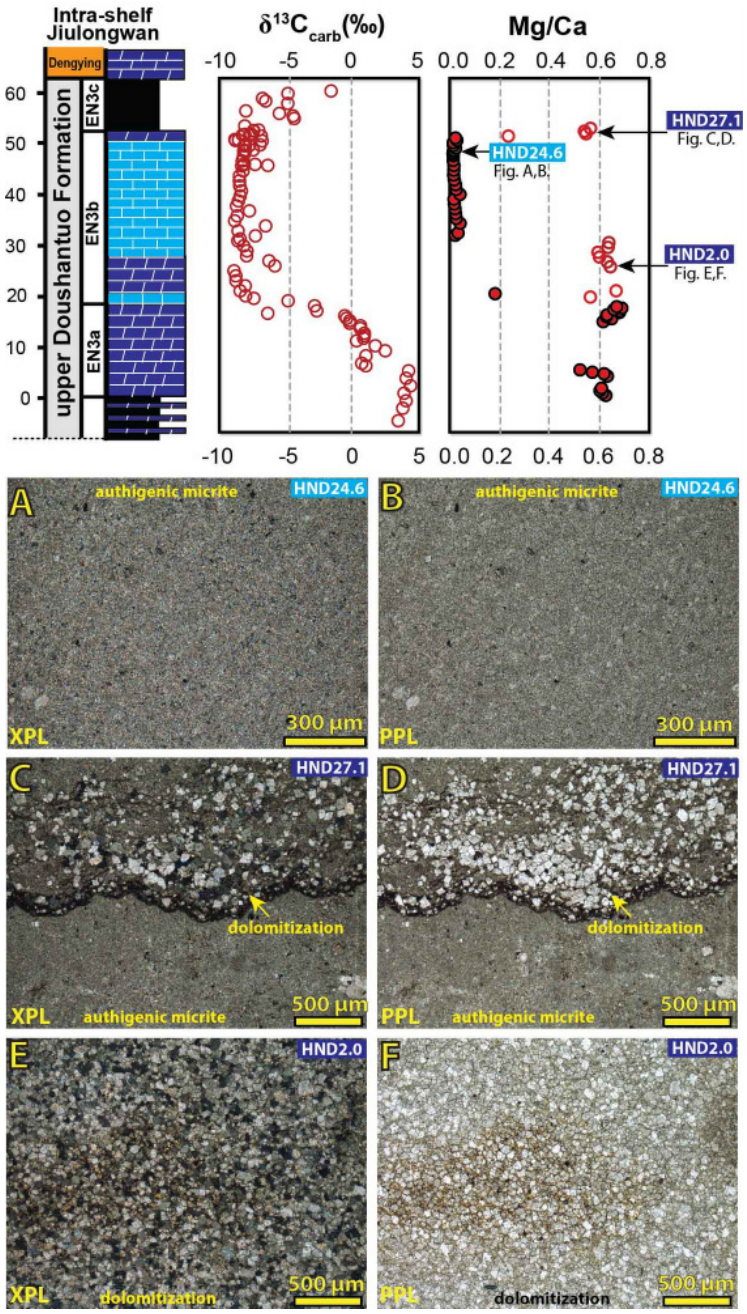

Figure 3.9: Petrographic images of samples from EN3b interval of the Doushantuo Formation in Jiulongwan section. (A,B) Petrographic images of sample HND24.6 under plane polarized light and cross polarized light. Sample is mainly composed of authigenic micrite, with low Mg/Ca ratio; (C,D) Petrographic images of sample HND27.1 under plane polarized light and cross polarized light. This sample is partitally altered by dolomitization, with a higher Mg/Ca ratio; (E,F) Petrographic images of sample HND2.0 under plane polarized light and cross polarized light. This sample is altered by dolomitization, with a higher Mg/Ca ratio.

Based on data presented here, it appears that methane was an important constituent of the dissolved organic carbon pool in Ediacaran seawater (Rothman et al., 2003), which along with fossil organic matter derived from the erosion of exposed strata (Kaufman et al., 2007), buffered the $\delta^{13}C$ composition of bulk organic matter in Shuram Excursion sediments. Given the confluence of events, it appears that oxidation of methane and other dissolved organic constituents was linked directly to a middle Ediacaran pulse of sulfate to the oceans attendant with the rise of atmospheric oxygen and enhanced weathering rates (Kaufman et al., 2007; Lyons et al., 2014; Xiao, 2014). In Modern marine environments rich in sulfate, the upward methane flux in the SMTZ is exhausted through sulfate reduction (Jørgensen, 1982) (**Fig. 3.10**), except in areas with active methane cold seeps and hydrate deposits where methane can escape to seawater. Our observation of methane-derived authigenic calcite in the upper Doushantuo Formation, coupled with progressive stratigraphic depletion of ^{34}S in co-existing pyrite and trace sulfate deposited during the Shuram Excursion in South China and elsewhere (Fike et al., 2006; Kaufman et al., 2007; McFadden et al., 2008), supports the view that the biogeochemical event was driven by a pulsed increase of oceanic sulfate. This interpretation suggests that cold-seep environments where carbonates were formed are more ancient than previously documented (Bristow and Grotzinger, 2013).

Given that observational evidence for authigenic calcite is currently restricted to the Shuram Excursion preserved in the upper Doushantuo Formation of South China, it is uncertain whether other strongly negative carbon isotope anomalies of the

Neoproterozoic Era, including the post-glacial cap carbonates (Hoffman et al., 1998b), or other spatial (i.e., related to facies across contemporary platforms) and temporal variations in carbon isotope abundances of carbonates (Jiang et al., 2007) may be explained by the variable admixture of these syn-sedimentary cements. We suggest that detailed petrographic and mineralogical studies accompany those that use secular variations in seawater carbon isotope abundances as tools for correlation or environmental interpretation.

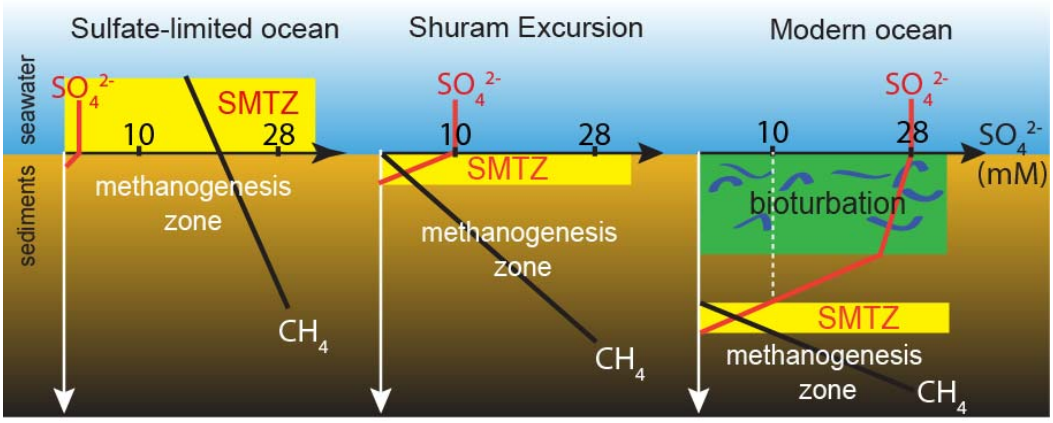

Figure 3.10: Progressive deepening of sulfate-methane transition zone (SMTZ) driven by increasing seawater sulfate. Based on observation of modern marine sediments, anaerobic oxidation of methane (AOM) within SMTZ requires sulfate concentration in pore water to be < 10 mM (Jørgensen and Kasten, 2006). Projected to the Shuram Excursion, the formation of authigenic carbonates within SMTZ located near the sediment-water interface requires seawater sulfate to be ca. 10 mM.

The Shuram Excursion neatly subdivides the Ediacaran Period into a pre-event interval dominated by multicellular algae and a post-event interval characterized by the sudden appearance of soft-bodied macro-metazoans (Xiao, 2014). Insofar as the biogeochemical anomaly is connected to middle Ediacaran oxidation, the flux of sulfate from the continents would have been accompanied by nutrients, including phosphorous, which would explain the occurrence of bedded

phosphorites at this level. To allow global syn-deposition of authigenic calcite, SMTZ during the Shuram anomaly was likely near the sediment-water interface (**Fig. 3.10**) assuming sulfate concentrations approached ca. 10 mM similar to those in modern SMTZs (Jørgensen and Kasten, 2006). The occurrence of seafloor-precipitated aragonite fans associated with the Shuram anomaly supports this view (Kaufman et al., 2007; Loyd et al., 2013). Our field, petrographic, and geochemical observations of authigenic calcite in the upper Doushantuo provide a solution to the Shuram puzzle, and open a window to further exploration of perturbations of the ancient carbon cycle. For example, in intervals lacking in oceanic sulfate, including most of the Precambrian, it seems possible that methane could have been directly released to the atmosphere (Habicht et al., 2002) were it not oxidized through microbial denitrification or iron reduction within sediments or the water column. On the contrary, the remarkable instability in $\delta^{13}C$ across the Precambrian-Cambrian transition (Maloof et al., 2010) likely results from variable formation of authigenic carbonate during pulses in seawater sulfate abundance, which may be related to the ventilation of the sediments through bioturbation (Canfield and Farquhar, 2009). In summary, the global enhancement of seawater sulfate during terminal Precambrian time fundamentally changed the exogenic carbon cycle by more efficiently oxidizing organic matter in sediments and seawater, thereby paving the way for Modern oceans with flourishing animal life.

Chapter 4: Environmental context for the terminal Ediacaran biomineralization of animals

4.1 Abstract

In terminal Ediacaran strata of South China, the onset of calcareous biomineralization is preserved in the paleontological transition from *Conotubus* to *Cloudina* in repetitious limestone facies of the Dengying Formation. Both fossils have similar size, funnel-in-funnel construction, and epibenthic lifestyle, but *Cloudina* is biomineralized whereas *Conotubus* is not. To provide environmental context for this evolutionary milestone, we conducted a high-resolution elemental and stable isotope study of the richly fossiliferous Gaojiashan Member. Coincident with the first appearance of *Cloudina* is a significant positive carbonate carbon isotope excursion (up to +6‰) and an increase in the abundance and ^{34}S composition of pyrite. In contrast, $\delta^{34}S$ values of carbonate-associated sulfate remain steady throughout the succession, resulting in anomalously large (>70‰) sulfur isotope fractionations in the lower half of the member. The fractionation trend likely relates to changes in microbial communities, with sulfur disproportionation dominating in the lower interval while microbial sulfate reduction was the principal metabolic pathway in the upper. We speculate that the coupled paleontological and biogeochemical anomalies may have coincided with an increase in terrestrial weathering fluxes of sulfate, alkalinity, and nutrients to the depositional basin, which stimulated primary productivity, the spread of an oxygen minimum zone, and the development of euxinic conditions in subtidal and basinal environments. Enhanced

production and burial of organic matter is thus directly connected to the carbon isotope anomaly, and likely promoted pyritization as the main taphonomic pathway for *Conotubus* and other soft-bodied Ediacara biota. Oxidative weathering and water column sulfate reduction may have also enhanced seawater alkalinity and facilitated the early rise of animal biomineralization.

4.2 Introduction

The earliest animal to have developed a biomineralized carbonate exoskeleton is *Cloudina* — named after the famed Precambrian paleontologist Preston Cloud (1912–1991) and recognized in terminal Ediacaran (ca. 550–541 Ma) sedimentary successions worldwide (Conway Morris et al., 1990; Gaucher and Germs, 2009; Cortijo et al., 2010; Zhuravlev et al., 2012). This animal, which is suggested to be an ancient cnidarian-grade (Grant, 1992; Cortijo et al., 2010) or annelid-like organism (Hua et al., 2005), had an epibenthic lifestyle and constructed a thin-walled funnel-in-funnel shell of high-Mg calcite with its apex attached to the substrate (Grant, 1990; Zhuravlev et al., 2012; Cai et al., 2014). *Cloudina* was associated with microbial reefs, and may have been a reef builder like modern-day corals that inhabit oligotrophic shelf environments where they band together in search of hard substrates and for protection against predators (Penny et al., 2014; Wood and Curtis, 2015).

Biomineralization of *Cloudina* is widely believed to have been a response to predation given the significant number of borings found on its fossil shells (Bengtson and Zhao, 1992; Hua et al., 2003; Porter, 2011). Alternatively, some have considered

terminal Ediacaran biomineralization as a physiological response to regulate calcium concentrations in circulatory fluids (Simkiss, 1977; Kempe et al., 1989; Simkiss, 1989), or to environmental perturbations involving oscillations in atmospheric pCO_2 and seawater chemistry (Knoll, 2003; Knoll and Fischer, 2011). Environmental drivers, however, are particularly difficult to assess insofar as these should also have a broad effect on general biotic diversification and vice versa (Gaidos et al., 2007; Butterfield, 2009; Butterfield, 2011; Lenton et al., 2014). Insofar as there is a metabolic cost to biomineralization, the biological benefits to the organisms, including protection against predation and the physiological response of organisms to rapidly changing seawater chemistry in the terminal Ediacaran Period, should be balanced (Knoll, 2003; Xiao, 2014).

To this end, we investigated a Lagerstätte of Ediacaran animals in the Gaojiashan Member of the Dengying Formation in South China (**Fig. 4.1**) (Hua et al., 2007; Cai et al., 2010). Within the member's repetitious limestone facies, the first appearance of *Cloudina* is immediately preceded by *Conotubus*, a soft-bodied antecedent exquisitely preserved through pyritization with similar construction, size, and lifestyle (Cai et al., 2011; Cai et al., 2014). To explore this unique paleontological juxtaposition and provide environmental context for the earliest examples of animal biomineralization and pyritization, we sampled the Gaojiashan Member at high stratigraphic resolution for elemental and isotopic compositions. Our time-series measurements reveal that these evolutionary and taphonomic events are associated with profound biogeochemical shifts in both the carbon and sulfur cycles, and we

speculate that they may have been facilitated by profound environmental perturbations in the marine realm ultimately driven by enhanced oxidative weathering of the continents.

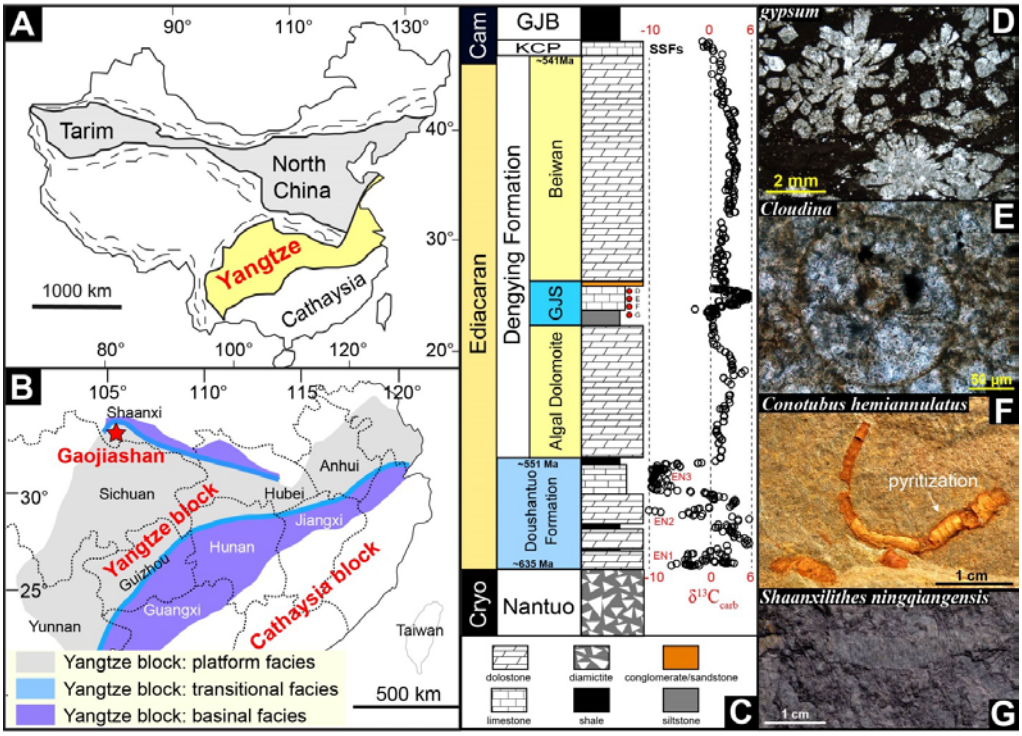

Figure 4.1: Tectonic framework of China, with the Yangtze Craton highlighted in yellow. (**B**) Ediacaran depositional environments on the Yangtze Craton (Jiang et al., 2011). (**C**) $\delta^{13}C_{carb}$ record of the Dengying Formation in the Gaojiashan section. GJS = Gaojiashan, KCP = Kuanchuanpu, GJB = Guojiaba; $\delta^{13}C_{carb}$ data for Doushantuo Formation are from McFadden et al. (2008). (**D**) Calcite pseudomorph after gypsum ca. 46.5 m above the base of the Gaojiashan Member. (**E**) *Cloudina* in the Gaojiashan Member ca. 42 m above the base. (**F**) Pyritized tubular fossil *Conotubus hemiannulatus* (Cai et al., 2011). (G) Enigmatic body fossil *Shaanxilithes ningqiangensis* (Meyer et al., 2012).

4.3 Methods

In this study, the Gaojiashan Member was systematically sampled at high resolution for integrated chemostratigraphic and geochronological investigations. Geochemical analyses were conducted in the Paleoclimate CoLaboratory at

University of Maryland. Details of the methods used in the CoLaboratory can be found in previous publications (e.g. McFadden et al., 2008; Zhelezinskaia et al., 2014; Cui et al., 2015), but are briefly outlined below. Methods for carbon, oxygen, and pyrite sulfur isotope analyses and elemental concentration analysis could be found in Chapter 2.

4.3.1 Sulfate sulfur isotope analyses

Bulk carbonate powders were used for extraction of carbonate-associated sulfate (or CAS). Around 100 g of crushed bulk sample, which were repeatedly leached with 10% NaCl solutions (10x with stirring for at least two hours), and then washed with Milli-Q water (3x) prior to acidification of the leached powders with 3 M HCl. CAS precipitates were then collected as $BaSO_4$ three days after $BaCl_2$ was added to the solution. The residues and the $BaSO_4$ precipitates were packed into folded tin cups with V_2O_5 for combustion to SO_2 in a Eurovector elemental analyzer in-line with a second Elementar Isoprime isotope ratio mass spectrometer, which measured isotope abundances. Uncertainties for sulfur isotope measurements determined by multiple analyses of standard materials during analytical sessions are better than 0.3‰.

4.3.2 Detrital zircon dating

For all aspects of zircon dating we followed the procedures described in Martin et al. (2015). Zircon grains were isolated using conventional mineral separation techniques including rock pulverization by hand using a mortar and pestle, removal of silt and clay by hand panning in water, removal of magnetic grains using a

Frantz magnetic barrier separator, and density separation using methylene iodide. Zircon grains were then poured onto double-sided tape and cast them in an epoxy disk along with approximately 10 shards of the Sri Lanka zircon standard (564±3 Ma) (Gehrels et al., 2008). After hand polishing to expose the interiors of the grains, we produced backscattered electron and cathodoluminescence images using the JEOL JXA-8900R electron probe microanalyzer at the University of Maryland.

The cores of 49 and 175 zircon grains were dated from samples 09G-35.3 and 09G-37.9, respectively, by laser ablation–inductively coupled plasma–mass spectrometry in the Arizona LaserChron Center at the University of Arizona, taking care to avoid multiple cathodoluminescence zones, inclusions, and cracks. Ablation of the zircon was performed using a New Wave UP193HE Excimer laser and a spot diameter of 30 μm. The ablated zircon was carried in helium into the plasma source of a Nu Plasma HR multi-collector mass spectrometer, and analyses followed the protocols described in Martin et al. (2015).

Corrections for inter-element fractionation of Pb/U and common Pb, as well as other data reduction, were performed off-line using an Excel program developed at the Arizona LaserChron Center. We removed from further consideration analyses with: (1) high ^{204}Pb, (2) greater than 5% error on the ^{206}Pb/^{207}Pb date, (3) greater than 5% error on the ^{206}Pb/^{238}U date, (4) greater than 25% normal discordance or 8% reverse discordance, (5) high U concentration, or (6) high U/Th ratio. The remaining analyses were used in our interpretations (**Table C.1; Fig. 4.3**). Isoplot was used to

calculate weighted means and to produce concordia and probability density plots (Ludwig, 2008).

$^{206}Pb/^{238}U$ dates are usually more precise than $^{206}Pb/^{207}Pb$ dates for zircon younger than about 1.4 Ga, whereas the reverse is true for older grains. However, $^{206}Pb/^{207}Pb$ dates are only minimally affected by recent lead loss, so in most cases they more closely indicate the time of crystallization for zircon older than about 1 Ga. Therefore, during interpretation we used $^{206}Pb/^{238}U$ dates for grains younger than 1 Ga and $^{206}Pb/^{207}Pb$ dates for older zircon grains.

4.4 Stratigraphic and geochronological constraint

Carbonates of the Dengying platform are sandwiched between the Ediacaran Doushantuo Formation (ca. 635-551 Ma) (Jiang et al., 2011) and the early Cambrian Kuanchuanpu Formation (Steiner et al., 2004) in the southern Shaanxi region (**Fig. 4.1**). Based on the 551 Ma U-Pb zircon depositional age of a volcanic ash at the interface between the uppermost Doushantuo and basal Dengying formations (Condon et al., 2005) and an estimated 541 Ma age for the Ediacaran-Cambrian boundary (Amthor et al., 2003; Chen et al., 2015), the >650 m thick Dengying Formation represents the last 10 million years of the Ediacaran Period. The Dengying Formation at Gaojiashan is subdivided into three intervals, including the Algal Dolomite, Gaojiashan, and Beiwan members (**Fig. 4.1**), which are typically correlated to Hamajing, Shibantan, and Baimatuo members, respectively, in the Yangtze Gorges area (Zhou and Xiao, 2007; Zhu et al., 2007; Duda et al., 2015).

At the studied section, the Gaojiashan Member is 55 m in thickness, including a siltstone interval in the lower part, repetitious siltstone-mudstone-limestone facies with microbial mats in the middle part, and a coarse sandstone/conglomerate at the top (**Fig. 4.2**) (Cai et al., 2010). The lower Gaojiashan Member contains the enigmatic fossil *Shaanxilithes ningqiangensis* preserved in siltstone facies (Meyer et al., 2012). The middle Gaojiashan Member contains *Conotubus hemiannulatus* and *Gaojiashania cyclus* preserved in thin, normally graded calcisiltite-siltstone beds interpreted as distal event deposits, followed by the first appearance of the biomineralized animal *Cloudina* preserved in intraclastic limestones approximately 40 m above the base of the succession (**Fig. 4.1**). A distinctive horizon with bedded gypsum occurs in the upper part of the Gaojiashan Member (**Figs. 4.1D, 4.2F-G**).

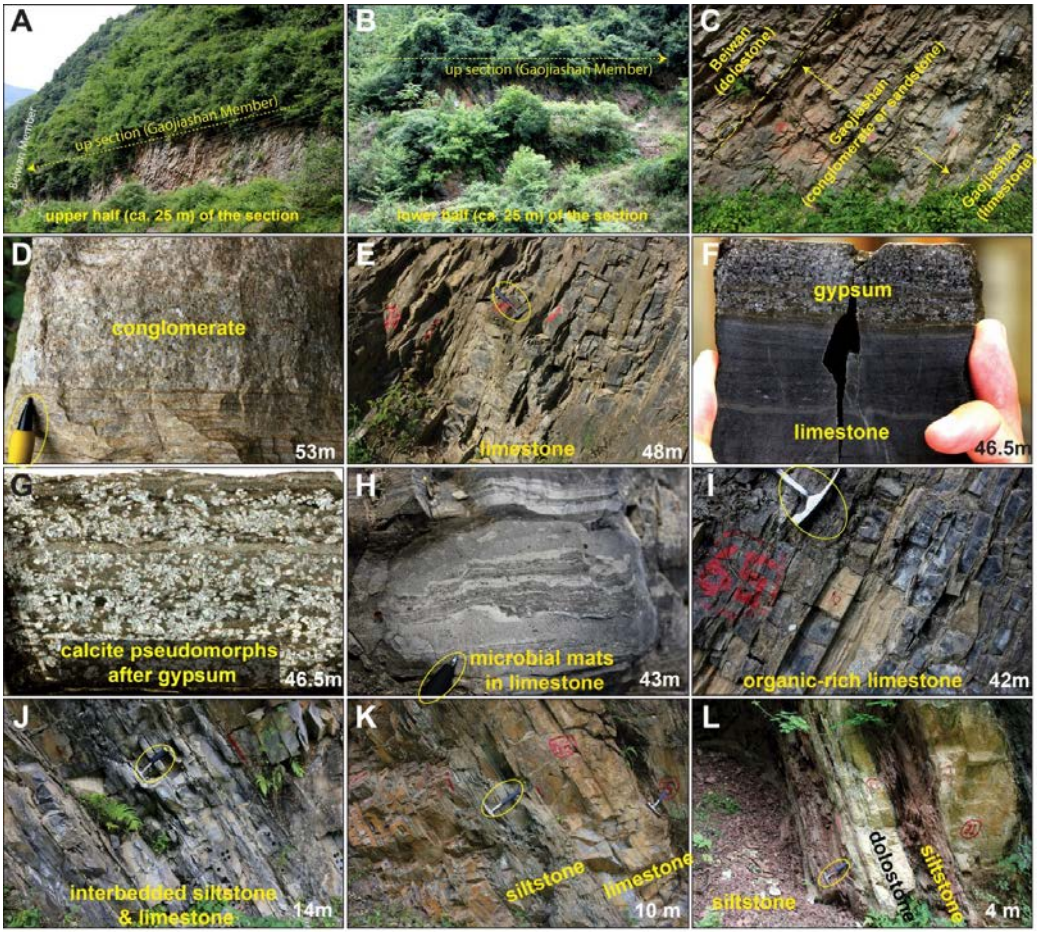

Figure 4.2: Field photographs of the Gaojiashan Member. Hammers or pencils for scale are circled. (A, B) An overview of the upper and lower section (each ca. 25 meters in thickness). (C) Boundary bewteen the Beiwan and Gaojiashan members. (D) Conglomerate in the uppemost interval. (E) Bedded limestone at 48 m. (F, G) Gypsum pseudomorphs at 46.5 m where crystals have been dissolved and replaced by calcite. (H, I) Organic-rich limestones with abudant microbial mats corresponding to the peak of the carbon isotope excursion at ca. 43 m. (J) Interbedded siltstone and limestone at 14 m. (K, L) Siltstones in the lower Gaojiashan Member.

Detrital zircon from two closely-spaced siltstone beds at 16.7 m (sample 09G-35.3) and 14.1 m (sample 09G-37.9) above the base of the Gaojiashan member yielded a youngest population of four U-Pb ages ranging from 543 to 550 Ma from sample 09G-37.9, with a weighted mean age of 548 ± 8 Ma (MSWD = 0.11) (**Fig. 4.3, Table C.1)**. This maximum depositional age based on detrital zircon ages is

within the 551–541 Ma age estimate of the Dengying Formation based on U-Pb zircon ages from bedded ash layers in South China and Oman (Amthor et al., 2003; Condon et al., 2005; Chen et al., 2015). However, most of the detrital zircons had ages between 750 and 850 Ma, with a scattering of solitary dates spanning from 1300 to 2700 Ma.

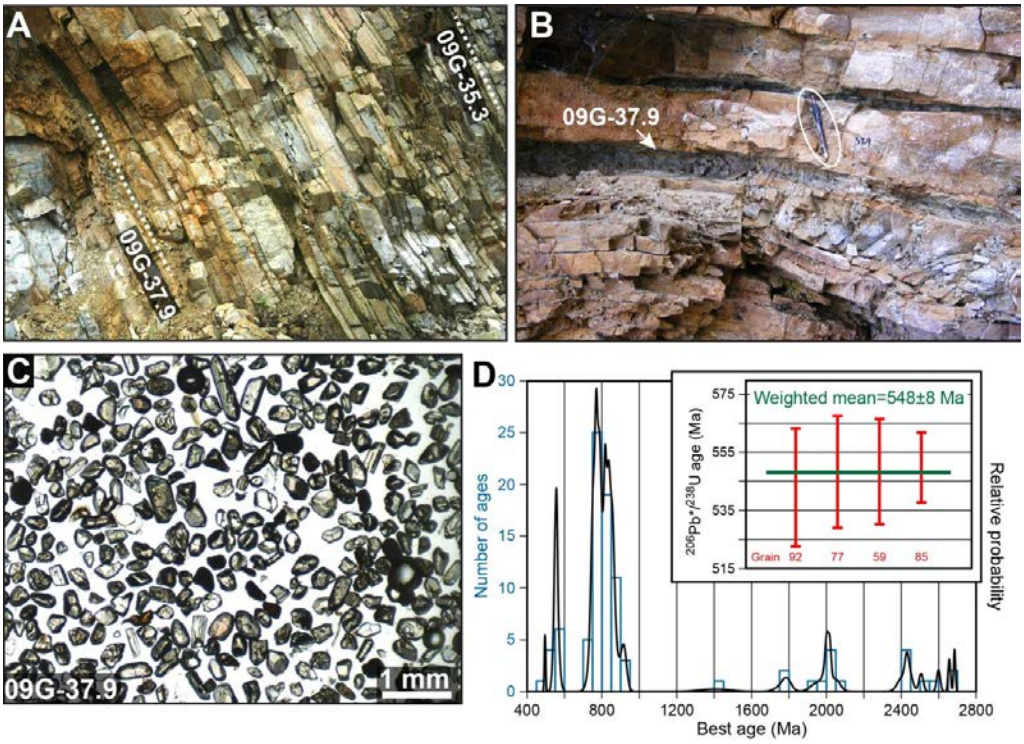

Figure 4.3: (A) Field photo showing the position of the two detrital zircon samples (09G-35.3, 09G-37.9) in the lower Gaojiashan Member. The view is about 3 m wide. (B) Close view of bed 09G-37.9. (C) Separated and mounted detrital zircon from sample 09G-37.9. (D) Histogram and relative probability plot for detrital zircon ages from sample 09G-37.9. Best age is $^{206}Pb/^{238}U$ date for grains younger than 1 Ga and $^{206}Pb/^{207}Pb$ date for older zircon. Histogram bars represent 50 Ma intervals. Inset: $^{206}Pb/^{238}U$ ages for the four youngest analyses with uncertainties that overlap at the 1-sigma level. The weighted mean of these four ages is 548±8 Ma (MSWD=0.11) from which we interpret a maximum possible depositional age of 560 Ma.

4.5 Results

In total 113 limestone and calcareous siltstone samples from the Gaojiashan Member were analyzed for elemental abundances and isotopic compositions (**Figs. 4.4-4.5; Tables C.2-C.4**). Carbonate percentages in the samples are generally high (>90%), except in the lower member where limestones and siltstones are interbedded. Time-series $\delta^{13}C_{carb}$ reveals a $\delta^{13}C_{carb}$ positive excursion (up to +6‰) in the upper part of the Gaojiashan Member, coinciding with the fossil transition from *Conotubus* to *Cloudina*. Coupled with this $\delta^{13}C_{carb}$ excursion, time-series $\delta^{13}C_{org}$ data reveal a negative excursion (down to –30‰); calculated carbon isotope fractionations ($\Delta\delta^{13}C_{carb\text{-}org}$) show peak values up to +36‰ in this interval. Pyrite S isotope ($\delta^{34}S_{pyrite}$) values measured from bulk acidified residues (assuming pyrite S >> organic S) show a wide range from –30‰ to +30‰ in the Gaojiashan Member, with more negative values in the lower half of the section, and more positive values in the upper half. On the contrary, sulfur isotope compositions of carbonate-associated sulfate ($\delta^{34}S_{CAS}$) remain generally invariant around ca. +40‰ throughout the Gaojiashan Member. Both total sulfur (TS) and total organic carbon (TOC) are notably low through most of the succession, but are elevated in the cloudinid interval. Time-series Mg/Ca show the dominance of limestone in the Gaojiashan Member with only slightly more dolomitic samples with higher Rb/Sr associated with interbedded siltstones in the lower interval. Sr/Ca ratios reveal a positive excursion in the upper section, mimicking the $\delta^{13}C_{carb}$ anomaly, while Ce/Ce* values through the section remain constant at values near to 0.5, with the exception of two samples at the top of the Gaojiashan Member with higher values.

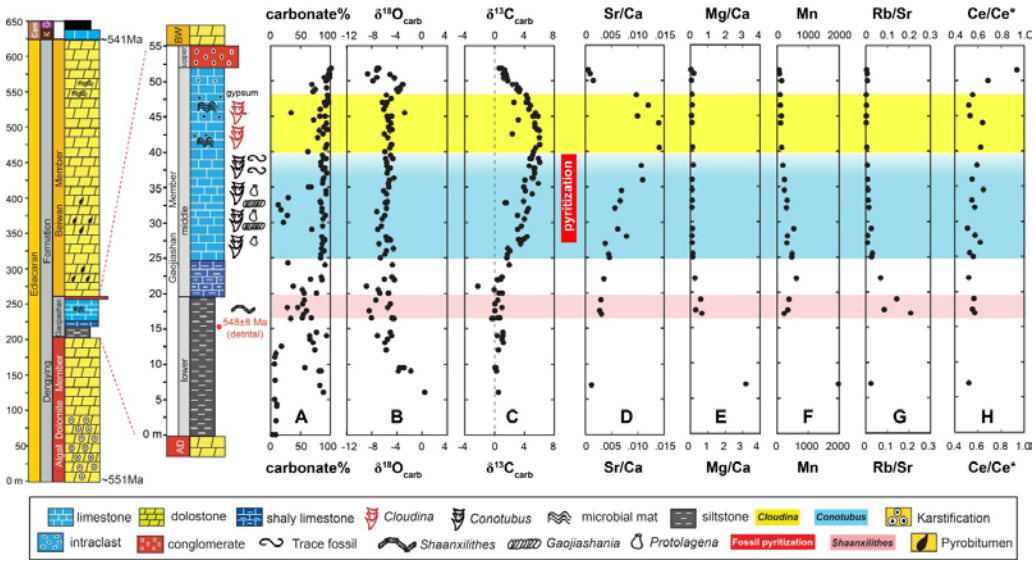

Figure 4.4: Time-series litho-, bio-, and chemo-stratigraphy of the Gaojiashan Member, including fossil occurrences of *Conotubus* and *Cloudina*, as well as geochemical profiles of carbonate content (wt. %), carbonate carbon ($\delta^{13}C_{carb}$, ‰ V-PDB) and oxygen ($\delta^{18}O_{carb}$, ‰ V-PDB) isotopes, Sr/Ca, Mg/Ca, Rb/Sr, [Mn] (ppm), and Ce anomaly (Ce/Ce*) calculated using the formula $Ce/Ce^* = Ce_{PAAS}/([Pr]^2_{PAAS}/[Nd]_{PAAS})$ (Ling et al., 2013). K = Kuanchuanpu, G = Guojiaba, Cam = Cambrian, BW = Beiwan, AD = Algal Dolomite.

4.6 Discussion

4.6.1 Diagenesis

Confidence in our ability to interpret environmental changes associated with the paleontological transitions in the Gaojiashan requires that we evaluate the degree of alteration of the limestone samples. Based on the low [Mn] and Rb/Sr, and the smooth temporal trends in other geochemical indicators defined by high-resolution sampling, the limestones appear to be especially well preserved (**Fig. 4.4**). However, insofar as carbonates are susceptible to isotopic exchange with meteoric or hydrothermal fluids after burial, stable isotope compositions of carbonate phases might reflect diagenetic overprints over depositional signatures. For example, the lithification of marine carbonates associated with the flushing of meteoric fluids

could cause coupled depletions in both ^{13}C and ^{18}O, assuming the alkalinity was sourced from soil respiration (Knauth and Kennedy, 2009). Isotopic coupling in carbonates might also result from burial diagenesis (Derry, 2010; Bristow et al., 2011) assuming hot fluid temperatures and alkalinity formed through anaerobic processes. In either case the carbonates would be predictably recrystallized or contain appreciable amounts of neomorphic calcite. These petrographic features are certainly not observed in the fine-grained Gaojiashan limestones, which reveal a significant positive $\delta^{13}C_{carb}$ excursion at the same time that $\delta^{18}O_{carb}$ values remain steady. A cross plot of the carbon and oxygen isotope abundances in these samples reveals no clear correlation. Insofar as oxygen isotopes would be more likely to be altered during water-rock interactions (Jacobsen and Kaufman, 1999), the $\delta^{13}C_{carb}$ excursion recorded in the Gaojiashan Member is likely to reflect true secular changes in seawater composition.

The degree of carbonate preservation may also be evaluated through the analyses of CAS abundances and sulfur isotope compositions. Published studies have shown that CAS in marine carbonates can be affected by secondary processes related to pyrite oxidation (Marenco et al., 2008), which could occur in the outcrop or in the laboratory, or the addition of secondary atmospheric sulfate (SAS) to carbonates exposed in desert environments (Peng et al., 2014). On the other hand, CAS studies of modern carbonate sediments where there was active pore-water sulfate reduction indicate minimal alteration of bulk carbonate sulfur isotope compositions (Lyons et al., 2004). While Gaojiashan CAS abundances are generally low (ranging from near 0

to 150 ppm), their $\delta^{34}S_{CAS}$ values are invariant at ca. +40‰ throughout the succession (**Fig. 4.5**). We believe that the sulfur isotope invariance, which is consistent with time-series $\delta^{34}S_{sulfate}$ analyses of bedded anhydrites (ca. +40‰) in equivalent terminal Ediacaran strata from Oman (Fike and Grotzinger, 2008), supports the view that the Gaojiashan carbonates are exceptionally well preserved and reflective of global seawater conditions.

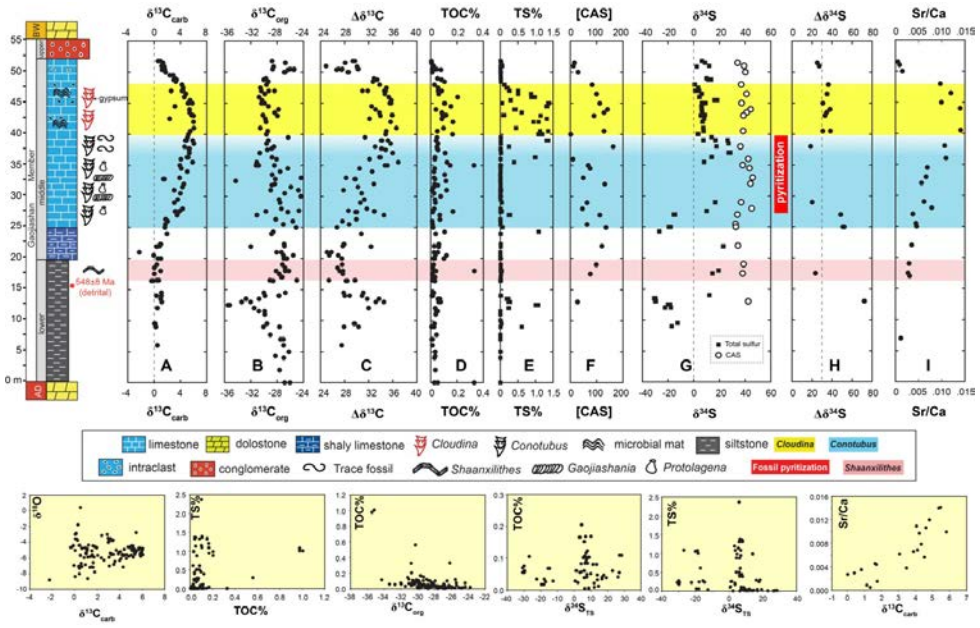

Figure 4.5: Time-series litho-, bio-, and chemo-stratigraphy of the Gaojiashan Member, including fossil occurrences of *Conotubus* and *Cloudina*, as well as geochemical profiles of carbonate carbon ($\delta^{13}C_{carb}$, ‰ V-PDB) and organic carbon ($\delta^{13}C_{org}$, ‰ V-PDB) isotopes, carbon isotope fractionations ($\Delta\delta^{13}C_{carb\text{-}org}$), pyrite sulfur ($\delta^{34}S_{TS}$, ‰ V- CDT) and CAS sulfur ($\delta^{13}C_{CAS}$, ‰ V-CDT) isotopes, sulfur isotope fracionations ($\Delta\delta^{34}S_{CAS\text{-}pyrite}$), total organic carbon content (TOC), total sulfur content (TS), carbonate-associated sulfate concentration ([CAS] in ppm). The small panels in the bottom are cross plots of $\delta^{13}C_{carb}$–$\delta^{18}O_{carb}$, TOC–TS, $\delta^{13}C_{org}$–TOC, $\delta^{34}S_{TS}$–TOC , $\delta^{34}S_{TS}$–TS , $\delta^{13}C_{carb}$–Sr/Ca. BW = Beiwan, AD = Algal Dolomite.

To further evaluate diagenesis in the Gaojiashan Member samples we compared abundances of TOC and pyrite against each other, as well as with their carbon and sulfur isotope compositions, respectively. In neither case do we see a

systematic relationship (**Fig. 4.5**), although the two samples with the highest TOC do have the lowest $\delta^{13}C$ signatures. Low overall TOC might result from either microbial (Borowski et al., 1996; Jørgensen et al., 2004; Ries et al., 2009; Borowski et al., 2013) or thermochemical (Cai et al., 2001; Cai et al., 2003; Cai et al., 2004) sulfate reduction after deposition, which could result in progressive ^{34}S-enrichment of product sulfide preserved as pyrite. However, the sedimentary rocks have not been buried deeply enough to drive the thermal reactions. Furthermore, we find no systematic relationship in TOC-TS or TOC- $\delta^{34}S$ cross plots, suggesting that these secondary processes did not significantly impact the Gaojiashan samples.

4.6.2 Redox constraints for the Gaojiashan Member

Multiple lines of evidence suggest that the paleontological transition in the middle Gaojiashan Member is accompanied by strong ocean stratification (**Fig. 4.6**). Support for this interpretation comes from the negative excursion in the ^{13}C abundance of total organic carbon (TOC) – which mirrors the positive $\delta^{13}C_{carb}$ excursion – resulting in the greatest degree of $\Delta\delta^{13}C$ in the *Cloudina* interval. In light of the abundance of microbial fabrics, these decoupled time-series carbon isotope trends could plausibly have resulted from organic matter derived from benthic microbial mats where anaerobic chemoautotrophs utilized locally recycled ^{13}C-depleted DIC to form biomass with lower $\delta^{13}C_{org}$ values (Hayes, 1993). Alternatively, there may have been an enhanced flux of organic matter derived from anoxygenic photoautotrophs like the green and purple sulfur bacteria that utilize H_2S as a source of electrons during photosynthesis (Johnston et al., 2009). These photoautotrophs typically exist along redox chemoclines and utilize respired CO_2, which is typically

depleted in ^{13}C relative to its atmospheric equivalent (e.g. Brocks et al., 2005). In either case, the spread of anoxic/euxinic conditions across the platform would have promoted organic matter burial (Hayes et al., 1983) and the positive $\delta^{13}C_{carb}$ excursion. High abundances of organic S compounds, indicative of euxinic conditions, are revealed by biomarker studies of the Gaojiashan-equivalent Shibantan Member (Duda et al., 2014) that may have extended onto the continental shelf. Further evidence for the spread of anoxia associated with the decoupled $\delta^{13}C$ excursions is found in the profoundly negative $\delta^{238}U$ signatures of Gaojiashan limestones (Zhang et al., 2015), and our sulfur isotope measurements through the whole of the succession.

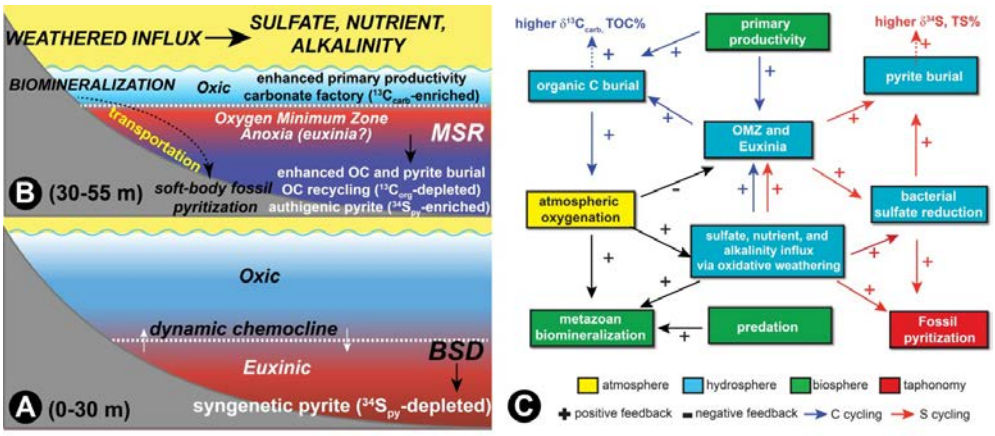

Figure 4.6: Conceptual weathering and biogeochemical model for the Gaojiashan Member. (A) During Stage 1 the basin was stratified with oxic surface water above euxinic deep water. Bacterial S disproportionation (BSD) may be an important contributor to the sulfur cycle. (B) During Stage 2 the basin was strongly influenced by the spread of an oxygen minimum zone (OMZ) beneath oxic surface waters. This likely occurred as a result of sea level regression and enhanced continental weathering, which resulted in a larger sulfate pool in the ocean, elevated ocean alkalinity, and microbial sulfate reduction (MSR) as the dominant pathway for microbioal sulfur cycling. (C) Biogeochemical feedback loops that link the carbon and sulfur cycles to atmospheric oxygenation, animal evolution, and fossil preservation.

Time-series analyses of the Gaojiashan Member reveal a profound rise in $\delta^{34}S_{pyrite}$ values from as low as –30‰ in the lower half of the member to peak values near +30‰ between 35 and 40 m before falling rapidly to values averaging around +10‰ in the *Cloudina*-bearing beds (**Fig. 4.5**). In contrast, the $\delta^{34}S$ of carbonate associated sulfate (CAS) remain steady at values of ca. +40‰ throughout the Gaojiashan Member. The calculated sulfur isotope contrasts ($\Delta\delta^{34}S$) range widely in the lower half of the succession, with maximal values up to 72‰, but in the upper half $\Delta\delta^{34}S$ is relatively constant at ca. 30 – 35‰ (**Fig. 4.5**). Interpreting the environmental significance of these remarkable stratigraphic variations requires the recognition that the $\delta^{34}S_{CAS}$ and $\delta^{34}S_{pyrite}$ signatures are inherited from different parts of the depositional basin. Sulfate incorporation into primary carbonate sediments would occur within the water column (Lyons et al., 2004), whereas pyrite would form either in euxinic bottom waters or within sediments. Considering this spatial separation, local sulfate availability could dictate the $\delta^{34}S$ isotopic difference between CAS and pyrite, particularly if pyrite is formed in non-bioturbated and microbially-sealed sediments where the water-sediment interface represents a significant diffusion barrier. While such a scenario might apply to discrete intervals within the Gaojiashan – including the *Shaanxilithes* and *Conotubus* zones (**Fig. 4.5**) – other parts of the succession have measured $\Delta\delta^{34}S$ differences that are significantly larger. Furthermore, the constancy of the $\delta^{34}S_{CAS}$ values through the Gaojiashan suggests that the perturbation in the terminal Ediacaran sulfur cycle did not involve changes in the marine sulfate isotopic composition. Thus, the ~60‰ shift in $\delta^{34}S$ of pyrite from the lower to the upper Gaojiashan Member may require a change in biologically-induced

fractionations involving both the reductive and oxidative paths of the sulfur cycle (i.e. bacterial S disproportionation, or BSD) (Canfield and Thamdrup, 1994), or microbial sulfate reduction (MSR) in very low sulfate reduction rate (SRR) (Canfield et al., 2010; Leavitt et al., 2013; Wu and Farquhar, 2013; Wing and Halevy, 2014).

In the case of BSD, sulfur is reclyced via both reductive side and oxidative side. On the reductive side, the magnitude of kinetic sulfur isotope fractionation (ε_{SR}) during dissimilatory MSR has been observed to correlate directly with extracellular sulfate concentrations. Experiment from pure cultures indicating maximal fractionation of 66‰ at sulfate concentrations similar to modern seawater at 28 mM (Sim et al., 2011), while ε_{SR} may be suppressed at very low sulfate abundances (<200 μM) (Habicht et al., 2002). On the oxidative side, the sulfide produced through MSR is typically re-oxidized to elemental sulfur, which is subsequently disproportionated to sulfate and sulfide, by coupling with the reduction of O_2, NO_3^-, or iron and manganese compounds (Canfield and Thamdrup, 1994). Disproportionation reactions thus can significantly augment the fractionations induced during MSR, resulting in isotopic contrasts between reactant sulfate and product sulfide of greater than 70‰ (**Fig. 4.5**).

Alternatively, microbial sulfate reduction alone in very low sulfate reduction rate could also lead to large fractionation. Recent studies of euxinic systems indicate that large kinetic fractionations are achievable by both isolated and natural populations of sulfate reducers (Canfield et al., 2010). Furthermore, environmentally

controlled experiments suggest that MSR-related fractionation could be strain specific (Bradley et al., 2015), or be related to sulfate reduction rates that are dependent on the availability of organic substrates as electron donors (Canfield et al., 2010; Leavitt et al., 2013; Leavitt, 2014). In this case the magnitude of fractionation is inversely correlated with the rate of sulfate reduction (e.g., Xiao et al., 2010).

With these constraints in mind, the $\Delta\delta^{34}S$ >70‰ in the lower interval of the Gaojiashan may reflect bacterial S disproportionation (BSD) coupled with MSR as the pathway of S clycing, or result from MSR in very low SRR. The former scenario may reflect oxidized surface ocean conditions with sulfur re-oxidation occurring along a chemocline above euxinic deep waters (**Fig. 4.6A**).

The low TOC abundances in the Gaojiashan samples hamper our ability to further evaluate redox conditions in the depositional basin based on C/S ratios. Based on systematic studies of modern environments and Phanerozoic shales (Berner and Raiswell, 1983; Berner and Raiswell, 1984), very low C/S ratios might indicate euxinic marine conditions. Although the C/S proxy is not well calibrated for carbonates, the preponderance of Gaojiashan limestones with values <1 suggests the possibility of euxinic conditions in the depositional basin, if the low TOC samples may be used in this manner. This view is consistent with the high Ce/Ce* values in the upper Gaojiashan samples (**Fig. 4.4**), although carbonates have notoriously low REE abundances. Thus, these REE abundances should be interpreted with caution.

4.6.3 Global indicators of dynamic redox conditions

Time-series comparison of terminal Ediacaran successions in South China, Oman, and Namibia reveal both similarities and differences that suggest the oxidation state of the basins may have been locally controlled (**Fig. 4.7**). Global seawater conditions appear to be reflected in the similarities between South China and Oman. For example, in the uppermost Buah Formation of Oman, paired CAS-pyrite measurements reveal large magnitude sulfur isotope fractionations (with $\Delta\delta^{34}S$ at about 50‰) stratigraphically prior to the first occurrence of *Cloudina* (Conway Morris et al., 1990), just as we have documented for the lower Gaojiashan Member. The larger fractionation seen in two basins suggests the dominanace of sulfur disproportionation reactions (Fike et al., 2006; Fike and Grotzinger, 2008), which is supported by a recent multiple sulfur isotope study indicating enhanced sulfide re-oxidation in the uppermost Buah (Wu et al., 2015). Disproportionation reactions likely dominated over MSR insofar as the latter would have been discouraged if there was active photoautotrophic sulfide oxidation (**Fig. 4.6A**) (Habicht and Canfield, 2001). Stratigraphically higher in the Ara Formation where *Cloudina* occurs in carbonates interbedded with evaporites, the $\delta^{34}S$ compositions of pyrite and CAS are notably invariant with a smaller magnitude of fractionation (ca. 30‰) (Fike and Grotzinger, 2008), again exactly matching our observations from the upper Gaojiashan. The ^{34}S enrichments in pyrite and the smaller sulfur isotope differences between reduced and oxidized phases are best explained by high rate of MSR, which we view as the dominant sulfur metabolism associated with the spread of anoxic

bottom waters (**Figs. 4.6B-C**). In sum, the correlated observations from South China and Oman indicate a global environmental control on biological sulfur fractionations.

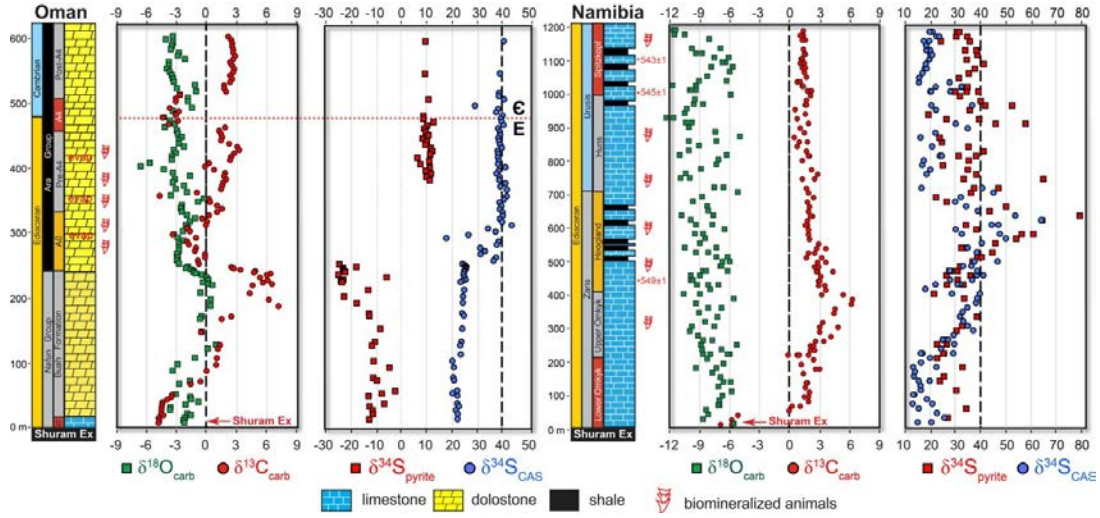

Figure 4.7: Time-series carbon and sulfur isotopic profiles from late Ediacaran strata in Oman (Fike and Grotzinger, 2008) and Namibia (Ries et al., 2009). The remarkable difference in sulfur isotope trends between Oman and Namibia may result from effects of local conditions (e.g. different organic carbon flux, sulfate concentration) on microbial sulfate reduction rate and sulfur isotope fractionations, but may also reflect analytical issues (see text).

To the contrary, time-series data from *Cloudina*-bearing strata of the Nama Group in southern Namibia provide a completely different pattern of ^{34}S enrichments and fractionation. In this case strongly positive $\delta^{34}S_{pyrite}$ values are most-often paired with anomalously low and scattered $\delta^{34}S_{CAS}$ values, resulting in inversely fractionated $\Delta\delta^{34}S$ values (Ries et al., 2009). Stratigraphically coherent CAS results are only seen in the Omkyk Member where there is a positive $\delta^{34}S_{CAS}$ shift from ca. +10 up to +40‰, which is similar to the trend encompassing the transition to the *Cloudina*-bearing beds in Oman and South China (**Fig. 4.7**), and in the uppermost Spitzkop Member below the Ediacaran-Cambrian boundary. In this case, however, the CAS sulfur isotope compositions are depleted in ^{34}S by ~ 30‰ relative to equivalent upper

Ara strata in Oman. Based on our experience with quantitative preparation techniques, it would appear that the Namibian CAS samples were not adequately leached of non-CAS components. In contrast to our extensive efforts to remove the non-carbonate fraction (see Methods), Ries et al. (2009) leached the CAS powders with Milli-Q water only once, and this is unlikely to have removed sulfate on mineral surfaces formed through pyrite oxidation (Marenco et al., 2008) or the addition of secondary atmospheric sulfate (SAS) (Peng et al., 2014). The presence of these contaminants would cause $\delta^{34}S_{CAS}$ values to be more negative and hence would not reflect depositional conditions. In our view the inversely fractionated sulfur isotopes from this succession should be interpreted with caution, although they do highlight the potential redox differences between equivalent terminal Ediacaran basins.

In addition, there are notably time-series carbon isotope contrasts between the three terminal Ediacaran successions in South China, Oman, and Namibia. The time-series Dengying data set suggests the possibility of three separate positive excursion **(Fig. 4.1)**, with the differences between them likely associated with sediment accumulation rates in the three intervals. In contrast, there is significant $\delta^{13}C_{carb}$ variability in the evaporite-rich succession from Oman (Fike and Grotzinger, 2008; Wu et al., 2015), including negative anomalies within the *cloudinid* interval interspersed with at least two positive excursions **(Fig. 4.7)**. In Namibia there is only one post-Shuram positive $\delta^{13}C_{carb}$ excursion followed by a long plateau of moderately positive (ca. +1 to +3‰) values leading up to the Ediacaran-Cambrian boundary **(Fig. 4.7)** (Ries et al., 2009). Other terminal Ediacaran successions, including those in

northern India, also reveal significant differences in carbon isotope stratigraphic profiles (Kaufman et al., 2006). Taken together, the intra-basinal variability in carbon and sulfur isotope compositions likely reflect differences in depositional environments and redox conditions in the various basins. This dynamic view of terminal Ediacaran environmental change clearly set the stage for the Ediacaran experiment in animal life, and may provide constraints regarding alkalinity and biomineralization in the oceans at this time.

4.6.4 Enhanced alkalinity in the terminal Ediacaran ocean

The generally low TOC contents of the Gaojiashan limestones could reflect either depositional or diagenetic processes. Pervasive water column or sediment recycling of organic matter and anaerobic conversion to alkalinity could have resulted in the formation of ubiquitous authigenic carbonates (Higgins et al., 2009; Schrag et al., 2013) and hence decrease the TOC flux to sediments. Formed through iron or sulfate reduction of available organic substrates, the addition of authigenic carbonate to the sediments would however have resulted in a negative (rather than a positive) carbon isotope excursion. Alternatively, the generally low TOC may reflect significant dilution with abundant carbonate formed from highly alkaline oceans. In this case the source of the alkalinity was likely to be silicate weathering, as indicated by the significant rise in $^{87}Sr/^{86}Sr$ in the terminal Ediacaran Period (Kaufman et al., 1993; Kaufman et al., 1997; Halverson et al., 2007). Elevated alkalinity at this time is consistent with the presence of aragonite crystal fans preserved in the time-equivalent Nama Group (Grotzinger, 2000; Grotzinger et al., 2005) (Hall et al., 2013) in

Namibia, which records a singular Ediacaran positive $\delta^{13}C_{carb}$ excursion (Kaufman et al., 1991; Saylor et al., 1998). Overall high alkalinity is consistent with the dominance of carbonate in terminal Ediacaran successions worldwide, and may explain the extremely high accumulation rate estimated for the Dengying (i.e. >650 m for 10 million years), as compared with the underlying Doushatuo (i.e. <200 m for 84 million years) (**Fig. 4.1**).

Enhanced terminal Ediacaran alkalinity may also be interpreted from our time-series elemental results from the Gaojiashan, as well as inter- and intra-basinal equivalents. In particular the [Sr] and Sr/Ca data measured from the Gaojiashan limestones reveal positive excursions in step with the positive $\delta^{13}C_{carb}$ anomaly (**Fig. 4.8**). A similar [Sr] excursion coincident with peak $\delta^{13}C$ compositions of carbonates is noted in the Gaojiashan-equivalent Shibantan Member in the Yangtze Gorges area (Sawaki et al., 2010). A rise in [Sr] is also noted in the broadly equivalent Nama Group in southern Namibia (Ries et al., 2009) although this geochemical anomaly post-dates the first appearance of *Cloudina* and the singular positive $\delta^{13}C$ excursion in the thick sedimentary succession. The apparent [Sr] rise in Namibia is potentially complicated by the admixture of siliciclastics within the carbonates by using aqua regia acid, which would attack both carbonate and siliclastic components in their dissolution procedure. Nonetheless, all sections show positive [Sr] excursion in *Cloudina*-bearing intervals. Based on the invariance of time-series Mg/Ca in the Gaojiashan section (**Fig. 4.4**), influence of dolomitization on time-series Sr/Ca variations could be precluded. Given that the dominant source of Sr in the ocean is

from the chemical weathering of the continental crust (Shields, 2007; McArthur et al., 2012), enhanced [Sr] and Sr/Ca values supports the view that enhanced weathering and the delivery of alkalinity from silicate weathering buffered the shallow oceans in the terminal Ediacaran Period.

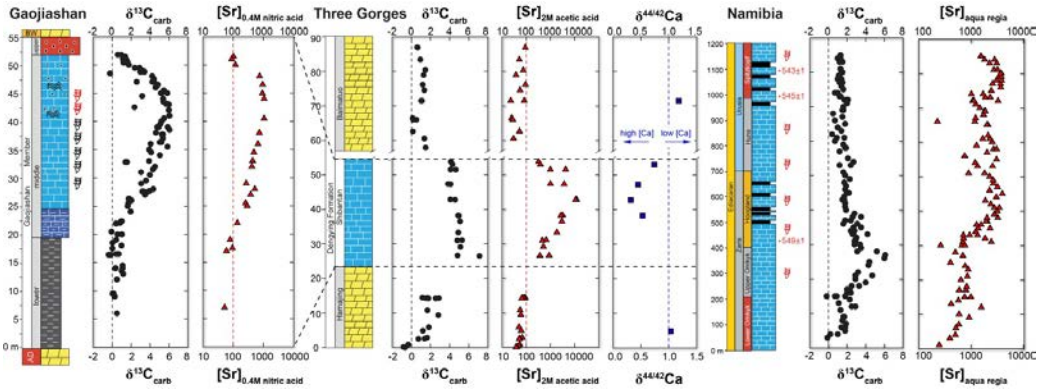

Figure 4.8: Time-series litho-, bio-, and chemo-stratigraphy of the terminal Ediacaran Gaojiashan Member in the study area, Three Gorges area, and Namabia, including geochenical profiles of carbonate carbon isotopes ($\delta^{13}C_{carb}$, ‰ V-PDB), strontium concentration ([Sr] in ppm, plotted in log scale), and $\delta^{44/42}Ca$ (‰). Data for the section in Three Gorges area are from Sawaki et al. (2010) and Sawaki et al. (2014). Data for the section in Namibia are from Ries et al. (2009). Note that the Sr concentrations are measured by using different concentration of acid in different groups. The negative $\delta^{44}Ca$ excursion in the Gaojiashan-equivalent Shibantan Member has been interpreted to reflect high Ca concentration in terminal Ediacaran seawater (Sawaki et al., 2014).

Emerging support for the alkalinity hypothesis comes from time-series Ca isotope ($\delta^{44}Ca$) measurements of the Shibantan Member. In this case, a sharp negative excursion in $\delta^{44}Ca$ (down to 0.3‰) is interpreted to reflect anomalously high Ca concentration in the ocean, in contrast with the underlying Doushantuo Formation, which has generally high $\delta^{44}Ca$ (ca. 1.0‰) values (Sawaki et al., 2014). In concert, these sedimentological and geochemical observations of *Cloudina*-bearing strata in South China and elsewhere suggest that the terminal Ediacaran ocean was highly

alkaline. If true, high concentrations of Ca and alkalinity likely facilitated the calcareous biomineralization of Earth's earliest animals.

4.6.5 Environmental context of pyritization and biomineralization

Based on our time-series geochemical observations from the Gaojiashan Member, the first appearance of *Cloudina* coincided with the development of anoxic and episodically euxinic conditions across the shelf environment. It is likely, however, that this first biomineralized metazoan lived in the oxidized shallower water column and was swept into deeper anoxic settings by storm events (Cai et al., 2010) (**Fig. 4.5B**). In contrast, our geochemical results suggest that *Conotubus* and other soft-bodied Ediacara biotas thrived at a time of more generally oxidizing conditions within the water column prior to the peak of the $\delta^{13}C$ excursion. In the equivalent Shibantan Member in the Yangtze Gorges region, the soft-bodied Lagerstätte are preserved in subtidal environments and are closely associated with abundant bilaterian burrows, suggesting moderate levels of bioturbation (Chen et al., 2013; Chen et al., 2014b; Meyer et al., 2014). It is notable that *Conotubus* and many Ediacara remains, as well as the microbial surfaces, were preserved in these environments through pyritization (Gehling, 1999; Schiffbauer et al., 2014). In the "death mask" model, pyritization of a decomposing metazoan would stabilize its surface and allow the external form of the organism to be imprinted with exquisite detail; in the case of the Gaojiashan Member, similar pyritization process may have also molded *Conotubus* tubes from inside. Based on *in-situ* SIMS $\delta^{34}S$ analyses, it has been proposed that pyritization of *Conotubus* was fueled by the degradation of labile

organic tissues through MSR (Schiffbauer et al., 2014) near the sediment-water interface. Consistent with pyritization as a widespread fossilization pathways, many soft-bodied fossils and associated microbial surfaces in the Gaojiashan and Shibantan exposures are coated with iron oxides and jarosite (an iron-bearing sulfate mineral) that are the oxidative weathering products of early diagenetic pyrite (Hall et al., 2013).

The balance between the ecological pressures and physiological responses that resulted in the biomineralization of *Cloudina* are nicely viewed from the Gaojiashan Member and its equivalents in South China. On the one hand, Hua et al. (2003) highlighted the large number of drill holes on *Cloudina* shells in the Dengying Formation and hypothesized that predation tipped the balance towards calcification as a means of protection. On the other, our time-series results emphasize clear changes in seawater chemistry that are associated with this evolutionary milestone. We interpret the geochemical trends to reflect enhanced terminal Ediacaran chemical weathering that introduced nutrients, which drove primary productivity, the spread of anoxia, and higher rates of organic carbon burial. Silicate weathering would also have delivered alkalinity (bases required to neutralize aqueous solutions) and cations including calcium to seawater, promoting rapid carbonate accumulation in shallow marine settings. In addition, sulfate delivery would have further stimulated MSR, which would provide an additional source of seawater alkalinity depending on the extent of water column anoxia. Biomineralization could then have been a means to remove excess calcium from the newly-developed circulatory systems of evolving

metazoans (Simkiss, 1977) in the context of higher overall seawater alkalinity in the terminal Ediacaran Period (Grotzinger et al., 2005)

Consistent with our hypothesis that there may be a close linkage between changes in ocean chemistry and the earliest example of calcareous biomineralization by animals, studies on the Phanerozoic record further demontrate the critical vital effect on biomineral formation by seawater chemistry. It has been proposed that secular oscillations in the composition of seawater may have been largely driven by fluctuations in the rate of ocean crust production (Hardie, 1996; Hardie, 2003), which may have profound influence on the evolution of skeletal animals. Although the secretion of biominerals may occur in an environment isolated from seawater (Weiner and Dove, 2003), seawater chemistry could indirectly determine skeletal mineralogy by affecting the physiological costs of biomineralization (Knoll, 2003), resulting in distinct patterns of skeleton evolution through Earth history. Indeed, extensive compilation of non-skeletal carbonates and biomineralized animal fossils reveals that the Mg/Ca ratio and Ca concentration of seawater in aragonite or calcite seas have strong correlation with the secular changes of skeletal mineralogy during the Phenerozoic (Stanley and Hardie, 1998; Stanley, 2006; Porter, 2010). High-Mg calcite and aragonite skeletals dominated in the aragonite sea while low-Mg calcite skeletals dominated in the calcite sea during the Phanerozoic. Such a pattern has further shown to be true for the Cambrian Period, when the first massive biodiversification of skeletal animals occured (Porter, 2007). It has been suggested by Porter (2010) that calcite and aragonite seas do have a strong influence on carbonate

skeletal mineralogy, and this appears to be true particularly at the time mineralized skeletons first evolve. In the case of the terminal Ediacaran ocean when the first animal biomineralization evolved, the widespread appearance of seafloor aragonite fans (Grotzinger, 2000; Grotzinger et al., 2005; Hall et al., 2013) supports an aragonite sea (rather than a calcite sea). The high-Mg calcite in mineralogy of *Cloudina* (Grant, 1990; Zhuravlev et al., 2012) is consistent with this scenario, indicating a potential causal link between ocean chemistry and biomineral formation.

4.6.6 Temporal growth in the oceanic sulfate reservoir

Projected to the world stage and viewed through the long lens of Earth history, paired sulfur isotope data in the terminal Ediacaran Gaojiashan Member stand out among the highest $\delta^{34}S_{sulfate}$ values (up to +40‰) and largest S isotope fractionations (ca. +70‰) for the whole Precambrian (**Fig. 4.9**). Such a pattern may reflect a strongly stratified ocean, which would be particularly meaningful during the terminal Ediacaran when a putative atmospheric and oceanic oxygenation event occurred (i.e. Neoproterozoic Oxygenation Event, or NOE) (Derry et al., 1992; Kaufman et al., 1993; Kaufman et al., 2007; Frei et al., 2009; Shields-Zhou and Och, 2011; Och and Shields-Zhou, 2012; Lyons et al., 2014). The lack of appreciable isotope fractionation between oxidized and reduced sulfur reservoirs in the Archean has been argued to reflect sulfate concentration ($[SO_4^{2-}]$) levels of < 200 μM in these oceans (Habicht et al., 2002), and a more recent model constrains suggests Neoarchean $[SO_4^{2-}]$ between ~1 and 10 μM (Zhelezinskaia et al., 2014). During the early Paleoproterozoic Great Oxidation Event (GOE) sulfate levels are very likely to have risen, and at around 2.1

Ga may have been as high as 2.5 mM based on the presence of evaporites in carbonate-rich successions [e.g. Kona Dolomite in Bekker et al. (2006) and Tulomozero Formation in Reuschel et al. (2012)]. An early Mesoproterozoic estimate based on a sulfur isotope model indicates that [SO_4^{2-}] may have fallen again to concentrations between <0.1 to 0.35 mM (Luo et al., 2015) potentially related to widespread euxinia (Canfield, 1998). Based on a rate-dependent model for sulphur isotope changes in the gypsum-bearing Mesoproterozoic carbonate succession of arctic Canada, Kah et al. (2004) suggest that oceanic [SO_4^{2-}] rose again to concentrations between 1.5 and 4.5 mM, but are still low (up to only 15% of modern levels) by 1.2 Ga.

In contrast, multiple lines of evidence suggest a sharp increase in seawater sulfate concentrations following the Cryogenian ice ages and associated with the terminal Ediacaran NOE. Coinciding with a profound negative carbon isotope anomaly down to –12‰ (i.e. the Shuram Excursion) (Grotzinger et al., 2011), time-series sulfur isotopes profiles worldwide reveal a parallel decrease in both $\delta^{34}S_{pyrite}$ and $\delta^{34}S_{CAS}$ (Cui et al., 2015) that may reflect the growth of the Ediacaran sulfate pool (Fike et al., 2006; Halverson and Hurtgen, 2007; Kaufman et al., 2007; McFadden et al., 2008). Consistent with this view, psuedomorphs of gypsum are found in the Shuram intervals of the Wonoka (Calver, 2000) and Doushantuo formations (Lu et al., 2013). Above the Shuram, an increasing number of bedded evaporite horizons have been discovered in terminal Ediacaran successions, including the Dengying (Siegmund and Erdtmann, 1994; Duda et al., 2015; and this study) and

Ara formations (Fike and Grotzinger, 2010), as well as the Hanseran Evaporite Group in northwestern India (Strauss et al., 2001; Mazumdar and Strauss, 2006). A recent quantative model analysis based on time-series sulfur isotope records through the Ediacaran suggests that oceanic [SO_4^{2-}] was low (<5 mM) in the aftermath of the Marinoan ice age (ca. 635 Ma), but then rose sharply (to ~5–10 mM) across the Ediacaran-Cambrian boundary (Algeo et al., 2015).

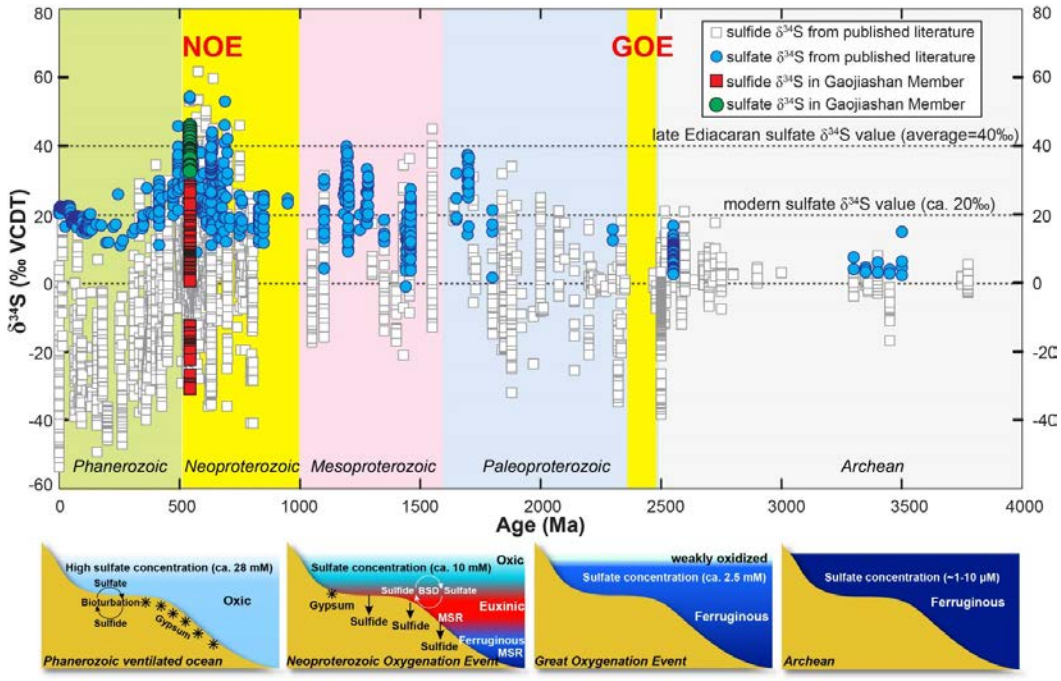

Figure 4.9: Evaporite, CAS, and pyrite sulfur isotope data through Earth history. Paired $\delta^{34}S$ data are compiled from the literature [after (Canfield and Farquhar, 2009; Och and Shields-Zhou, 2012; Sahoo et al., 2012)]. Recently published Neoarchean $\delta^{34}S$ data have also been included (e.g. Paris et al., 2014; Zhelezinskaia et al., 2014). The sulfate concentration constraints are ca. 1-10 μM during Archean (Habicht et al., 2002; Zhelezinskaia et al., 2014), ca. 2.5 mM after the GOE (Shen et al., 2002; Canfield, 2004; Kah et al., 2004; Hurtgen et al., 2005; Bekker et al., 2006; Canfield and Farquhar, 2009; Reuschel et al., 2012), and ca. 10 mM during NOE (Canfield and Farquhar, 2009; Algeo et al., 2015). $\delta^{34}S_{sulfate}$ compostion of the terminal Ediacaran ocean (ca. +40‰) was determined by measurements of bedded evaporites in Oman (Fike and Grotzinger, 2008). GOE = Great Oxidation Event; NOE = Neoproterozoic Oxidation Event. The four conceptual biogeochemical models for redox architectures of the ocean during Archean, GOE, NOE and Phanerozoic are shown in the panels beneath the time-series data. See the main text for detailed discussions.

The trigger for the terminal Ediacaran rise in seawater sulfate remains a question of considerable debate. It has been proposed by Canfield and Farquhar (2009) that the emergence of bioturbation near the Ediacaran-Cambrian boundary was the proximate cause insofar as sediment mixing would result in enhanced sulfide oxidation and recycling. While bioturbation clearly modified ecosystems in the Fortunian Stage of the Cambrian Period (Bottjer et al., 2000; Meysman et al., 2006), there is little support for vertical penetration by animals through sedimentary layers dominated by microbial mats in the Shuram or terminal Ediacaran intervals (e.g. Carbone and Narbonne, 2014; Meyer et al., 2014). Alternatively, it seems very likely that the rise in Ediacaran sulfate concentration is through enhanced oxidative weathering of exposed pyrite in continental rocks and oceanic sedimentary rocks exposed by sealevel regression. (Kaufman et al., 2007). This scenario is particular meaningful given the profound increase in seawater $^{87}Sr/^{86}Sr$ (from ca. 0.7080 to 0.7090) recorded globally in carbonates deposited during the Shuram Excursion (Burns et al., 1994; Calver, 2000; Melezhik et al., 2009; Sawaki et al., 2010; Cui et al., 2015). The Sr isotope shift most-likely accompanied enhanced silicate weathering (Kaufman et al., 1993; Halverson et al., 2007; Cui et al., 2015), which lead to an increase in the delivery of nutrient and sulfate to the oceans. By stimulating photosynthesis, these continental fluxes would on the one hand result in the oxidation of surface environments, while on the other, the remineralization of organic matter along marginal marine settings would simultaneously result in the expansion of oxygen minimum zones (OMZs). Oceanic redox stratification would have simultaneously stimulated the oxidative side of the sulfur cycle through widespread

sulfur disproportionation along chemoclines (Canfield and Thamdrup, 1994; Fike et al., 2006; Wu et al., 2015) and the reductive side through microbial sulfate reduction within the anoxic plumes. Both microbial processes would have delivered ^{32}S sulfur as pyrite into the sediments and thereby drive oceanic sulfate compositions to positive $\delta^{34}S$ extremes (Canfield, 2004).

4.7 Conclusions

Terminal Ediacaran strata of the Gaojiashan Member preserve a dynamic record of carbon and sulfur cycling between the atmosphere, hydrosphere, lithosphere and biosphere. Both the carbon and sulfur isotope anomalies were likely linked to atmospheric oxygenation that, coupled with tectonic events, triggered an enhanced flux of sediments, sulfate and nutrients into the ocean. We speculate that this resulted in an episode of oceanic anoxia that promoted enhanced organic C and pyrite burial thereby driving the isotope anomalies. As a positive feedback, enhanced burial of reduced carbon and sulfur would have led to further atmospheric oxygenation. As a negative feedback, surface oxygenation would also ameliorate the expansion of an oxygen minimum zone by O_2 diffusion from the atmosphere. The delicate balance between the two is expressed as oscillations in the carbon and sulfur isotope abundances of seawater proxies (Kaufman et al., 1993; Halverson et al., 2010) and the buildup of terminal Ediacaran seawater alkalinity [*cf.* Rothman et al. (2003) and McFadden et al. (2008) for a DOC-dominated early Ediacaran viewpoint]. *Cloudina* evolved in this dynamic environmental context, and through ecological experiments driven by chemical fluctuations with the depositional basin, as well as predation

pressures, developed the ability to biomineralize calcareous skeletons for the first time in Earth history.

Chapter 5: Conclusions and future directions

5.1 Conclusions

Studies in this dissertation combine Ediacaran lithostratigraphy, chemostratigraphy and – in the case of the Gaojiashan Member – biostratigraphy, in order to reconstruct the biogeochemical C and S cycling of the Ediacaran Earth-life system. Given the intimate link between C and S cycles in the ocean (Berner and Raiswell, 1983; Berner, 1989), paired C ($\delta^{13}C_{carb}$ and $\delta^{13}C_{org}$) and paired S ($\delta^{34}S_{pyrite}$ and $\delta^{34}S_{sulfate}$) isotopes have been used as the key tools for such study (e.g. Fike et al., 2006; Fike and Grotzinger, 2008; McFadden et al., 2008; Li et al., 2010). Thus, most of our conclusions rest on the interpretation of time-series $\delta^{13}C$–$\delta^{34}S$ isotopes.

Our chemostratigraphy study in sections at different depths (Chapter 2, ***Fig. 5.1)*** provides a revised stratigraphic correlation for the Doushantuo Formation across the ocean margin. Previous work (Li et al., 2010) on redox structure of the Ediacaran ocean assumes a complete correlation between Doushantuo Formation in shallow (Jiulongwan) and deep (Zhongling) sections, however, our results suggest that this is likely to be a mis-correlation. Based on integrated time-series $\delta^{13}C$–$\delta^{34}S$–$^{87}Sr/^{86}Sr$ data, it turns out that the Doushantuo Formations in the inner shelf (Xiaofenghe) section and outer shelf (Yangjiaping/Zhongling) section are incomplete, either due to stratigraphic truncation, or a diachronous nature of the Doushantuo–Dengying boundary. Our study emphasizes the importance of stratigraphic correlation when

reconstructing redox models for ancient ocean maragins. Any robust model should be based on solid stratigraphic correlations.

The study of the Doushantuo Formation in the Zhongling section (Chapter 3) is focused on sedimentology and *in-situ* geochemical analyses of authigenic carbonates. Previous work on the Precambrian chemostratigraphy is mainly based on bulk-rock isotope analysis (e.g. Li et al., 2010), which obscured the critical signatures of micrite-sized authigenic carbonates. Our results, for the first time, reveal a strong correlation between proportion of authigenic carbonates and bulk carbonate $\delta^{13}C$, $\delta^{18}O$ compositions, suggesting important contributions from authigenesis in $\delta^{13}C$ and $\delta^{18}O$ variations. Projected to the world stage, it is suggested that authigenesis in the Ediacaran ocean during the Shuram Excursion was triggered by an increased seawater sulfate concentration, which is also consistent with a hypothesized rise in atmospheric oxygen in the Neoproterozoic Era (Derry et al., 1992; Kaufman et al., 1993; Frei et al., 2009; Shields-Zhou and Och, 2011; Och and Shields-Zhou, 2012). Our work highlights the importance of authigenic carbonates in the Precambrian C cycle, and suggests that any future interpretation on $\delta^{13}C$ variations should be accompanied with detailed petrographic investigation (*e.g.,* BSE imiging) to evaluate the effect of authigenesis in bulk geochemical signatures.

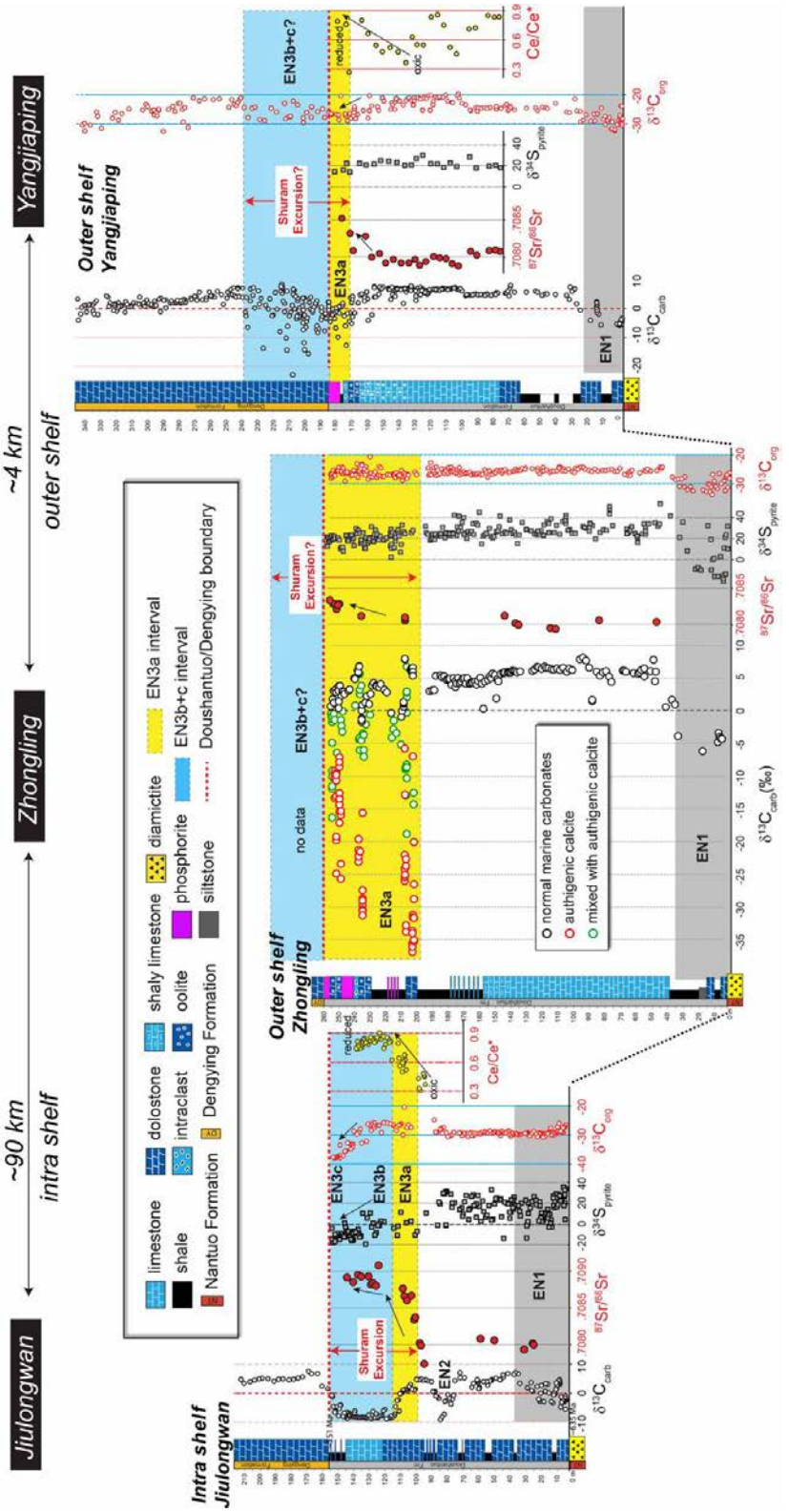

Figure 5.1: Chemostratigraphic correlation of Doushantuo Formation of sections at different depths.

A distinct feature of the late Ediacaran Gaojiashan Member of the Dengying Formtion (Chapter 4) is its coupled C and S anomaly, exceptional preservation of the earliest biomineralized animal *Cloudina* (Cai et al., 2013) and the taphonomic pyritization of fossil *Conotubus* (Cai et al., 2011; Schiffbauer et al., 2014). Paired C and S isotopes were analyzed in high stratigraphic resolution (**Fig. 5.2**). Based on the data, it is revealed that the Ediacaran ocean experienced dynamic and coupled C and S perturbations during the onset of animal biomineralization. Time-series carbonate $\delta^{13}C$ data reveal a positive excursion to +6‰, and pyrite $\delta^{34}S$ data show an increase from ca. –35‰ to +10‰, whereas carbonate-associated sulfate $\delta^{34}S$ data remain steady around +40‰ through the whole section. Strong decoupling of paired S isotopes suggest a large sulfate pool in the ocean with buffering effect of the sulfate. A decline in S isotope fractionation from ca. +70‰ to +35‰ is interpreted as a transition in sulfur cycling from a more oxidized redox condition with bacterial sulfur disproportionation to a more reducing redox condition with dominant microbial sulfate reduction. Integrating all the isotope and trace elemental changes (**Fig. 5.2**), it is proposed that an enhanced weathering flux may be coupled with the onset of animal biomineralization. High concentration of calcium, alkalinity and nutrients may facilitate this evolutionary innovation. However, we still lack a direct proxy for calcium or alkalinity of the Ediacaran seawater; further analysis of calcium isotopes in the Gaojiashan section may be helpful to better constrain the causal link between calcium concentration and calcareous biomineralization of animals.

5.2 Future directions: Implications for subdivision of the Ediacaran Period

Since the ratification of the Ediacaran Period in 2004 by IUGS (Knoll et al., 2006), intensive studies have been focused on providing additional radiometric constraints for this interval and constructing time-series stratigraphic schemes of biological and geochemical change. (e.g. Condon et al., 2005; Fike et al., 2006; Bowring, 2007; McFadden et al., 2008; Macdonald et al., 2013). With increasing time-series data, a more detailed subdivision for this period appears should be attainable, but correlation problems persist especially related to the position of the Gaskiers glaciation (Narbonne et al., 2012). When subdividing the Ediacaran Period, microfossil assemblage (Liu et al., 2014; Xiao et al., 2014b), negative C isotope anomalies (including the EN2 in South China and the Shuram Excursion) (Fike et al., 2006; McFadden et al., 2008), the Gaskier Glaciation (Bowring et al., 2003), and the first apparence of *Cloudina* (Amthor et al., 2003) have been used as critical markers that define potential stage boundaries (Narbonne et al., 2012).

My studies suggest that chemostratigraphy in a basin scale (Chapter 2 and 3), or global scale (Chapter 4) reveals both similarities and differences. Both global and local factors control C and S cycling and the consequent chemostratigraphic expression in local rock records. Thus, extrapolating local time-series profiles to a global scale during the Ediacaran subdivision should be done with caution. In particular, in the two proposed schemes on Ediacaran subdivision by Narbonne et al. (2012), it appears that the EN2 excursion in the middle Doushantuo Formation and its relationship with the Gaskiers glaciation plays an important role. Given the complicated origin of C isotope negative excursions in the Ediacaran Period (Schrag

et al., 2013), further detailed petrographic investigation is needed to identify potential authigenic signals. Without better understanding of the biogeochemical driver of these C isotope anomalies, it is still too early to use EN2 as tools for the Ediacaran subdivision on a global scale. In this light, it is believed that, for a further Ediacaran subdivision, chemostratigraphy should be combined with detailed petrographic observation, biostratigraphy and age constraints.

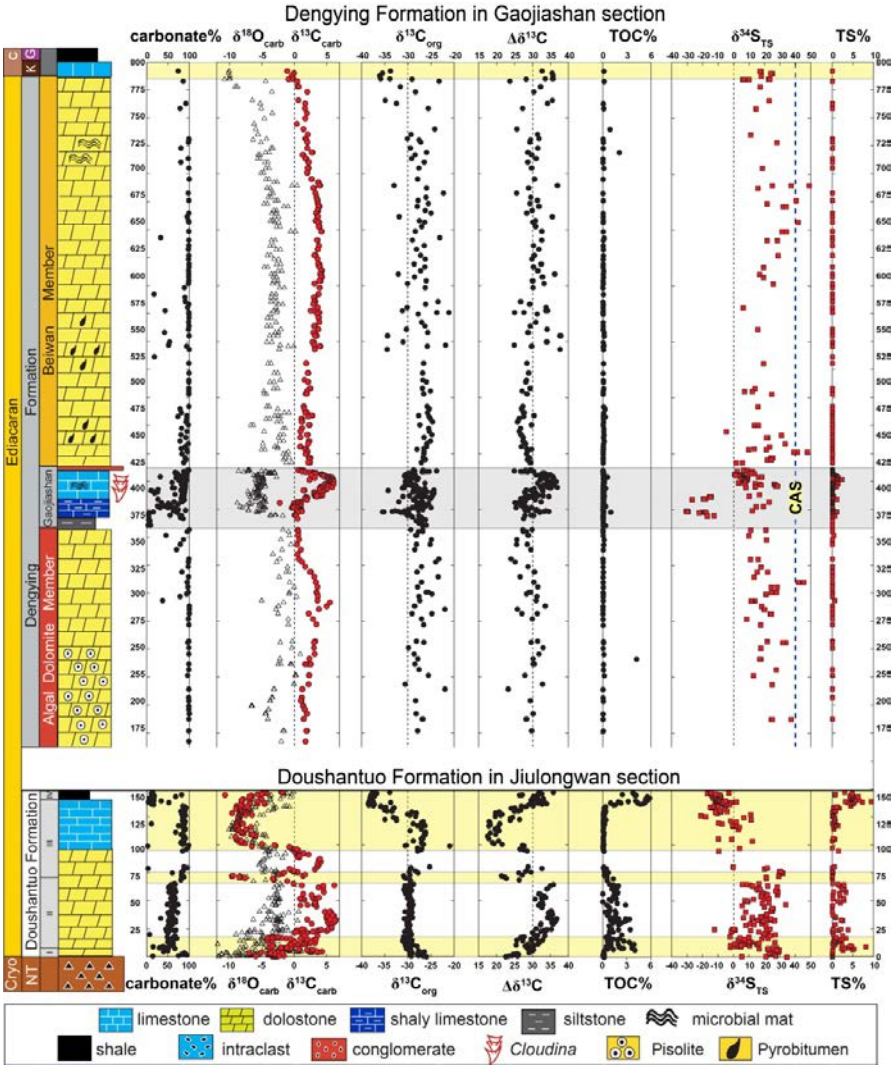

Figure 5.2: Time-series C and S isotope data of the Ediacaran Doushantuo Formtion in jiulongwan section (McFadden et al., 2008) and the Dengying Formation in Gaojiashan section (this study).

Appendix A

Table A.1: Time-series geochemical data of the upper 105 meters of Doushantuo Formation at Yangjiaping section.

Doushantuo	Height	lithology	Carbonate%	$\delta^{13}C_{carb}$	$\delta^{18}O_{carb}$	$\delta^{13}C_{org}$	$\Delta^{13}C$	$\delta^{34}S_{py}$	TS%	$^{87}Sr/^{86}Sr$	Sr	Mn/Sr	Fe/Sr	Rb/Sr	Ce/(Pr^2/Nd)
	m		wt.%	‰,VPDB	‰,VPDB	‰,VPDB	‰,VPDB	‰,VCDT	wt.%		ppm				
Yd1	1	limestone	68.1	5.2	–6.0	–25.3	30.4	16.6	0.15	0.70810	681	0.13	7.65	0.0074	0.8
Yd2	4	limestone	69.3	4.8	–5.8	–25.5	30.3	19.2	0.45	0.70812	520	0.15	10.92	0.0154	0.8
Yd3	8	dolostone	62.3	4.8	–6.0	–25.0	29.8	18.3	0.86	0.70811	491	0.18	17.17	0.0138	0.9
Yd5	16	dolostone	70.1	4.8	–6.3	–26.3	31.1	16.5	0.23	0.70805	394	0.12	7.22	0.0063	0.7
Yd6	20	limestone	81	4.7	–6.7	–26.1	30.7	27.1	0.06	0.70810	385	0.16	6.58	0.011	0.7
Yd8	28	phosphatic limestone	97.2	7.1	–7.6	–20.5	27.6	17.9	0.03	0.70790	286	0.03	1.12	0.0009	0.5
Yd9	32	limestone	97.6	6.7	–7.6	–23.3	29.9	21.4	0.05	0.70793	1353	0.01	0.34	0.0002	0.5
Yd10	36	limestone	94.4	6.8	–6.6	–20.9	27.8	17.2	1.05	0.70800	775	0.04	3.15	0.0028	0.8
Yd11	40	dolostone	76.6	6.2	–5.6	–21.7	27.9	20.4	1.11	0.70801	558	0.13	9.11	0.0072	0.9
Yd12	44	dolostone	96.7	6	–5.1	–24.1	30	20.5	0.05	0.70803	899	0.11	4.97	0.0038	0.8
Yd13	49	limestone	95.2	6.5	–7.0	–21.3	27.8	28.9	0.05	0.70796	697	0.03	0.74	0.0003	0.6
Yd14	53	limestone	96.2	6.2	–7.3	–21.9	28.1	25.6	0.04	0.70791	689	0.02	0.89	0.0002	0.6
Yd15	56	oolitic limestone	97.6	6.4	–6.7	–21.8	28.2	19.5	0.11	0.70799	1119	0.03	0.81	0.0012	0.6
Yd16	60	oolitic limestone	97.3	6.9	–6.9	–22.1	29	19.2	0.01	0.70794	1483	0.01	0.09	0.0002	0.4
Yd17	65	oolitic limestone	98.7	6.9	–7.4	–22.9	29.7	21.8	0.05	0.70794	612	0.01	0.22	0.0006	0.5
Yd18	70	oolitic limestone	98.4	6.9	–7.7	–23.4	30.3	23.1	0.03	0.70799	578	0.03	0.3	0.0007	0.5
Yd19	75	oolitic limestone	98.9	6.7	–7.7	–22.9	29.6	23.6	0.05	0.70794	850	0.02	0.22	0.0008	0.5
Yd20	79	oolitic limestone	97.5	3.8	–8.0	–24.8	28.6	20.3	0.02	0.70807	559	0.05	0.4	0.0006	0.5
Yd21	84	oolitic limestone	73.9	3.4	–8.3	–21.1	24.5	19.6	1.08	0.70802	831	0.03	0.33	0.0003	0.7
Yd22	88	oolitic limestone	91.3	4.6	–6.4	–26.0	30.6	20.9	0.5	0.70831	586	0.15	5.53	0.0024	0.8
Yd24	96	oolitic limestone	98.7	–1.8	–6.8	–28.7	26.9	21	0.01	0.70811	964	0.04	0.18	0.0002	0.3
Yd25	98	limestone	84.3	–2.7	–5.1	–29.5	26.8	14.5	0.14	0.70835	893	0.05	0.69	0.0003	0.8
Yd26	103.4	phosphorite	59	–6.8	–6.3	–29.2	22.3	13	0.32	0.70856	1662	0.02	0.9	0.0016	0.8

Table A.2: Time series geochemical data of the Doushantuo Formation in Zhongling section.

Zhongling	Height	Carbonate%	TOC%	$\delta^{13}C_{org}$	$\delta^{34}S_{pyrite}$	Pyrite%	$^{87}Sr/^{86}Sr$	Formation
	m	wt.%	wt.%	‰,VPDB	‰,VCDT	wt.%		
12ZL+0.2	259.2	94.5	0.01	-26.5	22.0	0.0		Dengying Fm
12ZL+0.1	259.1	94.8	0.00	-26.8	15.5	0.1		Dengying Fm
12ZL-0.2	258.8	92.8	0.00	-27.9	12.9	0.5		Doushantuo Fm
12ZL-0.5	258.5	88.8	0.01	-26.6	21.7	0.4		Doushantuo Fm
12ZL-0.9	258.1	88.3	0.05	-27.5	20.3	0.4		Doushantuo Fm
14ZL-1.3	257.7						0.70832	Doushantuo Fm
12ZL-1.4	257.6	85.1	0.01	-25.1	17.5	0.2		Doushantuo Fm
12ZL-2.0	257	93.3	0.00	-27.1	18.8	0.4		Doushantuo Fm
12ZL-2.5	256.5	74.8	0.00	-27.1	21.8	1.9		Doushantuo Fm
12ZL-2.5	256.5	74.8	0.00	-27.1	21.3	1.8		Doushantuo Fm
12ZL-2.7	256.3	72.1	0.00		23.3	0.4		Doushantuo Fm
12ZL-2.7	256.3	72.1	0.00		21.2	0.1		Doushantuo Fm
12ZL-3.4	255.6	90.2	0.01	-25.5	19.3	0.1		Doushantuo Fm
14ZL-3.5	255.5						0.70828	Doushantuo Fm
12ZL-4.0	255	94.2	0.05	-25.4	19.8	0.1		Doushantuo Fm
12ZL-4.5	254.5	94.6	0.02	-25.3	22.6	0.2	0.70827	Doushantuo Fm
12ZL-5	254	87.4	0.04	-24.2	20.6	0.1		Doushantuo Fm
14ZL-5.6	253.4						0.70820	Doushantuo Fm
14ZL-6.5	252.5						0.70826	Doushantuo Fm
14ZL-6.6	252.4						0.70827	Doushantuo Fm
12ZL-6.7	252.3	86.9	0.03	-25.6	20.5	0.1		Doushantuo Fm
12ZL-7	252	80.6	0.04	-24.0	20.9	0.4		Doushantuo Fm
12ZL-7.5	251.5						0.70827	Doushantuo Fm
12ZL-7.8	251.2	84.8	0.11	-24.4	18.8	0.1		Doushantuo Fm
12ZL-8.5	250.5	80.8	0.13	-25.6	10.6	0.6		Doushantuo Fm
12ZL-9	250	61.4	0.34	-26.0	12.2	1.1		Doushantuo Fm
12ZL-10	249	65.8	0.46	-26.2	12.2	0.8		Doushantuo Fm
12ZL-10.3	248.7	56.7	0.48	-25.8	8.4	0.7		Doushantuo Fm
12ZL-13	246	53.5	0.52	-27.2	18.2	0.4		Doushantuo Fm
12ZL-13.8	245.2	61.3	0.68	-26.8	19.8	0.4		Doushantuo Fm
12ZL-16	243	94.6	0.06	-26.9	18.8	0.1		Doushantuo Fm
12ZL-16.8	242.2	95.4	0.04	-23.0	20.9	0.0		Doushantuo Fm
12ZL-17.2	241.8	92.4	0.18	-27.6	13.6	0.3		Doushantuo Fm
12ZL-18.5	240.5	87.8	0.04	-23.9	30.0	0.1		Doushantuo Fm
12ZL-19	240	98.4	0.06	-24.6	25.5	0.0		Doushantuo Fm
12ZL-20	239	95.5	0.07	-23.3	28.2	0.0		Doushantuo Fm
12ZL-21	238	93.7	0.04	-25.9	25.7	0.1		Doushantuo Fm
12ZL-21.5	237.5	74.9	0.00	-25.9	15.4	0.1		Doushantuo Fm
12ZL-21.6	237.4	58.0	0.04	-24.7	17.8	0.2	0.70811	Doushantuo Fm
12ZL-22	237	45.5	0.12	-26.7	17.2	0.2		Doushantuo Fm
12ZL-23	236	98.5	0.05	-25.5	25.9	0.0		Doushantuo Fm
12ZL-24	235	66.2	0.14	-28.4	11.5	0.2		Doushantuo Fm

12ZL-25	234	86.7	0.22	-27.4	21.0	0.1		Doushantuo Fm
12ZL-25.8	233.2	53.1	0.50	-26.2	15.9	1.1		Doushantuo Fm
12ZL-26.5	232.5	37.2	0.29	-27.5	18.7	0.3		Doushantuo Fm
12ZL-26.5	232.5	37.2	0.29	-27.5	17.8	0.2		Doushantuo Fm
12ZL-27.5	231.5	40.9	0.42	-26.4	21.3	0.5		Doushantuo Fm
12ZL-28.4	230.6	76.7	0.15	-25.8	31.7	0.1		Doushantuo Fm
12ZL-29.4	229.6	64.2	0.87	-27.7	21.7	0.2		Doushantuo Fm
12ZL-30.4	228.6	50.4	0.72	-27.0	24.4	0.2		Doushantuo Fm
12ZL-31	228	95.7	0.15	-23.9	28.5	0.0		Doushantuo Fm
12ZL-31.5	227.5	52.4	1.19	-27.1	19.7	1.4		Doushantuo Fm
12ZL-32	227	96.9	0.14	-24.4	24.3	0.0		Doushantuo Fm
12ZL-33	226	34.6	1.13	-27.3	19.0	0.5		Doushantuo Fm
12ZL-34	225	38.5	1.02	-27.3	22.6	0.4		Doushantuo Fm
12ZL-36.5	222.5	41.7	0.80	-26.6	18.8	0.0		Doushantuo Fm
12ZL-36.5	222.5	41.7	0.80	-26.6	19.4	0.0		Doushantuo Fm
12ZL-38	221	34.3	1.17	-26.8	21.0	0.0		Doushantuo Fm
12ZL-40	219	25.9	0.12	-26.5		0.0		Doushantuo Fm
12ZL-40.5	218.5	68.3	0.22	-26.6	22.5	0.2		Doushantuo Fm
12ZL-40.5	218.5	68.3	0.22	-26.6	13.3	0.1		Doushantuo Fm
12ZL-40.5	218.5	68.3	0.22	-26.6	25.2	0.1		Doushantuo Fm
12ZL-40.9	218.1	56.4	0.17	-27.4	29.3	0.3		Doushantuo Fm
12ZL-40.9	218.1	56.4	0.17	-27.4	23.6	0.1		Doushantuo Fm
12ZL-41	218	62.6	0.13	-26.6	2.6	0.0		Doushantuo Fm
12ZL-41.3	217.7	59.2	0.12	-27.7	11.0	0.0		Doushantuo Fm
12ZL-41.3	217.7	59.2	0.12	-27.7	14.9	0.0		Doushantuo Fm
12ZL-42	217	52.2	0.13	-26.1	26.2	0.2		Doushantuo Fm
12ZL-43	216	64.9	0.11	-27.0	11.7	0.2		Doushantuo Fm
12ZL-43.6	215.4	39.6	0.40	-27.1	18.1	0.0		Doushantuo Fm
12ZL-43.7	215.3	52.1	0.00	-27.4	24.4	0.0		Doushantuo Fm
12ZL-44	215	64.8	0.92	-26.9	21.8	0.0		Doushantuo Fm
12ZL-45.4	213.6	60.7	0.38	-25.3	26.6	0.1		Doushantuo Fm
12ZL-45.4	213.6	60.7	0.38	-25.3	28.8	0.0		Doushantuo Fm
12ZL-46	213	54.0	0.57	-28.8	22.7	0.1		Doushantuo Fm
12ZL-47	212	37.0	0.00	-26.2	7.4	0.0		Doushantuo Fm
12ZL-47.5	211.5	82.9	0.05	-27.1	14.9	0.0		Doushantuo Fm
12ZL-48	211	75.6	0.01	-26.6	33.4	0.0		Doushantuo Fm
12ZL-49	210	97.3	0.06	-27.9	26.8	0.0		Doushantuo Fm
12ZL-49.5	209.5	95.5	0.04	-26.7				Doushantuo Fm
12ZL-49.8	209.2	95.5	0.09	-26.9	24.9	0.0	0.70805	Doushantuo Fm
14ZL-49.8d	209.2	95.5	0.09	-26.9	24.9	0.0	0.70808	Doushantuo Fm
14ZL-49.8f	209.2	95.5	0.09	-26.9	24.9	0.0	0.70809	Doushantuo Fm
12ZL-54	205	94.1	0.04	-25.8	25.9	0.0		Doushantuo Fm
12ZL-55	204	96.6	0.07	-26.6	28.1	0.0		Doushantuo Fm
12ZL-63	196	83.7	0.70	-26.9	32.1	0.1		Doushantuo Fm
12ZL-63.5	195.5	77.8	0.41	-26.5	25.9	0.1		Doushantuo Fm
12ZL-64.5	194.5	79.2	0.40	-26.8	24.3	0.0		Doushantuo Fm
12ZL-66	193	38.7	0.00	-25.6	18.8	0.1		Doushantuo Fm

12ZL-67	192	72.8	0.98	-26.5	19.6	0.1		Doushantuo Fm
12ZL-67.7	191.3	76.3	0.57	-27.0	20.4	0.0		Doushantuo Fm
12ZL-67.7	191.3	76.3	0.57	-27.0	24.7	0.0		Doushantuo Fm
12ZL-69	190	71.0	0.66	-26.8	19.7	0.0		Doushantuo Fm
12ZL-70	189	44.0	0.17	-26.4	23.3	0.0		Doushantuo Fm
12ZL-73	186	41.7	0.47	-26.2	22.5	0.2		Doushantuo Fm
12ZL-74	185	49.1	0.42	-25.5	31.4	0.0		Doushantuo Fm
12ZL-75.5	183.5	38.6	1.22	-26.2	21.4	0.4		Doushantuo Fm
12ZL-77	182	49.1	0.32	-25.8	24.9	0.3		Doushantuo Fm
12ZL-78	181	53.6	0.44	-25.8	23.9	0.7		Doushantuo Fm
12ZL-79	180	57.1	0.57	-25.7	23.4	0.5		Doushantuo Fm
12ZL-80.2	178.8	63.4	2.33	-26.1	25.6	0.1		Doushantuo Fm
12ZL-81.5	177.5	65.6	1.12	-26.2	42.8	0.2		Doushantuo Fm
12ZL-82.8	176.2	42.5	0.01	-25.7		0.0		Doushantuo Fm
12ZL-82.9	176.1	56.7	1.61	-26.8	23.5	0.1		Doushantuo Fm
12ZL-83.5	175.5	55.5	0.48	-26.0	31.7	0.1		Doushantuo Fm
12ZL-84.5	174.5	62.7	2.09	-26.3	41.9	0.1		Doushantuo Fm
12ZL-85.5	173.5	52.0	1.06	-25.7	31.0	0.2		Doushantuo Fm
12ZL-86.5	172.5	67.3	2.25	-26.3	35.9	0.0		Doushantuo Fm
12ZL-87.5	171.5	64.7	1.93	-26.2	40.6	0.2		Doushantuo Fm
12ZL-88.5	170.5	64.9	1.73	-26.0	26.0	0.1		Doushantuo Fm
12ZL-89.5	169.5	63.7	0.62	-25.8	20.5	0.2		Doushantuo Fm
12ZL-90.5	168.5	60.2	1.84	-26.8	27.2	0.0		Doushantuo Fm
12ZL-92	167	66.0	0.99	-26.5	25.3	0.0		Doushantuo Fm
12ZL-92.5	166.5	72.3	1.06	-26.5	27.4	0.1		Doushantuo Fm
12ZL-93.5	165.5	60.5	1.98	-26.7	34.5	0.2		Doushantuo Fm
12ZL-94	165	59.6	1.65	-26.4	24.2	0.1		Doushantuo Fm
12ZL-95.5	163.5	60.7	1.02	-26.3	35.1	0.1		Doushantuo Fm
12ZL-96.5	162.5	54.7	0.97	-26.8	33.4	0.2		Doushantuo Fm
12ZL-97.5	161.5	57.7	1.44	-26.6	45.6	0.1		Doushantuo Fm
12ZL-99	160	58.1	0.83	-25.0	15.1	0.2		Doushantuo Fm
12ZL-100	159	63.4	0.78	-25.8	22.7	0.1		Doushantuo Fm
12ZL-101	158	80.9	0.53	-27.6	24.2	0.3		Doushantuo Fm
12ZL-102	157	76.4	0.35	-25.4	25.2	0.0		Doushantuo Fm
12ZL-104	155	62.8	0.81	-26.6	30.0	0.0		Doushantuo Fm
12ZL-105	154	60.6	1.09	-25.8	22.6	0.1		Doushantuo Fm
12ZL-106	153	58.0	0.53	-26.0	21.1	0.2		Doushantuo Fm
12ZL-107	152	55.5	1.22	-25.2	22.4	0.1		Doushantuo Fm
12ZL-108.5	150.5	55.4	1.87	-25.6	27.1	0.0		Doushantuo Fm
12ZL-109.5	149.5	67.3	0.85	-25.2	27.8	0.0		Doushantuo Fm
12ZL-110.2	148.8	75.7	0.11	-26.2	31.8	0.1		Doushantuo Fm
12ZL-110.8	148.2	75.8	0.43	-25.4	42.0	0.1		Doushantuo Fm
12ZL-112.2	146.8	70.9	0.22	-25.0	24.9	0.0		Doushantuo Fm
12ZL-114	145	70.8	0.60	-25.9	26.6	0.0	0.70812	Doushantuo Fm
12ZL-115	144	75.6	0.50	-25.8	25.5	0.0		Doushantuo Fm
12ZL-117	142	72.4	0.62	-25.7	38.2	0.2		Doushantuo Fm
12ZL-117	142	72.4	0.62	-25.7	38.2	0.2		Doushantuo Fm

12ZL-118	141	70.1	0.70	-25.5	28.6	0.0		Doushantuo Fm
12ZL-119	140	76.9	0.70	-24.8	25.0	0.0		Doushantuo Fm
12ZL-120	139	71.4	0.51	-25.2	26.3	0.1		Doushantuo Fm
12ZL-121	138	74.8	0.48	-25.2	24.0	0.0	0.70802	Doushantuo Fm
12ZL-122	137	76.9	0.48	-25.2	15.8	0.0		Doushantuo Fm
12ZL-123	136	68.8	0.59	-24.5	24.0	0.0	0.70799	Doushantuo Fm
12ZL-125	134	62.9	0.28	-24.9	35.8	0.0		Doushantuo Fm
12ZL-133	126	82.2	0.81	-25.4	24.4	0.1		Doushantuo Fm
12ZL-134.5	124.5	71.4	0.61	-26.3	24.0	0.2		Doushantuo Fm
12ZL-134.5	124.5	71.4	0.61	-26.3	25.5	0.6		Doushantuo Fm
12ZL-136	123	81.4	0.42	-25.6	24.4	0.1		Doushantuo Fm
12ZL-137	122	84.3	0.57	-25.4	28.0	0.2		Doushantuo Fm
12ZL-139	120	79.1	0.84	-25.1	33.5	0.1		Doushantuo Fm
12ZL-141	118	82.8	0.52	-25.9	37.1	0.2		Doushantuo Fm
12ZL-142	117	78.8	0.42	-25.6	34.9	0.1		Doushantuo Fm
12ZL-143.5	115.5	78.9	0.94	-25.6	39.3	0.1		Doushantuo Fm
12ZL-145.5	113.5	80.1	0.69	-25.4	26.0	0.2	0.70795	Doushantuo Fm
12ZL-147	112	81.9	0.61	-24.4	33.1	0.0	0.70794	Doushantuo Fm
12ZL-149	110	79.4	0.74	-25.4	24.4	0.0		Doushantuo Fm
12ZL-151	108	86.2	0.67	-25.5	36.9	0.1		Doushantuo Fm
12ZL-153	106	77.5	0.72	-24.8	42.5	0.1		Doushantuo Fm
12ZL-153	106	77.5	0.72	-24.8	34.9	0.1		Doushantuo Fm
12ZL-153	106	77.5	0.72	-24.8	40.3	0.1		Doushantuo Fm
12ZL-155.5	103.5	77.1	0.57	-25.8	28.8	0.1		Doushantuo Fm
12ZL-157	102	73.5	0.15	-25.9	25.4	0.0		Doushantuo Fm
12ZL-159	100	65.0	0.61	-24.9	25.3	0.0		Doushantuo Fm
12ZL-164	95	92.4	0.28	-24.9	32.0	0.1		Doushantuo Fm
12ZL-166	93	87.8	0.15	-25.2	30.2	0.1		Doushantuo Fm
12ZL-168	91	82.6	0.44	-25.7	27.5	0.2		Doushantuo Fm
12ZL-170	89	68.7	0.39	-24.7	32.9	0.1		Doushantuo Fm
12ZL-172	87	64.8	0.81	-25.6	20.1	0.1		Doushantuo Fm
12ZL-175	84	65.6	1.28	-25.3	26.1	0.0	0.70806	Doushantuo Fm
12ZL-177	82	80.9	0.56	-25.3	28.7	0.2		Doushantuo Fm
12ZL-179	80	75.4	0.76	-25.1	28.2	0.1		Doushantuo Fm
12ZL-181	78	76.6	0.90	-25.0	43.8	0.1		Doushantuo Fm
12ZL-181	78	76.6	0.90	-25.0	48.6	0.1		Doushantuo Fm
12ZL-181	78	76.6	0.90	-25.0	51.0	0.1		Doushantuo Fm
12ZL-183	76	77.3	0.92	-25.7	32.8	0.0		Doushantuo Fm
12ZL-184.5	74.5	69.9	0.24	-25.6		0.0		Doushantuo Fm
12ZL-192	67	79.7	0.84	-25.8	29.5	0.1		Doushantuo Fm
12ZL-193	66	84.7	0.33	-25.5	26.0	0.1		Doushantuo Fm
12ZL-194	65	87.4	0.40	-25.2	27.7	0.1		Doushantuo Fm
12ZL-199	60	59.4	0.38	-26.1	17.6	0.1		Doushantuo Fm
12ZL-199	60	59.4	0.38	-26.1	16.6	1.4		Doushantuo Fm
12ZL-202	57	74.5	0.25	-25.3	24.6	0.4		Doushantuo Fm
12ZL-203	56	81.9	0.56	-25.6	34.3	0.0		Doushantuo Fm
12ZL-204	55	83.7	0.67	-24.8	31.0	0.1		Doushantuo Fm

12ZL-204	55	83.7	0.67	-24.8	24.3	0.1		Doushantuo Fm
12ZL-204	55	83.7	0.67	-24.8	27.9	0.1		Doushantuo Fm
12ZL-204	55	83.7	0.67	-24.8	27.5	0.1		Doushantuo Fm
12ZL-206	53	77.3	0.50	-25.5	34.4	0.1		Doushantuo Fm
12ZL-210	49	91.2	0.38	-25.3	35.5	0.1		Doushantuo Fm
12ZL-212	47	97.0	0.20	-24.1	32.0	0.1	0.70803	Doushantuo Fm
12ZL-213	46	75.0	0.46	-24.5	34.1	0.0		Doushantuo Fm
12ZL-213.5	45.5	84.9	0.51	-24.0	53.8	0.0		Doushantuo Fm
12ZL-220	39	56.5	0.22	-27.5	42.2	0.1		Doushantuo Fm
12ZL-222	37	15.6	0.40	-28.5		0.0		Doushantuo Fm
12ZL-224	35	3.5	0.02	-28.3		0.0		Doushantuo Fm
12ZL-226	33	21.0	0.15	-28.2	21.7	0.1		Doushantuo Fm
12ZL-228	31	2.9	0.20	-27.4	36.2	0.8		Doushantuo Fm
12ZL-243	16	8.3	0.00	-30.0		0.0		Doushantuo Fm
12ZL-244	15	4.9	0.00	-30.2	32.7	0.3		Doushantuo Fm
12ZL-245	14	5.5	0.00	-30.9		0.0		Doushantuo Fm
12ZL-246	13	7.3	0.23	-26.6	19.6	5.9		Doushantuo Fm
12ZL-247	12	3.2	0.31	-29.0	0.0	1.8		Doushantuo Fm
12ZL-248	11	3.0	0.48	-30.8	1.4	5.1		Doushantuo Fm
12ZL-254	5	5.4	0.55	-32.4	-20.4	3.6		Doushantuo Fm
12ZL-254	5	5.4	0.33	-32.3	-17.5	2.7		Doushantuo Fm
12ZL-254	5	5.4	0.33	-32.3	-20.4	3.6		Doushantuo Fm
12ZL-254	5	5.4	0.33	-32.3	-15.0	3.9		Doushantuo Fm
12ZL-254.5	4.5	51.9	0.10	-27.5	11.3	0.5		Doushantuo Fm
12ZL-255.1	3.9	28.5	0.16	-27.6	21.7	3.2		Doushantuo Fm
12ZL-255.1	3.9	28.5	0.16	-26.8	21.7	3.2		Doushantuo Fm
12ZL-255.7	3.3	77.4	0.08	-31.1	24.1	0.2		Doushantuo Fm
12ZL-256.7	2.3	89.5	0.06	-27.9	32.1	0.3		Doushantuo Fm

Appendix B

Table B.1 Time-series C, O and S isotope data of the Doushantuo (DST) and Deying (DY) formations in Zhongling section.

Zhongling	Height	Carbonate%	TOC%	$\delta^{13}C_{carb}$	$\delta^{18}O_{carb}$	$\delta^{13}C_{org}$	$\Delta\delta^{13}C$	$\delta^{34}S_{py}$	Pyrite%	Fm
12ZL+0.2	259.2	94.5	0.01	-1.0	-4.9	-26.5	25.5	22.0	0.0	DY
12ZL+0.1	259.1	94.8	0.00	2.1	-6.5	-26.8	29.0	15.5	0.1	DY
12ZL-0.2	258.8	92.8	0.00	-0.6	-5.9	-27.9	27.3	12.9	0.5	DST
12ZL-0.5	258.5	88.8	0.01	-1.0	-6.3	-26.6	25.5	21.7	0.4	DST
12ZL-0.9	258.1	88.3	0.05	-1.0	-4.2	-27.5	26.5	20.3	0.4	DST
12ZL-0.9	258.1	88.3	0.05	-1.9	-4.5	-27.5	25.6	20.3	0.4	DST
12ZL-0.9	258.1	88.3	0.05	-1.1	-4.7	-27.5	26.4	20.3	0.4	DST
12ZL-0.9	258.1	88.3	0.05	-1.5	-5.7	-27.5	26.0	20.3	0.4	DST
12ZL-1.4	257.6	85.1	0.01	0.5	-4.5	-25.1	25.6	17.5	0.2	DST
12ZL-2.0	257	93.3	0.00	-0.6	-5.5	-27.1	26.5	18.8	0.4	DST
12ZL-2.5	256.5	74.8	0.00	-1.5	-5.2	-27.1	25.5	21.8	1.9	DST
12ZL-2.5	256.5	74.8	0.00	-1.5	-5.2	-27.1	25.5	21.3	1.8	DST
12ZL-2.7	256.3	72.1	0.00	1.6	-6.6			23.3	0.4	DST
12ZL-2.7	256.3	72.1	0.00	1.6	-6.6			21.2	0.1	DST
12ZL-3.4	255.6	90.2	0.01	2.9	-6.8	-25.5	28.3	19.3	0.1	DST
14ZL-3.5f	255.5			1.1	-8.5					DST
12ZL-4.0	255	94.2	0.05	-6.6	-7.6	-25.4	18.8	19.8	0.1	DST
12ZL-4.5	254.5	94.6	0.02	3.1	-8.0	-25.3	28.4	22.6	0.2	DST
12ZL-4.5	254.5	94.6	0.02	2.7	-7.2	-25.3	28.0	22.6	0.2	DST
12ZL-4.5	254.5	94.6	0.02	1.9	-7.9	-25.3	27.3	22.6	0.2	DST
12ZL-5	254	87.4	0.04	2.7	-6.8	-24.2	26.8	20.6	0.1	DST
14ZL-6.5g	252.5			3.6	-7.0					DST
14ZL-6.5h	252.5			2.9	-7.2					DST
14ZL-6.6g	252.4			-1.6	-4.5					DST
14ZL-6.6d	252.4			0.2	-5.0					DST
12ZL-6.7	252.3	86.9	0.03	1.3	-6.9	-25.6	26.9	20.5	0.1	DST
12ZL-7	252	80.6	0.04	-2.5	-4.8	-24.0	21.5	20.9	0.4	DST
14ZL-7.5f	251.5			3.7	-4.5					DST
12ZL-7.8	251.2	84.8	0.11	-0.2	-5.7	-24.4	24.2	18.8	0.1	DST
12ZL-8.5	250.5	80.8	0.13	2.1	-4.0	-25.6	27.8	10.6	0.6	DST

12ZL-9	250	61.4	0.34	2.8	-3.4	-26.0	28.8	12.2	1.1	DST
12ZL-10	249	65.8	0.46	2.8	-3.6	-26.2	29.0	12.2	0.8	DST
12ZL-10.3	248.7	56.7	0.48	2.4	-4.2	-25.8	28.2	8.4	0.7	DST
12ZL-13	246	53.5	0.52	2.9	-3.1	-27.2	30.1	18.2	0.4	DST
12ZL-13.8	245.2	61.3	0.68	3.1	-2.4	-26.8	29.9	19.8	0.4	DST
12ZL-16	243	94.6	0.06	0.7	-7.9	-26.9	27.5	18.8	0.1	DST
12ZL-16.8	242.2	95.4	0.04	4.8	-5.0	-23.0	27.8	20.9	0.0	DST
12ZL-17.2	241.8	92.4	0.18	4.7	-5.2	-27.6	32.3	13.6	0.3	DST
12ZL-18.5	240.5	87.8	0.04	-4.5	-7.8	-23.9	19.4	30.0	0.1	DST
12ZL-19	240	98.4	0.06	2.4	-7.3	-24.6	27.0	25.5	0.0	DST
12ZL-19	240	98.4	0.06	3.0	-8.0	-24.6	27.6	25.5	0.0	DST
14ZL-19b	240	98.4	0.06	6.0	-6.7	-24.6	30.6	25.5	0.0	DST
14ZL-19.5b	239.5			5.6	-6.7					DST
14ZL-19.5c	239.5			5.8	-6.8					DST
12ZL-20	239	95.5	0.07	3.7	-6.7	-23.3	27.0	28.2	0.0	DST
12ZL-20	239	95.5	0.05	3.7	-6.7	-23.1	26.8	28.2	0.0	DST
14ZL-20c	239	95.5	0.05	6.7	-7.1	-23.3	30.0	28.2	0.0	DST
14ZL-20d	239	95.5	0.05	6.6	-6.7	-23.3	30.0	28.2	0.0	DST
12ZL-21	238	93.7	0.04	-3.6	-7.3	-25.9	22.2	25.7	0.1	DST
12ZL-21.5	237.5	74.9	0.00	-0.6	-6.2	-25.9	25.3	15.4	0.1	DST
12ZL-21.6	237.4	58.0	0.04	0.0	-5.3	-24.7	24.7	17.8	0.2	DST
12ZL-21.6	237.4	58.0	0.04	-1.7	-5.8	-24.7	22.9	17.8	0.2	DST
12ZL-21.6	237.4	58.0	0.04	-1.9	-5.2	-24.7	22.8	17.8	0.2	DST
12ZL-21.6	237.4	58.0	0.04	-1.6	-6.1	-24.7	23.1	17.8	0.2	DST
12ZL-21.6	237.4	58.0	0.04	-1.3	-5.8	-24.7	23.4	17.8	0.2	DST
12ZL-21.6	237.4	58.0	0.04	-3.8	-5.4	-24.7	20.9	17.8	0.2	DST
12ZL-21.6	237.4	58.0	0.04	-1.5	-5.2	-24.7	23.2	17.8	0.2	DST
12ZL-21.6	237.4	58.0	0.04	-0.1	-4.8	-24.7	24.6	17.8	0.2	DST
12ZL-22	237	45.5	0.12	0.7	-4.1	-26.7	27.4	17.2	0.2	DST
12ZL-23	236	98.5	0.05	-2.2	-7.3	-25.5	23.3	25.9	0.0	DST
12ZL-24	235	66.2	0.14	1.1	-5.0	-28.4	29.4	11.5	0.2	DST
12ZL-25	234	86.7	0.22	2.1	-3.4	-27.4	29.5	21.0	0.1	DST
12ZL-25.8	233.2	53.1	0.50	-0.8	-7.3	-26.2	25.5	15.9	1.1	DST
12ZL-26.5	232.5	37.2	0.29	0.9	-5.1	-27.5	28.4	18.7	0.3	DST
12ZL-26.5	232.5	37.2	0.29	0.9	-5.1	-27.5	28.4	17.8	0.2	DST
12ZL-27.5	231.5	40.9	0.42	2.4	-4.8	-26.4	28.8	21.3	0.5	DST
12ZL-28.4	230.6	76.7	0.15	3.7	-3.9	-25.8	29.5	31.7	0.1	DST
12ZL-29.4	229.6	64.2	0.87	4.1	-2.8	-27.7	31.8	21.7	0.2	DST

12ZL-30.4	228.6	50.4	0.72	3.7	-2.7	-27.0	30.7	24.4	0.2	DST
12ZL-31	228	95.7	0.15	3.7	-5.5	-23.9	27.5	28.5	0.0	DST
12ZL-31.5	227.5	52.4	1.19	3.6	-2.3	-27.1	30.7	19.7	1.4	DST
12ZL-32	227	96.9	0.14			-24.4		24.3	0.0	DST
12ZL-33	226	34.6	1.13	3.4	-2.8	-27.3	30.7	19.0	0.5	DST
12ZL-34	225	38.5	1.02	3.9	-1.9	-27.3	31.2	22.6	0.4	DST
12ZL-36.5	222.5	41.7	0.80	3.1	-2.7	-26.6	29.7	18.8	0.0	DST
12ZL-36.5	222.5	41.7	0.80	3.1	-2.7	-26.6	29.7	19.4	0.0	DST
12ZL-38	221	34.3	1.17	2.7	-1.8	-26.8	29.5	21.0	0.0	DST
12ZL-40	219	25.9	0.12	-4.2	-4.0	-26.5	22.2		0.0	DST
12ZL-40.5	218.5	68.3	0.22			-26.6		22.5	0.2	DST
12ZL-40.5	218.5	68.3	0.22			-26.6		13.3	0.1	DST
12ZL-40.5	218.5	68.3	0.22			-26.6		25.2	0.1	DST
12ZL-40.9	218.1	56.4	0.17	-0.5	-2.0	-27.4	26.9	29.3	0.3	DST
12ZL-40.9	218.1	56.4	0.17	-0.5	-2.0	-27.4	26.9	23.6	0.1	DST
12ZL-41	218	62.6	0.13	-3.0	-3.4	-26.6	23.6	2.6	0.0	DST
12ZL-41.3	217.7	59.2	0.12	-1.6	-2.1	-27.7	26.1	11.0	0.0	DST
12ZL-41.3	217.7	59.2	0.12	-1.6	-2.1	-27.7	26.1	14.9	0.0	DST
12ZL-42	217	52.2	0.13			-26.1		26.2	0.2	DST
12ZL-43	216	64.9	0.11	-3.6	-3.7	-27.0	23.5	11.7	0.2	DST
12ZL-43.6	215.4	39.6	0.40			-27.1		18.1	0.0	DST
12ZL-43.7	215.3	52.1	0.00			-27.4		24.4	0.0	DST
12ZL-44	215	64.8	0.92			-26.9		21.8	0.0	DST
12ZL-45.4	213.6	60.7	0.38			-25.3		26.6	0.1	DST
12ZL-45.4	213.6	60.7	0.38			-25.3		28.8	0.0	DST
12ZL-46	213	54.0	0.57	-5.3	-4.3	-28.8	23.5	22.7	0.1	DST
12ZL-47	212	37.0	0.00			-26.2		7.4	0.0	DST
12ZL-47.5	211.5	82.9	0.05	-1.1	-3.5	-27.1	26.0	14.9	0.0	DST
12ZL-48	211	75.6	0.01	-0.2	-3.1	-26.6	26.4	33.4	0.0	DST
12ZL-49	210	97.3	0.06	0.4	-6.0	-27.9	28.3	26.8	0.0	DST
14ZL-49f	210	97.3	0.06	0.9	-6.1	-27.9	28.9	26.8	0.0	DST
14ZL-49-2b	210	97.3	0.06	1.0	-5.8	-27.9	28.9	26.8	0.0	DST
14ZL-49-2d	210	97.3	0.06	1.2	-5.6	-27.9	29.1	26.8	0.0	DST
12ZL-49.5	209.5	95.5	0.04			-26.7				DST
12ZL-49.8	209.2	95.5	0.09	2.8	-5.3	-26.9	29.6	24.9	0.0	DST
14ZL-49.8d	209.2	95.5	0.09	7.7	-4.7	-26.9	34.6	24.9	0.0	DST
14ZL-49.8f	209.2	95.5	0.09	7.8	-4.4	-26.9	34.7	24.9	0.0	DST
14ZL-49.8a	209.2	95.5	0.09	6.6	-4.9	-26.9	33.4	24.9	0.0	DST

14ZL-53.5b	205.5			6.1	-5.9					DST
12ZL-54	205	94.1	0.04	6.3	-6.0	-25.8	32.1	25.9	0.0	DST
14ZL-54d	205	94.1	0.04	6.0	-5.7	-25.8	31.8	25.9	0.0	DST
14ZL-54.3f	204.7			5.8	-5.4					DST
12ZL-55	204	96.6	0.07	6.4	-5.6	-26.6	33.1	28.1	0.0	DST
14ZL-55-2d	204	96.6	0.07	5.8	-5.4	-26.6	32.4	28.1	0.0	DST
14ZL-55g	204	96.6	0.07	5.2	-5.5	-26.6	31.8	28.1	0.0	DST
12ZL-63	196	83.7	0.70			-26.9		32.1	0.1	DST
12ZL-63.5	195.5	77.8	0.41			-26.5		25.9	0.1	DST
12ZL-64.5	194.5	79.2	0.40			-26.8		24.3	0.0	DST
12ZL-66	193	38.7	0.00	2.8	-6.4	-25.6	28.4	18.8	0.1	DST
12ZL-67	192	72.8	0.98	2.5	-5.4	-26.5	29.0	19.6	0.1	DST
12ZL-67.7	191.3	76.3	0.57	3.0	-3.8	-27.0	30.0	20.4	0.0	DST
12ZL-67.7	191.3	76.3	0.57	3.0	-3.8	-27.0	30.0	24.7	0.0	DST
12ZL-69	190	71.0	0.66	3.0	-3.7	-26.8	29.8	19.7	0.0	DST
12ZL-70	189	44.0	0.17	5.2	-1.3	-26.4	31.6	23.3	0.0	DST
12ZL-73	186	41.7	0.47	5.3	-1.9	-26.2	31.5	22.5	0.2	DST
12ZL-74	185	49.1	0.42	5.0	-2.7	-25.5	30.5	31.4	0.0	DST
12ZL-75.5	183.5	38.6	1.22	5.1	-2.2	-26.2	31.4	21.4	0.4	DST
12ZL-77	182	49.1	0.32	4.6	-3.5	-25.8	30.4	24.9	0.3	DST
12ZL-78	181	53.6	0.44	4.7	-3.3	-25.8	30.5	23.9	0.7	DST
12ZL-79	180	57.1	0.57	4.7	-3.6	-25.7	30.4	23.4	0.5	DST
12ZL-80.2	178.8	63.4	2.33	3.8	-3.7	-26.1	29.9	25.6	0.1	DST
12ZL-81.5	177.5	65.6	1.12	4.8	-4.1	-26.2	31.0	42.8	0.2	DST
12ZL-82.8	176.2	42.5	0.01	3.4	-6.4	-25.7	29.2		0.0	DST
12ZL-82.9	176.1	56.7	1.61	4.4	-4.9	-26.8	31.2	23.5	0.1	DST
12ZL-83.5	175.5	55.5	0.48	4.0	-6.3	-26.0	30.0	31.7	0.1	DST
12ZL-84.5	174.5	62.7	2.09	4.9	-5.5	-26.3	31.2	41.9	0.1	DST
12ZL-85.5	173.5	52.0	1.06	4.1	-7.0	-25.7	29.8	31.0	0.2	DST
12ZL-86.5	172.5	67.3	2.25	4.3	-5.2	-26.3	30.6	35.9	0.0	DST
12ZL-87.5	171.5	64.7	1.93	4.7	-5.3	-26.2	30.9	40.6	0.2	DST
12ZL-88.5	170.5	64.9	1.73	4.8	-6.1	-26.0	30.9	26.0	0.1	DST
12ZL-89.5	169.5	63.7	0.62	4.0	-6.5	-25.8	29.8	20.5	0.2	DST
12ZL-90.5	168.5	60.2	1.84	4.8	-5.8	-26.8	31.6	27.2	0.0	DST
12ZL-92	167	66.0	0.99	4.0	-4.4	-26.5	30.5	25.3	0.0	DST
12ZL-92.5	166.5	72.3	1.06	4.1	-4.6	-26.5	30.6	27.4	0.1	DST
12ZL-93.5	165.5	60.5	1.98	4.2	-6.5	-26.7	30.9	34.5	0.2	DST
12ZL-94	165	59.6	1.65	4.1	-6.3	-26.4	30.5	24.2	0.1	DST

12ZL-95.5	163.5	60.7	1.02	4.3	-6.3	-26.3	30.6	35.1	0.1	DST
12ZL-96.5	162.5	54.7	0.97	3.8	-6.3	-26.8	30.6	33.4	0.2	DST
12ZL-97.5	161.5	57.7	1.44	4.4	-6.3	-26.6	31.0	45.6	0.1	DST
12ZL-99	160	58.1	0.83	4.9	-4.8	-25.0	29.9	15.1	0.2	DST
12ZL-100	159	63.4	0.78	4.0	-6.3	-25.8	29.8	22.7	0.1	DST
12ZL-101	158	80.9	0.53	0.2	-4.3	-27.6	27.8	24.2	0.3	DST
12ZL-102	157	76.4	0.35	4.3	-4.2	-25.4	29.7	25.2	0.0	DST
12ZL-104	155	62.8	0.81	4.6	-6.6	-26.6	31.2	30.0	0.0	DST
12ZL-105	154	60.6	1.09	5.1	-5.0	-25.8	30.9	22.6	0.1	DST
12ZL-106	153	58.0	0.53	4.8	-4.6	-26.0	30.9	21.1	0.2	DST
12ZL-107	152	55.5	1.22	5.5	-5.0	-25.2	30.7	22.4	0.1	DST
12ZL-108.5	150.5	55.4	1.87	5.3	-4.3	-25.6	30.9	27.1	0.0	DST
12ZL-109.5	149.5	67.3	0.85	1.7	-7.0	-25.2	26.9	27.8	0.0	DST
12ZL-110.2	148.8	75.7	0.11	4.7	-6.7	-26.2	30.9	31.8	0.1	DST
12ZL-110.8	148.2	75.8	0.43	4.4	-7.0	-25.4	29.7	42.0	0.1	DST
12ZL-112.2	146.8	70.9	0.22	5.4	-6.6	-25.0	30.4	24.9	0.0	DST
12ZL-114	145	70.8	0.60	5.6	-6.9	-25.9	31.4	26.6	0.0	DST
12ZL-114	145	70.8	0.60	5.7	-7.0	-25.9	31.5	26.6	0.0	DST
12ZL-115	144	75.6	0.50	5.7	-6.6	-25.8	31.6	25.5	0.0	DST
12ZL-115	144	75.6	0.50	5.7	-6.2	-25.8	31.6	25.5	0.0	DST
12ZL-117	142	72.4	0.62	5.8	-6.7	-25.7	31.5	38.2	0.2	DST
12ZL-117	142	72.4	0.62	5.7	-6.6	-25.7	31.3	38.2	0.2	DST
12ZL-118	141	70.1	0.70	5.7	-6.1	-25.5	31.2	28.6	0.0	DST
12ZL-118	141	70.1	0.70	5.7	-5.7	-25.5	31.2	28.6	0.0	DST
12ZL-118	141	70.1	0.70	6.1	-7.9	-25.5	31.6	28.6	0.0	DST
12ZL-119	140	76.9	0.70	5.7	-6.1	-24.8	30.5	25.0	0.0	DST
12ZL-119	140	76.9	0.70	5.7	-5.8	-24.8	30.6	25.0	0.0	DST
12ZL-120	139	71.4	0.51	6.0	-6.0	-25.2	31.2	26.3	0.1	DST
12ZL-120	139	71.4	0.51	6.0	-5.9	-25.2	31.2	26.3	0.1	DST
12ZL-120	139	71.4	0.51	6.2	-8.3	-25.2	31.4	26.3	0.1	DST
12ZL-121	138	74.8	0.48	6.0	-6.8	-25.2	31.1	24.0	0.0	DST
12ZL-122	137	76.9	0.48	5.9	-6.9	-25.2	31.1	15.8	0.0	DST
12ZL-123	136	68.8	0.59	5.7	-7.0	-24.5	30.2	24.0	0.0	DST
12ZL-125	134	62.9	0.28	5.9	-6.5	-24.9	30.8	35.8	0.0	DST
12ZL-133	126	82.2	0.81	5.9	-6.8	-25.4	31.4	24.4	0.1	DST
12ZL-134.5	124.5	71.4	0.61	6.2	-6.8	-26.3	32.5	24.0	0.2	DST
12ZL-134.5	124.5	71.4	0.61	6.1	-7.4	-26.3	32.5	25.5	0.6	DST
12ZL-136	123	81.4	0.42	6.6	-6.5	-25.6	32.2	24.4	0.1	DST

12ZL-137	122	84.3	0.57	6.5	-6.8	-25.4	31.9	28.0	0.2	DST
12ZL-139	120	79.1	0.84	6.3	-7.2	-25.1	31.3	33.5	0.1	DST
12ZL-141	118	82.8	0.52	6.6	-6.7	-25.9	32.5	37.1	0.2	DST
12ZL-142	117	78.8	0.42	6.4	-7.1	-25.6	31.9	34.9	0.1	DST
12ZL-143.5	115.5	78.9	0.94	6.4	-7.0	-25.6	32.0	39.3	0.1	DST
12ZL-145.5	113.5	80.1	0.69	6.2	-7.2	-25.4	31.6	26.0	0.2	DST
12ZL-147	112	81.9	0.61	6.1	-7.3	-24.4	30.5	33.1	0.0	DST
12ZL-149	110	79.4	0.74	6.3	-7.2	-25.4	31.7	24.4	0.0	DST
12ZL-149	110	79.4	0.74	5.6	-8.1	-25.4	31.0	24.4	0.0	DST
12ZL-149	110	79.4	0.74	5.6	-8.1	-25.4	31.0	24.4	0.0	DST
12ZL-151	108	86.2	0.67	6.1	-7.6	-25.5	31.6	36.9	0.1	DST
12ZL-153	106	77.5	0.72	5.9	-8.0	-24.8	30.6	42.5	0.1	DST
12ZL-153	106	77.5	0.72	6.4	-6.5	-24.8	31.2	34.9	0.1	DST
12ZL-153	106	77.5	0.72	5.9	-8.0	-24.8	30.6	40.3	0.1	DST
12ZL-155.5	103.5	77.1	0.57	4.5	-7.9	-25.8	30.3	28.8	0.1	DST
12ZL-155.5	103.5	77.1	0.57	5.8	-6.7	-25.8	31.6	28.8	0.1	DST
12ZL-155.5	103.5	77.1	0.57	4.5	-7.9	-25.8	30.3	28.8	0.1	DST
12ZL-157	102	73.5	0.15	6.3	-6.8	-25.9	32.2	25.4	0.0	DST
12ZL-159	100	65.0	0.61	6.1	-5.9	-24.9	31.0	25.3	0.0	DST
12ZL-164	95	92.4	0.28	3.7	-8.3	-24.9	28.6	32.0	0.1	DST
12ZL-164	95	92.4	0.28	7.7	-8.0	-24.9	32.7	32.0	0.1	DST
12ZL-164	95	92.4	0.28	3.7	-8.3	-24.9	28.6	32.0	0.1	DST
12ZL-166	93	87.8	0.15	8.0	-8.2	-25.2	33.2	30.2	0.1	DST
12ZL-168	91	82.6	0.44	7.1	-8.6	-25.7	32.8	27.5	0.2	DST
12ZL-168	91	82.6	0.44	7.5	-8.0	-25.7	33.2	27.5	0.2	DST
12ZL-168	91	82.6	0.44	7.1	-8.6	-25.7	32.8	27.5	0.2	DST
12ZL-170	89	68.7	0.39	6.4	-8.0	-24.7	31.2	32.9	0.1	DST
12ZL-172	87	64.8	0.81	1.3	-7.4	-25.6	26.9	20.1	0.1	DST
12ZL-172	87	64.8	0.81	1.5	-7.7	-25.6	27.1	20.1	0.1	DST
12ZL-175	84	65.6	1.28	4.0	-8.8	-25.3	29.2	26.1	0.0	DST
12ZL-175	84	65.6	1.28	5.8	-8.5	-25.3	31.1	26.1	0.0	DST
12ZL-175	84	65.6	1.28	4.0	-8.8	-25.3	29.2	26.1	0.0	DST
12ZL-177	82	80.9	0.56	4.0	-9.2	-25.3	29.2	28.7	0.2	DST
12ZL-177	82	80.9	0.56	5.2	-8.0	-25.3	30.4	28.7	0.2	DST
12ZL-177	82	80.9	0.56	4.0	-9.2	-25.3	29.2	28.7	0.2	DST
12ZL-179	80	75.4	0.76	5.7	-8.6	-25.1	30.8	28.2	0.1	DST
12ZL-181	78	76.6	0.90	5.9	-8.4	-25.0	30.9	43.8	0.1	DST
12ZL-181	78	76.6	0.90	5.9	-8.4	-25.0	30.9	48.6	0.1	DST

12ZL-181	78	76.6	0.90	5.9	-8.4	-25.0	30.9	51.0	0.1	DST
12ZL-183	76	77.3	0.92	5.1	-8.1	-25.7	30.7	32.8	0.0	DST
12ZL-184.5	74.5	69.9	0.24	4.2	-7.4	-25.6	29.9		0.0	DST
12ZL-192	67	79.7	0.84	6.0	-8.3	-25.8	31.8	29.5	0.1	DST
12ZL-193	66	84.7	0.33	6.0	-8.8	-25.5	31.5	26.0	0.1	DST
12ZL-194	65	87.4	0.40	5.8	-8.5	-25.2	31.0	27.7	0.1	DST
12ZL-199	60	59.4	0.38	5.6	-4.8	-26.1	31.7	17.6	0.1	DST
12ZL-199	60	59.4	0.38	5.6	-4.8	-26.1	31.7	16.6	1.4	DST
12ZL-202	57	74.5	0.25	5.5	-8.7	-25.3	30.8	24.6	0.4	DST
12ZL-203	56	81.9	0.56	5.7	-8.7	-25.6	31.3	34.3	0.0	DST
12ZL-204	55	83.7	0.67	6.1	-8.7	-24.8	30.9	31.0	0.1	DST
12ZL-204	55	83.7	0.67	6.1	-8.7	-24.8	30.9	24.3	0.1	DST
12ZL-204	55	83.7	0.67	6.1	-8.7	-24.8	30.9	27.9	0.1	DST
12ZL-204	55	83.7	0.67	6.1	-8.7	-24.8	30.9	27.5	0.1	DST
12ZL-206	53	77.3	0.50	4.9	-9.0	-25.5	30.4	34.4	0.1	DST
12ZL-206	53	77.3	0.50	5.1	-9.2	-25.5	30.6	34.4	0.1	DST
12ZL-206	53	77.3	0.50	6.4	-8.4	-25.5	31.8	34.4	0.1	DST
12ZL-206	53	77.3	0.50	6.3	-8.8	-25.5	31.8	34.4	0.1	DST
12ZL-206	53	77.3	0.50	4.9	-9.0	-25.5	30.4	34.4	0.1	DST
12ZL-206	53	77.3	0.50	6.4	-8.4	-25.5	31.8	34.4	0.1	DST
12ZL-210	49	91.2	0.38	3.4	-9.7	-25.3	28.7	35.5	0.1	DST
12ZL-210	49	91.2	0.38	5.9	-9.5	-25.3	31.2	35.5	0.1	DST
12ZL-210	49	91.2	0.38	3.4	-9.7	-25.3	28.7	35.5	0.1	DST
12ZL-212	47	97.0	0.20	7.7	-7.7	-24.1	31.8	32.0	0.1	DST
12ZL-213	46	75.0	0.46	4.3	-9.8	-24.5	28.8	34.1	0.0	DST
12ZL-213	46	75.0	0.46	4.4	-8.3	-24.5	28.8	34.1	0.0	DST
12ZL-213	46	75.0	0.46	4.3	-9.8	-24.5	28.8	34.1	0.0	DST
12ZL-213.5	45.5	84.9	0.51	5.5	-9.7	-24.0	29.5	53.8	0.0	DST
12ZL-213.5	45.5	84.9	0.51	5.8	-8.6	-24.0	29.8	53.8	0.0	DST
12ZL-213.5	45.5	84.9	0.51	5.5	-9.7	-24.0	29.5	53.8	0.0	DST
12ZL-220	39	56.5	0.22	0.4	-7.2	-27.5	27.9	42.2	0.1	DST
12ZL-222	37	15.6	0.40			-28.5			0.0	DST
12ZL-224	35	3.5	0.02	1.5	-4.3	-28.3	29.8		0.0	DST
12ZL-226	33	21.0	0.15	0.8	-3.9	-28.2	29.0	21.7	0.1	DST
12ZL-228	31	2.9	0.20	-4.0	-10.7	-27.4	23.4	36.2	0.8	DST
12ZL-243	16	8.3	0.00			-30.0			0.0	DST
12ZL-244	15	4.9	0.00	-6.3	-12.1	-30.2	23.9	32.7	0.3	DST
12ZL-245	14	5.5	0.00			-30.9			0.0	DST

12ZL-246	13	7.3	0.23			-26.6		19.6	5.9	DST
12ZL-247	12	3.2	0.31			-29.0		0.0	1.8	DST
12ZL-248	11	3.0	0.48			-30.8		1.4	5.1	DST
12ZL-254	5	5.4	0.55	-5.0	-13.0	-32.4	27.5	-20.4	3.6	DST
12ZL-254	5	5.4	0.33	-5.0	-13.0	-32.3	27.3	-17.5	2.7	DST
12ZL-254	5	5.4	0.33	-5.0	-13.0	-32.3	27.3	-20.4	3.6	DST
12ZL-254	5	5.4	0.33	-5.0	-13.0	-32.3	27.3	-17.5	2.7	DST
12ZL-254	5	5.4	0.33	-5.0	-13.0	-32.3	27.3	-15.0	3.9	DST
12ZL-254.5	4.5	51.9	0.10	-3.5	-7.1	-27.5	24.0	11.3	0.5	DST
12ZL-255.1	3.9	28.5	0.16	-4.1	-9.5	-27.6	23.5	21.7	3.2	DST
12ZL-255.1-2	3.9	28.5	0.16	-4.1	-9.5	-26.8	22.7	21.7	3.2	DST
12ZL-255.7	3.3	77.4	0.08	-4.4	-11.1	-31.1	26.8	24.1	0.2	DST
12ZL-256.7	2.3	89.5	0.06	-4.4	-9.2	-27.9	23.5	32.1	0.3	DST

Table B.2 Carbonate C and O isotope data of normal marine carbonates in Doushantuo Formation at Zhongling section.

sample	Height	$\delta^{13}C_{carb}$	$\delta^{18}O_{carb}$
12ZL+35	294	-1.3	-4.8
12ZL+34	293	3.3	-3.8
12ZL+33	292	4.0	-4.2
12ZL+30	289	1.6	-4.1
12ZL+0.2	259.2	-1.0	-4.9
12ZL+0.1	259.1	2.1	-6.5
12ZL-1.4	257.6	0.5	-4.5
12ZL-2.7	256.3	1.6	-6.6
12ZL-3.4	255.6	2.9	-6.8
14ZL-3.5f	255.5	1.1	-8.5
12ZL-4.5-3	254.5	3.1	-8.0
12ZL-5	254	2.7	-6.8
14ZL-6.5g	252.5	3.6	-7.0
14ZL-6.5h	252.5	2.9	-7.2
14ZL-6.6d	252.4	0.2	-5.0
12ZL-6.7	252.3	1.3	-6.9
14ZL-7.5f	251.5	3.7	-4.5
12ZL-8.5	250.5	2.1	-4.0
12ZL-9	250	2.8	-3.4
12ZL-10	249	2.8	-3.6
12ZL-10.3	248.7	2.4	-4.2
12ZL-13	246	2.9	-3.1
12ZL-13.8	245.2	3.1	-2.4
12ZL-16.8	242.2	4.8	-5.0
12ZL-17.2	241.8	4.7	-5.2
14ZL-19b	240	6.0	-6.7
14ZL-19.5b	239.5	5.6	-6.7
14ZL-19.5c	239.5	5.8	-6.8
14ZL-20c	239	6.7	-7.1
14ZL-20d	239	6.6	-6.7
12ZL-21.6	237.4	0.0	-5.3
12ZL-21.6-1	237.4	-1.7	-5.8
12ZL-21.6-3	237.4	-1.9	-5.2
12ZL-21.6-4	237.4	-1.6	-6.1
12ZL-21.6-5	237.4	-1.3	-5.8
12ZL-21.6-8	237.4	-1.5	-5.2
12ZL-21.6-9	237.4	-0.1	-4.8
12ZL-22	237	0.7	-4.1
12ZL-24	235	1.1	-5.0
12ZL-25	234	2.1	-3.4
12ZL-26.5	232.5	0.9	-5.1
12ZL-27.5	231.5	2.4	-4.8
12ZL-28.4	230.6	3.7	-3.9
12ZL-29.4	229.6	4.1	-2.8
12ZL-31	228	3.7	-5.5
12ZL-31.5	227.5	3.6	-2.3
12ZL-33	226	3.4	-2.8
12ZL-34	225	3.9	-1.9
12ZL-36.5	222.5	3.1	-2.7
12ZL-38	221	2.7	-1.8

12ZL-40.9	218.1	-0.5	-2.0
12ZL-47.5	211.5	-1.1	-3.5
12ZL-48	211	-0.2	-3.1
12ZL-49	210	0.4	-6.0
14ZL-49f	210	0.9	-6.1
14ZL-49-2b	210	1.0	-5.8
14ZL-49-2d	210	1.2	-5.6
14ZL-49.8d	209.2	7.7	-4.7
14ZL-49.8f	209.2	7.8	-4.4
14ZL-49.8	209.2	6.6	-4.9
14ZL-53.5b	205.5	6.1	-5.9
12ZL-54	205	6.3	-6.0
14ZL-54d	205	6.0	-5.7
14ZL-54.3f	204.7	5.8	-5.4
12ZL-55	204	6.4	-5.6
14ZL-55-2d	204	5.8	-5.4
14ZL-55g	204	5.2	-5.5
12ZL-66	193	2.8	-6.4
12ZL-67.7	191.3	3.0	-3.8
12ZL-69	190	3.0	-3.7
12ZL-70	189	5.2	-1.3
12ZL-73	186	5.3	-1.9
12ZL-74	185	5.0	-2.7
12ZL-75.5	183.5	5.1	-2.2
12ZL-77	182	4.6	-3.5
12ZL-78	181	4.7	-3.3
12ZL-79	180	4.7	-3.6
12ZL-80.2	178.8	3.8	-3.7
12ZL-81.5	177.5	4.8	-4.1
12ZL-82.8	176.2	3.4	-6.4
12ZL-82.9	176.1	4.4	-4.9
12ZL-83.5	175.5	4.0	-6.3
12ZL-84.5	174.5	4.9	-5.5
12ZL-85.5	173.5	4.1	-7.0
12ZL-86.5	172.5	4.3	-5.2
12ZL-87.5	171.5	4.7	-5.3
12ZL-88.5	170.5	4.8	-6.1
12ZL-89.5	169.5	4.0	-6.5
12ZL-90.5	168.5	4.8	-5.8
12ZL-92	167	4.0	-4.4
12ZL-92.5	166.5	4.1	-4.6
12ZL-93.5	165.5	4.2	-6.5
12ZL-94	165	4.1	-6.3
12ZL-95.5	163.5	4.3	-6.3
12ZL-96.5	162.5	3.8	-6.3
12ZL-97.5	161.5	4.4	-6.3
12ZL-99	160	4.9	-4.8
12ZL-100	159	4.0	-6.3
12ZL-101	158	0.2	-4.3
12ZL-102	157	4.3	-4.2
12ZL-104	155	4.6	-6.6
12ZL-105	154	5.1	-5.0
12ZL-106	153	4.8	-4.6
12ZL-107	152	5.5	-5.0
12ZL-108.5	150.5	5.3	-4.3
12ZL-109.5	149.5	1.7	-7.0
12ZL-110.2	148.8	4.7	-6.7
12ZL-110.8	148.2	4.4	-7.0
12ZL-112.2	146.8	5.4	-6.6
12ZL-114	145	5.6	-6.9
12ZL-114	145	5.7	-7.0
12ZL-115	144	5.7	-6.6
12ZL-115	144	5.7	-6.2
12ZL-117	142	5.8	-6.7
12ZL-117	142	5.7	-6.6
12ZL-118	141	5.7	-6.1
12ZL-118	141	5.7	-5.7
12ZL-119	140	5.7	-6.1
12ZL-119	140	5.7	-5.8
12ZL-120	139	6.0	-6.0
12ZL-120	139	6.0	-5.9
12ZL-121	138	6.0	-6.8
12ZL-122	137	5.9	-6.9
12ZL-123	136	5.7	-7.0
12ZL-125	134	5.9	-6.5
12ZL-133	126	5.9	-6.8
12ZL-134.5	124.5	6.2	-6.8
12ZL-134.5	124.5	6.1	-7.4
12ZL-136	123	6.6	-6.5
12ZL-137	122	6.5	-6.8
12ZL-139	120	6.3	-7.2
12ZL-141	118	6.6	-6.7
12ZL-142	117	6.4	-7.1
12ZL-143.5	115.5	6.4	-7.0
12ZL-145.5	113.5	6.2	-7.2
12ZL-147	112	6.1	-7.3
12ZL-149	110	6.3	-7.2
12ZL-151	108	6.1	-7.6
12ZL-153	106	6.4	-6.5
12ZL-155.5	103.5	5.8	-6.7
12ZL-157	102	6.3	-6.8
12ZL-159	100	6.1	-5.9
12ZL-164	95	7.7	-8.0
12ZL-166	93	8.0	-8.2
12ZL-168	91	7.5	-8.0
12ZL-170	89	6.4	-8.0
12ZL-172	87	1.3	-7.4
12ZL-172	87	1.5	-7.7
12ZL-175	84	5.8	-8.5
12ZL-177	82	5.2	-8.0
12ZL-179	80	5.7	-8.6
12ZL-181	78	5.9	-8.4
12ZL-183	76	5.1	-8.1
12ZL-184.5	74.5	4.2	-7.4
12ZL-192	67	6.0	-8.3
12ZL-193	66	6.0	-8.8
12ZL-194	65	5.8	-8.5
12ZL-199	60	5.6	-4.8
12ZL-202	57	5.5	-8.7
12ZL-203	56	5.7	-8.7
12ZL-204	55	6.1	-8.7
12ZL-206	53	5.1	-9.2
12ZL-206	53	6.3	-8.8
12ZL-210	49	5.9	-9.5

12ZL-212	47	7.7	-7.7
12ZL-213	46	4.4	-8.3
12ZL-213.5	45.5	5.8	-8.6
12ZL-220	39	0.4	-7.2
12ZL-224	35	1.5	-4.3
12ZL-226	33	0.8	-3.9
12ZL-228	31	-4.0	-10.7
12ZL-244	15	-6.3	-12.1
12ZL-254	5	-5.0	-13.0
12ZL-254.5	4.5	-3.5	-7.1
12ZL-255.1	3.9	-4.1	-9.5
12ZL-255.7	3.3	-4.4	-11.1
12ZL-256.7	2.3	-4.4	-9.2

Table B.3 Carbonate C and O isotope data of normal marine carbonates mixed with authigenic carbonates in Doushantuo Formation at Zhongling section.

sample	Height	$\delta^{13}C_{carb}$	$\delta^{18}O_{carb}$
12ZL-0.2	258.8	-0.6	-5.9
12ZL-0.5	258.5	-1.0	-6.3
12ZL-0.9	258.1	-9.3	-7.8
12ZL-0.9-3	258.1	-16.5	-5.9
12ZL-0.9-4	258.1	-12.1	-7.4
12ZL-0.9-5	258.1	-10.2	-7.8
12ZL-0.9-7	258.1	-11.7	-8.1
12ZL-0.9	258.1	-5.0	-6.9
12ZL-0.9-1	258.1	-1.9	-4.5
12ZL-0.9-2	258.1	-1.1	-4.7
12ZL-0.9-6	258.1	-1.5	-5.7
12ZL-0.9	258.1	-1.0	-4.2
12ZL-2.0	257	-0.6	-5.5
12ZL-2.5	256.5	-1.5	-5.2
14ZL-3.5e	255.5	-9.4	-8.8
12ZL-4.0	255	-6.6	-7.6
12ZL-4.5-4	254.5	2.7	-7.2
12ZL-4.5-5	254.5	1.9	-7.9
14ZL-6.6g	252.4	-1.6	-4.5
12ZL-7.0	252	-2.5	-4.8
14ZL-7.5a	251.5	-3.4	-5.3
12ZL-7.8	251.2	-0.2	-5.7
12ZL-16	243	0.7	-7.9
12ZL-18.5	240.5	-4.5	-7.8
12ZL-19	240	-6.2	-8.5
14ZL-19c	240	-4.3	-8.0
14ZL-19-2d	240	5.5	-6.6
12ZL-19	240	2.4	-7.3
12ZL-19	240	3.0	-8.0
14ZL-20b	239	-4.7	-7.9
12ZL-20	239	3.7	-6.7
12ZL-21	238	-3.6	-7.3
12ZL-21.5	237.5	-0.6	-6.2
12ZL-21.6-2	237.4	-6.1	-6.1
12ZL-21.6-6	237.4	-7.2	-7.4
12ZL-21.6-7	237.4	-3.8	-5.4
12ZL-23	236	-2.2	-7.3
12ZL-25.8	233.2	-0.8	-7.3
12ZL-40	219	-4.2	-4.0
12ZL-41	218	-3.0	-3.4
12ZL-41.3	217.7	-1.6	-2.1
12ZL-43	216	-3.6	-3.7
12ZL-46	213	-5.3	-4.3
14ZL-49d	210	-9.1	-7.4
14ZL-49e	210	-8.8	-7.3
14ZL-49.2c	209.8	-13.1	-8.0
12ZL-49.8	209.2	-8.4	-7.2
12ZL-49.8-3	209.2	-8.4	-7.5
12ZL-49.8-6	209.2	-8.8	-7.3
12ZL-49.8-8	209.2	-10.5	-7.4
14ZL-49.8e	209.2	-18.9	-9.0
14ZL-49.8b	209.2	-0.5	-6.3
12ZL-49.8-1	209.2	2.8	-5.3
12ZL-49.8-2	209.2	1.9	-6.3
12ZL-49.8-4	209.2	2.7	-5.8
12ZL-49.8-5	209.2	2.7	-5.7
12ZL-49.8-7	209.2	2.6	-5.7
12ZL-49.8-9	209.2	2.8	-5.3
14ZL-49.8a	209.2	6.6	-4.9
14ZL-54.3e	204.7	-14.4	-7.5
14ZL-54.3g	204.7	-12.7	-7.2

Table B.4 Carbonate C and O isotope data of authigenic calcite nodules or cements.

sample	Height	$\delta^{13}C_{carb}$	$\delta^{18}O_{carb}$
14ZL-3.5b	255.5	-13.5	-8.9
14ZL-3.5d	255.5	-10.3	-8.7
14ZL-3.5c	255.5	-10.5	-8.7
14ZL-3.5a	255.5	-10.5	-8.7
14ZL-3.5	255.5	-9.4	-8.8
12ZL-4.5	254.5	-20.0	-8.6
12ZL-4.5-1	254.5	-25.2	-8.2
12ZL-4.5-2	254.5	-19.5	-7.8
14ZL-4.5d	254.5	-13.3	-8.5
14ZL-4.5a	254.5	-9.7	-8.7
14ZL-4.5c	254.5	-10.9	-8.5
14ZL-4.5b	254.5	-10.9	-8.5
14ZL-4.5e	254.5	-10.0	-8.5
14ZL-6.5a	252.5	-7.3	-8.6
14ZL-6.5b	252.5	-13.5	-8.9
14ZL-6.5c	252.5	-14.6	-9.1
14ZL-6.5e	252.5	-8.8	-8.8
14ZL-6.5d	252.5	-13.6	-8.8
14ZL-6.5f	252.5	-8.0	-8.5
14ZL-6.6e	252.4	-12.8	-8.6
14ZL-6.6b	252.4	-14.6	-8.7
14ZL-6.6a	252.4	-15.7	-8.6
14ZL-6.6c	252.4	-17.4	-8.4
14ZL-6.6f	252.4	-13.7	-8.5
14ZL-7.5e	251.5	-26.0	-8.7
14ZL-7.5c	251.5	-16.2	-8.5
14ZL-7.5b	251.5	-15.6	-8.8
14ZL-7.5d	251.5	-23.7	-9.0
12ZL-19	240	-19.9	-11.0
14ZL-19-2a	240	-23.4	-10.0
14ZL-19-2c	240	-22.6	-10.0
14ZL-19-2e	240	-21.5	-10.0
14ZL-20a	239	-21.8	-9.7
12ZL-21.6	237.4	-30.0	-9.3
12ZL-21.6-A	237.4	-30.7	-9.4
12ZL-21.6-B	237.4	-15.8	-8.9
12ZL-21.6-C	237.4	-29.0	-9.2
12ZL-21.6-D	237.4	-30.9	-9.0
12ZL-21.6-E	237.4	-31.6	-8.6
12ZL-21.6-F	237.4	-31.0	-8.3
12ZL-21.6-G	237.4	-27.8	-9.0
12ZL-21.6-H	237.4	-29.3	-8.9
12ZL-21.6-I	237.4	-31.6	-8.7
14ZL-49a	210	-22.3	-9.3
14ZL-49b	210	-6.0	-9.4
14ZL-49c	210	-24.5	-9.4
14ZL-49-2a	210	-26.3	-9.3
14ZL-49-2c	210	-25.7	-9.6
14ZL-49.2a	209.8	-13.0	-9.4
14ZL-49.2b	209.8	-25.4	-9.5
12ZL-49.8	209.2	-34.1	-9.8
12ZL-49.8	209.2	-33.1	-9.6
14ZL-49.8g	209.2	-22.9	-9.0
14ZL-49.8c	209.2	-24.0	-9.1
14ZL-54a	205	-34.0	-9.1
14ZL-54b	205	-35.9	-9.1
14ZL-54c	205	-37.2	-9.1
14ZL-54e	205	-34.3	-9.1
14ZL-54	205	-36.4	-8.8
14ZL-54.3b	204.7	-31.5	-9.0
14ZL-54.3c	204.7	-31.9	-9.3
14ZL-54.3d	204.7	-7.1	-9.8
14ZL-55-2a	204	-35.6	-9.0
14ZL-55-2b	204	-32.0	-8.8
14ZL-55-2c	204	-35.4	-9.1
14ZL-55d	204	-26.8	-9.7
14ZL-55e	204	-29.1	-9.2
14ZL-55f	204	-20.3	-9.6

Table B.5 Carbonate C and O isotope data of late calcite veins.

sample	height	$\delta^{13}C_{carb}$	$\delta^{18}O_{carb}$
14ZL-19.5a	239.5	-4.2	-10.8
14ZL-53.5a	205.5	-1.3	-8.3
14ZL-54.3a	204.7	-1.3	-9.5
14ZL-19a	240	-2.1	-10.9
14ZL-19-2b	240	-5.2	-12.0
14ZL-55a	204	-1.7	-10.6
14ZL-55b	204	-1.5	-10.6
14ZL-55c	204	-2.1	-11.2
12ZL-120white	139	6.2	-8.3
12ZL-118white	141	6.1	-7.9
12ZL-67.7white	191.3	1.3	-9.0

Appendix C

Table C.1: U-Pb geochronologic analyses of two detrital zircon samples: sample 09G-35.3 at 16.7 m above the base of the Gaojiashan Member, and sample 09G-37.9 at 14.1 m above the base of the Gaojiashan Member.

				Isotope ratios							Apparent ages (Ma)								
Analysis	**U conc**	**206Pb**	**U**	**206Pb***	**±**	**207Pb***	**±**	**206Pb***	**±**	**error**	**206Pb***	**±**	**207Pb***	**±**	**206Pb***	**±**	**Best age**	**±**	**Concor**
	(ppm)	**204Pb**	**Th**	**207Pb***	**(%)**	**235U**	**(%)**	**238U**	**(%)**	**corr.**	**238U**	**(Ma)**	**235U**	**(Ma)**	**207Pb***	**(Ma)**	**(Ma)**	**(Ma)**	**(%)**
Sample 09G-35.3																			
09G_35.3-35	187	74028	1.3	15.5025	2.2	1.0704	3.5	0.1203	2.7	0.78	733	19	739	18	758	47	733	19	96.6
09G_35.3-32	144	59902	1.1	15.3032	1.3	1.1439	2.2	0.1270	1.8	0.81	771	13	774	12	785	28	771	13	98.1
09G_35.3-42	92	60665	1.0	15.3821	2.8	1.1391	3.6	0.1271	2.2	0.62	771	16	772	19	775	59	771	16	99.5
09G_35.3-25	51	19703	1.0	15.1667	4.6	1.1567	4.9	0.1272	1.7	0.35	772	12	780	27	804	96	772	12	96.0
09G_35.3-36	125	31363	1.0	15.4463	3.9	1.1440	5.0	0.1282	3.1	0.62	777	23	774	27	766	82	777	23	101.5
09G_35.3-34	171	257584	1.0	15.2477	1.9	1.1600	2.3	0.1283	1.3	0.57	778	10	782	13	793	40	778	10	98.1
09G_35.3-18	131	42412	1.1	15.2501	3.7	1.1604	3.9	0.1283	1.3	0.34	778	10	782	21	793	77	778	10	98.2
09G_35.3-22	48	13274	1.6	15.4505	4.7	1.1523	5.1	0.1291	2.0	0.39	783	15	778	28	765	100	783	15	102.3
09G_35.3-12	128	68600	0.9	15.6173	4.5	1.1419	4.6	0.1293	1.0	0.21	784	7	773	25	743	95	784	7	105.6
09G_35.3-16	79	24639	1.2	15.3244	4.4	1.1683	4.8	0.1299	1.9	0.40	787	14	786	26	783	92	787	14	100.6
09G_35.3-43	77	25745	1.1	15.2255	3.5	1.1798	3.7	0.1303	1.2	0.31	789	9	791	20	796	74	789	9	99.2
09G_35.3-10	177	69222	1.1	15.3673	2.9	1.1833	3.3	0.1319	1.6	0.48	799	12	793	18	777	62	799	12	102.8
09G_35.3-9	85	22382	1.3	15.3476	3.6	1.1917	3.9	0.1327	1.5	0.38	803	11	797	21	779	75	803	11	103.0
09G_35.3-44	118	56773	1.2	15.2220	2.6	1.2063	4.0	0.1332	3.1	0.77	806	23	803	22	797	54	806	23	101.2
09G_35.3-30	515	119229	1.3	15.0130	0.8	1.2388	1.8	0.1349	1.6	0.90	816	12	818	10	826	16	816	12	98.8
09G_35.3-26	137	61036	1.1	14.8602	4.7	1.2811	4.8	0.1381	0.8	0.17	834	6	837	27	847	98	834	6	98.4
09G_35.3-6	418	51343	1.4	14.8177	0.8	1.2864	1.4	0.1382	1.2	0.81	835	9	840	8	853	18	835	9	97.9
09G_35.3-2	102	67734	0.7	14.6056	4.1	1.3153	4.8	0.1393	2.4	0.50	841	19	852	28	883	86	841	19	95.3
09G_35.3-8	109	35580	1.4	14.5821	3.1	1.3200	3.4	0.1396	1.5	0.44	842	12	855	20	886	63	842	12	95.1
09G_35.3-28	170	52415	1.7	15.1371	2.4	1.2799	2.5	0.1405	0.9	0.36	848	7	837	14	808	49	848	7	104.8
09G_35.3-37	262	284971	0.6	14.7084	1.4	1.3275	1.9	0.1416	1.3	0.66	854	10	858	11	868	30	854	10	98.3
09G_35.3-19	115	60890	0.9	15.2002	4.3	1.2992	4.8	0.1432	2.0	0.41	863	16	845	27	800	91	863	16	107.9
09G_35.3-29	86	36224	1.3	14.2682	4.1	1.3841	4.2	0.1432	0.8	0.19	863	6	882	25	931	85	863	6	92.7
09G_35.3-13	158	80526	1.7	15.0542	2.2	1.3230	2.4	0.1444	1.0	0.42	870	8	856	14	820	46	870	8	106.1
09G_35.3-11	63	56839	2.1	8.0293	0.9	6.4943	1.3	0.3782	0.9	0.71	2068	16	2045	11	2022	16	2022	16	102.3
09G_35.3-23	59	73444	1.3	6.3439	1.0	10.0847	1.4	0.4640	1.0	0.71	2457	21	2443	13	2430	17	2430	17	101.1
09G_35.3-SL1	507	99303	4.7	16.8564	1.2	0.7666	2.4	0.0937	2.1	0.87	577	11	578	10	579	26	577	11	99.7
09G_35.3-SL2	519	108448	3.5	16.8648	0.9	0.7667	1.3	0.0938	1.0	0.75	578	5	578	6	578	19	578	5	100.0
09G_35.3-SL3	374	47653	7.2	17.3053	0.8	0.7015	3.0	0.0880	2.9	0.96	544	15	540	12	522	17	544	15	104.3
09G_35.3-SL4	567	126544	4.6	17.2833	1.3	0.7017	1.8	0.0880	1.3	0.69	543	7	540	8	524	29	543	7	103.6
09G_35.3-SL5	504	174202	4.8	16.7913	0.8	0.7457	2.4	0.0908	2.2	0.94	560	12	566	10	587	17	560	12	95.4
09G_35.3-SL6	526	167629	3.7	16.6846	1.7	0.7770	2.2	0.0940	1.4	0.62	579	8	584	10	601	37	579	8	96.3
09G_35.3-SL7	503	183314	3.7	16.9211	1.0	0.7800	1.4	0.0957	1.0	0.70	589	6	585	6	571	22	589	6	103.3

09G_35.3-SL8	567	114796	4.6	17.2393	1.8	0.6866	1.9	0.0858	0.6	0.31	531	3	531	8	530	40	531	3	100.2
09G_35.3-SL9	522	79614	3.7	16.9611	0.8	0.7567	1.5	0.0931	1.2	0.82	574	7	572	6	566	18	574	7	101.5
09G_35.3-SL10	521	224839	3.9	16.9502	1.2	0.7460	1.6	0.0917	1.0	0.64	566	5	566	7	567	27	566	5	99.8
09G_35.3-SL11	567	90518	4.9	17.0072	1.1	0.7229	1.5	0.0892	1.0	0.65	551	5	552	6	560	25	551	5	98.4
09G_35.3-SL12	512	222464	4.7	16.8788	0.8	0.7783	1.7	0.0953	1.4	0.86	587	8	585	7	576	18	587	8	101.8
09G_35.3-SL13	536	95916	3.6	16.8217	1.4	0.7531	2.0	0.0919	1.4	0.73	567	8	570	9	583	29	567	8	97.1
09G_35.3-SL14	507	93729	4.6	17.2111	0.7	0.7164	1.2	0.0894	0.9	0.79	552	5	549	5	534	16	552	5	103.5
09G_35.3-SL15	556	235036	5.0	16.9758	1.7	0.7349	1.9	0.0905	0.8	0.41	558	4	559	8	564	38	558	4	99.1
09G_35.3-SL16	513	175300	4.8	16.7703	1.2	0.7738	1.4	0.0941	0.8	0.56	580	5	582	6	590	26	580	5	98.3
09G_35.3-SL17	538	154639	3.6	16.9006	0.7	0.7717	2.7	0.0946	2.6	0.97	583	14	581	12	573	15	583	14	101.6
09G_35.3-SL18	437	127509	7.7	17.0409	1.6	0.7333	1.9	0.0906	1.1	0.55	559	6	558	8	555	35	559	6	100.7
09G_35.3-SL19	566	141406	4.8	17.1792	1.0	0.7037	1.3	0.0877	0.7	0.58	542	4	541	5	538	23	542	4	100.8
Sample 09G-37.9																			
09G_37.9-51	317	11411	1.4	16.7472	2.9	0.6586	3.0	0.0800	0.8	0.25	496	4	514	12	593	63	496	4	83.6
09G_37.9-92	360	21113	1.1	17.0373	2.1	0.7111	2.7	0.0879	1.8	0.66	543	9	545	12	556	45	543	9	97.7
09G_37.9-77	122	41578	2.0	17.1322	4.7	0.7145	5.0	0.0888	1.7	0.33	548	9	547	21	544	104	548	9	100.9
09G_37.9-59	221	81615	1.7	17.0194	1.4	0.7193	2.1	0.0888	1.6	0.75	548	8	550	9	558	30	548	8	98.3
09G_37.9-85	284	39767	1.7	17.1268	1.5	0.7167	1.8	0.0890	0.9	0.50	550	5	549	7	544	33	550	5	101.0
09G_37.9-158	260	63375	2.2	16.9812	1.9	0.7316	2.2	0.0901	0.9	0.43	556	5	557	9	563	42	556	5	98.8
09G_37.9-96	130	15711	1.9	16.9291	4.9	0.7362	5.2	0.0904	1.8	0.34	558	9	560	22	570	107	558	9	97.9
09G_37.9-167	332	62910	2.5	16.9315	1.9	0.7379	2.0	0.0906	0.8	0.38	559	4	561	9	569	41	559	4	98.2
09G_37.9-125	291	49358	1.7	17.0983	1.6	0.7314	2.2	0.0907	1.5	0.69	560	8	557	10	548	35	560	8	102.1
09G_37.9-144	271	52161	1.9	17.2058	2.0	0.7325	2.5	0.0914	1.5	0.60	564	8	558	11	534	43	564	8	105.5
09G_37.9-131	243	58363	1.8	17.1555	2.6	0.7445	3.3	0.0926	2.0	0.62	571	11	565	14	541	57	571	11	105.6
09G_37.9-94	196	12928	1.6	15.3507	1.8	1.0880	3.5	0.1211	3.0	0.85	737	21	748	19	779	39	737	21	94.6
09G_37.9-29	124	25676	1.1	15.7387	2.9	1.0683	3.5	0.1219	2.1	0.58	742	14	738	19	726	61	742	14	102.1
09G_37.9-17	53	9991	1.1	15.3722	4.6	1.0998	4.9	0.1226	1.6	0.34	746	12	753	26	776	96	746	12	96.1
09G_37.9-93	124	45553	1.4	15.5012	3.3	1.0920	3.5	0.1228	1.3	0.36	747	9	749	19	758	69	747	9	98.4
09G_37.9-58	107	15638	1.5	15.5722	2.8	1.0880	2.9	0.1229	1.0	0.33	747	7	748	16	749	59	747	7	99.8
09G_37.9-82	64	13969	1.7	15.2325	4.8	1.1188	5.3	0.1236	2.2	0.42	751	16	762	29	795	101	751	16	94.5
09G_37.9-60	155	27912	0.7	15.4332	2.1	1.1110	2.3	0.1244	0.9	0.39	756	6	759	12	768	44	756	6	98.4
09G_37.9-70	87	32639	1.5	15.4545	3.9	1.1156	4.3	0.1250	1.7	0.40	760	12	761	23	765	83	760	12	99.3
09G_37.9-111	112	30007	1.3	15.7626	4.0	1.0940	4.4	0.1251	1.8	0.40	760	13	750	23	723	86	760	13	105.1
09G_37.9-120	119	80052	0.9	15.5939	3.2	1.1074	3.4	0.1252	1.2	0.36	761	9	757	18	746	67	761	9	102.0
09G_37.9-102	67	26990	1.0	15.5405	4.9	1.1196	5.9	0.1262	3.3	0.57	766	24	763	32	753	103	766	24	101.7
09G_37.9-97	94	52942	0.8	15.1567	4.2	1.1503	4.6	0.1264	1.8	0.40	768	13	777	25	806	88	768	13	95.3
09G_37.9-126	160	139976	1.0	15.7179	4.1	1.1111	4.1	0.1267	0.8	0.18	769	5	759	22	729	86	769	5	105.4
09G_37.9-10	120	53650	1.5	15.6171	2.0	1.1196	2.1	0.1268	0.8	0.37	770	6	763	11	743	42	770	6	103.6
09G_37.9-114	129	37738	0.8	15.3464	3.3	1.1397	3.6	0.1268	1.6	0.44	770	12	772	20	780	69	770	12	98.8
09G_37.9-100	63	15170	0.9	15.3503	5.0	1.1408	5.2	0.1270	1.6	0.31	771	12	773	28	779	104	771	12	98.9
09G_37.9-15	68	16871	1.2	15.4148	3.3	1.1395	4.3	0.1274	2.8	0.64	773	20	772	23	770	70	773	20	100.4
09G_37.9-35	114	31421	1.4	15.2600	2.2	1.1515	3.1	0.1274	2.1	0.68	773	15	778	17	791	47	773	15	97.7
09G_37.9-110	94	45954	0.9	14.9738	3.3	1.1779	3.7	0.1279	1.7	0.44	776	12	790	20	831	70	776	12	93.4
09G_37.9-30	89	52146	0.9	15.4982	3.4	1.1431	3.9	0.1285	1.8	0.47	779	13	774	21	759	72	779	13	102.7
09G_37.9-133	162	66129	0.8	15.5694	2.5	1.1394	2.9	0.1287	1.3	0.46	780	10	772	15	749	54	780	10	104.1
09G_37.9-105	105	30960	1.4	15.3767	2.9	1.1563	3.4	0.1290	1.8	0.52	782	13	780	19	775	62	782	13	100.8
09G_37.9-40	135	31818	1.5	15.4301	2.1	1.1541	2.5	0.1292	1.4	0.56	783	10	779	14	768	43	783	10	101.9
09G_37.9-136	281	44471	0.9	15.5435	1.7	1.1496	2.3	0.1296	1.6	0.70	786	12	777	13	753	35	786	12	104.4

09G_37.9-151	93	21431	0.7	15.5307	3.7	1.1511	4.2	0.1297	2.1	0.49	786	15	778	23	754	78	786	15	104.2
09G_37.9-49	123	14915	1.0	15.3874	3.5	1.1634	4.0	0.1298	1.9	0.48	787	14	784	22	774	74	787	14	101.7
09G_37.9-39	130	41683	1.2	15.3346	2.2	1.1722	2.4	0.1304	0.9	0.37	790	7	788	13	781	47	790	7	101.1
09G_37.9-160	87	34497	1.0	15.2647	4.7	1.1822	4.9	0.1309	1.4	0.28	793	10	792	27	791	98	793	10	100.3
09G_37.9-42	158	60480	1.6	15.1031	3.2	1.1969	3.8	0.1311	2.0	0.53	794	15	799	21	813	67	794	15	97.7
09G_37.9-63	63	24016	1.3	15.3058	2.8	1.1837	3.4	0.1314	1.9	0.56	796	14	793	19	785	59	796	14	101.4
09G_37.9-45	111	46253	1.4	15.4941	3.0	1.1764	3.7	0.1322	2.2	0.60	800	17	790	20	759	62	800	17	105.4
09G_37.9-16	106	56054	1.6	14.7395	3.1	1.2507	3.7	0.1337	1.9	0.52	809	15	824	21	864	65	809	15	93.6
09G_37.9-165	123	37073	0.9	15.0854	3.3	1.2245	4.3	0.1340	2.8	0.65	810	21	812	24	816	68	810	21	99.4
09G_37.9-41	182	56648	2.3	15.1263	1.8	1.2224	2.1	0.1341	1.1	0.50	811	8	811	12	810	38	811	8	100.2
09G_37.9-69	140	49302	0.7	15.3658	4.0	1.2043	4.3	0.1342	1.5	0.36	812	12	803	24	777	84	812	12	104.5
09G_37.9-26	216	71380	1.8	14.9282	1.6	1.2466	2.0	0.1350	1.2	0.60	816	9	822	11	837	33	816	9	97.5
09G_37.9-65	309	124808	1.5	15.1048	1.1	1.2341	1.3	0.1352	0.6	0.48	817	5	816	7	813	23	817	5	100.6
09G_37.9-38	88	27100	2.5	14.9723	4.8	1.2476	5.2	0.1355	2.1	0.39	819	16	822	30	831	101	819	16	98.5
09G_37.9-66	399	167420	0.7	15.1157	1.0	1.2396	1.5	0.1359	1.1	0.74	821	9	819	9	811	22	821	9	101.2
09G_37.9-47	75	23591	0.9	14.9006	4.9	1.2620	5.2	0.1364	1.7	0.32	824	13	829	29	841	102	824	13	98.0
09G_37.9-156	243	51173	1.5	14.9863	1.2	1.2584	1.9	0.1368	1.5	0.79	826	12	827	11	829	24	826	12	99.7
09G_37.9-138	297	95703	0.7	15.1467	1.3	1.2453	2.3	0.1368	1.9	0.83	827	15	821	13	807	26	827	15	102.4
09G_37.9-1	128	38449	1.0	14.8944	4.1	1.2724	4.3	0.1375	1.1	0.25	830	8	833	24	842	86	830	8	98.6
09G_37.9-112	60	21429	1.8	14.8312	4.7	1.2847	5.0	0.1382	1.9	0.38	834	15	839	29	851	97	834	15	98.1
09G_37.9-67	206	112038	2.0	14.9218	1.3	1.2793	1.7	0.1384	1.1	0.64	836	8	837	9	838	27	836	8	99.7
09G_37.9-109	219	97473	1.3	14.7535	1.5	1.2947	2.0	0.1385	1.3	0.67	836	11	843	12	862	31	836	11	97.0
09G_37.9-43	82	48027	2.0	14.7533	3.6	1.2986	3.7	0.1389	1.0	0.27	839	8	845	21	862	74	839	8	97.3
09G_37.9-98	157	68135	1.0	15.1027	2.3	1.2740	2.7	0.1396	1.4	0.53	842	11	834	15	813	47	842	11	103.6
09G_37.9-74	94	45285	1.0	14.8372	3.7	1.3047	4.0	0.1404	1.4	0.34	847	11	848	23	850	78	847	11	99.6
09G_37.9-5	156	63512	1.3	14.9280	2.2	1.3042	2.9	0.1412	1.8	0.64	851	15	848	16	837	46	851	15	101.7
09G_37.9-23	122	27348	1.1	14.7203	2.2	1.3227	5.4	0.1412	4.9	0.91	852	39	856	31	867	45	852	39	98.3
09G_37.9-71	202	50198	1.7	14.7883	1.4	1.3168	2.2	0.1412	1.7	0.77	852	13	853	13	857	29	852	13	99.4
09G_37.9-107	82	35011	1.1	15.1206	2.9	1.2884	3.3	0.1413	1.6	0.49	852	13	841	19	811	61	852	13	105.1
09G_37.9-169	88	90624	0.9	14.2735	3.2	1.3700	3.7	0.1418	1.8	0.49	855	14	876	21	930	66	855	14	91.9
09G_37.9-86	136	76918	1.2	14.9334	2.4	1.3097	2.8	0.1419	1.5	0.51	855	12	850	16	837	51	855	12	102.2
09G_37.9-104	101	47046	1.5	14.8686	3.5	1.3191	3.6	0.1422	0.9	0.25	857	7	854	21	846	72	857	7	101.4
09G_37.9-90	91	21547	2.2	14.8517	2.9	1.3282	3.1	0.1431	1.3	0.41	862	10	858	18	848	59	862	10	101.6
09G_37.9-154	76	21226	1.5	14.6725	4.7	1.3490	4.9	0.1436	1.5	0.30	865	12	867	29	873	97	865	12	99.0
09G_37.9-61	97	31046	2.4	14.5221	3.1	1.3784	3.6	0.1452	1.7	0.48	874	14	880	21	895	65	874	14	97.7
09G_37.9-164	146	67948	1.4	14.4182	2.1	1.4226	2.9	0.1488	2.0	0.69	894	17	898	17	909	43	894	17	98.3
09G_37.9-163	95	13737	2.2	14.7315	2.9	1.4207	3.4	0.1518	1.8	0.52	911	15	898	20	865	60	911	15	105.3
09G_37.9-56	128	10065	3.0	14.1326	1.6	1.4949	2.6	0.1532	2.0	0.77	919	17	928	16	950	33	919	17	96.7
09G_37.9-116	93	106525	1.4	14.6757	2.9	1.4422	3.2	0.1535	1.4	0.43	921	12	907	19	873	60	921	12	105.5
09G_37.9-145	42	53998	1.7	11.2259	4.2	2.9640	4.4	0.2413	1.3	0.29	1394	16	1398	34	1406	81	1406	81	99.1
09G_37.9-84	53	33397	1.1	9.2590	2.0	4.5760	2.3	0.3073	1.0	0.44	1727	15	1745	19	1766	37	1766	37	97.8
09G_37.9-174	75	72434	2.4	9.1495	1.2	4.9204	1.6	0.3265	1.0	0.63	1821	16	1806	13	1788	22	1788	22	101.9
09G_37.9-88	61	17183	1.5	8.4003	1.8	5.4437	3.2	0.3317	2.7	0.84	1846	43	1892	27	1942	31	1942	31	95.1
09G_37.9-27	51	58019	1.3	8.1509	1.2	6.0552	1.8	0.3580	1.4	0.75	1973	23	1984	16	1996	21	1996	21	98.8
09G_37.9-19	166	206903	1.1	8.1236	0.4	6.3105	1.0	0.3718	0.9	0.90	2038	16	2020	9	2002	8	2002	8	101.8
09G_37.9-50	80	77255	0.6	8.1089	0.7	6.3651	1.3	0.3743	1.1	0.83	2050	19	2027	12	2005	13	2005	13	102.2
09G_37.9-153	39	80844	0.9	8.0949	2.5	6.4973	2.7	0.3815	1.1	0.42	2083	20	2046	24	2008	44	2008	44	103.7
09G_37.9-118	151	130666	0.9	8.0486	0.4	6.2363	1.8	0.3640	1.8	0.98	2001	31	2010	16	2018	7	2018	7	99.2

09G_37.9-139	46	64155	0.7	7.8989	1.3	6.7518	1.8	0.3868	1.2	0.67	2108	21	2079	16	2051	23	2051	23	102.8
09G_37.9-57	36	80659	2.2	6.4474	1.6	9.8462	3.0	0.4604	2.6	0.85	2441	52	2420	28	2403	27	2403	27	101.6
09G_37.9-24	65	131852	0.9	6.3972	1.5	9.1725	2.4	0.4256	1.8	0.76	2286	34	2355	22	2416	26	2416	26	94.6
09G_37.9-46	178	357315	1.3	6.3461	0.6	9.7309	1.3	0.4479	1.1	0.89	2386	23	2410	12	2430	10	2430	10	98.2
09G_37.9-101	36	46485	1.3	6.2833	1.0	10.2767	1.6	0.4683	1.2	0.79	2476	25	2460	14	2447	16	2447	16	101.2
09G_37.9-28	49	53175	2.4	6.0652	0.7	10.9307	1.7	0.4808	1.6	0.92	2531	33	2517	16	2506	11	2506	11	101.0
09G_37.9-80	143	210418	2.0	5.7386	0.6	11.4786	1.2	0.4777	1.1	0.88	2517	22	2563	11	2599	10	2599	10	96.9
09G_37.9-130	125	80288	1.5	5.5423	0.4	11.3348	1.8	0.4556	1.8	0.98	2420	36	2551	17	2657	6	2657	6	91.1
09G_37.9-161	274	267903	1.4	5.4500	0.3	13.5735	1.8	0.5365	1.8	0.99	2769	40	2720	17	2685	5	2685	5	103.1
09G_37.9-SL1	486	208482	4.3	17.0926	1.0	0.7326	2.7	0.0908	2.5	0.93	560	13	558	12	549	22	560	13	102.1
09G_37.9-SL2	523	92804	5.0	16.9406	1.2	0.7498	1.6	0.0921	1.1	0.69	568	6	568	7	568	25	568	6	100.0
09G_37.9-SL3	488	123725	4.3	17.0667	1.1	0.7402	1.6	0.0916	1.2	0.73	565	6	563	7	552	24	565	6	102.4
09G_37.9-SL4	608	212162	4.8	16.8637	1.9	0.7601	2.3	0.0930	1.3	0.55	573	7	574	10	578	42	573	7	99.1
09G_37.9-SL5	545	184249	3.9	16.9137	1.1	0.7579	1.7	0.0930	1.3	0.76	573	7	573	8	572	25	573	7	100.2
09G_37.9-SL6	509	143368	4.9	16.8256	1.2	0.7563	1.7	0.0923	1.3	0.73	569	7	572	8	583	26	569	7	97.6
09G_37.9-SL7	492	91788	4.4	17.1929	1.6	0.7066	2.4	0.0881	1.9	0.76	544	10	543	10	536	35	544	10	101.6
09G_37.9-SL8	538	104433	3.6	17.0327	1.2	0.7319	1.3	0.0904	0.6	0.47	558	3	558	6	556	25	558	3	100.3
09G_37.9-SL9	526	235308	4.9	16.9373	1.2	0.7454	1.5	0.0916	0.9	0.62	565	5	566	6	569	25	565	5	99.3
09G_37.9-SL10	535	172710	3.8	16.8680	0.8	0.7569	1.1	0.0926	0.6	0.60	571	3	572	5	578	18	571	3	98.8
09G_37.9-SL11	505	95917	5.1	17.0147	0.8	0.7507	1.7	0.0926	1.5	0.87	571	8	569	7	559	18	571	8	102.2
09G_37.9-SL12	490	101560	4.5	17.0798	1.4	0.7123	2.5	0.0882	2.0	0.83	545	11	546	10	550	30	545	11	99.0
09G_37.9-SL13	507	181040	4.0	16.8742	1.6	0.7366	1.8	0.0902	0.8	0.43	556	4	560	8	577	35	556	4	96.5
09G_37.9-SL14	539	165769	4.9	17.0907	1.6	0.7479	1.7	0.0927	0.6	0.34	571	3	567	7	549	34	571	3	104.1
09G_37.9-SL15	511	129624	4.1	16.8360	0.8	0.7583	1.8	0.0926	1.6	0.89	571	9	573	8	582	18	571	9	98.1
09G_37.9-SL16	504	79623	5.3	16.9462	1.2	0.7427	1.5	0.0913	1.0	0.64	563	5	564	7	567	25	563	5	99.2
09G_37.9-SL17	471	110455	4.6	17.2658	1.1	0.7199	1.7	0.0902	1.2	0.73	556	6	551	7	527	25	556	6	105.6
09G_37.9-SL18	537	92908	3.8	16.9555	0.5	0.7387	0.8	0.0908	0.6	0.74	561	3	562	3	566	12	561	3	99.0
09G_37.9-SL19	541	210761	5.0	16.8503	1.4	0.7589	1.7	0.0927	0.9	0.54	572	5	573	8	580	31	572	5	98.6
09G_37.9-SL20	540	122874	3.8	16.9974	1.0	0.7449	1.3	0.0918	0.9	0.65	566	5	565	6	561	22	566	5	101.0
09G_37.9-SL21	513	124292	5.2	17.1240	0.8	0.7315	1.5	0.0908	1.3	0.85	561	7	557	7	545	18	561	7	102.9
09G_37.9-SL22	505	195233	5.1	16.9244	1.6	0.7505	1.7	0.0921	0.7	0.39	568	4	569	7	570	34	568	4	99.6
09G_37.9-SL23	501	94912	4.4	17.0121	1.4	0.7406	2.3	0.0914	1.9	0.81	564	10	563	10	559	30	564	10	100.8
09G_37.9-SL24	525	181254	3.7	16.9362	0.9	0.7399	1.3	0.0909	0.9	0.71	561	5	562	6	569	20	561	5	98.6
09G_37.9-SL25	507	128398	4.0	17.0104	1.1	0.7334	2.0	0.0905	1.7	0.85	558	9	559	9	559	23	558	9	99.8
09G_37.9-SL26	591	249429	4.8	16.9668	0.9	0.7496	1.3	0.0922	1.0	0.75	569	5	568	6	565	19	569	5	100.7
09G_37.9-SL27	551	676425	3.6	16.8674	1.1	0.7542	1.2	0.0923	0.5	0.39	569	3	571	5	578	24	569	3	98.5
09G_37.9-SL28	509	209116	5.0	17.0760	1.0	0.7415	1.3	0.0918	0.9	0.65	566	5	563	6	551	22	566	5	102.8
09G_37.9-SL29	450	113021	4.6	17.1945	1.5	0.7148	2.0	0.0891	1.4	0.67	550	7	548	9	536	33	550	7	102.7
09G_37.9-SL30	510	146677	3.8	16.9566	0.8	0.7404	1.4	0.0911	1.2	0.82	562	6	563	6	566	18	562	6	99.2
09G_37.9-SL31	561	130953	4.8	16.8185	1.1	0.7564	1.4	0.0923	0.9	0.64	569	5	572	6	584	23	569	5	97.4
09G_37.9-SL32	477	128689	4.4	16.9765	1.0	0.7417	1.5	0.0913	1.2	0.78	563	6	563	7	564	21	563	6	100.0
09G_37.9-SL33	505	132748	5.0	17.1987	1.3	0.7399	1.4	0.0923	0.6	0.45	569	3	562	6	535	28	569	3	106.3
09G_37.9-SL34	503	158055	4.2	16.8941	1.7	0.7233	2.5	0.0886	1.9	0.75	547	10	553	11	574	36	547	10	95.3
09G_37.9-SL35	543	85084	3.7	16.9115	1.3	0.7447	1.8	0.0913	1.2	0.68	563	7	565	8	572	29	563	7	98.5
09G_37.9-SL36	596	162409	5.0	17.0130	1.1	0.7475	1.5	0.0922	1.0	0.67	569	6	567	7	559	25	569	6	101.8
09G_37.9-SL37	550	127866	3.9	16.9634	1.1	0.7397	1.6	0.0910	1.1	0.71	561	6	562	7	565	25	561	6	99.3
09G_37.9-SL38	554	174607	3.8	17.0836	1.1	0.7364	1.7	0.0912	1.3	0.77	563	7	560	7	550	23	563	7	102.4
09G_37.9-SL39	503	147190	5.0	16.9648	1.4	0.7508	1.6	0.0924	0.7	0.47	570	4	569	7	565	31	570	4	100.8

09G_37.9-SL40	444	98671	4.6	16.9163	2.0	0.7350	2.5	0.0902	1.6	0.62	557	8	560	11	571	43	557	8	97.4
09G_37.9-SL41	533	176522	3.6	16.9119	1.6	0.7490	2.0	0.0919	1.2	0.60	567	6	568	8	572	34	567	6	99.1
09G_37.9-SL42	490	96534	4.3	17.0464	1.3	0.7482	1.6	0.0925	0.9	0.60	570	5	567	7	555	27	570	5	102.8
09G_37.9-SL43	507	117709	5.1	16.9997	1.0	0.7505	1.4	0.0925	0.9	0.67	570	5	569	6	561	22	570	5	101.8
09G_37.9-SL44	497	119877	4.4	16.9570	1.4	0.7214	2.2	0.0887	1.7	0.78	548	9	552	9	566	30	548	9	96.8
09G_37.9-SL45	553	143572	4.9	16.9078	1.5	0.7456	1.6	0.0914	0.6	0.39	564	3	566	7	572	32	564	3	98.5
09G_37.9-SL46	506	197192	4.2	16.9428	1.6	0.7464	1.8	0.0917	0.7	0.37	566	4	566	8	568	36	566	4	99.6
09G_37.9-SL47	507	329227	5.1	16.9883	0.8	0.7450	1.0	0.0918	0.6	0.57	566	3	565	4	562	18	566	3	100.7
09G_37.9-SL48	478	78305	4.4	17.0303	1.4	0.7252	2.0	0.0896	1.4	0.69	553	7	554	8	557	31	553	7	99.3

*=radiogenic lead.

Notes:

1. Analyses with >5% uncertainty (1-sigma) in 206Pb/238U age or >5% uncertainty (1-sigma) in 206Pb/207Pb age are not included.
2. Concordance is 206Pb/238U age / 206Pb/207Pb age.
3. Analysis with >25% discordance (<75% concordance) are not included.
4. Analyses with >8% reverse discordance (>108% concordance) are not included.
5. Analyses were conducted by LA-MC-ICPMS, as described by Martin et al. (2015).
6. Uncertainties for individual analyses are reported at the 1-sigma level, and include only measurement errors.
7. Systematic errors for 206Pb/238U and 206Pb/207Pb ages are about 2% and 1% (2-sigma), respectively.
8. U concentration and U/Th are calibrated relative to Sri Lanka zircon standard, and are accurate to about 20%.
9. Common Pb correction is from measured 204Pb.
10. Common Pb composition interpreted from Stacey and Kramers (1975).
11. Common Pb composition assigned uncertainties of 1.5 for 206Pb/204Pb, 0.3 for 207Pb/204Pb, and 2.0 for 208Pb/204Pb.
12. U/Pb and 206Pb/207Pb fractionation is calibrated relative to fragments of a large Sri Lanka zircon with age 563.5 ± 3.2 Ma (2-sigma).
13. U decay constants and composition as follows: 238U = 9.8485 x 10-10, 235U =1.55125 x 10-10, 238U/235U = 137.88.
14. Best age is 206Pb/207Pb age for zircons older than 1000 Ma and 206Pb/238U age for younger grains.
15. Analyses labeled "SL" are of the Sri Lanka zircon standard.

Additional reference:

Stacey, J., and J. Kramers (1975), Approximation of terrestrial lead isotope evolution by a two-stage model, Earth Planet. Sci. Lett., 26, 207–221.

Table C.2: Time-series carbonate C isotope data of the Doushantuo and Dengying formations plotted in Figure 1 of the main text. Data for the Doushantuo Formation are measured in Jiulongwan section (McFadden et al., 2008). Data for the Dengying Formation are measured from the Gaojiashan section in this study. KCP-Kuanchuanpu Formation, BW- Beiwan Member, GJS-Gaojiashan Member, AD-Algal Dolomite Member, DST - Doushantuo Formation.

sample	Height	$\delta^{13}C$	strata
09B-371.5	794.5	-1.1	BW
09B-369.5	792.5	-0.1	BW
09B-367	790.0	-0.4	BW
09B-364.2	787.2	-0.4	BW
09B-364.2	787.2	-0.1	BW
09B-363.9	786.9	-0.9	BW
09B-362	785.0	0.4	BW
09B-357	780.0	0.5	BW
09B-357	780.0	0.7	BW
09B-352	775.0	2.0	BW
09B-344	767.0	0.6	BW
09B-341	764.0	1.7	BW
09B-336.5	759.5	1.6	BW
09B-332	755.0	1.9	BW
09B-327	750.0	1.7	BW
09B-322	745.0	0.4	BW
09B-317	740.0	1.4	BW
09B-312	735.0	2.1	BW
09B-308	731.0	1.7	BW
09B-307	730.0	1.9	BW
09B-304.5	727.5	2.0	BW
09B-299	722.0	2.0	BW
09B-299	722.0	2.0	BW
09B-295	718.0	2.8	BW
09B-295	718.0	2.7	BW
09B-292.8	715.8	1.4	BW
09B-292.8	715.8	1.3	BW
09B-289.2	712.2	1.9	BW
09B-289.2	712.2	1.7	BW
09B-286	709.0	2.2	BW
09B-286	709.0	2.3	BW
09B-280.5	703.5	2.2	BW
09B-280.5	703.5	2.0	BW
09B-276	699.0	2.0	BW
09B-276	699.0	2.0	BW
09B-269.9	692.9	2.7	BW
09B-269.9	692.9	2.6	BW
09B-267.2	690.2	3.7	BW
09B-267.2	690.2	3.7	BW
09B-264	687.0	4.0	BW
09B-264	687.0	3.9	BW
09B-261.8	684.8	3.0	BW
09B-261.8	684.8	2.9	BW
09B-257	680.0	3.3	BW
09B-257	680.0	3.2	BW
09B-253	676.0	3.4	BW
09B-253	676.0	3.4	BW
09B-250	673.0	3.6	BW
09B-250	673.0	3.5	BW
09B-247	670.0	3.7	BW
09B-247	670.0	3.7	BW
09B-244.3	667.3	3.9	BW
09B-244.3	667.3	3.7	BW
09B-240.5	663.5	3.7	BW
09B-240.5	663.5	3.6	BW
09B-238	661.0	3.5	BW
09B-238	661.0	3.3	BW
09B-234.7	657.7	3.6	BW
09B-234.7	657.7	3.7	BW
09B-231	654.0	3.3	BW
09B-231	654.0	3.3	BW
09B-229.5	652.5	3.8	BW
09B-229.5	652.5	3.7	BW
09B-225.5	648.5	3.9	BW
09B-225.5	648.5	3.8	BW
09B-221	644.0	4.2	BW
09B-221	644.0	4.1	BW
09B-212.7	635.7	3.6	BW
09B-212.7	635.7	3.5	BW
09B-207.5	630.5	3.8	BW
09B-207.5	630.5	3.8	BW
09B-204	627.0	3.6	BW
09B-204	627.0	3.7	BW
09B-198.5	621.5	3.3	BW
09B-198.5	621.5	3.1	BW
09B-195	618.0	3.6	BW
09B-195	618.0	3.6	BW
09B-190.2	613.2	3.9	BW
09B-190.2	613.2	3.7	BW
09B-187.5	610.5	4.0	BW
09B-187.5	610.5	3.9	BW
09B-184	607.0	4.3	BW
09B-184	607.0	4.1	BW
09B-181	604.0	4.2	BW
09B-181	604.0	4.0	BW
09B-178	601.0	4.3	BW
09B-178	601.0	4.1	BW
09B-174.5	597.5	4.1	BW
09B-174.5	597.5	3.9	BW
09B-172	595.0	3.1	BW
09B-172	595.0	3.1	BW
09B-168	591.0	3.9	BW
09B-168	591.0	3.9	BW
09B-162	585.0	3.7	BW
09B-162	585.0	3.8	BW
09B-159	582.0	3.2	BW
09B-159	582.0	3.0	BW
09B-155.1	578.1	3.3	BW
09B-155.1	578.1	3.1	BW
09B-152.5	575.5	3.1	BW
09B-152.5	575.5	2.9	BW
09B-149.5	572.5	3.6	BW
09B-146.5	569.5	3.0	BW
09B-146.5	569.5	2.5	BW
09B-144.8	567.8	3.9	BW
09B-143.2	566.2	3.5	BW
09B-139.7	562.7	3.8	BW
09B-139.7	562.7	3.7	BW
09B-135.7	558.7	3.9	BW
09B-132	555.0	3.2	BW
09B-132	555.0	3.0	BW
09B-129	552.0	3.7	BW
09B-126	549.0	3.2	BW
09B-126	549.0	2.9	BW
09B-123A	546.0	3.4	BW
09B-123B	546.0	3.5	BW
09B-123A	546.0	3.2	BW
09B-119	542.0		BW
09B-117	540.0	3.1	BW
09B-117	540.0	2.8	BW
09B-114	537.0	3.1	BW
09B-113	536.0	4.0	BW
09B-113	536.0	3.9	BW
09B-110.2	533.2	3.2	BW
09B-97	520.0	1.9	BW
09B-97	520.0	1.8	BW
09B-87.9	510.9	2.2	BW
09B-87.9	510.9	2.1	BW
09B-81.4	504.4	1.6	BW
09B-79.5	502.5	2.2	BW
09B-79.5	502.5	2.1	BW
09B-73.6	496.6	2.5	BW
09B-73.6	496.6	2.4	BW
09B-71	494.0	2.0	BW
09B-68.5	491.5	1.8	BW
09B-68.3	491.3	1.9	BW
09B-56.5	479.5	1.5	BW
09B-56.5	479.5	1.4	BW
09B-54.2	477.2	1.5	BW
09B-50.7	473.7	2.0	BW
09B-50.7	473.7	1.7	BW
09B-48	471.0	2.8	BW
09B-48	471.0	2.7	BW
09B-47	470.0	2.1	BW
09B-45	468.0	1.2	BW
09B-45	468.0	1.1	BW
09B-42	465.0	1.2	BW
09B-42	465.0	1.1	BW
09B-39.2	462.2	2.4	BW
09B-39.2	462.2	2.3	BW
09B-36	459.0	1.2	BW
09B-36	459.0	1.2	BW
09B-33	456.0	0.9	BW
09B-30	453.0	2.1	BW
09B-30	453.0	1.9	BW
09B-27.4	450.4	0.9	BW
09B-24.1	447.1	2.2	BW
09B-24.1	447.1	2.3	BW
09B-21.7	444.7	2.1	BW

09B-19	442.0	1.0	BW
09B-19	442.0	0.9	BW
09B-17	440.0	1.8	BW
09B-16.2	439.2	1.7	BW
09B-16.2	439.2	1.7	BW
09B-14	437.0	2.1	BW
09B-12	435.0	1.8	BW
09B-12	435.0	1.8	BW
09B-8.5	431.5	2.5	BW
09B-8.5	431.5	2.2	BW
09B-6.6	429.6	2.3	BW
09B-3.9	426.9	2.4	BW
09B-3.9	426.9	2.2	BW
09G-0.2	419.8	0.9	GJS
09G-0.2	419.8	0.6	GJS
09G-0.2	419.8	0.6	GJS
14G-0.5	419.5	1.3	GJS
14G-1	419.0	1.1	GJS
14G-1.1	418.9	1.5	GJS
09G-1.5	418.5	1.6	GJS
09G-1.5	418.5	1.6	GJS
09G-1.5	418.5	1.5	GJS
14G-1.5	418.5	1.6	GJS
14G-1.6	418.4	1.2	GJS
14G-2	418.0	1.8	GJS
14G-2.5	417.5	2.9	GJS
14G-2.5	417.5	2.4	GJS
14G-3	417.0	3.2	GJS
09G-3.2-4	416.8	3.0	GJS
09G-3.2-2	416.8	3.4	GJS
09G-3.2-1	416.8	3.0	GJS
09G-3.2-1	416.8	3.0	GJS
09G-3.2-1	416.8	3.0	GJS
09G-3.2-2	416.8	3.4	GJS
09G-3.2-2	416.8	3.4	GJS
09G-3.2-4	416.8	3.0	GJS
09G-3.2-4	416.8	3.0	GJS
14G-3.5	416.5	-0.2	GJS
14G-4	416.0	4.2	GJS
14G-4.5	415.5	4.4	GJS
09G-5	415.0	4.2	GJS
09G-5	415.0	4.4	GJS
09G-5	415.0	4.3	GJS
14G-5	415.0	2.6	GJS
14G-5.5	414.5	4.8	GJS
14G-6	414.0	4.6	GJS
14G-6.5	413.5	5.5	GJS
09G-7	413.0	5.1	GJS

09G-7	413.0	5.2	GJS
09G-7	413.0	5.2	GJS
14G-7	413.0	5.8	GJS
14G-7.5	412.5	3.2	GJS
14G-8	412.0	5.4	GJS
14G-8.5	411.5	5.4	GJS
09G-8.9	411.1	5.7	GJS
09G-8.9	411.1	5.7	GJS
09G-8.9	411.1	5.8	GJS
14G-9	411.0	6.0	GJS
14G-9.5	410.5	2.4	GJS
14G-10	410.0	6.0	GJS
09G-11	409.0	6.0	GJS
09G-11	409.0	6.1	GJS
09G-11	409.0	6.0	GJS
14G-11.5	408.5	5.5	GJS
14G-12	408.0	5.2	GJS
14G-12.5	407.5	5.1	GJS
09G-13	407.0	4.7	GJS
09G-13	407.0	4.8	GJS
09G-13	407.0	4.9	GJS
14G-13	407.0	5.9	GJS
14G-13.5	406.5	6.1	GJS
14G-14	406.0	4.6	GJS
09G-14.3	405.7	5.3	GJS
09G-14.3	405.7	5.4	GJS
09G-14.3	405.7	5.3	GJS
14G-14.5	405.5	5.3	GJS
14G-15	405.0	5.3	GJS
09G-15.7	404.3	5.1	GJS
09G-15.7	404.3	5.0	GJS
09G-15.7	404.3	5.2	GJS
14G-16	404.0	4.1	GJS
14G-16.5	403.5	5.8	GJS
14G-17lst	403.0	3.9	GJS
14G-17lami	403.0	3.9	GJS
14G-17.5	402.5	4.1	GJS
14G-18	402.0	5.0	GJS
14G-19	401.0	3.9	GJS
09G-19.2	400.8	1.6	GJS
09G-19.2	400.8	1.6	GJS
09G-19.2	400.8	1.4	GJS
14G-20	400.0	4.5	GJS
14G-20.5	399.5	4.3	GJS
14G-21	399.0	3.1	GJS
14G-21.5	398.5	4.0	GJS
14G-22.5	397.5	3.6	GJS
14G-23	397.0	3.1	GJS

14G-24	396.0	4.3	GJS
14G-24.3	395.7	3.9	GJS
09G-24.4	395.6	3.2	GJS
09G-24.4	395.6	3.2	GJS
09G-24.4	395.6	3.3	GJS
14G-24.5-core	395.5	3.7	GJS
14G-24.5-rim	395.5	3.4	GJS
14G-25	395.0	3.5	GJS
09G-25.7	394.3	1.8	GJS
09G-25.7	394.3	1.8	GJS
09G-25.7	394.3	1.7	GJS
14G-26	394.0	2.0	GJS
14G-26.5	393.5	1.7	GJS
14G-27	393.0	1.6	GJS
09G-28	392.0	2.0	GJS
09G-28	392.0	1.9	GJS
09G-28	392.0	1.9	GJS
09G-29.7	390.3	1.0	GJS
09G-29.7	390.3	0.9	GJS
09G-29.7	390.3	1.0	GJS
14G-30	390.0	0.8	GJS
09G-30.1	389.9	0.4	GJS
09G-30.1	389.9	0.4	GJS
09G-30.1	389.9	0.5	GJS
14G-31	389.0	-2.3	GJS
14G-31.5	388.5	-0.1	GJS
09G-32	388.0	1.0	GJS
09G-32	388.0	1.0	GJS
09G-32	388.0	1.0	GJS
14G-32	388.0	0.6	GJS
14G-33	387.0	0.4	GJS
14G-33.5	386.5	0.0	GJS
14G-34	386.0	1.0	GJS
14G-34.5	385.5	0.0	GJS
09G-35.5	384.5	0.6	GJS
09G-35.5	384.5	0.6	GJS
09G-35.5	384.5	0.7	GJS
14G-35.5	384.5	0.4	GJS
09G-35.6	384.4	-0.4	GJS
09G-35.6	384.4	-0.2	GJS
09G-35.6	384.4	-0.1	GJS
14G-37.5	382.5	1.1	GJS
09G-38	382.0	0.4	GJS
09G-38	382.0	0.3	GJS
09G-38	382.0	0.4	GJS
14G-38	382.0	1.1	GJS
14G-38.5	381.5	1.0	GJS
14G-39	381.0	1.2	GJS

09G-40	380.0	0.5	GJS
09G-40	380.0	0.5	GJS
09G-40	380.0	0.5	GJS
09G-42.5-L	377.5	0.0	GJS
09G-42.5	377.5	0.0	GJS
09G-42.5	377.5	0.1	GJS
09G-42.5	377.5	0.2	GJS
09G-42.5-L	377.5	0.1	GJS
09G-42.5-L	377.5	0.1	GJS
09G-43	377.0	0.2	GJS
14G-43	377.0	0.3	GJS
09G-46	374.0	0.5	GJS
09A-56.3	363.7	0.5	AD
09A-58	362.0	0.6	AD
09A-61.6	358.4	0.6	AD
09A-65.5	354.5	0.7	AD
09A-70	350.0	0.4	AD
09A-74.9	345.1	1.0	AD
09A-79	341.0	0.5	AD
09A-83.6	336.4	0.7	AD
09A-86.5	333.5	1.2	AD
09A-91	329.0	1.7	AD
09A-95.9	324.1	2.5	AD
09A-95.9D	324.1	2.4	AD
09A-100.4	319.6	3.1	AD
09A-105.5	314.5	3.3	AD
09A-110	310.0	3.6	AD
09A-115	305.0	3.4	AD
09A-116.6	303.4	3.6	AD
09A-119	301.0	3.6	AD
09A-122.8	297.2	3.6	AD
09A-124.5	295.5	5.5	AD
09A-128	292.0	5.0	AD
09A-131	289.0	3.8	AD
09A-135	285.0	2.2	AD
09A-140	280.0	2.9	AD
09A-145	275.0	3.4	AD
09A-161	259.0	3.2	AD
09A-162	258.0	3.1	AD
09A-167.2	252.8	3.0	AD
09A-173	247.0	3.2	AD
09A-177.5	242.5	2.3	AD
09A-182.5	237.5	2.1	AD
09A-182.5	237.5	1.7	AD
09A-182.5	237.5	2.0	AD
09A-182.6	237.4	2.5	AD
09A-182.6	237.4	2.4	AD
09A-182.6	237.4	2.5	AD

09A-193	227.0	2.3	AD
09A-193	227.0	2.3	AD
09A-193	227.0	2.3	AD
09A-201.4	218.6	2.2	AD
09A-201.4	218.6	2.2	AD
09A-206	214.0	1.2	AD
09A-206	214.0	1.3	AD
09A-206	214.0	1.2	AD
09A-213.7	206.3	1.1	AD
09A-213.7	206.3	1.2	AD
09A-213.7	206.3	1.2	AD
09A-217	203.0	1.1	AD
09A-217	203.0	1.1	AD
09A-217	203.0	1.0	AD
09A-221.8	198.2	1.3	AD
09A-221.8	198.2	1.4	AD
09A-221.8	198.2	1.4	AD
09A-225	195.0	1.6	AD
09A-225	195.0	1.6	AD
09A-225	195.0	1.6	AD
09A-229	191.0	1.9	AD
09A-229	191.0	1.9	AD
09A-229	191.0	2.0	AD
09A-234	186.0	1.5	AD
09A-234	186.0	1.4	AD
09A-234	186.0	1.5	AD
09A-245	175.0	1.9	AD
09A-245	175.0	2.0	AD
09A-245	175.0	1.9	AD
09A-255	165.0	1.7	AD
09A-255	165.0	1.7	AD
09A-255	165.0	1.7	AD
JLW2-43.0	163.0	1.7	DST
JLW2-39.0	159.0	0.9	DST
JLW2-36.4	156.4	-1.2	DST
JLW2-36.2	156.2	-1.8	DST
JLW2-36.0	156.0	-1.8	DST
JLW2-35.5	155.5	-5.0	DST
JLW2-35.0	155.0	-10.7	DST
JLW2-34.5	154.5	-6.9	DST
JLW2-34.0	154.0	-6.7	DST
JLW2-33.5	153.5	-5.0	DST
JLW2-32.0	152.0	-8.2	DST
JLW2-31.5	151.5	-5.7	DST
JLW2-31.0	151.0	-4.6	DST
JLW-30.5	150.5	-4.6	DST
JLW2-29.0	149.0	-8.2	DST
JLW2-28.2	148.2	-7.2	DST

JLW2-28.1	148.1	-7.6	DST
JLW2-28.0	148.0	-7.6	DST
JLW2-27.4	147.4	-7.8	DST
JLW2-27.3	147.3	-8.2	DST
JLW2-27.2	147.2	-8.4	DST
JLW2-27.1	147.1	-7.9	DST
JLW2-27.0	147.0	-7.0	DST
JLW2-26.3	146.3	-9.0	DST
JLW2-26.2	146.2	-8.7	DST
JLW2-26.1	146.1	-8.9	DST
JLW2-26.0	146.0	-7.0	DST
JLW2-25.3	145.3	-8.2	DST
JLW2-25.3	145.2	-7.1	DST
JLW2-25.1	145.1	-7.9	DST
JLW2-25.0	145.0	-8.3	DST
JLW2-24.2	144.2	-7.6	DST
JLW2-24.1	144.1	-8.2	DST
JLW2-24.0	144.0	-8.3	DST
JLW2-23.0	143.0	-8.3	DST
JLW2-22.0	142.0	-8.4	DST
JLW2-20.4	141.4	-8.3	DST
JLW2-20.3	141.3	-7.5	DST
JLW2-20.2	141.2	-8.3	DST
JLW2-20.1	141.1	-6.5	DST
JLW2-21.0	141.0	-8.5	DST
JLW2-20.0	140.0	-8.4	DST
JLW2-19.0	139.0	-8.6	DST
JLW2-18.0	138.0	-8.6	DST
JLW2-17.0	137.0	-8.6	DST
JLW2-16.0	136.0	-8.5	DST
JLW2-15.0	135.0	-8.6	DST
JLW2-14.0	134.0	-8.7	DST
JLW2-13.0	133.0	-8.9	DST
JLW2-12.0	132.0	-7.9	DST
JLW2-11.0	131.0	-8.8	DST
JLW2-10.0	130.0	-9.0	DST
JLW2-9.0	129.0	-6.7	DST
JLW2-8.0	128.0	-8.7	DST
JLW2-7.0	127.0	-7.4	DST
JLW2-6.4	126.4	-8.6	DST
JLW2-6.0	126.0	-8.8	DST
JLW2-5.0	125.0	-8.3	DST
JLW2-4.0	124.0	-8.1	DST
JLW2-3.0	123.0	-8.1	DST
JLW2-2.0	122.0	-6.4	DST
JLW2-1.0	121.0	-6.0	DST
JLW2-0.0	120.0	-9.0	DST
JLW1-40.0	119.0	-8.9	DST

JLW1-39.0	118.0	-8.9	DST
JLW1-38.0	117.0	-8.2	DST
JLW1-37.0	116.0	-8.6	DST
JLW1-36.0	115.0	-8.2	DST
JLW1-35.5	114.5	-7.6	DST
JLW1-35.0	114.0	-5.0	DST
JLW1-34.0	113.0	-3.0	DST
JLW1-33.0	112.0	-2.9	DST
JLW1-32.5	111.5	-6.5	DST
JLW1-32.0	111.0	-0.8	DST
JLW1-31.5	110.5	-0.7	DST
JLW1-31.0	110.0	-0.4	DST
JLW1-30.5	109.5	-0.4	DST
JLW1-30.0	109.0	0.4	DST
JLW1-29.5	108.5	0.4	DST
JLW1-28.5	107.5	0.7	DST
JLW1-28.0	107.0	0.7	DST
JLW1-27.5	106.5	0.6	DST
JLW1-27.0	106.0	0.1	DST
JLW1-26.0	105.0	1.5	DST
JLW1-25.0	104.0	2.2	DST
JLW1-24.0	103.0	0.8	DST
JLW1-22.5	101.5	0.5	DST
JLW1-22.0	101.0	0.8	DST
JLW1-21.0	100.0	4.0	DST
JLW1-19.5	98.5	3.8	DST
JLW1-18.0	97.0	4.1	DST
JLW1-16.5	95.5	3.6	DST
JLW1-15.0	94.0	3.8	DST
JLW1-13.5	92.5	3.5	DST
JLW1-11.0	90.0	3.2	DST
JLW1-10.0	89.0	-0.1	DST
JLW1-9.0	88.0	-0.1	DST
JLW1-8.5	87.5	0.0	DST
JLW1-8.0	87.0	-1.6	DST
JLW1-7.0	86.0	-1.8	DST
JLW1-6.0	85.0	-2.3	DST
JLW1-5.0	84.0	-9.4	DST
JLW1-4.0	83.0	-8.5	DST
JLW1-2.5	81.5	-7.6	DST
JLW1-2.0	81.0	-3.3	DST
JLW1-1.0	80.0	-3.1	DST
JLW1-0.0	79.0	-1.1	DST
JLW-84	78.0	-2.3	DST
JLW-83	77.0	-4.2	DST
JLW-82	76.0	-2.5	DST
JLW-81.2	75.2	-1.3	DST
JLW-80.3	74.3	3.6	DST

JLW-77	71.0	6.2	DST
JLW-76.8	70.8	4.5	DST
JLW-74.1	68.1	4.5	DST
JLW-69	63.0	1.4	DST
JLW-68	62.0	2.7	DST
JLW-65.5	59.5	3.8	DST
JLW-65.2	59.2	3.5	DST
JLW-65	59.0	3.4	DST
JLW-64.9	58.9	2.9	DST
JLW-64.5	58.5	0.9	DST
JLW-64.1	58.1	1.0	DST
JLW-64	58.0	1.4	DST
JLW-61.3	55.3	3.2	DST
JLW-59	53.0	3.2	DST
JLW-58.5	52.5	2.1	DST
JLW-57	51.0	3.5	DST
JLW-56.6	50.6	3.5	DST
JLW-56	50.0	3.5	DST
JLW-55.7	49.7	3.8	DST
JLW-53	47.0	4.3	DST
JLW-50.4	44.4	3.9	DST
JLW-50	44.0	3.8	DST
JLW-42.2	42.2	5.5	DST
JLW-42.0	42.0	4.7	DST
JLW-39.0	39.0	5.9	DST
JLW-35.0	35.0	5.5	DST
JLW-34.0	34.0	6.2	DST
JLW-32.2	32.2	5.8	DST
JLW-31.0	31.0	2.7	DST
JLW-26.0	26.0	1.2	DST
JLW-23.5	23.5	2.9	DST
JLW-23.1	23.1	0.3	DST
JLW-22.5	22.5	0.0	DST
JLW-19.5	19.5	1.6	DST
JLW-18.5	18.5	-2.5	DST
JLW-18.1	18.1	-2.8	DST
JLW-17.7	17.7	-3.3	DST
JLW-17.1	17.1	-0.6	DST
JLW-16.7	16.7	2.0	DST
JLW-15.0	15.0	-3.4	DST
JLW-14.1	14.1	0.1	DST
JLW-13.8	13.8	2.6	DST
JLW-12.5	12.5	2.4	DST
JLW-11.6	11.6	-0.5	DST
JLW-10.0	10.0	-3.4	DST
JLW-9.1	9.1	-3.8	DST
JLW-8.5	8.5	-1.1	DST
JLW-8.0	8.0	-0.5	DST

JLW-7.5	7.5	-0.8	DST
JLW-7.0	7.0	0.7	DST
JLW-6.7	6.7	2.8	DST
JLW-6.5	6.5	0.9	DST
JLW-6.3	6.3	2.0	DST
JLW-6.0	6.0	2.8	DST
JLW-5.7	5.7	2.1	DST
JLW-5.5	5.5	2.3	DST
JLW-5.1	5.1	3.4	DST
JLW-4.7	4.7	2.5	DST
JLW-4.5	4.5	3.8	DST

JLW-4.3	4.3	2.4	DST
JLW-4.2	4.2	2.8	DST
JLW-4.0	4.0	-17.3	DST
JLW-3.9	3.9	-16.5	DST
JLW-3.8	3.8	-5.1	DST
JLW-3.7	3.7	-14.2	DST
JLW-3.5	3.5	-1.8	DST
JLW-3.2	3.2	-14.0	DST
JLW-3.1	3.1	-3.6	DST
JLW-2.9	2.9	-3.8	DST
JLW-2.7	2.7	-3.7	DST

JLW-2.5	2.5	-3.0	DST
JLW-2.3	2.3	-3.6	DST
JLW-2.2	2.2	-3.2	DST
JLW-2.0	2.0	-3.1	DST
JLW-1.8	1.8	-3.0	DST
JLW-1.7	1.7	-3.1	DST
JLW-1.5	1.5	-3.5	DST
JLW-1.3	1.3	-3.1	DST
JLW-1.1	1.1	-3.2	DST
JLW-0.9	0.9	-2.3	DST
JLW-0.8	0.8	-1.6	DST

JLW-0.7	0.7	-2.5	DST
JLW-0.6-1	0.6	-27.9	DST
JLW-0.6-2	0.6	-36.3	DST
JLW-0.6-3	0.6	-5.9	DST
JLW-0.5	0.5	-2.6	DST
JLW-0.5-1	0.5	-33.6	DST
JLW-0.5-2	0.5	-18.3	DST
JLW-0.3	0.3	-2.6	DST
JLW-0.1	0.1	-3.0	DST

References: McFadden, K.A., Huang, J., Chu, X., Jiang, G., Kaufman, A.J., Zhou, C., Yuan, X., Xiao, S., 2008. Pulsed oxidation and biological evolution in the Ediacaran Doushantuo Formation. Proceedings of the National Academy of Sciences, 105(9): 3197-3202, doi: 10.1073/pnas.0708336105.

Table C.3: Time-series C, O, and S isotope data of the Gaojiashan Member.

samples	height	carbonate%	$\delta^{18}O$	$\delta^{13}C_{carb}$	$\delta^{13}C_{org}$	TOC%	$\Delta\delta^{13}C$	$\delta^{34}S_{TS}$	TS%	$\delta^{34}S_{CAS}$	[CAS] ppm	$\Delta\delta^{34}S$
09G-0.2	51.8	98.6	-6.9	0.9	-28.8	0.01	29.7	6.4	0.004			
09G-0.2	51.8	98.6	-7.1	0.6	-28.8	0.01	29.4	6.4	0.004			
09G-0.2	51.8	98.6	-7.1	0.6	-28.8	0.01	29.4	6.4	0.004			
14G-0.5	51.5	95.6	-7.2	1.3	-26.8	0.00	28.1	8.8	0.021	34.1	16	25.3
14G-0.5	51.5	95.6	-7.2	1.3	-26.7	0.01	28.1	8.8	0.021	34.1	16	25.3
14G-1	51	96.2	-8.6	1.1	-23.8	0.02	24.9	12.0	0.053	39.2	12	27.1
14G-1.1	50.9	93.9	-5.1	1.5	-28.5	0.02	30.1	2.3	0.004			
09G-1.5	50.5	96.1	-7.2	1.6	-28.7	0.01	30.3					
09G-1.5	50.5	96.1	-7.2	1.6	-28.7	0.01	30.2					
09G-1.5	50.5	96.1	-7.2	1.5	-28.7	0.01	30.2					
14G-1.5	50.5	86.8	-4.5	1.6	-26.0	0.02	27.6		0.005			
14G-1.5	50.5	86.8	-4.5	1.6	-25.4	0.04	27.0		0.005			
14G-1.6	50.4	89.0	-4.4	1.2	-26.3	0.02	27.5		0.004			
14G-1.6	50.4	89.0	-4.4	1.2	-25.4	0.08	26.7		0.004			
14G-2	50	89.9	-7.8	1.8	-26.9	0.01	28.7		0.002	40.2	29	
14G-2	50	89.9	-7.8	1.8	-26.8		28.5		0.002	40.2	29	
14G-2.5	49.5	66.5	-3.0	2.9					0.008			
14G-2.5	49.5	66.5	-3.1	2.4					0.008			
14G-3	49	90.8	-3.5	3.2	-29.7	0.05	32.9	10.0	0.010			
09G-3.2-4	48.8	71.9	-3.5	3.0	-30.0	0.08	33.0	11.4	0.012			

09G-3.2-2	48.8	71.9	-3.8	3.4	-30.0	0.08	33.4	13.5	0.014			
09G-3.2-1	48.8	71.9	-4.0	3.0	-30.0	0.08	33.0	11.4	0.012			
09G-3.2-1	48.8	71.9	-3.9	3.0	-30.0	0.08	33.0	13.5	0.014			
09G-3.2-1	48.8	71.9	-4.0	3.0	-30.0	0.08	33.0	11.4	0.012			
09G-3.2-2	48.8	71.9	-3.7	3.4	-30.0	0.08	33.4	13.5	0.014			
09G-3.2-2	48.8	71.9	-3.8	3.4	-30.0	0.08	33.4	11.4	0.012			
09G-3.2-4	48.8	71.9	-3.5	3.0	-30.0	0.08	33.0	13.5	0.014			
09G-3.2-4	48.8	71.9	-3.6	3.0	-30.0	0.08	33.0	11.4	0.012			
14G-3.5	48.5	68.3	-6.4	-0.2	-29.4	0.10	29.1		0.013			
14G-4	48	92.2	-5.7	4.2	-29.6	0.03	33.8	0.6	0.103	37.0	83	36.4
14G-4	48	92.2	-5.7	4.2	-29.6	0.03	33.8	0.8	0.119	37.0	83	36.2
14G-4.5	47.5	93.4	-4.9	4.4	-30.5	0.06	34.9	3.5	0.174			
14G-4.5	47.5	93.4	-4.9	4.4	-30.5	0.06	34.9	3.5	0.211			
09G-5	47	94.5	-5.5	4.2	-30.4	0.06	34.6	1.1	0.251			
09G-5	47	94.5	-5.6	4.4	-30.4	0.06	34.8	1.6	0.257			
09G-5	47	94.5	-5.6	4.3	-30.4	0.06	34.7	1.1	0.251			
14G-5	47	87.4	-6.3	2.6	-29.3	0.06	31.9	4.2	0.503			
14G-5	47	87.4	-6.3	2.6	-28.4	0.08	31.0	4.2	0.503			
14G-5.5	46.5	89.3	-5.8	4.8	-29.9	0.06	34.7	6.2	0.873	41.1	100	34.9
14G-5.5	46.5	89.3	-5.8	4.8	-29.9	0.06	34.7	6.0	0.505	41.1	100	35.1
14G-6	46	80.3	-6.1	4.6	-30.8	0.20	35.3	4.6	0.984			
14G-6	46	80.3	-6.1	4.6	-30.8	0.20	35.3	4.3	0.880			
14G-6.5	45.5	31.6	-2.8	5.5	-30.3	0.56	35.7	16.1	0.287			
14G-6.5	45.5	31.6	-2.8	5.5	-30.3	0.56	35.7	18.3	0.293			
09G-7	45	88.4	-4.9	5.1	-30.4	0.10	35.5	7.2	0.046			
09G-7	45	88.4	-4.8	5.2	-30.4	0.10	35.6	9.1	0.046			
09G-7	45	88.4	-4.8	5.2	-30.4	0.10	35.6	7.2	0.046			
14G-7	45	79.7	-5.6	5.8	-29.9	0.11	35.7	6.4	1.358	37.2	112	30.9
14G-7	45	79.7	-5.6	5.8	-29.9	0.11	35.7	6.5	1.387	37.2	112	30.8
14G-7.5	44.5	69.3	-5.4	3.2	-29.3	0.15	32.5	6.0	1.312			
14G-7.5	44.5	69.3	-5.4	3.2	-29.3	0.15	32.5	6.3	1.338			
14G-8	44	90.7	-4.9	5.4	-27.8	0.04	33.1	6.3	0.397	44.3	141	38.0
14G-8	44	90.7	-4.9	5.4	-27.8	0.04	33.1	6.1	0.431	44.3	141	38.2
14G-8.5	43.5	86.6	-5.3	5.4	-28.4	0.08	33.8	6.6	0.610	41.2	128	34.6
14G-8.5	43.5	86.6	-5.3	5.4	-28.4	0.08	33.8	6.5	0.602	41.2	128	34.7
09G-8.9	43.1	91.4	-4.7	5.7	-30.2	0.12	35.9	7.2	0.108			
09G-8.9	43.1	92.4	-4.9	5.7	-30.2	0.10	35.9	8.8	0.097			
09G-8.9	43.1	93.4	-4.7	5.8	-30.2	0.09	36.0	7.2	0.083			
14G-9	43	78.5	-5.1	6.0	-27.9	0.10	33.9	5.9	2.363	38.7	91	32.8
14G-9	43	78.5	-5.1	6.0	-27.9	0.10	33.9	5.5	1.144	38.7	91	33.2
14G-9.5	42.5	85.0	-6.0	2.4	-29.8	0.08	32.1	8.1	1.320			
14G-10	42	76.0	-5.5	6.0	-29.7	0.17	35.6	6.9	0.944			
14G-10	42	76.0	-5.5	6.0	-29.7	0.17	35.6	6.9	1.088			
09G-11	41	91.4	-4.8	6.0	-30.5	0.10	36.6	7.5	0.447			
09G-11	41	91.4	-4.8	6.1	-30.5	0.10	36.6	7.5	0.447			
09G-11	41	91.4	-4.9	6.0	-30.5	0.10	36.6	7.5	0.447			
14G-11.5	40.5	89.1	-5.1	5.5	-29.4	0.05	34.9	7.7	1.359	38.5	129	30.8
14G-11.5	40.5	89.1	-5.1	5.5	-29.4	0.05	34.9		1.127	38.5	129	38.5

14G-12	40	59.7	-5.9	5.2	-29.6	0.17	34.8	3.7	1.087		2	
14G-12	40	59.7	-5.9	5.2	-29.6	0.17	34.8	3.2	1.195		2	
14G-12.5	39.5	83.9	-5.0	5.1	-26.3	0.05	31.4	13.9	0.011			
09G-13	39	90.1	-4.6	4.7	-29.3	0.04	34.1	26.3	0.006			
09G-13	39	90.1	-4.6	4.8	-29.3	0.04	34.1	16.9	0.009			
09G-13	39	90.1	-4.7	4.9	-29.3	0.04	34.2	16.9	0.009			
14G-13	39	86.0	-5.8	5.9	-29.3	0.04	35.2	7.6	1.363			
14G-13	39	86.0	-5.8	5.9	-29.3	0.04	35.2	7.5	1.315			
14G-13.5	38.5	81.4	-5.6	6.1	-29.6	0.06	35.7	27.0	0.011			
14G-14	38	81.6	-5.6	4.6	-28.5	0.05	33.1	17.7	0.246	36.3	163	18.6
09G-14.3	37.7	88.1	-5.1	5.3	-28.8	0.05	34.1		0.005			
09G-14.3	37.7	88.1	-5.0	5.4	-28.8	0.05	34.2		0.005			
09G-14.3	37.7	88.1	-5.1	5.3	-28.8	0.05	34.1		0.005			
14G-14.5	37.5	85.1	-5.4	5.3	-29.5	0.06	34.8		0.007			
14G-15	37	91.2	-5.5	5.3	-30.6	0.11	36.0	27.1	0.015			
14G-15	37	91.2	-5.5	5.3	-30.6	0.11	36.0	28.0	0.014			
14G-15	37	91.2	-5.5	5.3	-30.6	0.11	36.0	28.5	0.015			
09G-15.7	36.3	86.2	-4.5	5.1	-28.8	0.03	33.9	14.0	0.996			
09G-15.7	36.3	86.2	-4.5	5.0	-28.8	0.03	33.8	14.0	0.983			
09G-15.7	36.3	86.2	-4.5	5.2	-28.8	0.03	34.0	14.0	0.983			
14G-16	36	85.0	-5.2	4.1	-28.1	0.03	32.1		0.003	42.4	11	
14G-16.5	35.5	84.5	-5.4	5.8	-31.1	0.12	36.9	8.0	0.389			
14G-17	35	60.6	-5.3	3.9	-31.2	0.15	35.1		0.010	38.1	68	
14G-17	35	64.9	-5.3	3.9	-30.8	0.33	34.7		0.005	38.1	68	
09G-17	35				-28.4				0.000			
14G-17.5	34.5	90.1	-6.1	4.1	-26.4	0.03	30.5		0.004	43.4	75	
14G-18	34	90.1	-5.6	5.0	-27.5	0.03	32.6		0.002			
14G-18.5	33.5	26.8			-28.7	0.11			0.000			
14G-19	33	80.3	-5.5	3.9	-24.4	0.03	28.2		0.006	45.8	49	
09G-19.2	32.8	81.4	-5.6	1.6	-28.3	0.03	29.8		0.004			
09G-19.2	32.8	81.4	-5.7	1.6	-28.3	0.03	29.8		0.004			
09G-19.2	32.8	81.4	-5.8	1.4	-28.3	0.03	29.7		0.004			
14G-19.5	32.5	9.9			-34.3	0.12			0.000			
14G-20	32	83.3	-5.7	4.5	-28.3	0.03	32.9		0.003	44.2	131	
09G-20.2	31.8	14.6			-28.8	0.05						
14G-20.5	31.5	83.1	-7.2	4.3	-25.9	0.02	30.2		0.003			
09G-21	31	25.5			-29.0	0.12			0.018			
14G-21	31	89.1	-5.9	3.1	-24.8	0.01	27.8		0.001			
14G-21.5	30.5	84.8	-6.3	4.0	-26.8	0.03	30.8		0.003			
14G-22	30	18.6			-24.4	0.08			0.000			
14G-22.5	29.5	84.4	-6.5	3.6	-27.7	0.03	31.3		0.004			
14G-23	29	66.2	-7.0	3.1	-27.5	0.04	30.6	16.7	0.040	36.9	64	20.2
14G-24	28	82.8	-5.7	4.3	-27.3	0.03	31.7		0.002	45.1	46	
14G-24.3	27.7	85.0	-5.3	3.9	-24.7	0.02	28.6		0.003			
09G-24.4	27.6	87.6	-5.4	3.2	-29.7	0.17	32.9	10.1	0.039			
09G-24.4	27.6	87.6	-5.5	3.2	-29.7	0.17	32.9	10.1	0.039			
09G-24.4	27.6	87.6	-5.6	3.3	-29.7	0.17	33.0	10.1	0.039			
14G-24.5	27.5	87.6	-5.0	3.7	-26.4	0.02	30.1		0.003			

14G-24.5	27.5	87.6	-5.6	3.4	-26.4	0.02	29.8		0.003			
14G-25	27	83.6	-6.8	3.5	-31.1	0.07	34.5	-15.6	0.272			
14G-25	27	83.6	-6.8	3.5	-31.1	0.07	34.5	-14.6	0.238	33.9	112	48.5
14G-25	27	83.6	-6.8	3.5	-31.1	0.07	34.5	-14.9	0.241	33.9	112	48.8
09G-25.7	26.3	82.3	-4.6	1.8	-28.2	0.07	30.0		0.000			
09G-25.7	26.3	82.3	-4.6	1.8	-28.2	0.07	29.9		0.000			
09G-25.7	26.3	82.3	-4.5	1.7	-28.2	0.07	29.9		0.000			
14G-26	26	86.6	-5.7	2.0	-25.6	0.01	27.6		0.002			
14G-26.5	25.5	81.2	-5.9	1.7	-27.0	0.01	28.8		0.005	32.5	64	
14G-27	25	80.9	-6.6	1.6	-25.1	0.02	26.7	-18.0	0.057	32.8	136	50.8
14G-27	25	80.9	-6.6	1.6	-25.1	0.02	26.7	-19.5	0.061	32.8	136	52.3
14G-27	25	80.9	-6.6	1.6	-25.1	0.02	26.7	-19.2	0.063	32.8	136	52.0
09G-28	24	88.4	-4.7	2.0	-28.8	0.04	30.8		0.007			
09G-28	24	88.4	-4.7	1.9	-28.8	0.04	30.8		0.005			
09G-28	24	88.4	-4.7	1.9	-28.8	0.04	30.8		0.007			
14G-27.7	24.3	26.1			-28.6	0.11		-26.9	1.091			
09G-29.7	22.3	82.1	-4.8	1.0	-26.9	0.06	27.9		0.008			
09G-29.7	22.3	82.1	-4.7	0.9	-26.9	0.06	27.9		0.008			
09G-29.7	22.3	82.1	-4.8	1.0	-26.9	0.06	27.9		0.008			
14G-30	22	64.0	-6.0	0.8	-26.9	0.03	27.7		0.007	34.4	120	
09G-30.1	21.9	83.4	-4.4	0.4	-32.0	0.06	32.4	23.0	0.007			
09G-30.1	21.9	83.4	-4.4	0.4	-32.0	0.06	32.4	23.0	0.007			
09G-30.1	21.9	83.4	-4.4	0.5	-32.0	0.06	32.4	23.0	0.007			
14G-31	21	35.0	-8.8	-2.3	-27.3	0.03	25.1		0.000			
14G-31	21	35.0	-8.8	-2.3	-28.1	0.05	25.8		0.000			
14G-31.5	20.5	50.5	-7.0	-0.1	-25.5	0.12	25.5		0.000			
14G-31.5	20.5	50.5	-7.0	-0.1	-27.0	0.03	26.9		0.000			
09G-32	20	73.9	-5.4	1.0	-26.5	0.10	27.5		0.005			
09G-32	20	73.9	-5.3	1.0	-26.5	0.10	27.6		0.005			
09G-32	20	73.9	-5.4	1.0	-26.5	0.10	27.6		0.005			
14G-32	20	53.2	-6.7	0.6	-27.0	0.02	27.5		0.000			
14G-32	20	53.2	-6.7	0.6	-27.0	0.03	27.5		0.000			
14G-33	19	53.7	-7.3	0.4	-27.2	0.02	27.6		0.008	38.8	98	
14G-33.5	18.5	50.9	-5.0	0.0	-26.8	0.02	26.8		0.006			
09G-34	18	25.1			-28.1	0.04		19.3	0.040			
14G-34	18	42.5	-5.5	1.0	-26.8	0.02	27.7		0.007			
14G-34	18	42.5	-5.5	1.0	-26.2	0.33	27.2		0.007			
14G-34.5	17.5	57.2	-8.4	0.0	-27.7	0.01	27.7	14.6	0.018	38.0	76	23.4
14G-34.5	17.5	57.2	-8.4	0.0	-27.7	0.01	27.7	14.6	0.021	38.0	76	23.4
14G-35	17	52.4			-27.4	0.02			0.009			
14G-35	17	52.4			-27.2	0.03						
09G-35.5	16.5	50.2	-4.8	0.6	-29.1	0.02	29.7		0.012			
09G-35.5	16.5	50.2	-4.8	0.6	-29.1	0.02	29.7		0.012			
09G-35.5	16.5	50.2	-4.7	0.7	-29.1	0.02	29.8		0.012			
14G-35.5	16.5	65.4	-8.0	0.4	-25.0	0.01	25.4		0.004			
09G-35.6	16.4	31.0	-4.7	-0.4	-28.6	0.03	28.2		0.000			
09G-35.6	16.4	31.0	-4.6	-0.2	-28.6	0.03	28.4		0.000			
09G-35.6	16.4	31.0	-4.4	-0.1	-28.6	0.03	28.5		0.000			

14G-37.5	14.5	74.0	-5.0	1.1	-30.0	0.02	31.1					
14G-37.5	14.5	74.0	-5.0	1.1	-26.7	0.02	27.9					
09G-38	14	62.6	-7.1	0.4	-27.7	0.02	28.0		0.005			
09G-38	14	62.6	-7.1	0.3	-27.7	0.02	28.0		0.005			
09G-38	14	62.6	-7.1	0.4	-27.7	0.02	28.1		0.005			
14G-38	14	90.9	-4.8	1.1	-29.8	0.01	30.9	12.1	0.020			
14G-38	14	90.9	-4.8	1.1	-29.8	0.01	30.9		0.006			
14G-38	14	90.9	-4.8	1.1	-27.7	0.01	28.8		0.006			
14G-38.5	13.5	62.9	-5.5	1.0	-32.7	0.06	33.7	-29.8	0.180			
14G-38.5	13.5	62.9	-5.5	1.0	-32.7	0.06	33.7	-30.4	0.221			
14G-38.5	13.5	62.9	-5.5	1.0	-32.7	0.06	33.7	-30.8	0.229			
14G-38.5	13.5	62.9	-5.5	1.0	-30.8	0.07	31.8	-30.8	0.229			
14G-39	13	68.4	-5.9	1.2	-33.4	0.06	34.5	-29.5	0.227	42.4	27	72.0
14G-39	13	68.4	-5.9	1.2	-33.4	0.06	34.5	-29.9	0.236	42.4	27	72.3
14G-39	13	68.4	-5.9	1.2	-33.4	0.06	34.5	-29.9	0.273	42.4	27	72.4
14G-39	13	68.4	-5.9	1.2	-32.0	0.08	33.2	-29.9	0.273	42.4	27	72.4
14G-39.5	12.5	15.3			-35.5	0.98		-20.1	1.062			
14G-39.5	12.5	15.3			-35.5	0.98		-18.8	1.079			
14G-39.5	12.5	15.3			-35.5	0.98		-18.4	1.006			
14G-39.5	12.5	15.3			-35.2	1.00		-18.4	1.006			
09G-40	12	71.2	-5.7	0.5	-31.5	0.03	32.0	-17.8	0.243			
09G-40	12	71.2	-5.7	0.5	-31.5	0.03	32.0	-22.4	0.227			
09G-40	12	71.2	-5.7	0.5	-31.5	0.03	32.0	-22.4	0.227			
14G-40.5	11.5	5.9			-30.8	0.04			0.000			
14G-40.5	11.5	5.9			-29.9	0.05			0.000			
14G-41	11	4.3			-29.8	0.04			0.000			
14G-42	10	3.7							0.000			
09G-42.5-L	9.5	54.7	-3.0	0.0	-29.5	0.03	29.6	-12.6	0.031			
09G-42.5	9.5	54.7	-3.6	0.0	-29.5	0.03	29.6	-12.6	0.031			
09G-42.5	9.5	54.7	-3.6	0.1	-29.5	0.03	29.6	-12.6	0.031			
09G-42.5	9.5	54.7	-3.6	0.2	-29.5	0.03	29.7	-12.6	0.031			
09G-42.5-L	9.5	54.7	-3.0	0.1	-29.5	0.03	29.6	-12.6	0.031			
09G-42.5-L	9.5	54.7	-2.9	0.1	-29.5	0.03	29.7	-12.6	0.031			
09G-43	9	78.2	-3.8	0.2	-30.1	0.03	30.3	-17.1	0.610			
14G-43	9	82.0	-1.8	0.3	-27.6	0.01	27.9		0.004			
14G-43	9	82.0	-1.8	0.3	-27.6	0.01	27.9		0.004			
09G-44.3	7.7	4.7			-29.0	0.04			0.000			
14G-45	7	79.6			-27.0	0.01			0.000			
14G-45	7	79.6			-27.5	0.01			0.000			
09G-46	6	85.6	0.4	0.5	-27.0	0.01	27.5					
14G-47	5	4.0			-26.2	0.03			0.000			
09G-47.7	4.3	7.5			-28.2	0.03						
14G-48	4	7.5			-27.0	0.03			0.000			
09G-50	2	6.5			-27.6	0.04						
09G-52	0	3.0				0.33			0.000			
14G-52	0	8.8			-26.8	0.05			0.000			
14G-52	0	8.8			-26.0	0.03			0.000			

Table C.4: Major and trace element concentrations of the Gaojiashan Member. Concentration units are all in ppm.

samples	height	Mg	Al	Mn	Fe	Rb	Sr	Th	U	Rb/Sr	Mg/Ca	Sr/Ca	Th/U	Ce/Ce*	Mn/Sr
14G-0.5	51.5	6944	103	64	1195	0.35	102	0.02	0.08	0.0034	0.035	0.0005	0.19	0.9	0.63
14G-1	51	20145	326	78	1258	0.62	90	0.02	0.12	0.0069	0.199	0.0009	0.14	1	0.87
14G-2	50	5048	433	149	765	0.91	120	0.05	0.17	0.0076	0.063	0.0015	0.28	0.7	1.24
14G-4	48	7502	712	99	2446	1.6	753	0.05	0.41	0.0021	0.097	0.0097	0.11	0.6	0.13
14G-5.5	46.5	7744	1427	110	3182	3.11	943	0.05	0.47	0.0033	0.098	0.012	0.10	0.5	0.12
14G-7	45	5789	735	137	6391	2.29	926	0.13	0.25	0.0025	0.062	0.0099	0.52	0.5	0.15
14G-8	44	6911	820	114	4419	2.01	1050	0.06	0.62	0.0019	0.092	0.014	0.10	0.6	0.11
14G-11.5	40.5	9056	2095	147	12214	4.53	1059	0.06	0.7	0.0043	0.120	0.0141	0.09	0.6	0.14
14G-14	38	12008	2642	182	10571	5.59	734	0.07	0.51	0.0076	0.174	0.0107	0.14	0.6	0.25
14G-16	36	5875	3717	236	3191	5.85	663	0.1	0.17	0.0088	0.097	0.0109	0.57	0.5	0.36
14G-17.5	34.5	7627	2629	234	3635	5.29	484	0.06	0.45	0.0109	0.108	0.0069	0.12	0.6	0.48
14G-19	33	7029	2418	324	4669	5.05	440	0.12	0.4	0.0115	0.105	0.0066	0.29	0.5	0.73
14G-20	32	6975	2909	300	6246	6.03	415	0.1	0.63	0.0145	0.095	0.0056	0.15	0.6	0.72
14G-23	29	5027	3742	537	7399	6.84	271	0.17	0.59	0.0252	0.114	0.0062	0.29	0.5	1.98
14G-24	28	5814	2450	331	4868	4.78	518	0.1	0.51	0.0092	0.088	0.0078	0.19	0.6	0.64
14G-25	27	10148	725	315	6176	3.03	380	0.08	0.69	0.008	0.101	0.0038	0.11	0.6	0.83
14G-26.5	25.5	8780	3238	483	5778	8	259	0.08	0.41	0.0309	0.149	0.0044	0.19	0.5	1.86
14G-27	25	8943	2745	471	6209	7.93	291	0.07	0.53	0.0273	0.140	0.0046	0.13	0.6	1.62
14G-30	22	10098	5595	622	5840	9.47	138	0.12	0.49	0.0688	0.257	0.0035	0.24	0.5	4.52
14G-33	19	16062	5844	386	9145	11.36	79	0.13	0.11	0.1436	0.598	0.0029	1.22	0.6	4.87
14G-34.5	17.5	10927	3619	345	5519	8.12	95	0.12	0.09	0.0855	0.314	0.0027	1.26	0.6	3.64
14G-35	17	13072	7418	228	6638	12.52	60	0.23	0.15	0.2079	0.665	0.0031	1.59	0.6	3.78
14G-45	7	143225	677	1970	2608	1.25	52	0.07	0.23	0.0239	3.191	0.0012	0.31	0.5	37.73

Bibliography

Ader, M., Macouin, M., Trindade, R.I.F., Hadrien, M.H., Yang, Z., Sun, Z., Besse, J., 2009. A multilayered water column in the Ediacaran Yangtze platform? Insights from carbonate and organic matter paired δ13C. Earth and Planetary Science Letters, 288(1–2): 213-227, doi: 10.1016/j.epsl.2009.09.024.

Ader, M., Sansjofre, P., Halverson, G.P., Busigny, V., Trindade, R.I.F., Kunzmann, M., Nogueira, A.C.R., 2014. Ocean redox structure across the Late Neoproterozoic Oxygenation Event: A nitrogen isotope perspective. Earth and Planetary Science Letters, 396(0): 1-13, doi: 10.1016/j.epsl.2014.03.042.

Algeo, T.J., Luo, G.M., Song, H.Y., Lyons, T.W., Canfield, D.E., 2015. Reconstruction of secular variation in seawater sulfate concentrations. Biogeosciences, 12(7): 2131-2151, doi: 10.5194/bg-12-2131-2015.

Amthor, J.E., Grotzinger, J.P., Schröder, S., Bowring, S.A., Ramezani, J., Martin, M.W., Matter, A., 2003. Extinction of Cloudina and Namacalathus at the Precambrian-Cambrian boundary in Oman. Geology, 31(5): 431-434, doi: 10.1130/0091-7613(2003)031<0431:EOCANA>2.0.CO;2.

An, Z., Jiang, G., Tong, J., Tian, L., Ye, Q., Song, H., Song, H., 2015. Stratigraphic position of the Ediacaran Miaohe biota and its constrains on the age of the upper Doushantuo δ13C anomaly in the Yangtze Gorges area, South China. Precambrian Research: 243-253, doi: 10.1016/j.precamres.2015.10.007.

Bekker, A., Karhu, J., Kaufman, A., 2006. Carbon isotope record for the onset of the Lomagundi carbon isotope excursion in the Great Lakes area, North America. Precambrian Research, 148(1): 145-180, doi: 10.1016/j.precamres.2006.03.008.

Bengtson, S., Zhao, Y., 1992. Predatorial borings in late Precambrian mineralized exoskeletons. Science, 257(5068): 367-369.

Bergmann, K.D., 2013. Constraints on the carbon cycle and climate during the early evolution of animals. Dissertation.

Berner, R.A., 1989. Biogeochemical cycles of carbon and sulfur and their effect on atmospheric oxygen over phanerozoic time. Palaeogeography, Palaeoclimatology, Palaeoecology, 75(1–2): 97-122, doi: 10.1016/0031-0182(89)90186-7.

Berner, R.A., Raiswell, R., 1983. Burial of organic carbon and pyrite sulfur in sediments over Phanerozoic time: a new theory. Geochem. Cosmochim. Acta, 47: 855-862, doi: 10.1016/0016-7037(83)90151-5.

Berner, R.A., Raiswell, R., 1984. C/S method for distinguishing freshwater from marine sedimentary rocks. Geology, 12(6): 365-368, doi: 10.1130/0091-7613(1984)12<365:CMFDFF>2.0.CO;2.

Bjerrum, C.J., Canfield, D.E., 2011. Towards a quantitative understanding of the late Neoproterozoic carbon cycle. Proceedings of the National Academy of Sciences, 108(14): 5542-5547, doi: 10.1073/pnas.1101755108.

Borowski, W.S., Paull, C.K., Ussler, W., 1996. Marine pore-water sulfate profiles

indicate in situ methane flux from underlying gas hydrate. Geology, 24(7): 655-658.
Borowski, W.S., Rodriguez, N.M., Paull, C.K., Ussler, W., 2013. Are 34S-enriched authigenic sulfide minerals a proxy for elevated methane flux and gas hydrates in the geologic record? Marine and Petroleum Geology, 43: 381-395, doi: 10.1016/j.marpetgeo.2012.12.009.
Bottjer, D.J., Hagadorn, J.W., Dornbos, S.Q., 2000. The Cambrian substrate revolution. GSA today, 10(9): 1-7.
Bowring, S., Myrow, P., Landing, E., Ramezani, J., Grotzinger, J., 2003. Geochronological constraints on terminal Neoproterozoic events and the rise of Metazoan, EGS-AGU-EUG Joint Assembly, pp. 13219.
Bowring, S.A., 2007. Geochronologic constraints on the chronostratigraphic framework of the Neoproterozoic Huqf Supergroup, sultanate of Oman. American Journal of Science, 307: 1097-1145.
Bradley, A.S., Leavitt, W.D., Schmidt, M., Knoll, A.H., Girguis, P.R., Johnston, D.T., 2015. Patterns of sulfur isotope fractionation during Microbial Sulfate Reduction. Geobiology: 1-11, doi: 10.1111/gbi.12149.
Bristow, T.F., Bonifacie, M., Derkowski, A., Eiler, J.M., Grotzinger, J.P., 2011. A hydrothermal origin for isotopically anomalous cap dolostone cements from south China. Nature, 474(7349): 68-71, doi: 10.1038/nature10096.
Bristow, T.F., Grotzinger, J.P., 2013. Sulfate availability and the geological record of cold-seep deposits. Geology, doi: 10.1130/g34265.1.
Brocks, J.J., Love, G.D., Summons, R.E., Knoll, A.H., Logan, G.A., Bowden, S.A., 2005. Biomarker evidence for green and purple sulphur bacteria in a stratified Palaeoproterozoic sea. Nature, 437(7060): 866-870.
Burns, S., Matter, A., 1993. Carbon isotopic record of the latest Proterozoic from Oman. Eclogae Geologicae Helvetiae, 86(2): 595-607, doi: 10.5169/seals-167254.
Burns, S.J., Haudenschild, U., Matter, A., 1994. The strontium isotopic composition of carbonates from the late Precambrian (~ 560-540 Ma) Huqf Group of Oman. Chemical Geology, 111(1–4): 269-282, doi: 10.1016/0009-2541(94)90094-9.
Butterfield, N., 2009. Oxygen, animals and oceanic ventilation: an alternative view. Geobiology, 7(1): 1-7, doi: 10.1111/j.1472-4669.2009.00188.x.
Butterfield, N.J., 2011. Animals and the invention of the Phanerozoic Earth system. Trends in Ecology & Evolution, 26(2): 81-87, doi: 10.1016/j.tree.2010.11.012.
Cai, C., Hu, W., Worden, R.H., 2001. Thermochemical sulphate reduction in Cambro–Ordovician carbonates in Central Tarim. Marine and Petroleum Geology, 18(6): 729-741, doi: 10.1016/S0264-8172(01)00028-9.
Cai, C., Worden, R.H., Bottrell, S.H., Wang, L., Yang, C., 2003. Thermochemical sulphate reduction and the generation of hydrogen sulphide and thiols (mercaptans) in Triassic carbonate reservoirs from the Sichuan Basin, China. Chemical Geology, 202(1): 39-57, doi: 10.1016/S0009-2541(03)00209-2.
Cai, C., Xie, Z., Worden, R.H., Hu, G., Wang, L., He, H., 2004. Methane-dominated

thermochemical sulphate reduction in the Triassic Feixianguan Formation East Sichuan Basin, China: towards prediction of fatal H 2 S concentrations. Marine and Petroleum Geology, 21(10): 1265-1279, doi: 10.1016/j.marpetgeo.2004.09.003.

Cai, Y., Hua, H., Schiffbauer, J.D., Sun, B., Yuan, X., 2014. Tube growth patterns and microbial mat-related lifestyles in the Ediacaran fossil Cloudina, Gaojiashan Lagerstätte, South China. Gondwana Research, 25(3): 1008-1018, doi: 10.1016/j.gr.2012.12.027.

Cai, Y., Hua, H., Xiao, S., Schiffbauer, J.D., Li, P., 2010. Biostratinomy of the late Ediacaran pyritized Gaojiashan Lagerstätte from southern Shaanxi, South China: importance of event deposits. Palaios, 25(8): 487-506, doi: 10.2110/palo.2009.p09-133r.

Cai, Y., Hua, H., Zhang, X., 2013. Tube construction and life mode of the late Ediacaran tubular fossil Gaojiashania cyclus from the Gaojiashan Lagerstätte. Precambrian Research, 224: 255-267, doi: 10.1016/j.precamres.2012.09.022.

Cai, Y., Schiffbauer, J.D., Hua, H., Xiao, S., 2011. Morphology and paleoecology of the late Ediacaran tubular fossil Conotubus hemiannulatus from the Gaojiashan Lagerstätte of southern Shaanxi Province, South China. Precambrian Research, 191(1): 46-57, doi: 10.1016/j.precamres.2011.09.002.

Cai, Y., Schiffbauer, J.D., Hua, H., Xiao, S., 2012. Preservational modes in the Ediacaran Gaojiashan Lagerstätte: Pyritization, aluminosilicification, and carbonaceous compression. Palaeogeography, Palaeoclimatology, Palaeoecology, 326: 109-117, doi: 10.1016/j.palaeo.2012.02.009.

Cai, Y., Xiao, S., Hua, H., Yuan, X., 2015. New material of the biomineralizing tubular fossil Sinotubulites from the late Ediacaran Dengying Formation, South China. Precambrian Research, doi: 10.1016/j.precamres.2015.02.002.

Calver, C.R., 2000. Isotope stratigraphy of the Ediacarian (Neoproterozoic III) of the Adelaide Rift Complex, Australia, and the overprint of water column stratification. Precambrian Research, 100(1–3): 121-150, doi: 10.1016/s0301-9268(99)00072-8.

Campbell, K.A., 2006. Hydrocarbon seep and hydrothermal vent paleoenvironments and paleontology: Past developments and future research directions. Palaeogeography, Palaeoclimatology, Palaeoecology, 232(2–4): 362-407, doi: 10.1016/j.palaeo.2005.06.018.

Canfield, D., 1998. A new model for Proterozoic ocean chemistry. Nature, 396(6710): 450-453.

Canfield, D.E., 2004. The evolution of the Earth surface sulfur reservoir. American Journal of Science, 304(10): 839-861, doi: 10.2475/ajs.304.10.839.

Canfield, D.E., Farquhar, J., 2009. Animal evolution, bioturbation, and the sulfate concentration of the oceans. Proceedings of the National Academy of Sciences, 106(20): 8123-8127, doi: 10.1073/pnas.0902037106.

Canfield, D.E., Farquhar, J., Zerkle, A.L., 2010. High isotope fractionations during sulfate reduction in a low-sulfate euxinic ocean analog. Geology, 38(5): 415-418, doi: 10.1130/G30723.1.

Canfield, D.E., Poulton, S.W., Narbonne, G.M., 2007. Late-Neoproterozoic deep-ocean oxygenation and the rise of animal life. Science, 315: 92-95, doi: 10.1126/science.1135013.
Canfield, D.E., Thamdrup, B., 1994. The production of 34S-depleted sulfide during bacterial disproportionation of elemental sulfur. Science, 266(5193): 1973-1975, doi: 10.1126/science.11540246.
Carbone, C., Narbonne, G.M., 2014. When life got smart: the evolution of behavioral complexity through the Ediacaran and early Cambrian of NW Canada. Journal of Paleontology, 88(2): 309-330, doi: 10.1666/13-066.
Chen, D., Zhou, X., Fu, Y., Wang, J., Yan, D., 2015. New U–Pb zircon ages of the Ediacaran–Cambrian boundary strata in South China. Terra Nova, 27(1): 62-68, doi: 10.1111/ter.12134.
Chen, Z., Zhou, C., Meyer, M., Xiang, K., Schiffbauer, J.D., Yuan, X., Xiao, S., 2013. Trace fossil evidence for Ediacaran bilaterian animals with complex behaviors. Precambrian Research, 224: 690-701, doi: 10.1016/j.precamres.2012.11.004.
Chen, Z., Zhou, C., Xiao, S., Wang, W., Guan, C., Hua, H., Yuan, X., 2014a. New Ediacara fossils preserved in marine limestone and their ecological implications. Scientific Reports, 4, doi: 10.1038/srep04180.
Chen, Z., Zhou, C., Xiao, S., Wang, W., Guan, C., Hua, H., Yuan, X., 2014b. New Ediacara fossils preserved in marine limestone and their ecological implications. Scientific Reports, 4: 4180; DOI:10.1038/srep04180.
Cloud, P., 1976. Beginnings of biospheric evolution and their biogeochemical consequences. Paleobiology: 351-387.
Condon, D., Zhu, M., Bowring, S., Wang, W., Yang, A., Jin, Y., 2005. U-Pb ages from the Neoproterozoic Doushantuo Formation, China. Science, 308: 95-98, doi: 10.1126/science.1107765.
Conway Morris, S., Mattes, B.W., Chen, M., 1990. The early skeletal organism *Cloudina*: New occurrences from Oman and possibly China. American Journal of Science, 290-A: 245-260.
Coplen, T.B., Brand, W.A., Gehre, M., Gröning, M., Meijer, H.A.J., Toman, B., Verkouteren, R.M., 2006. New Guidelines for δ13C Measurements. Analytical Chemistry, 78(7): 2439-2441, doi: 10.1021/ac052027c.
Cortijo, I., Martí Mus, M., Jensen, S., Palacios, T., 2010. A new species of Cloudina from the terminal Ediacaran of Spain. Precambrian Research, 176(1–4): 1-10, doi: 10.1016/j.precamres.2009.10.010.
Cui, H., Kaufman, A.J., Xiao, S., Zhu, M., Zhou, C., Liu, X.-M., 2015. Redox architecture of an Ediacaran ocean margin: Integrated chemostratigraphic (δ13C–δ34S–87Sr/86Sr–Ce/Ce*) correlation of the Doushantuo Formation, South China. Chemical Geology, 405: 48-62, doi: 10.1016/j.chemgeo.2015.04.009.
Darwin, C., 1859. On the origins of species by means of natural selection. London: Murray: 247.
DePaolo, D.J., Ingram, B.L., 1985. High-Resolution Stratigraphy with Strontium Isotopes. Science, 227(4689): 938-941, doi: 10.2307/1694776.
Derry, L.A., 2010. A burial diagenesis origin for the Ediacaran Shuram–Wonoka

carbon isotope anomaly. Earth and Planetary Science Letters, 294(1–2): 152-162, doi: 10.1016/j.epsl.2010.03.022.
Derry, L.A., Kaufman, A.J., Jacobsen, S.B., 1992. Sedimentary cycling and environmental change in the Late Proterozoic: evidence from stable and radiogenic isotopes. Geochimica et Cosmochimica Acta, 56(3): 1317-1329, doi: 10.1016/0016-7037(92)90064-P.
Deutsch, C., Brix, H., Ito, T., Frenzel, H., Thompson, L., 2011. Climate-forced variability of ocean hypoxia. Science, 333(6040): 336-339.
Ding, Q., Chen, Y., 1981. Discovery of soft metazoan from the Sinian System along eastern Yangtze Gorge, Hubei. Journal of the Wuhan College of Geology, 2: 53-57.
Duda, J.-P., Blumenberg, M., Thiel, V., Simon, K., Zhu, M., Reitner, J., 2014. Geobiology of a palaeoecosystem with Ediacara-type fossils: The Shibantan Member (Dengying Formation, South China). Precambrian Research, 255, Part 1(0): 48-62, doi: 10.1016/j.precamres.2014.09.012.
Duda, J.-P., Zhu, M., Reitner, J., 2015. Depositional dynamics of a bituminous carbonate facies in a tectonically induced intra-platform basin: the Shibantan Member (Dengying Formation, Ediacaran Period). Carbonates and Evaporites: 1-13, doi: 10.1007/s13146-015-0243-8.
Erwin, D.H., Valentine, J.W., 2012. The Cambrian explosion: the construction of animal biodiversity. Roberts.
Fedonkin, M.A., Gehling, J.G., Grey, K., Narbonne, G.M., Vickers-Rich, P., 2007. The rise of animals: evolution and diversification of the kingdom Animalia. John Hopkins University Press.
Fike, D.A., Grotzinger, J.P., 2008. A paired sulfate-pyrite δ34S approach to understanding the evolution of the Ediacaran-Cambrian sulfur cycle. Geochem. Cosmochim. Acta, 72: 2636-2648, doi: 10.1016/j.gca.2008.03.021.
Fike, D.A., Grotzinger, J.P., 2010. A δ34SSO4 approach to reconstructing biogenic pyrite burial in carbonate-evaporite basins: An example from the Ara Group, Sultanate of Oman. Geology, 38(4): 371-374, doi: 10.1130/g30230.1.
Fike, D.A., Grotzinger, J.P., Pratt, L.M., Summons, R.E., 2006. Oxidation of the Ediacaran Ocean. Nature, 444: 744-747, doi: 10.1038/nature05345.
Frei, R., Gaucher, C., Poulton, S.W., Canfield, D.E., 2009. Fluctuations in Precambrian atmospheric oxygenation recorded by chromium isotopes. Nature, 461(7261): 250-253.
Gaidos, E., Dubuc, T., Dunford, M., McAndrew, P., Padilla-GamiÑO, J., Studer, B., Weersing, K., Stanley, S., 2007. The Precambrian emergence of animal life: a geobiological perspective. Geobiology, 5(4): 351-373, doi: 10.1111/j.1472-4669.2007.00125.x.
Gaucher, C., Germs, G.J.B., 2009. Chapter 9.2 Skeletonised Metazoans and Protists. In: Gaucher, C., Sial, A.N., Frimmel, H.E., Halverson, G.P. (Eds.), Developments in Precambrian Geology. Elsevier, pp. 327-338, doi: 10.1016/S0166-2635(09)01623-5
Gehling, J.G., 1999. Microbial mats in terminal Proterozoic siliciclastics: Ediacaran

death masks. Palaios, 14(1): 40-57, doi: 10.2307/3515360.
Gehrels, G.E., Valencia, V.A., Ruiz, J., 2008. Enhanced precision, accuracy, efficiency, and spatial resolution of U‐Pb ages by laser ablation‐multicollector‐inductively coupled plasma‐mass spectrometry. Geochemistry, Geophysics, Geosystems, 9(3), doi: 10.1029/2007GC001805.
Gill, B.C., Lyons, T.W., Young, S.A., Kump, L.R., Knoll, A.H., Saltzman, M.R., 2011. Geochemical evidence for widespread euxinia in the Later Cambrian ocean. Nature, 469(7328): 80-83, doi: 10.1038/nature09700.
Goldstein, S.L., 1988. Decoupled evolution of Nd and Sr isotopes in the continental crust and the mantle. Nature, 336: 733-738.
Grant, S., 1990. Shell structure and distribution of Cloudina, a potential index fossil for the terminal Proterozoic. American Journal of Science, 290: 261-294.
Grant, S.W.F., 1992. Carbon isotopic vital effect and organic diagenesis, Lower Cambrian Forteau Formation, northwest Newfoundland: Implications for δ13C chemostratigraphy. Geology, 20(3): 243-246, doi: 10.1130/0091-7613(1992)020<0243:civeao>2.3.co;2.
Grazhdankin, D.V., Balthasar, U., Nagovitsin, K.E., Kochnev, B.B., 2008. Carbonate-hosted Avalon-type fossils in arctic Siberia. Geology, 36(10): 803-806, doi: 10.1130/G24946A.1.
Grotzinger, J., Adams, E., Schröder, S., 2005. Microbial–metazoan reefs of the terminal Proterozoic Nama Group (c. 550–543 Ma), Namibia. Geological Magazine, 142(05): 499-517, doi: 10.1017/S0016756805000907.
Grotzinger, J.P., 2000. Facies and paleoenvironmental setting of thrombolite-stromatolite reefs, terminal Proterozoic Nama Group (ca. 550–543 Ma), central and southern Namibia. Communications of the Geological Survey of Namibia, 12: 251-264.
Grotzinger, J.P., Fike, D.A., Fischer, W.W., 2011. Enigmatic origin of the largest-known carbon isotope excursion in Earth's history. Nature Geoscience, 4(5): 285-292, doi: 10.1038/NGEO1138.
Habicht, K.S., Canfield, D.E., 2001. Isotope fractionation by sulfate-reducing natural populations and the isotopic composition of sulfide in marine sediments. Geology, 29(6): 555-558, doi: 10.1130/0091-7613(2001)029<0555:IFBSRN>2.0.CO;2.
Habicht, K.S., Gade, M., Thamdrup, B., Berg, P., Canfield, D.E., 2002. Calibration of sulfate levels in the Archean ocean. Science, 298(5602): 2372-2374, doi: 10.1126/science.1078265.
Hall, M., Kaufman, A.J., Vickers-Rich, P., Ivantsov, A., Trusler, P., Linnemann, U., Hofmann, M., Elliott, D., Cui, H., Fedonkin, M., Hoffmann, K.-H., Wilson, S.A., Schneider, G., Smith, J., 2013. Stratigraphy, palaeontology and geochemistry of the late Neoproterozoic Aar Member, southwest Namibia: Reflecting environmental controls on Ediacara fossil preservation during the terminal Proterozoic in African Gondwana. Precambrian Research, 238(0): 214-232, doi: 10.1016/j.precamres.2013.09.009.
Halverson, G.P., Dudás, F.Ö., Maloof, A.C., Bowring, S.A., 2007. Evolution of the 87Sr/86Sr composition of Neoproterozoic seawater. Palaeogeography, Palaeoclimatology, Palaeoecology, 256(3–4): 103-129, doi:

10.1016/j.palaeo.2007.02.028.
Halverson, G.P., Hurtgen, M.T., 2007. Ediacaran growth of the marine sulfate reservoir. Earth and Planetary Science Letters, 263(1): 32-44, doi: 10.1016/j.epsl.2007.08.022.
Halverson, G.P., Wade, B.P., Hurtgen, M.T., Barovich, K.M., 2010. Neoproterozoic chemostratigraphy. Precambrian Research, 182(4): 337-350, doi: 10.1016/j.precamres.2010.04.007.
Hardie, L.A., 1996. Secular variation in seawater chemistry: An explanation for the coupled secular variation in the mineralogies of marine limestones and potash evaporites over the past 600 m.y. Geology, 24(3): 279-283, doi: 10.1130/0091-7613(1996)024<0279:svisca>2.3.co;2.
Hardie, L.A., 2003. Secular variations in Precambrian seawater chemistry and the timing of Precambrian aragonite seas and calcite seas. Geology, 31(9): 785-788, doi: 10.1130/G19657.1.
Hayes, J., Wedeking, K., Kaplan, I., 1983. Precambrian organic geochemistry-Preservation of the record, Earth's earliest biosphere: Its origin and evolution. Princeton, NJ, Princeton University Press, pp. 93-134
Hayes, J.M., 1993. Factors controlling 13C contents of sedimentary organic compounds: Principles and evidence. Marine Geology, 113(1–2): 111-125, doi: 10.1016/0025-3227(93)90153-M.
Higgins, J., Fischer, W., Schrag, D., 2009. Oxygenation of the ocean and sediments: consequences for the seafloor carbonate factory. Earth and Planetary Science Letters, 284(1): 25-33, doi: 10.1016/j.epsl.2009.03.039.
Hoffman, P.F., Kaufman, A.J., Halverson, G.P., Schrag, D., 1998a. Comings and goings of global glaciations on a Neoproterozoic tropical platform in Namibia. GSA today, 8(5): 1-9.
Hoffman, P.F., Kaufman, A.J., Halverson, G.P., Schrag, D.P., 1998b. A Neoproterozoic Snowball Earth. Science, 281: 1342-1346, doi: 10.1126/science.281.5381.1342.
Horita, J., 2014. Oxygen and carbon isotope fractionation in the system dolomite–water–CO2 to elevated temperatures. Geochimica et Cosmochimica Acta, 129: 111-124, doi: 10.1016/j.gca.2013.12.027.
Hua, H., Chen, Z., Yuan, X., 2007. The advent of mineralized skeletons in Neoproterozoic Metazoa—new fossil evidence from the Gaojiashan Fauna. Geological Journal, 42(3‐4): 263-279, doi: 10.1002/gj.1077.
Hua, H., Chen, Z., Yuan, X., Zhang, L., Xiao, S., 2005. Skeletogenesis and asexual reproduction in the earliest biomineralizing animal Cloudina. Geology, 33(4): 277-280, doi: 10.1130/g21198.1.
Hua, H., Pratt, B.R., Zhang, L.-Y., 2003. Borings in Cloudina shells: complex predator-prey dynamics in the terminal Neoproterozoic. Palaios, 18(4-5): 454-459, doi: 10.1669/0883-1351(2003)018<0454:BICSCP>2.0.CO;2.
Hurtgen, M.T., Arthur, M.A., Halverson, G.P., 2005. Neoproterozoic sulfur isotopes, the evolution of microbial sulfur species, and the burial efficiency of sulfide as sedimentary pyrite. Geology, 33(1): 41-44, doi: 10.1130/g20923.1.
Husson, J.M., Maloof, A.C., Schoene, B., Chen, C.Y., Higgins, J.A., 2015.

Stratigraphic expression of Earth's deepest δ13C excursion in the Wonoka Formation of South Australia. American Journal of Science, 315(1): 1-45, doi: 10.2475/01.2015.01.

Jacobsen, S.B., Kaufman, A.J., 1999. The Sr, C and O isotopic evolution of Neoproterozoic seawater. Chemical Geology, 161(1–3): 37-57, doi: 10.1016/s0009-2541(99)00080-7.

Jiang, G., Kaufman, A.J., Christie-Blick, N., Zhang, S., Wu, H., 2007. Carbon isotope variability across the Ediacaran Yangtze platform in South China: Implications for a large surface-to-deep ocean δ13C gradient. Earth and Planetary Science Letters, 261(1): 303-320, doi: 10.1016/j.epsl.2007.07.009.

Jiang, G., Shi, X., Zhang, S., Wang, Y., Xiao, S., 2011. Stratigraphy and paleogeography of the Ediacaran Doushantuo Formation (ca. 635–551Ma) in South China. Gondwana Research, 19(4): 831-849, doi: 10.1016/j.gr.2011.01.006.

Johnston, D., Poulton, S., Tosca, N., O'Brien, T., Halverson, G., Schrag, D., Macdonald, F., 2013. Searching for an oxygenation event in the fossiliferous Ediacaran of northwestern Canada. Chemical Geology, 362: 273-286, doi: 10.1016/j.chemgeo.2013.08.046.

Johnston, D.T., Wolfe-Simon, F., Pearson, A., Knoll, A.H., 2009. Anoxygenic photosynthesis modulated Proterozoic oxygen and sustained Earth's middle age. Proceedings of the National Academy of Sciences, 106(40): 16925-16929, doi: 10.1073/pnas.0909248106.

Jørgensen, B.B., 1982. Mineralization of organic matter in the sea bed—the role of sulphate reduction. Nature, doi: 10.1038/296643a0.

Jørgensen, B.B., Böttcher, M.E., Lüschen, H., Neretin, L.N., Volkov, I.I., 2004. Anaerobic methane oxidation and a deep H2S sink generate isotopically heavy sulfides in Black Sea sediments 1. Geochimica et Cosmochimica Acta, 68(9): 2095-2118, doi: 10.1016/j.gca.2003.07.017.

Jørgensen, B.B., Kasten, S., 2006. Sulfur cycling and methane oxidation, Marine Geochemistry. Springer, pp. 271-309, doi: 10.1007/3-540-32144-6

Kah, L.C., Lyons, T.W., Frank, T.D., 2004. Low marine sulphate and protracted oxygenation of the Proterozoic biosphere. Nature, 431(7010): 834-838, doi: 10.1038/nature02974.

Kaufman, A.J., Corsetti, F.A., Varni, M.A., 2007. The effect of rising atmospheric oxygen on carbon and sulfur isotope anomalies in the Neoproterozoic Johnnie Formation, Death Valley, USA. Chemical Geology, 237: 47-63, doi: 10.1016/j.chemgeo.2006.06.023.

Kaufman, A.J., Hayes, J.M., Knoll, A.H., Germs, G.J.B., 1991. Isotopic compositions of carbonates and organic carbon from upper Proterozoic successions in Namibia: stratigraphic variation and the effects of diagenesis and metamorphism. Precambrian Research, 49(3–4): 301-327, doi: 10.1016/0301-9268(91)90039-D.

Kaufman, A.J., Jacobsen, S.B., Knoll, A.H., 1993. The Vendian record of Sr and C isotopic variations in seawater: implications for tectonics and paleoclimate. Earth and Planetary Science Letters, 120(3): 409-430, doi: 10.1016/0012-

821X(93)90254-7.
Kaufman, A.J., Jiang, G., Christie-Blick, N., Banerjee, D., Rai, V., 2006. Stable isotope record of the terminal Neoproterozoic Krol platform in the Lesser Himalayas of northern India. Precambrian Research, 147: 156-185.
Kaufman, A.J., Knoll, A.H., Narbonne, G.M., 1997. Isotopes, ice ages, and terminal Proterozoic earth history. Proceedings of the National Academy of Sciences, 94(13): 6600-6605.
Kempe, S., Kazmierczak, J., 1994. The role of alkalinity in the evolution of ocean chemistry, organization of living systems, and biocalcification processes. Bulletin de l'Institut océanographique: 61-117.
Kempe, S., Kazmierczak, J., Degens, E.T., 1989. The soda ocean concept and its bearing on biotic evolution, Origin, Evolution, and Modern Aspects of Biomineralization in Plants and Animals. Springer, pp. 29-43
Knauth, L.P., Kennedy, M.J., 2009. The late Precambrian greening of the Earth. Nature, 460: 728-732, doi: 10.1038/nature08213.
Knoll, A., Walter, M., Narbonne, G.U.Y., Christie-Blick, N., 2006. The Ediacaran Period: a new addition to the geologic time scale. Lethaia, 39(1): 13-30, doi: 10.1080/00241160500409223.
Knoll, A.H., 2003. Biomineralization and evolutionary history. Reviews in mineralogy and geochemistry, 54(1): 329-356, doi: 10.2113/0540329.
Knoll, A.H., Carroll, S.B., 1999. Early animal evolution: emerging views from comparative biology and geology. Science, 284: 2129-2137.
Knoll, A.H., Fischer, W.W., 2011. Skeletons and ocean chemistry: The long view. Ocean Acidification: 67-82.
Knoll, A.H., Walter, M.R., Narbonne, G.M., Christie-Blick, N., 2004. A new period for the geologic time scale. Science, 305(5684): 621-622, doi: 10.1126/science.1098803.
Kunimitsu, Y., Setsuda, Y., Furuyama, S., Wang, W., Kano, A., 2011. Ediacaran chemostratigraphy and paleoceanography at a shallow marine setting in northwestern Hunan Province, South China. Precambrian Research, 191(3–4): 194-208, doi: 10.1016/j.precamres.2011.09.006.
Laflamme, M., Xiao, S., Kowalewski, M., 2009. Osmotrophy in modular Ediacara organisms. Proceedings of the National Academy of Sciences, 106(34): 14438-14443.
Langmuir, D., Hall, P., Drever, J., 1997. Environmental Geochemistry. Prentice Hall, New Jersey.
Le Guerroué, E., Allen, P.A., Cozzi, A., Etienne, J.L., Fanning, M., 2006. 50 Myr recovery from the largest negative δ13C excursion in the Ediacaran ocean. Terra Nova, 18(2): 147-153, doi: 10.1111/j.1365-3121.2006.00674.x.
Le Guerroué, E., Cozzi, A., 2010. Veracity of Neoproterozoic negative C-isotope values: the termination of the Shuram negative excursion. Gondwana Research, 17(4): 653-661, doi: 10.1016/j.gr.2009.11.002.
Leavitt, W.D., 2014. On the mechanisms of sulfur isotope fractionation during microbial sulfate reduction. Dissertation.
Leavitt, W.D., Bradley, A.S., Halevy, I., Johnston, D.T., 2013. Influence of sulfate reduction rates on the Phanerozoic sulfur isotope record. Proc. Natl Acad.

Sci. USA, 110: 11244-11249.
Lenton, T.M., Boyle, R.A., Poulton, S.W., Shields-Zhou, G.A., Butterfield, N.J., 2014. Co-evolution of eukaryotes and ocean oxygenation in the Neoproterozoic era. Nature Geoscience, doi: 10.1038/NGEO2108.
Li, C., Love, G.D., Lyons, T.W., Fike, D.A., Sessions, A.L., Chu, X., 2010. A stratified redox model for the Ediacaran ocean. Science, 328(5974): 80-83, doi: 10.1126/science.1182369.
Ling, H.-F., Chen, X., Li, D., Wang, D., Shields-Zhou, G.A., Zhu, M., 2013. Cerium anomaly variations in Ediacaran–earliest Cambrian carbonates from the Yangtze Gorges area, South China: Implications for oxygenation of coeval shallow seawater. Precambrian Research, 225: 110-127, doi: 10.1016/j.precamres.2011.10.011.
Liu, P., Xiao, S., Yin, C., Chen, S., Zhou, C., Li, M., 2014. Ediacaran acanthomorphic acritarchs and other microfossils from chert nodules of the upper Doushantuo Formation in the Yangtze Gorges area, South China. Journal of Paleontology, 88(sp72): 1-139, doi: 10.1666/13-009.
Liu, P., Yin, C., Chen, S., Tang, F., Gao, L., 2013. The biostratigraphic succession of acanthomorphic acritarchs of the Ediacaran Doushantuo Formation in the Yangtze Gorges area, South China and its biostratigraphic correlation with Australia. Precambrian Research, 225: 29-43, doi: 10.1016/j.precamres.2011.07.009.
Loyd, S.J., Marenco, P.J., Hagadorn, J.W., Lyons, T.W., Kaufman, A.J., Sour-Tovar, F., Corsetti, F.A., 2013. Local δ34S variability in ~580Ma carbonates of northwestern Mexico and the Neoproterozoic marine sulfate reservoir. Precambrian Research, 224: 551-569, doi: 10.1016/j.precamres.2012.10.007.
Lu, M., Zhu, M., Zhang, J., Shields-Zhou, G., Li, G., Zhao, F., Zhao, X., Zhao, M., 2013. The DOUNCE event at the top of the Ediacaran Doushantuo Formation, South China: Broad stratigraphic occurrence and non-diagenetic origin. Precambrian Research, 225: 86-109, doi: 10.1016/j.precamres.2011.10.018.
Ludwig, K., 2008. Isoplot 3.6, Berkeley Geochronology Center Special Publication 4. 77.
Luo, G., Ono, S., Huang, J., Algeo, T.J., Li, C., Zhou, L., Robinson, A., Lyons, T.W., Xie, S., 2015. Decline in oceanic sulfate levels during the early Mesoproterozoic. Precambrian Research, 258(0): 36-47, doi: 10.1016/j.precamres.2014.12.014.
Lyons, T.W., Reinhard, C.T., Planavsky, N.J., 2014. The rise of oxygen in Earth's early ocean and atmosphere. Nature, 506(7488): 307-315, doi: 10.1038/nature13068.
Lyons, T.W., Walter, L.M., Gellatly, A.M., Martini, A.M., Blake, R.E., 2004. Sites of anomalous organic remineralization in the carbonate sediments of South Florida, USA: the sulfur cycle and carbonate-associated sulfate. Geological Society of America Special Papers, 379: 161-176, doi: 10.1130/0-8137-2379-5.161.
Macdonald, F.A., Strauss, J.V., Sperling, E.A., Halverson, G.P., Narbonne, G.M.,

Johnston, D.T., Kunzmann, M., Schrag, D.P., Higgins, J.A., 2013. The stratigraphic relationship between the Shuram carbon isotope excursion, the oxygenation of Neoproterozoic oceans, and the first appearance of the Ediacara biota and bilaterian trace fossils in northwestern Canada. Chemical Geology(0), doi: 10.1016/j.chemgeo.2013.05.032.

Maliva, R.G., Knoll, A.H., Siever, R., 1989. Secular change in chert distribution: a reflection of evolving biological participation in the silica cycle. Palaios: 519-532, doi: 10.2307/3514743.

Maloof, A.C., Porter, S.M., Moore, J.L., Dudás, F.Ö., Bowring, S.A., Higgins, J.A., Fike, D.A., Eddy, M.P., 2010. The earliest Cambrian record of animals and ocean geochemical change. Geological Society of America Bulletin, 122(11-12): 1731-1774, doi: 10.1130/B30346.1.

Marenco, P.J., Corsetti, F.A., Hammond, D.E., Kaufman, A.J., Bottjer, D.J., 2008. Oxidation of pyrite during extraction of carbonate associated sulfate. Chemical Geology, 247(1–2): 124-132, doi: 10.1016/j.chemgeo.2007.10.006.

Martin, A.J., Southworth, S., Collins, J.C., Fisher, S.W., Kingman, E.R., 2015. Laurentian and Amazonian sediment sources to Neoproterozoic–lower Paleozoic Maryland Piedmont rocks. Geosphere, 11(4): 1042-1061, doi: 10.1130/GES01140.1.

Mazumdar, A., Strauss, H., 2006. Sulfur and strontium isotopic compositions of carbonate and evaporite rocks from the late Neoproterozoic–early Cambrian Bilara Group (Nagaur-Ganganagar Basin, India): Constraints on intrabasinal correlation and global sulfur cycle. Precambrian Research, 149(3–4): 217-230, doi: 10.1016/j.precamres.2006.06.008.

McArthur, J., Howarth, R., Shields, G., 2012. Strontium isotope stratigraphy. A geologic time scale: 127-144.

McFadden, K.A., Huang, J., Chu, X., Jiang, G., Kaufman, A.J., Zhou, C., Yuan, X., Xiao, S., 2008. Pulsed oxidation and biological evolution in the Ediacaran Doushantuo Formation. Proceedings of the National Academy of Sciences, 105(9): 3197-3202, doi: 10.1073/pnas.0708336105.

Meister, P., 2013. Two opposing effects of sulfate reduction on carbonate precipitation in normal marine, hypersaline, and alkaline environments. Geology, 41(4): 499-502, doi: 10.1130/G34185.1.

Melezhik, V.A., Pokrovsky, B.G., Fallick, A.E., Kuznetsov, A.B., Bujakaite, M.I., 2009. Constraints on 87Sr/86Sr of Late Ediacaran seawater: insight from Siberian high-Sr limestones. Journal of the Geological Society, 166(1): 183-191, doi: 10.1144/0016-76492007-171.

Meyer, M., D SCHIFFBAUER, J., Xiao, S., Cai, Y., Hua, H., 2012. Taphonomy of the upper Ediacaran enigmatic ribbonlike fossil Shaanxilithes. Palaios, 27(5): 354-372.

Meyer, M., Xiao, S., Gill, B.C., Schiffbauer, J.D., Chen, Z., Zhou, C., Yuan, X., 2014. Interactions between Ediacaran animals and microbial mats: Insights from Lamonte trevallis, a new trace fossil from the Dengying Formation of South China. Palaeogeography, Palaeoclimatology, Palaeoecology, 396: 62-74.

Meysman, F.J., Middelburg, J.J., Heip, C.H., 2006. Bioturbation: a fresh look at Darwin's last idea. Trends in Ecology & Evolution, 21(12): 688-695.
Mills, D.B., Ward, L.M., Jones, C., Sweeten, B., Forth, M., Treusch, A.H., Canfield, D.E., 2014. Oxygen requirements of the earliest animals. Proceedings of the National Academy of Sciences, 111(11): 4168-4172.
Moore, T.S., Murray, R., Kurtz, A., Schrag, D., 2004. Anaerobic methane oxidation and the formation of dolomite. Earth and Planetary Science Letters, 229(1): 141-154, doi: 10.1016/j.epsl.2004.10.015.
Mora, C., Wei, C.-L., Rollo, A., Amaro, T., Baco, A.R., Billett, D., Bopp, L., Chen, Q., Collier, M., Danovaro, R., 2013. Biotic and human vulnerability to projected changes in ocean biogeochemistry over the 21st century. PLoS biology, 11(10): e1001682.
Muscente, A.D., Hawkins, A.D., Xiao, S., 2015. Fossil preservation through phosphatization and silicification in the Ediacaran Doushantuo Formation (South China): a comparative synthesis. Palaeogeography, Palaeoclimatology, Palaeoecology(0), doi: http://dx.doi.org/10.1016/j.palaeo.2014.10.013.
Narbonne, G.M., 2004. Modular construction of early Ediacaran complex life forms. Science, 305(5687): 1141-1144.
Narbonne, G.M., 2005. The Ediacara biota: Neoproterozoic origin of animals and their ecosystems. Annu. Rev. Earth Planet. Sci., 33: 421-442, doi: 10.1146/annurev.earth.33.092203.122519.
Narbonne, G.M., Xiao, S., Shields, G.A., Gehling, J.G., 2012. Chapter 18 - The Ediacaran Period, The Geologic Time Scale. Elsevier, Boston, pp. 413-435, doi: 10.1016/B978-0-444-59425-9.00018-4
Nursall, J.R., 1959. Oxygen as a Prerequisite to the Origin of the Metazoa. Nature, 183(4669): 1170-1172, doi: 10.1038/1831170b0.
Och, L.M., Shields-Zhou, G.A., 2012. The Neoproterozoic oxygenation event: Environmental perturbations and biogeochemical cycling. Earth-Science Reviews, 110(1–4): 26-57, doi: 10.1016/j.earscirev.2011.09.004.
Ohfuji, H., Rickard, D., 2005. Experimental syntheses of framboids—a review. Earth-Science Reviews, 71(3): 147-170, doi: 10.1016/j.earscirev.2005.02.001.
Palmer, M., Edmond, J., 1992. Controls over the strontium isotope composition of river water. Geochimica et Cosmochimica Acta, 56(5): 2099-2111, doi: 10.1016/0016-7037(92)90332-D.
Paris, G., Adkins, J., Sessions, A., Webb, S., Fischer, W., 2014. Neoarchean carbonate–associated sulfate records positive Δ33S anomalies. Science, 346(6210): 739-741, doi: 10.1126/science.1258966.
Paytan, A., Kastner, M., Martin, E., Macdougall, J., Herbert, T., 1993. Marine barite as a monitor of seawater strontium isotope composition. Nature, 366(6454): 445-449, doi: 10.1038/366445a0.
Peng, Y., Bao Huiming, P.M.L., Kaufman J. Alan, Jiang Ganqing, Boyd Dustin, Wang Qinxian, Zhou Chuanming, Yuan Xunlai, Xiao Shuhai, Sean, L., 2014. Widespread contamination of carbonate-associated sulfate by present-day secondary atmospheric sulfate: evidence from triple oxygen isotopes. Geology, 42(9): 815-818, doi: 10.1130/G35852.1.

Penny, A., Wood, R., Curtis, A., Bowyer, F., Tostevin, R., Hoffman, K.-H., 2014. Ediacaran metazoan reefs from the Nama Group, Namibia. Science, 344(6191): 1504-1506, doi: 10.1126/science.1253393.
Peters, S.E., Gaines, R.R., 2012. Formation of the 'Great Unconformity' as a trigger for the Cambrian explosion. Nature, 484(7394): 363-366, doi: 10.1038/nature10969.
Peterson, K.J., Butterfield, N.J., 2005. Origin of the Eumetazoa: testing ecological predictions of molecular clocks against the Proterozoic fossil record. Proceedings of the National Academy of Sciences of the United States of America, 102(27): 9547-9552, doi: 10.1073/pnas.0503660102.
Pokrovskii, B., Melezhik, V., Bujakaite, M., 2006a. Carbon, oxygen, strontium, and sulfur isotopic compositions in late Precambrian rocks of the Patom Complex, central Siberia: Communication 1. results, isotope stratigraphy, and dating problems. Lithology and Mineral Resources, 41(5): 450-474, doi: 10.1134/s0024490206050063.
Pokrovskii, B.G., Melezhik, V.A., Bujakaite, M.I., 2006b. Carbon, oxygen, strontium, and sulfur isotopic compositions in late Precambrian rocks of the Patom Complex, central Siberia: Communication 2. Nature of carbonates with ultralow and ultrahigh δ13C values. Lithology and Mineral Resources, 41(6): 576-587, doi: 10.1134/s002449020606006x.
Pokrovsky, B.G., Bujakaite, M.I., 2015. Geochemistry of C, O, and Sr isotopes in the Neoproterozoic carbonates from the southwestern Patom paleobasin, southern Middle Siberia. Lithology and Mineral Resources, 50(2): 144-169, doi: 10.1134/S0024490215010046.
Porter, S., 2011. The rise of predators. Geology, 39(6): 607-608, doi: 10.1130/focus062011.1.
Porter, S.M., 2007. Seawater chemistry and early carbonate biomineralization. Science, 316(5829): 1302-1302.
Porter, S.M., 2010. Calcite and aragonite seas and the de novo acquisition of carbonate skeletons. Geobiology, 8(4): 256-277, doi: 10.1111/j.1472-4669.2010.00246.x.
Reuschel, M., Melezhik, V., Whitehouse, M., Lepland, A., Fallick, A., Strauss, H., 2012. Isotopic evidence for a sizeable seawater sulfate reservoir at 2.1 Ga. Precambrian Research, 192: 78-88, doi: 10.1016/j.precamres.2011.10.013.
Richter, F.M., Rowley, D.B., DePaolo, D.J., 1992. Sr isotope evolution of seawater: the role of tectonics. Earth and Planetary Science Letters, 109(1): 11-23.
Ries, J.B., Fike, D.A., Pratt, L.M., Lyons, T.W., Grotzinger, J.P., 2009. Superheavy pyrite (δ34Spyr>δ34SCAS) in the terminal Proterozoic Nama Group, southern Namibia: A consequence of low seawater sulfate at the dawn of animal life. Geology, 37(8): 743-746, doi: 10.1130/g25775a.1.
Rothman, D.H., Hayes, J.M., Summons, R.E., 2003. Dynamics of the Neoproterozoic carbon cycle. Proceedings of the National Academy of Sciences, 100(14): 8124-8129, doi: 10.1073/pnas.0832439100.
Sahoo, S.K., Planavsky, N.J., Kendall, B., Wang, X., Shi, X., Scott, C., Anbar, A.D., Lyons, T.W., Jiang, G., 2012. Ocean oxygenation in the wake of the Marinoan glaciation. Nature, 489(7417): 546-549, doi:

10.1038/nature11445.
Sawaki, Y., Ohno, T., Tahata, M., Komiya, T., Hirata, T., Maruyama, S., Windley, B.F., Han, J., Shu, D., Li, Y., 2010. The Ediacaran radiogenic Sr isotope excursion in the Doushantuo Formation in the Three Gorges area, South China. Precambrian Research, 176(1–4): 46-64, doi: 10.1016/j.precamres.2009.10.006.
Sawaki, Y., Tahata, M., Ohno, T., Komiya, T., Hirata, T., Maruyama, S., Han, J., Shu, D., 2014. The anomalous Ca cycle in the Ediacaran ocean: evidence from Ca isotopes preserved in carbonates in the Three Gorges area, South China. Gondwana Research, 25(3): 1070-1089, doi: 10.1016/j.gr.2013.03.008.
Saylor, B.Z., Kaufman, A.J., Grotzinger, J.P., Urban, F., 1998. A composite reference section for terminal Proterozoic strata of southern Namibia. Journal of Sedimentary Research, 68(6): 1223-1235, doi: 10.2110/jsr.68.1223.
Schiffbauer, J.D., Xiao, S., Cai, Y., Wallace, A.F., Hua, H., Hunter, J., Xu, H., Peng, Y., Kaufman, A.J., 2014. A unifying model for Neoproterozoic–Palaeozoic exceptional fossil preservation through pyritization and carbonaceous compression. Nature Communications, 5, doi: 10.1038/ncomms6754.
Schrag, D.P., Higgins, J.A., Macdonald, F.A., Johnston, D.T., 2013. Authigenic carbonate and the history of the global carbon cycle. Science, 339(6119): 540-543, doi: 10.1126/science.1229578.
Shen, Y., Canfield, D.E., Knoll, A.H., 2002. Middle Proterozoic ocean chemistry: Evidence from the McArthur Basin, northern Australia. American Journal of Science, 302(2): 81-109, doi: 10.2475/ajs.302.2.81.
Shields-Zhou, G., Och, L., 2011. The case for a Neoproterozoic oxygenation event: geochemical evidence and biological consequences. GSA Today, 21(3): 4-11, doi: 10.1130/GSATG102A.1.
Shields, G., 2007. A normalised seawater strontium isotope curve: possible implications for Neoproterozoic-Cambrian weathering rates and the further oxygenation of the Earth. eEarth, 2(2): 35-42, doi: 10.5194/ee-2-35-2007.
Siegmund, H., Erdtmann, B.-D., 1994. Facies and diagenesis of some upper proterozoic dolomites of South China. Facies, 31(1): 255-263.
Sim, M.S., Bosak, T., Ono, S., 2011. Large sulfur isotope fractionation does not require disproportionation. Science, 333(6038): 74-77, doi: 10.1126/science.1205103.
Simkiss, K., 1977. Biomineralization and detoxification. Calcified Tissue Research, 24(1): 199-200, doi: 10.1007/BF02223316.
Simkiss, K., 1989. Biomineralisation in the context of geological time. Transactions of the Royal Society of Edinburgh: Earth Sciences, 80(3-4): 193-199, doi: 10.1017/S0263593300028637.
Spötl, C., 2011. Long‐term performance of the Gasbench isotope ratio mass spectrometry system for the stable isotope analysis of carbonate microsamples. Rapid Communications in Mass Spectrometry, 25(11): 1683-1685.
Stanley, S.M., 2006. Influence of seawater chemistry on biomineralization throughout Phanerozoic time: Paleontological and experimental evidence. Palaeogeography, Palaeoclimatology, Palaeoecology, 232(2): 214-236, doi:

10.1016/j.palaeo.2005.12.010.
Stanley, S.M., Hardie, L.A., 1998. Secular oscillations in the carbonate mineralogy of reef-building and sediment-producing organisms driven by tectonically forced shifts in seawater chemistry. Palaeogeography, Palaeoclimatology, Palaeoecology, 144(1): 3-19, doi: 10.1016/S0031-0182(98)00109-6.
Steiner, M., Li, G., Qian, Y., Zhu, M., 2004. Lower Cambrian small shelly fossils of northern Sichuan and southern Shaanxi (China), and their biostratigraphic importance. Geobios, 37(2): 259-275, doi: 10.1016/j.geobios.2003.08.001.
Strauss, H., Banerjee, D.M., Kumar, V., 2001. The sulfur isotopic composition of Neoproterozoic to early Cambrian seawater — evidence from the cyclic Hanseran evaporites, NW India. Chemical Geology, 175(1–2): 17-28, doi: 10.1016/S0009-2541(00)00361-2.
Tahata, M., Ueno, Y., Ishikawa, T., Sawaki, Y., Murakami, K., Han, J., Shu, D., Li, Y., Guo, J., Yoshida, N., Komiya, T., 2013. Carbon and oxygen isotope chemostratigraphies of the Yangtze platform, South China: Decoding temperature and environmental changes through the Ediacaran. Gondwana Research, 23(1): 333-353, doi: 10.1016/j.gr.2012.04.005.
Wacey, D., Kilburn, M.R., Saunders, M., Cliff, J.B., Kong, C., Liu, A.G., Matthews, J.J., Brasier, M.D., 2015. Uncovering framboidal pyrite biogenicity using nano-scale CNorg mapping. Geology, 43(1): 27-30, doi: 10.1130/G36048.1.
Wang, L., Shi, X., Jiang, G., 2012a. Pyrite morphology and redox fluctuations recorded in the Ediacaran Doushantuo Formation. Palaeogeography, Palaeoclimatology, Palaeoecology, 333–334(0): 218-227, doi: 10.1016/j.palaeo.2012.03.033.
Wang, W., Zhou, C., Yuan, X., Chen, Z., Xiao, S., 2012b. A pronounced negative δ13C excursion in an Ediacaran succession of western Yangtze Platform: A possible equivalent to the Shuram event and its implication for chemostratigraphic correlation in South China. Gondwana Research, 22(3–4): 1091-1101, doi: 10.1016/j.gr.2012.02.017.
Wang, X., Shi, X., Jiang, G., Tang, D., 2014. Organic carbon isotope gradient and ocean stratification across the late Ediacaran-Early Cambrian Yangtze Platform. Science China Earth Sciences, 57(5): 919-929, doi: 10.1007/s11430-013-4732-0.
Watkins, J.M., Hunt, J.D., Ryerson, F.J., DePaolo, D.J., 2014. The influence of temperature, pH, and growth rate on the δ 18 O composition of inorganically precipitated calcite. Earth and Planetary Science Letters, 404: 332-343, doi: 10.1016/j.epsl.2014.07.036.
Weiner, S., Dove, P.M., 2003. An overview of biomineralization processes and the problem of the vital effect. Reviews in Mineralogy and Geochemistry, 54(1): 1-29.
Wilkin, R., Barnes, H., 1996. Pyrite formation by reactions of iron monosulfides with dissolved inorganic and organic sulfur species. Geochimica et Cosmochimica Acta, 60(21): 4167-4179, doi: 10.1016/S0016-7037(97)81466-4.
Wing, B.A., Halevy, I., 2014. Intracellular metabolite levels shape sulfur isotope fractionation during microbial sulfate respiration. Proceedings of the

National Academy of Sciences, 111(51): 18116-18125.
Wood, R., Curtis, A., 2015. Extensive metazoan reefs from the Ediacaran Nama Group, Namibia: the rise of benthic suspension feeding. Geobiology, 13: 112-122, doi: 10.1111/gbi.12122.
Wood, R.A., Poulton, S.W., Prave, A.R., Hoffmann, K.H., Clarkson, M.O., Guilbaud, R., Lyne, J.W., Tostevin, R., Bowyer, F., Penny, A.M., Curtis, A., Kasemann, S.A., 2015. Dynamic redox conditions control late Ediacaran metazoan ecosystems in the Nama Group, Namibia. Precambrian Research, 261(0): 252-271, doi: 10.1016/j.precamres.2015.02.004.
Wu, N., Farquhar, J., 2013. Metabolic rates and sulfur cycling in the geologic record. Proceedings of the National Academy of Sciences, 110(28): 11217-11218, doi: 10.1073/pnas.1309726110.
Wu, N., Farquhar, J., Fike, D.A., 2015. Ediacaran sulfur cycle: Insights from sulfur isotope measurements (Δ33S and δ34S) on paired sulfate–pyrite in the Huqf Supergroup of Oman. Geochimica et Cosmochimica Acta, 164(0): 352-364, doi: 10.1016/j.gca.2015.05.031.
Xiao, S., 2014. Oxygen and early animal evolution. In: Turekian, H.D.H.K. (Ed.), Treatise on Geochemistry (Second Edition). Elsevier, Oxford, pp. 231-250, doi: 10.1016/B978-0-08-095975-7.01310-3
Xiao, S., Hagadorn, J.W., Zhou, C., Yuan, X., 2007. Rare helical spheroidal fossils from the Doushantuo Lagerstätte: Ediacaran animal embryos come of age? Geology, 35(2): 115-118, doi: 10.1130/G23277A.1.
Xiao, S., Kaufman, A.J., 2006. Neoproterozoic geobiology and paleobiology, 27. Springer.
Xiao, S., Laflamme, M., 2009. On the eve of animal radiation: phylogeny, ecology and evolution of the Ediacara biota. Trends in Ecology & Evolution, 24(1): 31-40, doi: 10.1016/j.tree.2008.07.015.
Xiao, S., McFadden, K.A., Peek, S., Kaufman, A.J., Zhou, C., Jiang, G., Hu, J., 2012. Integrated chemostratigraphy of the Doushantuo Formation at the northern Xiaofenghe section (Yangtze Gorges, South China) and its implication for Ediacaran stratigraphic correlation and ocean redox models. Precambrian Research, 192–195(0): 125-141, doi: 10.1016/j.precamres.2011.10.021.
Xiao, S., Muscente, A., Chen, L., Zhou, C., Schiffbauer, J.D., Wood, A.D., Polys, N.F., Yuan, X., 2014a. The Weng'an biota and the Ediacaran radiation of multicellular eukaryotes. National Science Review: nwu061, doi: 10.1093/nsr/nwu061.
Xiao, S., Schiffbauer, J.D., McFadden, K.A., Hunter, J., 2010. Petrographic and SIMS pyrite sulfur isotope analyses of Ediacaran chert nodules: Implications for microbial processes in pyrite rim formation, silicification, and exceptional fossil preservation. Earth and Planetary Science Letters, 297(3–4): 481-495, doi: 10.1016/j.epsl.2010.07.001.
Xiao, S., Shen, B., Zhou, C., Xie, G., Yuan, X., 2005. A uniquely preserved Ediacaran fossil with direct evidence for a quilted bodyplan. Proceedings of the National Academy of Sciences of the United States of America, 102(29): 10227-10232, doi: 10.1073/pnas.0502176102.
Xiao, S., Yuan, X., Steiner, M., Knoll, A.H., 2002. Macroscopic carbonaceous

compressions in a terminal Proterozoic shale: A systematic reassessment of the Miaohe Biota, South China. Journal of Paleontology, 76(2): 347-376, doi: 10.1666/0022-3360(2002)076<0347:mcciat>2.0.co;2.
Xiao, S., Zhang, Y., Knoll, A.H., 1998. Three-dimensional preservation of algae and animal embryos in a Neoproterozoic phosphorite. Nature, 391(6667): 553-558, doi: 10.1038/35318.
Xiao, S., Zhou, C., Liu, P., Wang, D., Yuan, X., 2014b. Phosphatized acanthomorphic acritarchs and related microfossils from the Ediacaran Doushantuo Formation at Weng'an (South China) and their implications for biostratigraphic correlation. Journal of Paleontology, 88(1): 1-67, doi: 10.1666/12-157R.
Yin, Z., Zhu, M., Davidson, E.H., Bottjer, D.J., Zhao, F., Tafforeau, P., 2015a. Sponge grade body fossil with cellular resolution dating 60 Myr before the Cambrian. Proceedings of the National Academy of Sciences, 112(12): E1453-E1460, doi: 10.1073/pnas.1414577112.
Yin, Z., Zhu, M., Davidson, E.H., Bottjer, D.J., Zhao, F., Tafforeau, P., 2015b. Sponge grade body fossil with cellular resolution dating 60 Myr before the Cambrian. Proceedings of the National Academy of Sciences: 201414577.
Young, G.M., 2013. Evolution of Earth’s climatic system: Evidence from ice ages, isotopes, and impacts. GSA Today, 23(10): 4-10, doi: 10.1130/GSATG183A.1.
Young, G.M., 2015. Environmental upheavals of the Ediacaran period and the Cambrian “explosion” of animal life. Geoscience Frontiers, 6: 523-535, doi: 10.1016/j.gsf.2014.09.001.
Yuan, X., Chen, Z., Xiao, S., Zhou, C., Hua, H., 2011. An early Ediacaran assemblage of macroscopic and morphologically differentiated eukaryotes. Nature, 470(7334): 390-393, doi: 10.1038/nature09810.
Yuan, X., Xiao, S., Taylor, T., 2005. Lichen-like symbiosis 600 million years ago. Science, 308(5724): 1017-1020, doi: 10.1126/science.1111347.
Zhang, F., Kendall, B., Cui, H., Anbar, A.D., Xiao, S., Kaufman, A.J., 2015. An episode of widespread ocean anoxia during the latest Ediacaran Period revealed by light U isotope compositions in carbonates. GSA abstract.
Zhelezinskaia, I., Kaufman, A.J., Farquhar, J., Cliff, J., 2014. Large sulfur isotope fractionations associated with Neoarchean microbial sulfate reduction. Science, 346(6210): 742-744, doi: 10.1126/science.1256211.
Zhou, C., Jiang, S., Xiao, S., Chen, Z., Yuan, X., 2012. Rare earth elements and carbon isotope geochemistry of the Doushantuo Formation in South China: Implication for middle Ediacaran shallow marine redox conditions. Chinese Science Bulletin, 57(16): 1998-2006, doi: 10.1007/s11434-012-5082-6.
Zhou, C., Xiao, S., 2007. Ediacaran δ13C chemostratigraphy of South China. Chemical Geology, 237(1–2): 89-108, doi: 10.1016/j.chemgeo.2006.06.021.
Zhu, B., Becker, H., Jiang, S.-Y., Pi, D.-H., Fischer-Gödde, M., Yang, J.-H., 2013a. Re–Os geochronology of black shales from the Neoproterozoic Doushantuo Formation, Yangtze platform, South China. Precambrian Research, 225(0): 67-76, doi: 10.1016/j.precamres.2012.02.002.

Zhu, M., Lu, M., Zhang, J., Zhao, F., Li, G., Yang, A., Zhao, X., Zhao, M., 2013b. Carbon isotope chemostratigraphy and sedimentary facies evolution of the Ediacaran Doushantuo Formation in western Hubei, South China. Precambrian Research, 225(0): 7-28, doi: 10.1016/j.precamres.2011.07.019.

Zhu, M., Zhang, J., Yang, A., 2007. Integrated Ediacaran (Sinian) chronostratigraphy of South China. Palaeogeography, Palaeoclimatology, Palaeoecology, 254(1–2): 7-61, doi: 10.1016/j.palaeo.2007.03.025.

Zhuravlev, A.Y., Liñán, E., Vintaned, J.A.G., Debrenne, F., Fedorov, A.B., 2012. New finds of skeletal fossils in the terminal Neoproterozoic of the Siberian Platform and Spain. Acta Palaeontologica Polonica, 57(1): 205-224, doi: 10.4202/app.2010.0074.